AFRL-AFOSR-VA-TR-2024-0117

Instability Free Three-Dimensional Hypersonic Laminar Boundary Layer Steady-States for Linear and Nonlinear Stability Analyses

Alves, Leonardo
UNIVERSITY FEDERAL FLUMINENSE
RUA MIGUEL DE FRIAS 09
ICARAI NITEROI, , RJ 24220
BR

01/22/2024
Final Technical Report

Air Force Research Laboratory
Air Force Office of Scientific Research
Arlington, Virginia 22203
Air Force Materiel Command

REPORT DOCUMENTATION PAGE

PLEASE DO NOT RETURN YOUR FORM TO THE ABOVE ORGANIZATION.

1. REPORT DATE	2. REPORT TYPE	3. DATES COVERED	
20240122	Final	START DATE 20180815	END DATE 20220814

4. TITLE AND SUBTITLE
Instability Free Three-Dimensional Hypersonic Laminar Boundary Layer Steady-States for Linear and Nonlinear Stability Analyses

5a. CONTRACT NUMBER	5b. GRANT NUMBER	5c. PROGRAM ELEMENT NUMBER
	FA9550-18-1-0419	61102F
5d. PROJECT NUMBER	**5e. TASK NUMBER**	**5f. WORK UNIT NUMBER**

6. AUTHOR(S)
Leonardo Alves

7. PERFORMING ORGANIZATION NAME(S) AND ADDRESS(ES)
UNIVERSITY FEDERAL FLUMINENSE
RUA MIGUEL DE FRIAS 09
ICARAI NITEROI RJ 24220
BR

8. PERFORMING ORGANIZATION REPORT NUMBER

9. SPONSORING/MONITORING AGENCY NAME(S) AND ADDRESS(ES)	10. SPONSOR/MONITOR'S ACRONYM(S)	11. SPONSOR/MONITOR'S REPORT NUMBER(S)
Air Force Office of Scientific Research 875 N. Randolph St. Room 3112 Arlington, VA 22203	AFRL/AFOSR IOS	AFRL-AFOSR-VA-TR-2024-0117

12. DISTRIBUTION/AVAILABILITY STATEMENT
A Distribution Unlimited: PB Public Release

13. SUPPLEMENTARY NOTES

14. ABSTRACT
The major goal of this research project is to investigate the numerical computation of disturbance free and accurate steady-states for high-speed flows. Doing so is quite challenging due to physical and numerical reasons that are often intertwined. A major reason, also present in their low- speed counterparts, is related to disturbance growth due to physical instabilities in the flow. This means numerical simulations must be able to dampen these disturbances in order to reach disturbance free steady-states, i.e. they must be numerically stable even when the flow is physical unstable. Another major reason, now unique to high-speed flows, comes from compressibility effects, which are introduced by high temperature gradients and/or high Mach numbers, in the case of pure substances. These effects create many flow features, such as acoustic waves, shock waves, expansion fans, contact discontinuities and so on. This means numerical simulations must be able to properly capture such features in order to reach accurate steady-states. The procedures required to achieve steady-states with both characteristics are discussed in detail in this report.

15. SUBJECT TERMS

16. SECURITY CLASSIFICATION OF:			17. LIMITATION OF ABSTRACT	18. NUMBER OF PAGES
a. REPORT U	b. ABSTRACT U	c. THIS PAGE U	SAR	227

19a. NAME OF RESPONSIBLE PERSON	19b. PHONE NUMBER *(Include area code)*
ROGER GREENWOOD	000-000-0000

Standard Form 298 (Rev.5/2020)
Prescribed by ANSI Std. Z39.18

REPORT DOCUMENTATION PAGE

Form Approved
OMB No. 0704-0188

PLEASE DO NOT RETURN YOUR FORM TO THE ABOVE ORGANIZATION.

1. REPORT DATE *(DD-MM-YYYY)*	2. REPORT TYPE	3. DATES COVERED *(From - To)*
02-01-2024	Final Performance Report	Aug 15th, 2018 - Aug 14th, 2022

4. TITLE AND SUBTITLE

Instability Free Three-Dimensional Hypersonic Laminar Boundary-Layer Steady-States for Linear and Nonlinear Stability Analyses

5a. CONTRACT NUMBER

5b. GRANT NUMBER
FA9550-18-1-0419

5c. PROGRAM ELEMENT NUMBER

6. AUTHOR(S)

Alves, Leonardo S. de B.

5d. PROJECT NUMBER

5e. TASK NUMBER

5f. WORK UNIT NUMBER

7. PERFORMING ORGANIZATION NAME(S) AND ADDRESS(ES)

Universidade Federal Fluminense
Rua Miguel de Frias, 9
Icaraí, Niterói, RJ 24220-900, Brazil

8. PERFORMING ORGANIZATION REPORT NUMBER

9. SPONSORING/MONITORING AGENCY NAME(S) AND ADDRESS(ES)

Daniel Montes & Roger Greenwood
Souther Office of Aerospace Research & Development
Air Force Office of Scientific Research
Las Condes, Santiago, Chile

10. SPONSOR/MONITOR'S ACRONYM(S)
SOARD/AFOSR

11. SPONSOR/MONITOR'S REPORT NUMBER(S)

12. DISTRIBUTION/AVAILABILITY STATEMENT

Approved for public release, distribution unlimited.

13. SUPPLEMENTARY NOTES

14. ABSTRACT

The major goal of this research project is to investigate the numerical computation of disturbance free and accurate steady-states for high-speed flows. Doing so is quite challenging due to physical and numerical reasons that are often intertwined. A major reason, also present in their low-speed counterparts, is related to disturbance growth due to physical instabilities in the flow. This means numerical simulations must be able to dampen these disturbances in order to reach disturbance free steady-states, i.e. they must be numerically stable even when the flow is physical unstable. Another major reason, now unique to high-speed flows, comes from compressibility effects, which are introduced by high temperature gradients and/or high Mach numbers, in the case of pure substances. These effects create many flow features, such as acoustic waves, shock waves, expansion fans, contact discontinuities and so on. This means numerical simulations must be able to properly capture such features in order to reach accurate steady-states. The procedures required to achieve steady-states with both characteristics are discussed in detail in this report.

15. SUBJECT TERMS

16. SECURITY CLASSIFICATION OF:			17. LIMITATION OF ABSTRACT	18. NUMBER OF PAGES	19a. NAME OF RESPONSIBLE PERSON
a. REPORT	b. ABSTRACT	c. THIS PAGE			19b. TELEPHONE NUMBER *(Include area code)*
unclassified	unclassified	unclassified	UU		

Standard Form 298 (Rev. 8/98)
Prescribed by ANSI Std. Z39.18

Final Performance Report
on

Instability Free Three-Dimensional Hypersonic Laminar Boundary-Layer Steady-States for Linear and Nonlinear Stability Analyses

for
AFOSR Contract/Grant FA9550-18-1-0419

Prepared by

Leonardo S. de B. Alves
Principal Investigator
Departamento de Engenharia Mecânica,
Universidade Federal Fluminense,
Rua Passo da Pátria 156, Escola de Engeharia,
São Domingos, Niterói, RJ 24210-240, Brazil

Submitted to

Roger Greenwood
Director
Southern Office of Aerospace Research & Development
Air Force Office of Scientific Research
Av. Andres Belo, 2800,
Las Condes, Santiago, Chile

August 14th, 2022

Executive Summary

The major goal of this research project is to investigate the numerical computation of disturbance free and accurate steady-states for high-speed flows. Doing so is quite challenging due to physical and numerical reasons that are often intertwined. A major reason, also present in their low-speed counterparts, is related to disturbance growth due to physical instabilities in the flow. This means numerical simulations must be able to dampen these disturbances in order to reach disturbance free steady-states, i.e. they must be numerically stable even when the flow is physical unstable. Another major reason, now unique to high-speed flows, comes from compressibility effects, which are introduced by high temperature gradients and/or high Mach numbers, in the case of pure substances. These effects create many flow features, such as acoustic waves, shock waves, expansion fans, contact discontinuities and so on. This means numerical simulations must be able to properly capture such features in order to reach accurate steady-states. The procedures required to achieve steady-states with both characteristics, namely disturbance free and accurate, fall into three different categories. They are now discussed in detail using high-speed flows from each category as examples whose steady-states have been found difficult to generate.

All high-speed flows in the first category are physically stable. This means any time-accurate numerical method capable of simulating such physics can reach a disturbance free steady-state when run for large enough times. In other words, all disturbances originally present in the initial condition are eventually damped. Explicit marching schemes can then be employed, since a linear analysis reveals they are numerically stable for physically stable flows when small enough time steps are used. Both explicit Euler and third-order strong-stability-preserving explicit Runge-Kutta schemes were chosen here for this purpose. Hence, the major concern in this category is to accurately capture all the spatial flow features present in the steady-state. In order to do so here, low and high accuracy-order spatial discretization schemes were chosen. Low means second-order total-variation-diminishing schemes for the inviscid fluxes and second-order conservative central-difference schemes for the viscous fluxes whereas high means fifth-order weighted essentially non-oscillatory schemes for the inviscid fluxes and fourth-order conservative central-difference schemes for the viscous terms. Furthermore, inviscid fluxes can be treated using either flux-difference splitting, such as Roe, HLL and Roe-HLL schemes, or flux-vector splitting, such as the characteristic-wise Lax-Friedrichs scheme. These methods were verified here using several test cases that include scalar equations as well the one, two and three-dimensional compressible Navier-Stokes equations. Having verified these methods, two different problems were then studied at length. The first problem is the supersonic flow upstream of a two-dimensional cylinder. It is a classical problem often used to evaluate the accuracy of numerical schemes because of

the carbuncle phenomenon. It was studied in three steps. In the first step, all spatially grid converged simulations were run until the maximum residue converged in time. This approach led to accurate and symmetrical, i.e. no carbuncle, steady-states. In the second step, these steady-states were used as base flows for linear, modal and non-modal, global stability analyses. The asymptotic stability of this flow was confirmed by the former, but the latter revealed the presence of transient growth in the bow shock. In the third and final step, time/space accurate direct numerical simulations were performed using as initial conditions superpositions between these steady-states and low amplitude random disturbances introduced at the cylinder wall. After they propagate upstream, hit the shock and the impact of this initial burst dissipates, it is possible to observe the growth of a disturbance located at the bow shock. The fact that this disturbance has a low amplitude, grows algebraically in time by the same amount predicted by non-modal theory, approximately, and has a spatial profile very similar to the optimal non-modal eigenfunction suggests these simulations were indeed able to capture a nearly optimal transient growth for the first time in the literature. The second problem is the supersonic flow over a two-dimensional compression ramp. Steady-states were first generated using low spatial accuracy-order schemes. This choice was motivated by the fact that all similar studies found in the literature employed second-order schemes as well. However, maximum residue convergence in time was only possible when the Reynolds number was much smaller and the grid size was much larger than the ones employed in these same studies. Although spatial profiles around the bubble region appeared reasonably well grid converged, the leading edge shock was not. As a consequence, it introduced small amplitude disturbances that propagated into the bubble and prevented residue convergence in time. In order to fix this issue, high-order schemes were employed instead. This lead to maximum residue convergence in time and spatial grid convergence, i.e. disturbance free and accurate steady-states. These steady-states were then compared to triple deck theory, showing good agreement within the recirculation bubble region. They were also used as base flows for linear, modal and non-modal, global stability analyses. The former was used to calculate the neutral curve and, hence, the critical Reynolds and wave numbers. These, in turn, indicate that the onset of instability occurs to stationary three-dimensional disturbances. Two-dimensional disturbances, on the other hand, are asymptotically stable but seem to approach marginal stability as the Reynolds number increases. Furthermore, a group of convectively unstable oscillatory disturbances was found just upstream of the compression ramp. They behave as acoustic modes trapped within an impedance well, formed between the wall and the edge of the boundary-layer, that realign with the separation shock after they escape from the boundary-layer. Finally, the non-modal analysis revealed the existence of moderate transient growth at neutral conditions. It also increases in strength as a function of the Reynolds number squared.

All physically unstable high-speed flows are included in the second and third categories. Arguably, most of them are included in the former. Their

commonality lies in the nonzero value of the complex frequency that arises from their linear and time asymptotic physical stability analysis. Since the real and imaginary components of this frequency respectively describe the physical disturbance oscillation period and temporal growth rate, at least one of these components must then be nonzero for a high-speed flow to be included in this second category. Hence, the study of this category had two major goals. One is to investigate the performance of existing steady-state solvers for such flows and the other is to try and improve their performance. Steady-state solvers generally fall into two broad groups. Solvers in the first one use iterative methods to solve steady governing equations. Only Newton-type methods from this group are evaluated here. Solvers in the second group march the unsteady governing equations forward in time until their solution becomes time invariant. The implicit Euler scheme, Selective Frequency Damping, Boostconv and multi-step Minimal Gain Marching schemes are evaluated here. These are the methods whose performances are compared in oder to accomplish the first major goal. The second goal is accomplished with the development of multi-stage Minimal Gain Marching schemes. This was required to overcome a significant disadvantage of its multi-step counterpart over the implicit Euler scheme. The issue is that adjusting the control parameters of the multi-step version to achieve numerical stability at smaller time steps than capable by the implicit Euler scheme also moves this version from L-stable to A-stable. In other words, the asymptotic convergence rate towards steady-state decreases as the time step required for this version to become numerically stable decreases. On one hand, the multi-stage version is capable of maintaining L-stability as its control parameters are adjusted to achieve numerical stability at time steps that are smaller than possible with the implicit Euler scheme. On the other hand, its disadvantage over its multi-step counterpart and the implicit Euler scheme is the fact that the aforementioned advantage comes at the cost of solving an overall larger number of equations. Hence, the multi-stage version becomes competitive only when the time step cannot be made large enough for the implicit Euler scheme and its multi-step counterpart to converge in an efficient manner. Furthermore, Boostconv and Selective Frequency Damping were always less efficient. These conclusions were drawn from comparative analyses of a few test cases, namely the Lorenz equations, the modified Burgers' equation and the modified one-dimensional Navier-Stokes equations. The term modified refers to the introduction of a special source term in the original model that renders it convectively or absolutely unstable to stationary disturbances.

The third and final category includes physically unstable high-speed flows with a very specific characteristic. A linear and time asymptotic physical stability analysis of their steady-states reveals that their complex frequency is zero. A zero real frequency component means that the disturbance is stationary whereas a zero complex component means that the disturbance is marginally stable in time. In other words, these spatially developing flows are convectively unstable to stationary disturbances. This means that both numerical and physical steady excitation sources are capable of triggering

the time asymptotic and spatial growth of small amplitude disturbances that occurs downstream of this source and is time independent. Steady physical sources are usually included by design, so it is fairly straightforward to avoid them. Steady numerical excitation sources, on the other hand, can be quite difficult to remove from a code. The reason is anything preventing the spatial error distribution from being smooth can be considered such a source. A few typical examples include inaccurate initial and inlet conditions, any number of grid issues and inadequate variable numerical diffusion schemes. These numerical sources become an issue when evidence from the literature and the present investigation suggest that existing steady-state solvers cannot prevent the spatial growth of stationary disturbances downstream from these sources once they have been excited. The first major goal of the present investigation of this third category is to understand why these steady-state solvers do not work. This is achieved with a linear and time asymptotic numerical stability analysis of these solvers. It reveals that this is due to the consistency requirement for any convergent discrete numerical scheme, which forces their linear gain to be one whenever the complex disturbance frequency is zero. Hence, these solvers cannot modify the stationary disturbance amplitude in time, which allows them to grow in space. The second major goal of this investigation then becomes clear. Steady-state solvers must be improved upon to overcome this issue. This is achieved here with the development of the Frequency Displacement Procedure. It is a filter that can be added to any unsteady governing equation to push the oscillation frequency of its linear disturbances away from zero without modifying its steady-state. Doing so leads to physically stable stationary disturbances, which allows the use of time-accurate marching schemes to generate accurate and disturbance free steady-states. The exact version of this filter was applied to several test cases, namely the modified Burgers' equation, the modified entropy disturbance advection using the 1D compressible Navier-Stokes equations, the modified boundary-layer over a flat plate using the 2D compressible Navier-Stokes equations, and the Görtler problem using the 3D compressible Navier-Stokes equations. The term modified refers to the introduction of a special source term in the original model that renders it convectively unstable to stationary disturbances. This exact version of the filter, however, requires knowledge of the steady-state. For this reason, an approximate version was developed to remove the steady-state from the filter. So far, this approximate version was only test on the modified Burgers' equation. Nevertheless, it was able to constrain the time asymptotic spatial growth downstream of small amplitude steady sources. However, the approximate version does not work when this amplitude is large and additional improvements are still required.

Finally, it is important to emphasize that this project was developed in close collaboration with Pedro Paredes (NIA & NASA LaRC) and Vassilios Theofilis (UoL). The former received two students from UFF under ISEP grants whereas the students of the latter performed all the stability analyses reported in the first part of this project. Both collaborations continue to this day, through new grants funded by SOARD, EOARD and AFOSR.

Papers

Published

[1] R. D. Santos, L. S. de B. Alves and V. Theofilis, *Generation of Steady-State Flows with Minimal Gain Marching Schemes*, 13th ERCOFTAC SIG33 Workshop, Paraty, 2018.

[2] R. D. Santos, M. R. Volpini and L. S. de B. Alves, *Nonlinear Time-Step Resctriction on Minimal Gain Marching Schemes*, 25th ABCM COBEM, Uberlândia, COB2019-2277.

[3] R. T. Veloso, R. D. Santos and L. S. de B. Alves, *Comparative Analysis Between Steady-State Generation Methods*, 25th ABCM COBEM, Uberlândia, COB2019-1830.

[4] R. D. Santos and L. S. de B. Alves, *Generation of Steady-States with Discontinuities Using Minimal Gain Marching Schemes*, AIAA Aviation Forum, Dallas, AIAA2019-2839.

[5] L. S. de B. Alves, R. D. Santos, N. Cerulus and V. Theofilis. *Steady-States of Supersonic Flows Over Compression Ramps*. AIAA Scitech Forum, San Diego, AIAA2019-2321.

[6] A. Burtsev, H. R. D. Quintanilha Jr, V. Theofilis, R. D. Santos and L. S. de B. Alves, *Linear Instability Mechanisms of Supersonic Flow Past Blunt Bodies*, AIAA Scitech Forum, Virtual, AIAA2021-0050.

[7] R. D. Santos, M. S. S. Nunes, R. T. Veloso and L. S. de B. Alves. *Steady-States for Stationary and Convectively Unstable Flows*, XV ICTAM, Virtual, 108816, 2021.

[8] R. D. Santos, L. S. de B. Alves, N. Cerulus, H. R. D. Quintanilha Jr and V. Theofilis. *Accurate Two-Dimensional Steady-States for the Supersonic Flow Over a Compression Corner*, 33rd ICAS, Stockholm, ICAS2022-0887.

In Preparation

[9] N. Cerulus, R. D. Santos, H. R. D. Quintanilha Jr, L. S. de B. Alves and V. Theofilis, *Global Stability of Flows Over Compression Ramps*. **Journal of Fluid Mechanics**.

[10] N. Cerulus, R. D. Santos, H. R. D. Quintanilha Jr, V. Theofilis and L. S. de B. Alves, *Steady-State Residue Convergence for the Flow Over Compression Corners*. **Journal of Computational Physics**.

[11] R. B. Freitas, A. Burtsev, R. D. Santos, H. R. D. Quintanilha Jr, L. S. de B. Alves and V. Theofilis, *Optimal and Sub-Optimal Non-Modal Growth in Bow Shocks*. **Journal of Fluid Mechanics**.

[12] R. D. Santos, J. C. A. da Silva, M. S. S. Nunes, R. T. Veloso and L. S. de B. Alves, *Multi-Stage Minimal Gain Marching Schemes*. **Theoretical and Computational Fluid Dynamics**.

[13] J. C. A. da Silva, R. T. Veloso, M. S. S. Nunes, R. D. Santos, R. B. Freitas, and L. S. de B. Alves, *Stationary and Convectively Unstable Steady-States*. **Journal of Computational Physics**.

Dissertations and Theses

B.Sc. Final Reports

[1] Rodrigo Tavares Veloso, Análise Comparativa Entre Métodos de Geração de Regime Permanente, UFF, July, 2019. 🔗

M.Sc. Dissertations

[2] Mateus Sanglard Schuabb Nunes, Generation of Steady-States for Stationary and Convectively Unstable Flows Using the Frequency Displacement Procedure, UFF, July, 2021. 🔗

[3] Rodrigo Tavares Veloso, Análise de Métodos Numéricos de Marcha para Geração de Regimes Permanentes Instáveis, UFF, August, 2022. 🔗

[4] Juan Carlos Assis da Silva, Generating Physically Unstable Steady-States from Numerically Stable Marching Schemes, UFF, 2023 (tentative).

Ph.D. Theses

[5] Ricardo Dias dos Santos, Estudo Sobre os Métodos de Runge-Kutta com Forte Estabilidade Linear e Não-Lineares, UFF, December, 2020. 🔗

[6] Nicolas Cerulus*, Characterisation of the stability of compression corner geometries under supersonic flow conditions, UoL, May, 2022. 🔗

* did not receive funding from this project.

Contents

Prologue

Governing Equations

Let us consider an autonomous nonlinear dynamical system in form of the ordinary differential equations

$$\frac{d\mathbf{u}}{dt} = \mathbf{f}(\mathbf{u}) \quad , \tag{1}$$

where $\mathbf{u} = \{ u_1(t) , \ldots , u_N(t) \}$, $\mathbf{f}(\mathbf{u}) = \{ f_1(\mathbf{u}) , \ldots , f_N(\mathbf{u}) \}$ and N is the number of equations. Equation (1) is generally considered here as being obtained from the spatial discretization of one or more partial differential equations. Its steady version can be written as

$$\mathbf{f}(\mathbf{u}_s) = 0 \quad , \tag{2}$$

whose nonlinear solution $\mathbf{u}_s$ must satisfy

$$\frac{\partial \mathbf{u}_s}{\partial t} = 0 \quad , \tag{3}$$

where the subscript s stands for *steady*, since it is assumed here that the steady-state $\mathbf{u}_s$ represents a fixed point. Solving an unsteady system of equations such as the one presented in Eq. (1) requires initial conditions. These initial conditions are conveniently chosen here to be given by

$$\mathbf{u}(0) = \mathbf{u}_s + \epsilon \, \mathbf{u}_0 \quad , \tag{4}$$

which represents an $O(\epsilon)$ disturbance superposed to the $O(1)$ steady-state $\mathbf{u}_s$ at $t = 0$, where $\epsilon \ll 1$ is the dimensionless disturbance small amplitude parameter. Hence, $\mathbf{u}_0$ represents the $O(1)$ spatially discretized version of the initial disturbance shape. The use of Eq. (4) provides a quite common way to track the initially linear and eventually nonlinear temporal evolution of desired small amplitude disturbances present in an otherwise laminar flow. Such an approach is often employed to identify the mechanisms responsible for the transition from a laminar steady-state to a fully turbulent flow. This transition process can also be better understood using alternative linear and nonlinear stability analyses, but these tools also require a steady-state.

The main goal of this project is to provide disturbance free and accurate steady-states for high-speed flows to aid the study of their transition (Leyva, 2017). It is important to note, however, that $\mathbf{u}_s$ is not always available, or even easy to calculate. This has led many researchers to use approximate solutions instead. Some well known examples are *i*) mean profiles, such as the ones obtained from averaged governing equations, e.g. the RANS equations, *ii*) similarity solutions, obtained from boundary-layer type equations, *iii*) ad hoc, or even physics-based, fits of experimental data and *iv*) poorly resolved solutions, obtained from numerical simulations that use dissipative schemes with low accuracy-order. Other possibilities exist, since the previous list is not exhaustive and shows only the most common examples. Hence, one often refers to such a time invariant approximate solution as a base-state $\mathbf{u}_b$, where the subscript b stands for *base*. In this context, the steady-state $\mathbf{u}_s$ is a disturbance free and accurate base-state $\mathbf{u}_b$. When they are not available, however, $\mathbf{u}_b$ should be a good enough representation of $\mathbf{u}_s$.

Steady-States for Stability Analysis

More insight into how close $\mathbf{u}_b$ must be to $\mathbf{u}_s$ can be gained by evaluating the physical stability of $\mathbf{u}_b$ and $\mathbf{u}_s$. Two details are of importance. First, the word *physical* means with respect to the time continuous model defined by the system of ordinary differential equations given by Eq. (1). Second, a linear stability analysis can be pursued since ϵ is assumed small.

In a physical sense, a nonlinear dynamical system is considered linearly stable when its base-state can be recovered, given enough time, after it was subjected to small amplitude perturbations. In mathematical terms, the flow can be decomposed as $\mathbf{u}_b$ superposed with $\mathbf{u}_p(t)$, i.e.

$$\mathbf{u}(t) = \mathbf{u}_b + \epsilon\,\mathbf{u}_p(t) + O(\epsilon^2) \quad , \tag{5}$$

and assumed linearly stable when $\mathbf{u}_p(t \to \infty) \to 0$ and, hence, $\mathbf{u}(t \to \infty) \to \mathbf{u}_b$, where $\mathbf{u}_p(t)$ is a linear perturbation since $\epsilon \ll 1$. Linear also means that $\mathbf{u}_p(t) \sim O(1)$, i.e. the perturbation superposed to $\mathbf{u}_b$ in Eq. (5) is $O(\epsilon)$. Furthermore, an equation for $\mathbf{u}_p(t)$ can be obtained by substituting Eq. (5) into Eq. (1) and collecting the terms of $O(\epsilon)$. Doing so yields

$$\epsilon\,\frac{d\mathbf{u}_p}{dt} \;=\; \mathbf{f}(\mathbf{u}_b + \epsilon\,\mathbf{u}_p(t)) + O(\epsilon^2) \quad , \tag{6}$$

since $\mathbf{u}_b$ should not vary in time because it is supposed to represent $\mathbf{u}_s$, which is time invariant according to Eq. (3). Using a Taylor series expansion around the base-state, one can also write

$$\begin{aligned} \mathbf{f}(\mathbf{u}_b + \epsilon\,\mathbf{u}_p(t)) \;&=\; \mathbf{f}(\mathbf{u}_b) \;+\; \left.\frac{\partial \mathbf{f}}{\partial \mathbf{u}}\right|_b (\mathbf{u}(t) - \mathbf{u}_b) \;+\; O((\mathbf{u}(t) - \mathbf{u}_b)^2) \\ &=\; \mathbf{f}(\mathbf{u}_b) \;+\; \epsilon\,\left.\frac{\partial \mathbf{f}}{\partial \mathbf{u}}\right|_b \mathbf{u}_p(t) \;+\; O(\epsilon^2) \quad , \end{aligned} \tag{7}$$

where the last step employed Eq. (5). In the above equation, $\partial\mathbf{f}/\partial\mathbf{u}|_b$ is the Jacobian of $\mathbf{f}$ with respect to $\mathbf{u}$ evaluated at $\mathbf{u} = \mathbf{u}_b$. This partial derivative can be written in matrix form as

$$\mathcal{A}(\mathbf{u}) \;=\; \frac{\partial \mathbf{f}}{\partial \mathbf{u}} \;=\; \begin{pmatrix} \frac{\partial f_1}{\partial u_1} & \cdots & \frac{\partial f_1}{\partial u_N} \\ \vdots & \ddots & \vdots \\ \frac{\partial f_N}{\partial u_1} & \cdots & \frac{\partial f_N}{\partial u_N} \end{pmatrix} \quad , \tag{8}$$

which leads to the required Jacobian $\mathcal{A}(\mathbf{u}_b) = \partial\mathbf{f}/\partial\mathbf{u}|_b$ when $\mathbf{u}(t)$ is replaced by $\mathbf{u}_b$ in the above formula. Equation (6) then becomes

$$\frac{d\mathbf{u}_p}{dt} \;=\; \mathcal{A}(\mathbf{u}_b)\,\mathbf{u}_p(t) \;+\; \frac{\mathbf{f}(\mathbf{u}_b)}{\epsilon} \;+\; O(\epsilon) \quad . \tag{9}$$

Equation (9) further simplifies to

$$\frac{d\mathbf{u}_d}{dt} \;=\; \mathcal{A}(\mathbf{u}_s)\,\mathbf{u}_d(t) \;+\; O(\epsilon) \quad , \tag{10}$$

when $\mathbf{u}_b = \mathbf{u}_s$ and, hence, $\mathbf{u}_p = \mathbf{u}_d$. It is important to emphasize here that the perturbation $\mathbf{u}_p$ is generally different from the disturbance $\mathbf{u}_d$ when $\mathbf{u}_b \neq \mathbf{u}_s$. This nomenclature is used to highlight the fact that $\mathbf{u}_d$ is the true physical representation of a disturbance whereas the $\mathbf{u}_p$ is the latter contaminated by numerical errors caused by any differences between $\mathbf{u}_b$ and $\mathbf{u}_s$. This means the requirement that Eq. (9) for the perturbation $\mathbf{u}_p$ and Eq. (10) for the disturbance $\mathbf{u}_d$ should provide equivalent results allows the establishment of two different criteria to quantify how close $\mathbf{u}_b$ must be to $\mathbf{u}_s$. The first one quantifies how close the base-state residue must be to zero, i.e.

$$\mathbf{f}(\mathbf{u}_b) \leqslant O(\epsilon^2) \quad , \tag{11}$$

whereas the second criterium requires additional steps. Using a Taylor series expansion around the steady-state yields

$$\begin{aligned} \mathbf{f}(\mathbf{u}_s + \epsilon\,\mathbf{u}_d(t)) &= \mathbf{f}(\mathbf{u}_s) + \left.\frac{\partial \mathbf{f}}{\partial \mathbf{u}}\right|_s (\mathbf{u}(t) - \mathbf{u}_s) + O((\mathbf{u}(t) - \mathbf{u}_s)^2) \\ &= \epsilon \left.\frac{\partial \mathbf{f}}{\partial \mathbf{u}}\right|_s \mathbf{u}_d(t) + O(\epsilon^2) \quad , \end{aligned} \tag{12}$$

where the last step employed

$$\mathbf{u}(t) = \mathbf{u}_s + \epsilon\,\mathbf{u}_d(t) + O(\epsilon^2) \quad , \tag{13}$$

as well as Eq. (2). Noting that Eqs. (5) and (13) imply that Eqs. (7) and (12) yield the same $\mathbf{f}(\mathbf{u})$, it is possible to use Eqs. (8) and (11) to impose

$$\mathcal{A}(\mathbf{u}_s)\,\mathbf{u}_d(t) - \mathcal{A}(\mathbf{u}_b)\,\mathbf{u}_p(t) \leqslant O(\epsilon) \quad , \tag{14}$$

which can be re-written with

$$\begin{aligned} \mathcal{A}(\mathbf{u}_b)\,\mathbf{u}_p(t) &= \left\{ \mathcal{A}(\mathbf{u}_s) + \left.\frac{\partial \mathcal{A}}{\partial \mathbf{u}}\right|_s (\mathbf{u}_b - \mathbf{u}_s) + O((\mathbf{u}_b - \mathbf{u}_s)^2) \right\} \\ &\times \left\{ \mathbf{u}_d(t) - \frac{\mathbf{u}_b - \mathbf{u}_s}{\epsilon} + O(\epsilon) \right\} \quad , \end{aligned} \tag{15}$$

obtained using the Taylor series expansion of $\mathcal{A}(\mathbf{u}_b)$ around $\mathcal{A}(\mathbf{u}_s)$ and the relation $\mathbf{u}_p - \mathbf{u}_d = (\mathbf{u}_s - \mathbf{u}_b)/\epsilon + O(\epsilon)$, which comes from combining Eqs. (5) and (13). Substituting Eq. (15) into Eq. (14) leads to

$$\mathbf{u}_b - \mathbf{u}_s \leqslant O(\epsilon^2) \quad , \tag{16}$$

which is the second criterion. In other words, it quantifies how close the base-state must be to the steady-state.

The above derivation states the minimum accuracy requirements for the calculation of a base-state, which are given by Eqs. (11) and (16). They were derived in such a way as to guarantee that a linear stability analysis based on this base-state provides reliable results. In other words, the solution of Eq. (9)

using base-state $\mathbf{u}_b$ is equivalent to the solution of Eq. (10) using steady-state $\mathbf{u}_s$. Such an analysis provides strong theoretical evidence as to why it is so important to use disturbance free and accurate steady-states as base-states for stability analyses. The calculation of these steady-states, however, depends strongly on the time asymptotic behavior of Eq. (10). This linear physical stability is governed by the eigenvalues of $\mathcal{A}(\mathbf{u}_s)$. Furthermore, the calculation of these steady-states also depends on the ability of a numerical scheme to march Eq. (1) towards Eq. (2). This ability requires the numerical scheme to posses two important linear properties, namely consistency and stability. The former guarantees that Eq. (2) can be satisfied for non-trivial steady-states whereas the latter guarantees that disturbances can be damped. It must be noted that the word *numerical* means with respect to the time discrete model that is generated when applying numerical methods to march in time the system of ordinary differential equations given by Eq. (1). Hence, physical and numerical stability are not necessarily the same thing, although the latter depends on the former.

Physical and Numerical Stability

In order to better understand this dependence, one must first analyze the former. The continuous physical solution of Eq. (10) can be written as

$$\mathbf{u}_d(t) \;=\; \mathbf{u}_0\, e^{\mathcal{A}(\mathbf{u}_s)\, t} \quad , \tag{17}$$

where $O(\epsilon)$ were ignored and $\mathbf{u}_d(0) = \mathbf{u}_0$, according to Eqs. (4) and (13). One way to calculate the exponential of a matrix is

$$\mathbf{u}_d(t) \;=\; \sum_{j=1}^{N} c_j\, e^{\lambda_j\, t}\, \mathbf{v}_j \quad , \tag{18}$$

where λ_j and $\mathbf{v}_j$ respectively represent the eigenvalues and eigenvectors of $\mathcal{A}(\mathbf{u}_s)$ in the above linear combination. It should be noted that confluent eigenvalues can turn the coefficients c_j into polynomials in t. This issue, however, only has a temporary effect on the initial disturbance behavior, i.e. on $\mathbf{u}_d(t \to 0)$. In the context of steady-state calculations, on the other hand, it is the time asymptotic disturbance behavior that matters. The behavior of $\mathbf{u}_d(t \to \infty)$, in turn, is entirely governed by the eigenvalues λ_j, since exponential growth/decay in time always trumps algebraic growth/decay in time for large enough times. The linear asymptotic physical stability of the steady-state $\mathbf{u}_s$ that satisfies Eq. (1) is defined according to the real, i.e.

$$\begin{aligned} \mathrm{Re}[\lambda_j] \;&<\; 0 \;\;\rightarrow\;\; \text{stable} \\ \mathrm{Re}[\lambda_i] \;&=\; 0 \;\;\rightarrow\;\; \text{neutral} \\ \mathrm{Re}[\lambda_j] \;&>\; 0 \;\;\rightarrow\;\; \text{unstable} \end{aligned} \quad , \tag{19}$$

and the imaginary, i.e.

$$\begin{array}{rcl} \mathrm{Im}[\lambda_j] \,=\, 0 & \rightarrow & \text{stationary} \\ \mathrm{Im}[\lambda_j] \,\neq\, 0 & \rightarrow & \text{oscillatory} \end{array} \quad , \tag{20}$$

parts of these eigenvalues.

A consistent numerical method, however, is used to march Eq. (1) in time towards Eq. (2). Hence, the linear numerical stability of the time discrete version of this equation should be evaluated instead. Before doing so, it is convenient to re-write Eq. (10) as

$$\frac{d\hat{\mathbf{u}}}{dt} \,=\, \Lambda\, \hat{\mathbf{u}}(t) \quad , \tag{21}$$

using the eigendecomposition

$$\mathcal{A}(\mathbf{u}_s) \,=\, \mathcal{M}\, \Lambda\, \mathcal{M}^{-1} \quad , \tag{22}$$

and the transformed disturbance variable definition

$$\hat{\mathbf{u}}(t) \,=\, \mathcal{M}^{-1}\, \mathbf{u}_d(t) \quad , \tag{23}$$

since the time asymptotic disturbance behavior in a linear stability analysis can be evaluated through the eigenvalues alone, as discussed in the analysis of Eq. (18). In the above equations, Λ is the diagonal matrix containing all eigenvalues λ_j and $\mathcal{M}$ is the square matrix whose columns are the linearly independent eigenvectors $\mathbf{v}_j$. It must be noted that Eq. (21) represents a decoupled system of equations. Hence, either physical or numerical solutions for each element $\hat{u}_j$ of the vector $\hat{\mathbf{u}}$ can be sought independently. Discrete numerical solutions, however, are usually written as functions of

$$G_j \,=\, \frac{\hat{u}_j^{n+1}}{\hat{u}_j^{n}} \,=\, e^{\lambda_j\, \Delta t} \quad , \tag{24}$$

where $n+1$ and n are the unknown and known time step indexes, respectively, Δt is the time step, $t_{n+1} = t_n + \Delta t$ and G_j is the gain. Since the eigenvalues are complex numbers, in general, the gain can be written in polar form as

$$G_j \,=\, \alpha_j\, e^{i\, \phi_j} \quad , \tag{25}$$

where $i = \sqrt{-1}$, $\alpha_j = \mathrm{abs}[G_j] = |G_j|$ is the modulus and $\phi_j = \arg[G_j]$ is the phase angle of the gain. The latter two are calculated using relations

$$\alpha_j \,=\, \sqrt{\mathrm{Re}[G_j]^2 + \mathrm{Im}[G_j]^2} \quad \text{and} \quad \phi_j = \arctan\left[\frac{\mathrm{Im}[G_j]}{\mathrm{Re}[G_j]}\right] \quad , \tag{26}$$

from complex algebra. The linear asymptotic numerical stability of the steady-state $\mathbf{u}_s$ that satisfies the time discrete version of Eq. (1) is then defined by the gain absolute value, i.e.

$$\begin{array}{rcl} \alpha_j \,<\, 1 & \rightarrow & \text{stable} \\ \alpha_j \,=\, 1 & \rightarrow & \text{neutral} \\ \alpha_j \,>\, 1 & \rightarrow & \text{unstable} \end{array} \quad , \tag{27}$$

and the relative phase shift error, i.e.

$$\begin{aligned} c_j &< 1 \quad \rightarrow \quad \text{lagging} \\ c_j &= 1 \quad \rightarrow \quad \text{in phase} \\ c_j &> 1 \quad \rightarrow \quad \text{leading} \end{aligned} \quad , \tag{28}$$

which is defined as the phase angle ratio

$$c_j \;=\; \frac{c_N}{c_P} \;=\; \frac{\phi_j}{\mathrm{Im}[\lambda_j]\,\Delta t} \quad , \tag{29}$$

where c_N and c_P stand for numerical and physical phase angles, respectively. A comparison between Eqs. (19) and (27), as well as Eqs. (20) and (28), shows that physical and numerical linear stability are not necessarily the same, but the latter depends on the former.

Marching Towards Steady-States

A deeper understanding of these differences and dependences can be gained by studying specific marching schemes in more detail. Doing so also reveals how these schemes can be used to obtain a solution of Eq. (2) by solving Eq. (1) instead. The explicit and implicit Euler schemes are used here for this more detailed analysis. When applied to Eq. (1), they yield

$$\mathbf{u}^{n+1} = \mathbf{u}^n + \Delta t\, \mathbf{f}(\mathbf{u}^n) \quad , \tag{30}$$

as well as

$$\mathbf{u}^{n+1} = \mathbf{u}^n + \Delta t\, \mathbf{f}(\mathbf{u}^{n+1}) \quad , \tag{31}$$

respectively, where $\mathbf{u}^n = \mathbf{u}(t_n)$. The question now is how to evaluate when, or even if, the steady-state has been reached by these marching schemes. It can be answered by the previously derived criteria shown in Eqs. (11) and (16). The latter criterion implies that the solution increment must satisfy

$$\mathbf{u}^{n+1} - \mathbf{u}^n \;\leqslant\; O(\epsilon^2) \quad , \tag{32}$$

whereas the former criterion implies that the residue must satisfy

$$\mathbf{f}(\mathbf{u}^{n+1}) \;\leqslant\; O(\epsilon^2) \quad , \tag{33}$$

noting that Eq. (32) must be used with Eq. (33).

The linear and time asymptotic numerical stability analysis of Eqs. (30) and (31) with respect to the steady-state $\mathbf{u}_s$ can be performed by applying, respectively, the explicit and implicit Euler schemes to Eq. (21), and then solving for the gain defined in Eq. (24). This yields

$$G_j \;=\; 1 \,+\, \lambda_j\, \Delta t \quad , \tag{34}$$

for the explicit Euler scheme and

$$G_j = \frac{1}{1 - \lambda_j \Delta t} \quad , \tag{35}$$

for the implicit Euler scheme. An analogy with iterative schemes can be drawn from the fact that the Newton method is recovered from the implicit Euler scheme in the limite of an infinite time step. Nevertheless, the linear and time asymptotic numerical stability regions associated with Eqs. (34) and (35) are shown in the left and right columns of Fig. 1, respectively. A few important conclusions can be drawn from this figure. They can be separated into three different major groups.

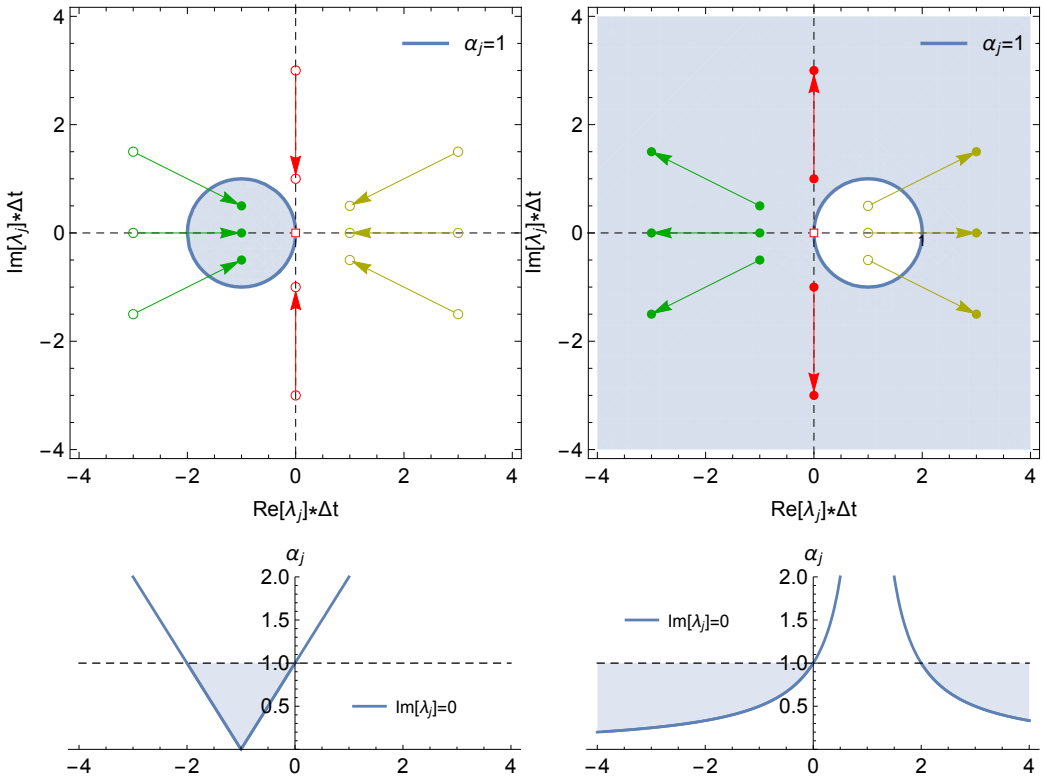

Figure 1: Linear and time asymptotic numerical stability regions for both explicit (left) and implicit (right) Euler schemes. Top row shows numerically neutral contour line ($\alpha_j = 1$) in the complex and physical dimensionless eigenvalue ($\lambda_j \Delta t$) plane. Symbols show physically stable (green), neutral (red) and unstable (yellow) disturbances. They can be numerically stable (filled circle), neutral (empty square) and unstable (empty circle). Arrows point in the numerically stabilizing directions when changing the time step ($\Delta t_1 \leftrightarrow \Delta t_2$). Bottom row shows numerically neutral ($\alpha_j = 1$) contour line as a function of the time step (Δt) for physically unstable ($\mathrm{Re}[\lambda_j] > 0$), neutral ($\mathrm{Re}[\lambda_j] = 0$) and stable ($\mathrm{Re}[\lambda_j] < 0$) disturbances that are stationary ($\mathrm{Im}[\lambda_j] = 0$). Light blue color indicates numerically stable ($\alpha_j < 1$) regions.

1. Physically Stable Flows

Consider first a scenario where the time asymptotic behavior of all discrete linear disturbances is physically stable, i.e. $\mathrm{Re}[\lambda_j] < 0$ according to Eq. (19). They are represented by the green circles in Fig. 1. The explicit Euler scheme will drive Eq. (1) towards Eq. (2) only when they are also numerically stable, i.e. $\alpha_j < 1$ according to Eq. (27). These circles are filled in Fig. 1, since empty circles are numerically unstable. Hence, time steps Δt must be chosen small enough to place these disturbances within the unit circle given by $(\mathrm{Re}[\lambda_j\,\Delta t] + 1)^2 + (\mathrm{Im}[\lambda_j\,\Delta t])^2 < 1$. Otherwise they will be numerically (neutral) unstable when the fall (on) outside of the unit circle since ($\alpha_j = 1$) $\alpha_j > 1$. This trend is observed for the all other explicit schemes. The implicit Euler scheme, on the other hand, will drive Eq. (1) towards Eq. (2) for all positive time steps, i.e. $\Delta t > 0$. Furthermore, higher convergence rates towards steady-state are achieved when increasing the time step Δt because absolute values of the gain α_j will be smaller for all stable eigenvalues λ_j. This is true for all L-stable implicit schemes, since the time asymptotic behavior of their gains follows $\alpha_j \to 0$ as $\Delta t \to \infty$.

In all such physically stable scenarios, explicit marching schemes can be used to march a dynamical system towards steady-state. Implicit marching schemes are often more efficient, specially when stiffness is an issue. It must be emphasized, however, that this is only true on a linear basis. Nonlinear numerical stability requirements constrain the maximum time steps allowed, which severely limits the efficiency of implicit schemes. These nonlinear numerical properties are important for many high-speed flows, due to the presence of structures like shock waves. Hence, the use of explicit marching schemes for physically stable steady-states is common in these cases. The main issue at hand then becomes generating steady-states with a high spatial accuracy, despite being embedded with such complex structures. When the time asymptotic behavior of all linear disturbances present in the flow is not physically stable, however, explicit methods cannot reach steady-state. Two distinct scenarios then emerge, which are discussed next.

2. Physically Unstable Flows with $\lambda_j \neq 0$

The second scenario occurs when $\lambda_j \neq 0$. Since eigenvalues are complex numbers, three different possibilities must be considered. The first two of them refer to absolutely/globally unstable ($\mathrm{Re}[\lambda_j] > 0$) flows. In other words, the time asymptotic physically unstable behavior of linear disturbances shows temporal growth at a fixed spatial location. Both possibilities arise from the fact that this instability is also either stationary ($\mathrm{Im}[\lambda_j] = 0$) or oscillatory ($\mathrm{Im}[\lambda_j] \neq 0$). They are illustrated in Fig. 1 as yellow circles. The third possibility refers to oscillatory ($\mathrm{Im}[\lambda_j] \neq 0$) and neutrally stable ($\mathrm{Re}[\lambda_j] = 0$) flows. It is important to note that neutral stability in time for spatially developing flows is analogous to convective instability. In other words, the time asymptotic physically unstable behavior of linear disturbances shows

spatial growth at a fixed time. They are illustrated as red circles in Fig. 1.

Figure 1 also shows that the explicit Euler scheme is always numerically unstable in the presence of $\lambda_j \neq 0$ physically unstable disturbances. This is true in general of explicit marching schemes, although some do have a small numerically stable region associated with physically unstable and oscillatory disturbances. This is the reason why the implicit Euler scheme is quite popular for this scenario. It is always able to drive Eq. (1) towards Eq. (2) when the flow is convectively unstable ($\mathrm{Re}[\lambda_j] = 0$) to oscillatory ($\mathrm{Im}[\lambda_j] \neq 0$) disturbances. It can also do the same for flows that are absolutely/globally unstable ($\mathrm{Re}[\lambda_j] > 0$) to stationary ($\mathrm{Im}[\lambda_j] = 0$) and oscillatory ($\mathrm{Im}[\lambda_j] \neq 0$) disturbances, as long as the time step Δt can be chosen large enough to place these disturbances outside its unit circle, given by $(\mathrm{Re}[\lambda_j\,\Delta t] - 1)^2 + (\mathrm{Im}[\lambda_j\,\Delta])^2 > 1$. This is true for all L-stable implicit marching schemes. As a direct consequence, this is true for the Newton method as well. Many other steady-state solvers can also be employed in this second scenario. They all have their advantages and disadvantages. For instance, nonlinearities introduced by initial conditions can prevent the maximum time step from being chosen large enough in these implicit marching schemes. In the best case scenario, this will prevent them from achieving a small enough α_j value, leading to low convergence rates towards steady-state. In the worst case scenario, this will prevent these implicit marching schemes from being able to place a physically unstable disturbance outside of the unit circle, leading to divergence from the desired steady-state. In the particular case of Newton-type methods, this leads to a strong sensitivity to poorly chosen initial guesses and, hence, the need to coupled them with continuation methods.

3. Physically Unstable Flows with $\lambda_j = 0$

Things, however, become significantly more complex for the third and final scenario. It involves flows that are convectively unstable ($\mathrm{Re}[\lambda_j] = 0$) to stationary ($\mathrm{Im}[\lambda_j] = 0$) disturbances. Since $\lambda_j = 0$ in this scenario, these disturbances are represented by the empty square sitting at the origin of Fig. 1. For the same reason, they cannot be moved away from this origin when increasing the time step Δt. Furthermore, $\alpha_j = 1$ at the origin of the stability region of all marching schemes due to consistency requirements. Hence, marching schemes do not allow these disturbances to change their amplitudes in time after a long enough time has passed, i.e. disturbance amplitudes neither decay nor grow in time. Under such circumstances, it might seem reasonable to assume this is not a relevant issue when initial disturbance amplitudes are small. However, this is not the case.

Convectively unstable flows act as noise amplifiers. This means that an unstable disturbance will be spatially amplified as it is convected downstream of its excitation source by the base flow. In other words, disturbances do not grow or decay in time, but they are still allowed to grow in space. Hence, they eventually contaminate the entire flow field downstream of the source location, often leading to a new nonlinear steady-state. A simple way to

eliminate this issue would be to remove the disturbance excitation sources from a simulation. However, it is not always possible to do so when these flows are unstable to stationary disturbances because there are many intrinsic mechanisms that can act as steady excitation sources. There are several examples stemming from a physical perspective. For instance, any isolated and small roughness element can act as such a source. The same is true for a small amplitude surface roughness. The number of examples is even larger from a numerical perspective. Spatial discretization schemes with variable numerical diffusion, poorly constructed grids, poorly specified inlet conditions and anything else preventing the spatial error distribution from being smooth can act as a numerical steady excitation source. Given these obstacles, disturbance free steady-states do appear to be unachievable using state-of-the-art steady-state solvers.

Part I

Physically Stable Flows

Chapter 1

Introduction

1.1 Motivation

This project focusses on the numerical computation of disturbance free and accurate steady-states because of their importance to linear and nonlinear stability analyses. The major targets are high-speed flows of pure substances. They are typically characterized by strong compressibility effects, introduced by high temperature gradients and/or high Mach numbers. These effects create many complex flow features, such as acoustic waves, shock waves, expansion fans, contact discontinuities and so on. Such features can, in turn, render it more difficult for numerical methods to compute these steady-states. Doing so in a manner that accurately captures all these important spatial features than requires sophisticated methods. One major contribution of this chapter is its description of how this can be done. An obvious but necessary disclaimer must be made. It should come as no surprise that the proposed approach is by no means the only way to do so. Nevertheless, this is done in the present chapter exclusively for flows that are physically stable in a linear and time asymptotic sense. Hence, these steady-states are disturbance free by default, since all disturbances can be numerically damped by standard marching and iterative schemes. This is the first out of the three scenarios covered in the prologue. Another major contribution of this chapter is the application of this approach to two relevant high-speed flows. The first one is the supersonic flow upstream of a two-dimensional cylinder. It is employed here to investigate the ability of the chosen discretization schemes to avoid the carbuncle phenomenon in steady-states. Furthermore, the parametric conditions under which linear and transient physical instabilities exist are also investigated. As far as the authors are aware, this has not yet been done in the literature. The second high-speed flow is the supersonic flow over a compression ramp. It is used here to investigate the possibility of generating high-order accurate and two-dimensional steady-states. Once again, as far as the authors are aware, only low-order accurate two-dimensional steady-states can be found in the literature. Finally, the parametric conditions under which both linear and time asymptotic as well as linear and transient three-dimensional physical instabilities exist are investigated.

1.2 Literature Review

1.2.1 Numerical Methods

The high-speed flows under study in this project are modeled by the unsteady and compressible Navier-Stokes equations for perfect fluids. These governing equations are solved using the method of lines. It applies a two step process that first generates a system of ordinary differential equations, represented by Eq. (1), from the partial differential equations composing the original model governing equations and then marches it forward in time. A wide range of methods can be applied to generate this system. Their review is beyond the scope of this project, but several relevant books can be used as a starting point (Versteeg and Malalasekera, 1995; Tannehill et al., 1997; Lomax et al., 2001; Hirsch, 2007; Butcher, 2008). This system is obtained here by applying finite-difference schemes under a generalized coordinate framework to the spatial operators of the model, which leads to $\mathbf{f}(\mathbf{u})$ in Eq. (1). A code was developed by Santos (2020) using the C programming language (Harbison and Steele Jr, 1995) to run all the simulations performed as part of this project. It is called 3D4S, which stands for one, two and three dimensional stable, steady-state solver. The finite-differences and marching schemes implemented in this code are described next.

Spatial Discretization

Apart from unconventional source terms that are not employed in the present work, all spatial operators in the unsteady and compressible Navier-Stokes equations for perfect fluids are applied to inviscid and viscous fluxes. Their respective discretizations are usually treated using different methodologies, whose implementations in 3D4S are briefly discussed below. Furthermore, the two versions of these implementations used throughout this project are also discussed, namely the low and high-order versions.

On one hand, the discretization of viscous flux spatial gradients employs the traditional second, fourth and sixth-order central-difference schemes in conservative form. The first one is used in the low-order version of 3D4S whereas the second one is used in its high-order version. It is important to note that the third one usually renders the resulting code too numerically unstable (Santiago and Alves, 2017) and, hence, it is not used here.

On the other hand, an accurate discretization of inviscid fluxes that can capture shocks is significantly more complex. This is due to the nonlinear stability properties that are required to prevent the Gibbs phenomenon near discontinuities. Monotone schemes are capable of doing so. This property states that *i*) new minima and maxima cannot created, *ii*) a local minimum cannot be reduced and *iii*) a local maximum cannot be increased. They are, however, first-order accurate. High-order accuracy requires the use of special techniques to control the oscillations induced by discretizing across the shock. A possibility is to relax the monotonicity requirement for something else less restrictive. Harten (1983) followed this path and proposed second-order

accurate schemes that are total variation diminishing (TVD). This property states that the solution total variation at a given time step is always smaller or equal than the solution total variation at the previous time step. These schemes also satisfy the entropy condition, which guarantees convergence of weak solutions of hyperbolic conservation laws. Furthermore, all monotone schemes are TVD and all TVD schemes are monotonicity preserving (Hirsch, 1991). This property states that a solution that is monotone at a given time step will remain monotone at the next time step. Furthermore, TVD schemes work by employing flux-limiters, which are weights placed on the forward and backward fluxes. They are designed to locally reduce the scheme to first-order accurate near discontinuities (Laney, 1998). There are many flux-limiters. Superbee (Roe, 1985) and Minmod (Roe, 1981b; Roe and Baines, 1982; Sweby and Baines, 1984) are the ones that introduce the least and most numerical diffusion, respectively. All others fall in between these two, such as the Monotonized Central Difference (van Leer, 1977), van Leer (van Leer, 1974), Koren (Koren, 1993), Sweby (Sweby, 1984), Osher (Chakravarthy and Osher, 1983), Ospre (Waterson and Deconinck, 1995) and van Albada (van Albada et al., 1982). The low-order version of 3D4S can use either the first-order accurate Euler discretization or the second-order accurate the TVD scheme developed by Harten (1983), coupled with any of these flux-limiters.

It is well known, however, that TVD schemes suffer from an accuracy order reduction near discontinuities (Boris and Book, 1973; van Leer, 1973, 1974). Furthermore, Goodman and LeVeque (1985) showed that they are first-order accurate for two-dimensional problems. A path towards higher-order accuracy is to relax the TVD requirement for something that is less restrictive. This was done by Harten et al. (1987) by introducing the class of essentially non-oscillatory (ENO) schemes. They represent higher-order generalizations of the first-order scheme developed by Godunov (1959) and its second-order extension developed by van Leer (1979), known as Monotonic Upstream-centered Scheme for Conservation Laws (MUSCL). ENO schemes choose between different candidate stencils in order to avoid including the discontinuity in the discretization. The selection is performed by comparing the local smoothness of the discretization on these different stencils, measured using divided diferences (Shu and Osher, 1988, 1989). Liu et al. (1994) developed a variation of these schemes known as weighted ENO (WENO) schemes that achieve higher-order accuracy and smoother numerical fluxes. Instead of using only one of the candidate stencils, as done in ENO, WENO uses a convex combination of all candidate stencils based on nonlinear weights determined by smoothness indicators. The high-order version of 3D4S can use several different fifth-order WENO schemes for unsteady simulations; such as the original WENO5-JS (Jiang and Shu, 1996), WENO5-M (Henrick et al., 2005), WENO5-Z (Borges et al., 2008) and WENO5-Z+ (Acker et al., 2016); and steady simulations; such as WENO5-ZQ (Zhu and Qiu, 2016) and its variants (Zhu and Shu, 2017, 2018, 2019; Zhang et al., 2019).

A distinguishing feature of the aforementioned upwind schemes is that their discretization must be performed according to the propagation direction

of the inviscid flux characteristics. There are essentially two different ways to identify these directions, which are known as the flux-difference and -vector splitting methods (Toro, 2009). The former are known as Riemann solvers whereas the latter are known as Boltzmann solvers, although they can also be considered Riemann solvers in a wider sense. On one hand, flux-difference splitting first discretizes the inviscid fluxes using their cell-faced values and only then separates their propagation directions to evaluate these values. Flux-vector splitting, on the other hand, first separates the inviscid fluxes according to their propagation directions and only then discretizes each part accordingly. It is important to note that they can also be categorized as either complete or incomplete solvers. The former resolves all waves that are present whereas the latter neglects some of these waves. 3D4S can currently employ many of these methods, such as Roe (Roe, 1981a), HLL (Harten et al., 1983) and Roe-HLL (Einfeldt, 1988) based on flux-difference splitting as well as Steger-Warming (Steger and Warming, 1981) and Lax-Friedrichs (Jiang and Shu, 1996) based on flux-vector splitting, which are applied to variables in either conservative or characteristic form.

Grid Generation

All the spatial discretization schemes described so far are implemented on a generalized coordinate framework using uniformly distributed points between 0 and 1 in all directions. Hence, the physical domain of interest must be mapped into this computational domain for all simulations. An analytical transformations are employed whenever they are available. If this is not the case, grid generation tools are required. This is an important issue because grid quality is directly related to the solution accuracy. For example, lack of convergence can be a consequence of poor grid quality (Tannehill et al., 1997). Two-dimensional grid generation tools, which can be extended towards three-dimensional geometries by either rotation or protrusion, are discussed.

There are two fundamental types of grids for multidimensional regions: structured and unstructured. They differ in the way in which the grid points are locally organized. Structured grids have regular connectivity which is implicitly taken into account. They have quadrilateral elements in two-dimensional domains or hexahedron elements in three-dimensional ones. On the other hand, unstructured grids are identified by irregular connectivity that must be explicitly described and stored. This type of grid usually employs triangles and tetrahedral elements in two- and three-dimensional problems, respectively (Liseikin, 2009). Besides that, they also differ in the type of method that can use them. While finite difference methods require structured grids, finite volume and finite element methods allow both types of grids. Since 3D4S is based on finite differences, this brief review focuses only on structured grid generation tools.

Since the pioneering work of Thompson (1982) in grid generation using a system of elliptic second-order partial differential equations, it is well-known that this procedure produces the best possible grids in the relation to smoothness and grid point distribution. If these elliptic differential equations are

solely based on a system of Laplace equations, the smoothness of the Laplace operator makes the grid evenly spaced throughout the domain. This makes grid refinement at specific locations, such as the wall for boundary-layer problems, more difficult. Hence, grids based solely on Laplace equations are unusable in practice. However, if these differential equations are of a Poisson-type, control functions can be specified. The key for a good elliptic grid is how to compute these control functions (Thompson et al., 1998). They are usually used to control grid clustering (Steger and Sorenson, 1979) as well as orthogonality at boundaries (Hsu and Lee, 1991), which is quite useful in boundary-layer problems. The grid generation procedure used here is based on the work of Spekreijse (1995) and was implemented by Nunes (2021).

Temporal Discretization

Having applied a spatial discretization on a given grid to the unsteady and compressible Navier-Stokes equations for perfect fluids in order to generate $\mathbf{f}(\mathbf{u})$, Eq. (1) can then be marched in time. This can be done in 3D4S, but using different methodologies to generate either time-accurate unsteady- or steady-states. As discussed in the prologue, time-accurate methodologies can be used to reach time asymptotic stable steady-states. Since this first part of the report focusses on high-speed flows that fall into this category, only time-accurate methodologies are discussed below. The discussion about the methodologies used by 3D4S to obtain the time asymptotic unstable steady-states is postponed to the second and third parts of this report.

The explicit Euler scheme is a good choice for time marching Eq. (1) towards time asymptotic stable steady-states not only due to its simplicity but also due to its parallelization efficiency. This is the approach used when employing 3D4S in this scenario. When time-accuracy is required for shock-capturing, however, high-order temporal integration should be used. Furthermore, this should be done in such a way as to preserve the nonlinear numerical stability properties of the chosen spatial discretization schemes. All time marching schemes with this property are known today as Strong-Stability-Preserving (SSP), although they were originally called TVD as well because this property does not allow the solution total variation to increase in time. High-order time marching schemes with this property preserve the nonlinear numerical stability properties of the Euler scheme, as long as their maximum time step is restricted. The SSP property was first proposed by Shu and Osher (1988), who proposed an explicit Runge-Kutta (RK) scheme with it. Although this SSP-RK scheme was originally presented in a format that did not belong to the traditional Butcher formulation (Butcher, 2008), it can be written in this way using appropriate algebraic procedures (Gottlieb and Shu, 1998; Spiteri and Ruuth, 2002). The nonlinear upper bound imposed on the maximum time step of high-order SSP marching schemes, which is smaller than its linear counterpart, led to the optimization of these schemes so they can achieve the largest possible maximum time steps. Gottlieb et al. (2009) derived optimal explicit SSP-RK schemes with up to fourth-order accuracy and five-stages. They are the ones used in 3D4S for time-accurate

simulations.

It is important to mention here that implicit SSP-RK schemes exist as well (Ferracina and Spijker, 2004), where optimal diagonally implicit schemes have been developed by Ferracina and Spijker (2005, 2008) with up to fourth-order accuracy and eight-stages and by Ketcheson et al. (2009) with up to sixth-order accuracy and eleven-stages. Second- and third-order accurate implicit-explicit (IMEX) RK schemes also exist (Pareschi and Russo, 2005), but only the explicit part is SSP. However, Santos and Alves (2021) have provided strong evidence that the nonlinear upper bound imposed on the time steps of implicit and IMEX SSP-RK schemes renders them inefficient when compared to their explicit counterparts. Hence, they are not used in 3D4S for time-accurate simulations.

A series of verification studies were performed on the 3D4S, in order to evaluate the implementation of the methods described in this subsection. Many different test cases were considered for these studies. They include the shock tube problem, the advection with a strong heat source, the advection of entropy disturbances and the propagation of confined thermoacoustic waves in a one-dimensional setting. Two-dimensional problems include the double Mach reflection, the supersonic flow upstream of a cylinder as well as the compression ramp. Finally, the three-dimensional supersonic flow over a curved ramp was also included as a test case. These verification studies are reported in subsection 3.1.

1.2.2 Supersonic Flow Upstream of a 2D Cylinder

Once verified, 3D4S was applied towards the simulation of both steady and time-accurate supersonic flows past bluff bodies. The main goal when doing so is to better understand the linear modal and non-modal instabilities at the windward face, where both subsonic and supersonic flows coexist.

The circular cylinder is arguably the most canonical blunt body geometry and, hence, has been the focus of several studies. Early numerical studies from the 1930's found approximate solutions for the velocity potential in the irrotational compressible flow around a cylinder (Imai, 1938; Tamada and Saito, 1939). Vorticity effects were latter found to have little effect on the shock curvature but increased the standoff distance (Hida, 1953). Early experimental studies from the 1960's were performed on a circular cylinder at Reynolds numbers between $4.5 \times 10^3 \leq Re_D \leq 6.65 \times 10^4$ and the Mach number $Ma = 5.7$ (McCarthy and Kubota, 1964). They found that the flow was laminar within this Reynolds number range and that transition in the wake occurs when the Reynolds number based on edge conditions and the standoff distance exceeds 85,000. Additional experiments documented surface pressure and wake flow profiles to determine the blunt body near wake characteristics in hypersonic conditions (Dewey, 1965).

Supersonic and hypersonic steady-states of the circular cylinder windward region became a benchmark problem for shock-capturing schemes since the discovery of the carbuncle phenomenon by Peery and Imlay (1988) and its

popularization by the in-depth analysis of Quirk (1994). In the cylinder case, it leads to stable and entropy-satisfying steady-states with an upstream shock protrusion mostly localized around the stagnation region. Many papers have been dedicated to the carbuncle phenomenon (Robinet et al., 2000; Pandolfi and Ambrosio, 2001; Coulombel et al., 2002; Dumbser et al., 2004; Chauvat et al., 2005), but the ones presented by Dumbser et al. (2004) and Elling (2009) deserve special attention. The former used a stability analysis based on the method of lines spatial discretization matrix generated by different solvers in order to identify when the carbuncle phenomenon would appear for each one whereas the latter showed that this phenomenon can have both numerical and physical origins. Although the carbuncle phenomenon has not yet been fully resolved, current understanding seems to indicate that it is only associated with complete Riemann solvers and becomes less severe as the accuracy order increases (Kemm, 2018).

Unfortunately, this seems to be the extent to which the windward region of the cylinder has been studied under supersonic/hypersonic flow conditions. The few other recent studies that remain focus on the leeward region instead. For instance, Canuto and Taira (2015) analyzed the steady and unsteady two-dimensional, viscous and subsonic compressible flows around a circular cylinder at Reynolds and Mach numbers between $20 \leq Re_D \leq 100$ and $0 \leq Ma \leq 0.5$, respectively. All simulations were performed using CharLES (Khalighi et al., 2011; Brès et al., 2012), a second-order accurate finite-volume solver integrated in time with a third-order explicit Runge-Kutta scheme. Compressibility effects were found to elongate the near wake for cases above and below the critical Reynolds number Re_c. At a fixed Re_D, the growth rate of the primary wake instability decreased with an increasing Ma, suggesting that compressibility effects are stabilizing. Another example was provided by Hinman and Johansen (2016), who studied the supersonic compressibility effects on the adiabatic boundary-layer separation occurring in a steady, two-dimensional and viscous flow at Reynolds numbers between $8 \times 10^3 \leq Re_D \leq 8 \times 10^4$ and the Mach number $Ma = 5.9$. This study was soon afterwards extended to Mach numbers between $6 \leq M \leq 10$ (Hinman and Johansen, 2017). Slip as well as no-slip boundary conditions were employed in an attempt to better understand the effects of the boundary-layer and off-body viscous forces on the separation location, compression fan and shock. These simulations in both studies were performed using the explicit second-order finite-volume solver rhoCentralFoam provided by the software OpenFOAM (Jasak et al., 2007). Finally, Park et al. (2016) conducted a computational investigation of the hypersonic steady wake, which includes temperature and chemistry effects for Reynolds numbers between $0.97 \times 10^4 \leq Re_D \leq 3.74 \times 10^4$ and the Mach number $Ma = 10$. All simulations were performed using an in-house explicit second-order finite volume solver (Jacobs et al., 2010). The effect of chemistry on the near wake was negligible for the low-enthalpy, high Reynolds number flows but more significant for the high-enthalpy, low Reynolds number flows. In the latter case, chemistry had most significant effect on the near wake size, the reattachment location, and also the vorticity

distribution within the recirculation region. Some wall surface results were validated against their own experimental data (Park et al., 2010).

A few other recent experimental studies are also available. Schmidt and Shepherd (2015) examined the wake behind the supersonic cylinder at Reynolds numbers between $2 \times 10^4 \leq Re \leq 5 \times 10^5$ and the Mach number $Ma = 4$. Periodic oscillations of the slip lines in the wake were observed with the Strouhal number increasing monotonically from 0.3 to 0.5 with an increasing Reynolds number. These oscillations were likely driven by acoustic signals propagating back and forth through the subsonic region between the separation points on the cylinder and the neck where the slip lines converge. Nagata et al. (2020) studied low Reynolds and Mach number flows between $1 \times 10^3 \leq Re \leq 5 \times 10^3$ and $0.1 \leq Ma \leq 0.5$, respectively, over a circular cylinder. Both numbers were found to have nonlinear effects on the vortex shedding frequency that were approximately proportional to the maximum width of the recirculation zone. They showed that the Mach number effect on the release location of the Kármán vortices, vortex shedding Strouhal number and maximum width of the recirculation changes at approximately $Re = 3000$. In addition, span wise phase differences for the surface pressure fluctuation and the vortex shedding due to the oblique instability wave on the separated shear layer caused by compressibility effects was recorded.

This review illustrates that the level of understanding currently available about instabilities on bluff bodies in general and on the circular cylinder in particular is presently missing in the supersonic and hypersonic regimes, compared to their incompressible counterpart. Furthermore, it shows that computational investigations of these instabilities have been performed using low-order accurate simulations. Hence, there ample ground to close this knowledge gap using the high-order accurate capabilities of 3D4S.

1.2.3 Supersonic Flow Over a 2D Compression Ramp

Once verified, 3D4S was also applied towards the simulation of both steady and time-accurate supersonic flows over a compression ramp. The main goal when doing so is to improve our understanding of both modal and non-modal linear instabilities associated with the separation and reattachment phenomena induced by the corner.

Early experimental studies of separation observed in shock / boundary-layer interaction (SBLI) problems for different geometrical variations from the classical flat plate were first performed more than half a century ago by Chapman et al. (1957, 1958). Separation is one of the key phenomena associated with the laminar-turbulence transition in high speed flows. The same can be said about its stable/unstable dynamics. Both are essential for the identification of the laminar / transitional / turbulent regions in such supersonic and hypersonic external flows. This is the very reason why SBLI problems are still the subject of intensive studies today (Dolling, 2001; Gaitonde, 2015). In this report, focus is placed on the supersonic flow over a compression ramp because of its unique features. As originally described

by Carter (1972), an adverse (favorable) pressure gradient appears upstream (downstream) of the corner, causing the incoming flat plate boundary-layer to separate (reattach). The creations of this recirculation region, or bubble, leads to the formation of a compression fan and, hence, a shock near both separation and reattachment locations.

A few early numerical studies are also worth citing. Carter (1972) used a first-order predictor-corrector scheme for time integration and a second-order finite-difference scheme for spatial discretization to obtain steady-states with (Mach,Reynolds) number pairs equal to $(M, Re) = (3, 1.68 \times 10^4)$, $(4, 6.8 \times 10^4)$ and $(6.06, 1.5 \times 10^5)$, with the latter based on the leading edge to corner length, using ramp angles of $\theta = 5^o$, 7.5^o and 10^o. Many relevant characteristics of these flows were quantified, such as incipient separation and bubble size, showing good agreement with experimental data (Lewis et al., 1968). Hung and MacCormack (1976) used the second-order accurate, in time and space, two-step MacCormack scheme to simulate this problem with $M = 14.1$, $Re = 1.04 \times 10^5$ and $\theta = 15^o$, 18^o and 24^o and also validate their pressure and skin friction coefficient results against available experimental data (Holden and Moselle, 1969). They also compared velocity profiles with inviscid theory and numerical simulations (Carter, 1972), showing important differences with respect to the former and good agreement with the latter. These two-dimensional simulations were replicated and extended to three dimensions by Rudy et al. (1991), who compared the performance of four different finite-difference and finite-volume based solvers. All aforementioned studies solved the compressible Navier-Stokes equations, where all variables are prescribed at the inlet and all variables are extrapolated at the outlet.

Only very recent studies are now described in more detail, since most of the earlier ones have already been reviewed elsewhere (Dolling, 2001; Gaitonde, 2015). Chuvakhov et al. (2017) obtained two and three-dimensional steady-states using the HSFlow solver, based on a quasi-monotonic Godunov-type scheme that is second-order accurate in both time and space, for a compression ramp with $M = 8$, $Re = 3.71 \times 10^5$ and $\theta = 15^o$. The latter simulations modeled the effect of small bluntness elements at the leading edge, which lead to the appearance of the stationary Görtler vortices that had been observed in their own experimental data. Sidharth et al. (2018) obtained two-dimensional steady-states using US3D, under an implicit Euler marching of a second-order spatial discretization based on a modified Steger-warming fluxes using MUSCL limiters, for a double corner with $M = 5$, $Re = 6.8 \times 10^5$ and $\theta = 12 - 20^o$. It was used in a bi-global linear and modal stability analysis, which identified an unstable stationary mode. This implied the existence of a three-dimensional steady-state, which was later confirmed by their three-dimensional US3D simulations. Dwivedi et al. (2019) extended these tools to include a resolvent analysis, applying them to the previously studied compression ramp (Chuvakhov et al., 2017). This allowed them to verify that the steady and three-dimensional reattachment streaks previously attributed to a centrifugal instability were in fact caused by baroclinic effects. They also verified that the streak spanwise wavelength was selected by the

perturbations present in both separation bubble and reattaching shear layer. Hao et al. (2021) obtained two-dimensional steady-states using the PHAROS solver, which uses an implicit line relaxation for time integration of a second-order spatial discretization based on a modified Steger-Warming scheme, for a compression ramp with $M = 7.7$, $Re = 4.2 \times 10^5$ and several ramp angles between $\theta = 11^o$ and 15^o. A bi-global linear stability analysis revealed the existence of stationary modes at both small and large spanwise wavelengths, but oscillatory modes were only found at the former. Recirculation bubble size and disturbance amplitudes increased when increasing ramp angle and decreasing wall temperature. These results were verified by unsteady three-dimensional simulations employing a third-order explicit SSP-RK scheme to march in time a higher-order spatial discretization, based on a fifth-order WENO scheme for inviscid fluxes and a sixth-order central-difference scheme for the viscous fluxes (Cao et al., 2021). Exposito et al. (2021) used the same aforementioned US3D solver to evaluate both blunt leading edge and finite span effects on three-dimensional steady-states with $Re = 1.07 \times 10^5$, $M = 9.66$, as well as $\theta = 10^o$ and 20^o, comparing it with triple deck theory. The separation region increased when increasing bluntness. Furthermore, three-dimensional effects were confined to the side edges, which appears to have prevented the appearance of secondary vortices.

The above review suggests that steady-states for the compression ramp problem have been obtained using at most second-order schemes in the spatial discretization. Hence, a main goal of the present report is to discuss the numerical issues associated with obtaining such steady-states using low and high-order schemes in both time and space. Furthermore, the impact of using these low and high accuracy steady-states on the results obtained by a linear stability analysis is also discussed. Finally, these studies have also focussed on high Reynolds number simulations. Hence, another major goal of this report is to investigate the parametric conditions for the onset of instability in compression ramps, which occurs at lower Reynolds numbers.

1.3 Objectives

This part of the report describes the construction of highly accurate steady-states for high-speed flows. It shows the many advantages of doing so using high-order discretization schemes, instead of their low-order counterparts. In the present chapter, focus is placed on supersonic/hypersonic flows with shocks that are physically stable in a linear and time asymptotic sense. These very accurate steady-states are then used as base flows in both modal and non-modal linear stability analyses to uncover correct physical instabilities in these flows. The next chapters pursue this matter by first performing verification studies and then investigating the two-dimensional supersonic flows upstream of a cylinder as well as over a compression ramp.

Chapter 2

Mathematical Formulation

2.1 Governing Equations

2.1.1 Scalar Equations

Before applying complex time integration and discretization schemes to more general conservation laws, it is quite useful to first test these schemes on scalar conservation laws. Consider the general equation

$$\frac{\partial u}{\partial t} + \frac{\partial f}{\partial x} = 0 \quad , \tag{2.1}$$

written in conservative form. When its flux f is given by

$$f(u) = \frac{u^2}{2} - \mu \frac{\partial u}{\partial x} \quad , \tag{2.2}$$

it becomes the well known viscous Burgers' equation, where t is time, x is the spatial coordinate, $u(x,t)$ is the streamwise velocity component and μ is the dynamic viscosity. In the inviscid limit, this flux becomes

$$f(u) = \frac{u^2}{2} \quad , \tag{2.3}$$

which is commonly called the inviscid Burgers' equation or the nonlinear wave equation. The popularity of this hyperbolic equation comes from its ability to model rarefaction waves that eventually smooth out as well as compression waves that eventually shock up. In the limit of a constant wave propagation velocity c, this flux becomes

$$f(u) = c\,u \quad , \tag{2.4}$$

which is commonly called the linear wave equation.

2.1.2 Navier-Stokes Equations

Dimensional Form

The generalization of these laws considered in this report are the unsteady and compressible mass, momentum and energy conservation equations in

chemical and thermal equilibrium. Direct numerical simulations (DNS) of these equations are often performed on their conservative form, namely

$$\frac{\partial \mathbf{Q}}{\partial t} + \frac{\partial \mathbf{E}}{\partial x_j} = \frac{\partial \mathbf{F}}{\partial x_j} \quad , \tag{2.5}$$

in Cartesian coordinates, where $j = 1$ to N. One, two and three-dimensional simulations use $N = 1$, 2 and 3, respectively. The conservative variable vector $\mathbf{Q}$, inviscid fluxes $\mathbf{E}$ and viscous fluxes $\mathbf{F}$ are given by

$$\mathbf{Q} = \left\{ \begin{array}{c} \rho \\ \rho\, u_i \\ \rho\, E \end{array} \right\} \ , \ \mathbf{E} = \left\{ \begin{array}{c} \rho\, u_j \\ \rho\, u_i\, u_j + p\, \delta_{i,j} \\ (\rho\, E + p)\, u_j \end{array} \right\} \text{ and } \mathbf{F} = \left\{ \begin{array}{c} 0 \\ \tau_{i,j} \\ \tau_{i,k}\, u_k - q_j \end{array} \right\} \ , \tag{2.6}$$

respectively, where ρ is the density, u_i are the velocity components, p is the pressure and $\delta_{i,j}$ is the Kronecker delta. The specific total energy E is the sum of the specific internal energy e and the specific kinetic energy, i.e.

$$E = e + \frac{1}{2}\, u_j\, u_j \quad . \tag{2.7}$$

Additional constitutive relations must now be defined to provide closure. The first one used here assumes that the fluid behavior is Newtonian and, hence, the shear-stress tensor components $\tau_{i,j}$ can be written as

$$\tau_{i,j} = \mu \left(\frac{\partial u_i}{\partial x_j} + \frac{\partial u_j}{\partial x_i} \right) + \lambda\, \frac{\partial u_k}{\partial x_k}\, \delta_{i,j} \quad , \tag{2.8}$$

where the Stokes hypothesis is invoked, namely

$$\lambda + \frac{2}{3}\, \mu = 0 \quad , \tag{2.9}$$

for the second viscosity coefficient λ. The second constitutive relation that is used here assumes that thermal diffusion is governed by Fourier's law, i.e. the heat-flux components can be defined as

$$q_j = -\kappa\, \frac{\partial T}{\partial x_j} \quad , \tag{2.10}$$

and κ is the thermal conductivity and T is the temperature. The third constitutive relation assumes the fluid behaves as a perfect gas, which allows one to employ the equation of state

$$p = \rho\, R\, T \quad , \tag{2.11}$$

where R is the gas constant. This can be further simplified by assuming the gas is calorically perfect, i.e. ideal. In other words, the specific heats at constant pressure C_P and volume C_V are constant, which leads to

$$h = C_P\, T \quad \text{and} \quad e = C_V\, T \quad , \tag{2.12}$$

where h is the specific enthalpy. Such an assumption allows the equation of state defined in Eq. (2.11) to be conveniently re-written as

$$p = (\gamma - 1)\left(\rho\, E - \frac{(\rho\, u_j)^2}{2\,\rho}\right) \quad , \tag{2.13}$$

using the thermodynamic relations

$$\gamma = \frac{C_P}{C_V} \quad \text{and} \quad R = C_P - C_V \quad , \tag{2.14}$$

since now it depends only on conservative variables, where γ is the ratio between specific heats at constant pressure and volume.

Dimensionless Form

It is important to re-write these equations in dimensionless form because this is how they are implemented in 3D4S. Furthermore, doing so highlights the relevant dimensionless parameters. This is achieved by defining

$$\begin{gathered} \rho^* = \frac{\rho}{\rho_R} \quad , \quad u_j^* = \frac{u_j}{U_R} \quad , \quad p^* = \frac{p}{\rho_R\, U_R^2} \quad , \quad T^* = \frac{T}{T_R} \quad , \\ x_j^* = \frac{x_j}{L_R} \quad , \quad t^* = \frac{t}{L_R/U_R} \quad , \quad \mu^* = \frac{\mu}{\mu_R} \quad \text{and} \quad \kappa^* = \frac{\kappa}{\kappa_R} \quad , \end{gathered} \tag{2.15}$$

where the superscript $*$ and the subscript R represent dimensionless and reference quantities, respectively. Dropping the superscript for the sake of simplicity, all previous equations retain their original format, except

$$\tau_{i,j} = \Pi_1 \left\{ \mu \left(\frac{\partial u_i}{\partial x_j} + \frac{\partial u_j}{\partial x_i} \right) + \lambda \frac{\partial u_k}{\partial x_k}\, \delta_{i,j} \right\} \quad , \tag{2.16}$$

$$q_j = -\Pi_2\, \kappa \frac{\partial T}{\partial x_j} \quad , \tag{2.17}$$

$$p = \Pi_3\, \rho\, T \quad , \tag{2.18}$$

which are modified by the generic dimensionless parameters

$$\Pi_1 = \frac{\mu_R}{\rho_R\, U_R\, L_R} \quad , \quad \Pi_2 = \frac{\kappa_R\, T_R}{\rho_R\, U_R^3\, L_R} \quad \text{and} \quad \Pi_3 = \frac{R\, T_R}{U_R^2} \quad , \tag{2.19}$$

noting that Eq. (2.13) only retains its original format if the definitions

$$e^* = \frac{e}{C_V\, T_R} \quad \text{and} \quad E^* = \frac{E}{U_R^2} \quad , \tag{2.20}$$

are added to Eq. (2.15).

When the reference state is defined using free stream conditions, which are represented here by the subscript ∞, Eq. (2.19) becomes

$$\Pi_1^{-1} = Re_\infty \quad , \quad \Pi_2^{-1} = (\gamma - 1)\, Re_\infty\, Pr_\infty\, Ma_\infty^2 \quad \text{and} \quad \Pi_3^{-1} = \gamma\, Ma_\infty^2 \quad , \tag{2.21}$$

where the Reynolds, Prandtl and Mach numbers are defined as

$$Re_\infty = \frac{\rho_\infty\, U_\infty\, L_\infty}{\mu_\infty} \quad , \quad Pr_\infty = \frac{\mu_\infty\, C_P}{\kappa_\infty} \quad \text{and} \quad Ma_\infty = \frac{U_\infty}{a_\infty} \quad , \tag{2.22}$$

respectively, noting that C_P is a constant and

$$a = \sqrt{\frac{\gamma\, p}{\rho}} \quad , \tag{2.23}$$

is the sound speed for a perfect gas. If the reference velocity is defined using the free stream perfect gas sound speed a_∞ instead of the free stream velocity U_∞, but all other reference states remain the same, Eq. (2.19) becomes

$$\Pi_1^{-1} = \frac{Re_\infty}{Ma_\infty} \quad , \quad \Pi_2^{-1} = \frac{(\gamma - 1)\, Re_\infty\, Pr_\infty}{Ma_\infty} \quad \text{and} \quad \Pi_3^{-1} = \gamma \quad , \tag{2.24}$$

which is the version currently implemented in 3D4S. Hence, one needs to specify the dimensionless parameters Re_∞, Ma_∞ and Pr_∞ in order to run 3D4S. Beyond these three dimensionless parameters, the only additional input required are dimensional reference temperature T_R and the dimensionless dynamic viscosity μ and thermal conductivity κ.

Fluid Properties

Hence, the last step is to briefly discuss the dependence of the fluid properties on the thermodynamic state of the high speed flows considered in this report. Both specific heats are constant, since the fluid is assumed to behave as a calorically perfect gas. Furthermore, the dynamic viscosity is assumed to follow Sutherland's law, which is given by

$$\mu(T) = \frac{1 + T_0}{T + T_0}\, T^{3/2} \quad , \tag{2.25}$$

in dimensionless form, where $T_0 = S/T_R$. Unless stated otherwise, $T_R = 273.15\, K$ and $S = 110.4\, K$. Finally, the thermal conductivity is obtained from a constant Prandtl number assumption. Since the variable Prandtl number can be written as $Pr = \mu\, C_P/\kappa = (\mu^*/\kappa^*)\, Pr_\infty$, one can write

$$\kappa(T) = \mu(T) \quad , \tag{2.26}$$

when it is assumed constant, i.e. $Pr = Pr_\infty$, where the $*$ has been dropped again for the sake of simplicity.

2.2 Numerical Methods

2.2.1 Spatial Discretization

Viscous Fluxes

Standard second and fourth-order central-difference schemes in conservative form are implemented in 3D4S. In order to illustrate how they work, consider the typical scalar viscous flux differentiation

$$\frac{\partial f}{\partial x} = \frac{\partial}{\partial x}\left(\mu \frac{\partial u}{\partial x}\right) \quad , \tag{2.27}$$

taken from Eqs. (2.1) and (2.2). Its second-order discretization uses

$$\left.\frac{\partial f}{\partial x}\right|_i = \frac{f_{i+1} - f_{i-1}}{2\,\Delta x} + O(\Delta x^2) \quad , \tag{2.28}$$

coupled with the second-order viscous flux approximation

$$f_i = \mu_i \frac{u_{i+1} - u_{i-1}}{2\,\Delta x} + O(\Delta x^2) \quad , \tag{2.29}$$

which maintains second-order accuracy as long as μ is smooth enough. Its fourth-order version can be derived in a similar fashion.

Inviscid Fluxes

The major numerical methods used for the spatial discretization of inviscid fluxes in 3D4S are now described in more detail. A hyperbolic scalar equation is considered first and then generalized to a system of equations. In the former scenario, the conservative discretization of Eq. (2.1) with (2.3) becomes

$$u_i^{n+1} = u_i^n - \frac{\Delta t}{\Delta x}\left(\bar{f}_{i+1/2} - \bar{f}_{i-1/2}\right) \quad , \tag{2.30}$$

where Δx represents the uniform spacing between consecutive grid points i and the marching scheme can be either explicit or implicit. In order to take into account the wave propagation directions, only the subclass of monotone fluxes known as flux-splitting needs to be considered. It satisfies $f(u) = f^+(u) + f^-(u)$, where $df^+(u)/du \geq 0$ and $df^-(u)/du \leq 0$. Furthermore, the process of calculating the numerical fluxes at the cell interfaces from the original function at the cell center, e.g. $f_i^{\pm} \rightarrow \bar{f}_{i+1/2}^{\pm}$, is called reconstruction. These numerical fluxes can also be split as

$$\bar{f}_{i+1/2} = \bar{f}_{i+1/2}^{+} + \bar{f}_{i+1/2}^{-} \quad , \tag{2.31}$$

where their positive $\bar{f}_{i+1/2}^{+}$ and negative $\bar{f}_{i+1/2}^{-}$ parts are obtained in different ways by different schemes.

Total Variation Diminishing Schemes

TVD schemes calculate the positive and negative interface numerical fluxes using expressions such as

$$\begin{aligned} \bar{f}^{+}_{i+1/2} &= f^{+}_{i} + \tfrac{1}{2}\psi(\theta^{+}_{i+1/2})(f^{+}_{i+1} - f^{+}_{i}) \quad \text{and} \\ \bar{f}^{-}_{i+1/2} &= f^{-}_{i+1} - \tfrac{1}{2}\psi(\theta^{-}_{i+1/2})(f^{-}_{i+1} - f^{-}_{i}) \quad , \end{aligned} \tag{2.32}$$

respectively, where $\theta_{i+1/2}$ is the local smoothness measurement and ψ is the flux-limiter function. The former is calculated using divided differences, i.e.

$$\theta^{+}_{i+1/2} = \frac{f^{+}_{i} - f^{+}_{i-1}}{f^{+}_{i+1} - f^{+}_{i}} \quad \text{and} \quad \theta^{-}_{i+1/2} = \frac{f^{-}_{i+2} - f^{-}_{i+1}}{f^{-}_{i+1} - f^{-}_{i}} \quad , \tag{2.33}$$

whereas the latter can be calculated in a variety of ways, such as

$$\psi(\theta) = \max[\,0\,,\,\min[\,1\,,\,2\,\theta\,]\,,\,\min[\,2\,,\,\theta\,]\,] \quad , \tag{2.34}$$

$$\psi(\theta) = \max[\,0\,,\,\min[\,1\,,\,\theta\,]\,] \quad , \tag{2.35}$$

$$\psi(\theta) = \max[\,0\,,\,\min[\,2\,,\,2\,\theta\,,\,(1+\theta)/2\,]\,] \quad , \tag{2.36}$$

$$\psi(\theta) = (\theta + |\theta|)/(1 + |\theta|) \quad , \tag{2.37}$$

$$\psi(\theta) = \max[\,0\,,\,\min[\,2\,,\,2\,\theta\,,\,(1+2\,\theta)/3\,]\,] \quad , \tag{2.38}$$

$$\psi(\theta) = \max[\,0\,,\,\min[\,1\,,\,\beta\,\theta\,]\,,\,\min[\,\beta\,,\,\theta\,]\,] \quad , \tag{2.39}$$

$$\psi(\theta) = \max[\,0\,,\,\min[\,\beta\,,\,\theta\,]\,] \quad , \tag{2.40}$$

$$\psi(\theta) = 1.5\,\theta\,(1+\theta)/(1+\theta+\theta^2) \quad \text{and} \tag{2.41}$$

$$\psi(\theta) = \theta\,(1+\theta)/(1+\theta^2) \quad , \tag{2.42}$$

which are called Superbee, Minmod, Monotonized Central (MC), vam Leer, Koren, Sweby with $1 \le \beta \le 2$, Osher with $1 \le \beta \le 2$, Ospre and van Albada. Their references have already been provided in subsection 1.2.1 and the behavior of some flux-limiters is shown in Fig. 2.1. It is important to note that the respective $i - 1/2$ interface formulas are obtained by replacing i by $i - 1$ in Eqs. (2.31), (2.32) and (2.33).

Essentially Non-Oscillatory Schemes

ENO schemes, on the other hand, calculate the positive and negative interface numerical fluxes using expressions such as

$$\bar{f}^{+}_{i+1/2} = \sum_{k=0}^{r-1} \omega^{+}_{k}\, q^{r+}_{k} \quad \text{and} \quad \bar{f}^{-}_{i+1/2} = \sum_{k=0}^{r-1} \omega^{-}_{r-1-k}\, q^{r-}_{k} \quad , \tag{2.43}$$

where q^{r}_{k} represents each numerical flux k used in the spatial discretization, r and ω_k respectively fix their stencil size and weight in the reconstruction

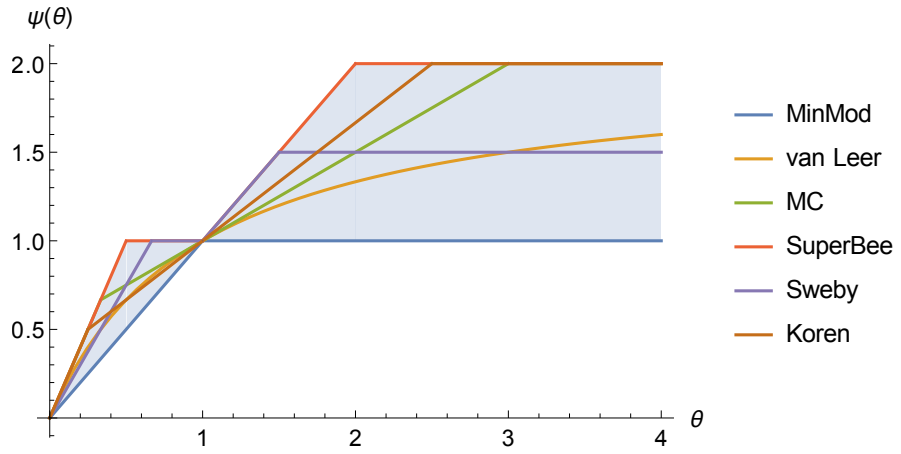

Figure 2.1: Local smoothness parameter dependence of some flux-limiters.

process. Expressions for the former are given by

$$q_k^{r+} = \sum_{n=0}^{r-1} \Gamma_k^n \, f^+_{i+n+1+k-r} \quad \text{and} \quad q_k^{r-} = \sum_{n=0}^{r-1} \Gamma_{k+1}^n \, f^-_{i+n+1+k+1-r} \quad , \tag{2.44}$$

which uses the coefficients Γ_k^n obtained from

$$\Gamma_k^n = \sum_{m=n+1}^{r} \frac{\sum_{l=0,l\neq m}^{r} \prod_{q=0,q\neq l,m}^{r} r-k-q}{\prod_{l=0,l\neq m}^{r} m-l} \quad , \tag{2.45}$$

and for the latter are given by

$$\omega_k^{\pm} = \frac{\alpha_k^{\pm}}{\sum_{n=0}^{r-1} \alpha_n^{\pm}} \quad , \tag{2.46}$$

which uses the coefficients $\alpha_k^{\pm}$ obtained from

$$\alpha_k^{\pm} = \frac{C_k^r}{(\varepsilon + IS_k^{\pm})^r} \quad , \tag{2.47}$$

where ϵ is an arbitrary positive real number introduced to avoid division by zero, usually chosen to be $\epsilon = 10^{-6}$, and the unique values of C_k^r are selected in such a way as to improve accuracy. Examples are given in Tab. 2.1, where it is possible to verify that $\sum_{k=0}^{r-1} C_k^r = 1$. Finally, IS_k represents a smoothness indicator, which is defined as

$$IS_k = \sum_{l=1}^{r-1} \sum_{j=1}^{r-l} \frac{(f[i+k+j-r, l])^2}{r-l} \quad , \tag{2.48}$$

where $f[\,\cdot\,,\,\cdot\,]$ is given by the recursive diference formula

$$f[\,i\,,\,0\,] = f_i \quad \text{and} \quad f[\,i\,,\,j\,] = f[\,i+1\,,\,j-1\,] - f[\,i\,,\,j-1\,] \quad , \tag{2.49}$$

for $j = 1\,,\,2\,,\,\ldots\,,\,r-1$.

Table 2.1: Coefficients required to provide optimal ENO weights.

C_k^r	$k=0$	$k=1$	$k=2$	$k=3$
$r=1$	1			
$r=2$	1/3	2/3		
$r=3$	1/10	6/10	3/10	
$r=4$	4/35	18/35	12/35	1/35

Weighted Essentially Non-Oscillatory Schemes

Finally, WENO schemes are ENO schemes that use different approaches to calculate the weights in order to improve accuracy near discontinuities. For instance, the original fifth-order accurate version, named here WENO5-JS, calculates the smoothness indicator IS_k according to a formula based on a weighted average between the first and second derivatives of the polynomial approximations for the numerical fluxes q_k^r. It, however, reduces to third-order accurate near discontinuities due to the magnitude of ϵ. Necessary and sufficient conditions for fifth-order accuracy were then derived to created the mapped WENO, or WENO5-M. It calculates the weights ω_k using new coefficients α_k obtained from the special function $\alpha_k = g(\omega_k^{(JS)})$, where $\omega_k^{(JS)}$ is the ω_k from WENO5-JS. This function has the special properties $g_k(0) = 1$, $g_k(1) = 1$, $g_k(\bar{\omega}_k) = \bar{\omega}_k$, $g_k'(\bar{\omega}_k) = 1$ and $g_k''(\bar{\omega}_k) = 0$ with $\bar{\omega}_k \in (0, 1)$, which make it monotonically increasing with a bounded slope. It allowed significantly smaller values of ϵ to be used. A computationally less expensive version of WENO5-M known as WENO5-Z was then developed. It is based on a linear combination of the smoothness indicators already available in WENO5-JS, which leads to a less dissipative and more accurate scheme than the original one. In this version, the coefficients α_k are obtained from $\alpha_k = C_k^r(1 + (|IS_0 + IS_2|/(\epsilon + IS_k))^2)$, which allows the use of significantly smaller values of ϵ and maintains fifth-order accuracy near discontinuities. Finally, an improvement on WENO5-Z known as WENO5-Z+ was developed to achieve better accuracy in smooth regions as well as better numerical stability. It does so by modifying the coefficients α_k formula to $\alpha_k = C_k^r(1 + ((\epsilon + IS_0 + IS_2)/(\epsilon + IS_k))^2 + \vartheta\,(\epsilon + IS_k)/\epsilon + IS_0 + IS_2))$, where $\vartheta = \Delta x^{2/3}$ was determined empirically. These are the WENO5 schemes implemented in 3D4S for time-accurate unsteady simulations. However, their residue does not settle down to machine precision levels at steady-state because they suffer from post-shock oscillations whose magnitude is proportional to the local truncation error. In order to fix this issue, a convex combination of quartic and linear polynomials on unequal sized stencils is used by the so-called WENO5-ZQ schemes. This is the WENO5 scheme implemented in 3D4S for disturbance free steady-state simulations. The references for all these WENO schemes have already been provided in subsection 1.2.1.

Flux Splitting

The aforementioned techniques for hyperbolic scalar equations now have to be generalized for a system of equations. Doing so, however, requires new techniques to calculate the fluxes in such a way that takes into account the propagation direction of their characteristic waves. Two major techniques exist to split these fluxes according to their propagation directions.

The first one is known as flux-difference splitting. Its first step is to employ a conservative discretization of Eq. (2.5), illustrated here for the particular cases where $\mathbf{F} = 0$ and $N = 1$, leading to

$$\mathbf{Q}_i^{n+1} = \mathbf{Q}_i^n - \frac{\Delta t}{\Delta x}\left(\bar{\mathbf{E}}_{i+1/2} - \bar{\mathbf{E}}_{i-1/2}\right) \quad , \tag{2.50}$$

which can be generalized for two ($N = 2$) and three ($N = 3$) dimensional flows in a straightforward manner. The flux-splitting comes in its second step. It writes the cell interface fluxes in the general form

$$\bar{\mathbf{E}}_{i+1/2} = \bar{\mathbf{E}}_{i+1/2}^{(CD)} - \bar{\mathbf{D}}_{i+1/2} \quad , \tag{2.51}$$

where the first term represents a central difference (CD) reconstruction of the interface flux and the second term represents numerical diffusion. Both can be written in many different ways. The former often takes the form

$$\bar{\mathbf{E}}_{i+1/2}^{(CD)} = \frac{1}{2}\left(\mathbf{E}_i + \mathbf{E}_{i+1}\right) \quad , \tag{2.52}$$

which leads to an unstable second-order central-difference discretization of the inviscid flux when employed by itself. Hence, the latter must be nonzero and it often takes the form

$$\bar{\mathbf{D}}_{i+1/2} = \sum_{k=-r}^{r} C_k^+ \, \Delta\mathbf{E}_{i+1/2+k}^+ - \sum_{k=-r}^{r} C_k^- \, \Delta\mathbf{E}_{i+1/2+k}^- \quad , \tag{2.53}$$

where the positive and negative flux-differences are defined as

$$\Delta\mathbf{E}_{i+1/2}^{\pm} = \mathbf{A}_{i+1/2}^{\pm} \cdot \Delta\mathbf{Q}_{i+1/2} \quad , \tag{2.54}$$

employing the variable difference, defined as

$$\Delta\mathbf{Q}_{i+1/2} = \mathbf{Q}_{i+1} - \mathbf{Q}_i \quad , \tag{2.55}$$

as well as the positive and negative inviscid Jacobians, defined as

$$\mathbf{A}_{i+1/2}^{\pm} = \mathbf{M}_{i+1/2} \cdot \mathbf{\Lambda}_{i+1/2}^{\pm} \cdot \mathbf{M}_{i+1/2}^{-1} \quad \text{with} \quad \mathbf{A} = \frac{\partial \mathbf{E}}{\partial \mathbf{Q}} \quad , \tag{2.56}$$

which are evaluated using the Roe averaged variables

$$(\cdot)_{i+1/2} = \frac{\sqrt{\rho_i}\,(\cdot)_i + \sqrt{\rho_{i+1}}\,(\cdot)_{i+1}}{\sqrt{\rho_i} + \sqrt{\rho_{i+1}}} \quad \text{and} \quad \rho_{i+1/2} = \sqrt{\rho_i\,\rho_{i+1}} \quad , \tag{2.57}$$

and the positive and negative eigenvalues

$$\mathbf{\Lambda}^{\pm}_{i+1/2} = \frac{1}{2}\left(\mathbf{\Lambda}_{i+1/2} \pm |\mathbf{\Lambda}_{i+1/2}|\right) \quad , \tag{2.58}$$

defined according to Steger and Warming, where $\mathbf{M}$ and $\mathbf{M}^{-1}$ are the right and left eigenvector matrixes that diagonalize the inviscid Jabobian $\mathbf{A}$ to generate its eigenvalue matrix $\mathbf{\Lambda}$. The values of r and $C_k^{\pm}$ set the accuracy order of the resulting spatial discretization. For instance, setting $r = 0$ and $C_0^+ = C_0^- = 1/2$ yields the classical Roe flux-difference splitting scheme. Unfortunately this approach does not satisfy the entropy conditions. Hence, an entropy fix must be employed. It works by correcting the eigenvalues when they change signs. References for the original Roe scheme as well as the HLL and Roe-HLL entropy fixes implemented in 3D4S with its TVD schemes have already been cited in subsection 1.2.1.

The second one is known as flux-vector splitting. Contrary to its flux-difference counterpart, its first step is to split the inviscid fluxes. In other words, the flux $\mathbf{E}$ in the hyperbolic version of Eq. (2.5) is first split as

$$\mathbf{E} = \mathbf{E}^+ + \mathbf{E}^- \quad , \tag{2.59}$$

which takes advantage of the homogeneity property of this flux, i.e.

$$\mathbf{E} = \mathbf{A} \cdot \mathbf{Q} \quad , \tag{2.60}$$

to split it using to its Jacobian as

$$\mathbf{A} = \mathbf{A}^+ + \mathbf{A}^- \quad , \tag{2.61}$$

where $\mathbf{A}$ is defined in Eq. (2.56), and write the positive and negative fluxes that were split in Eq. (2.59) as

$$\mathbf{E}^{\pm} = \frac{1}{2}\left(\mathbf{E} \pm \mathbf{A}^{\pm} \cdot \mathbf{Q}\right) \quad , \tag{2.62}$$

noting that many different choices for $\mathbf{A}^{\pm}$ exist. In most cases, an eigenvalue splitting is pursued, leading this expression to be re-written as

$$\mathbf{E}^{\pm} = \frac{1}{2}\left(\mathbf{E} \pm \mathbf{M} \cdot \bar{\mathbf{\Lambda}} \cdot \mathbf{M}^{-1} \cdot \mathbf{Q}\right) \quad , \tag{2.63}$$

where the choice of $\bar{\mathbf{\Lambda}}$ defines the splitting. For instance, choosing $\bar{\mathbf{\Lambda}} = \mathbf{\Lambda}^{\pm}$, defined in Eq. (2.58), returns the Steger and Warming splitting. However, the global (1D) and local (2 and 3D) Lax-Friedrichs splittings are implemented in 3D4S with its WENO schemes. It is important to note that the left and right eigenvector matrices $\mathbf{M}^{-1}$ and $\mathbf{M}$ are used to write the fluxes in characteristic variables before reconstruction and transform these variables back to the conservative ones after reconstruction, respectively. References for the flux-vector splitting discussed here is provided in subsection 1.2.1.

2.2.2 Grid Generation

Two-dimensional grid generation consists in transforming a unit square with Cartesian coordinates, $\boldsymbol{\xi} = [\xi, \eta]^T$, in the computational space $\mathcal{C}$ to a two-dimensional physical space $\mathcal{D}$ with arbitrary geometry and coordinates, $\mathbf{x} = [x, y]^T$. In general, just these two spaces are used. The basic idea is to introduce an intermediary coordinate system, $\mathbf{s} = [s, t]^T$, which is called parameter space $\mathcal{P}$. This space is used to compute the control functions which are defined by a transformation called *grid control map*. This transformation is an algebraic transformation that maps the computational space $\mathcal{C}$ onto the parameter space $\mathcal{P}$. In addition, an elliptic transformation maps the parameter space onto the domain in the physical space $\mathcal{D}$. Therefore, the main issue is to construct appropriate grid control maps in a way that the corresponding grid in physical space has the desired properties. Fig. 2.2 shows these three spaces. References are provided in subsection 1.2.1.

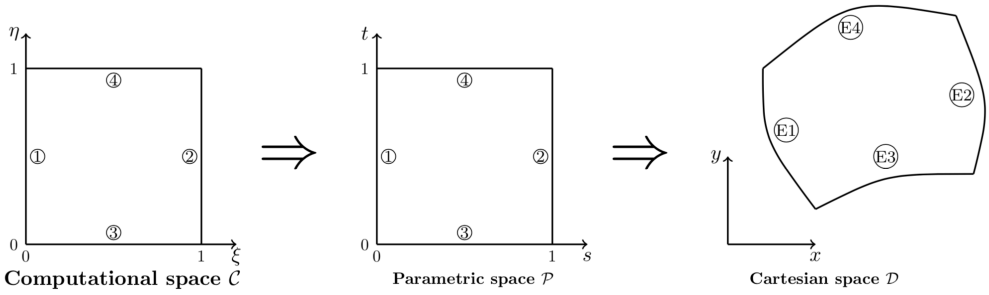

Figure 2.2: Transformation from computational (ξ, η) space to a physical domain $\mathcal{D}$ in Cartesian (x, y) space going through a parametric (s, t) space.

The elliptic partial differential equations used are

$$\begin{aligned} a_{22}\mathbf{x}_{\xi\xi} - 2a_{12}\mathbf{x}_{\xi\eta} + a_{11}\mathbf{x}_{\eta\eta} \;+\; & \left(a_{22}P_{11}^1 - 2a_{12}P_{12}^1 + a_{11}P_{22}^1\right)\mathbf{x}_\xi \\ & +\; \left(a_{22}P_{11}^2 - 2a_{12}P_{12}^2 + a_{11}P_{22}^2\right)\mathbf{x}_\eta = 0 \quad , \end{aligned} \tag{2.64}$$

where the subscripts ξ and η represent partial derivatives $\partial/\partial\xi$ and $\partial/\partial\eta$, respectively. Additionally, $a_{ij} = \langle \mathbf{a}_i, \mathbf{a}_j \rangle$ represents the inner product between different covariant base vectors $\mathbf{a}_i$, given by

$$\mathbf{a}_1 = \begin{bmatrix} \frac{\partial x}{\partial \xi} \\ \frac{\partial y}{\partial \xi} \end{bmatrix} = \mathbf{x}_\xi \quad \text{and} \quad \mathbf{a}_2 = \begin{bmatrix} \frac{\partial x}{\partial \eta} \\ \frac{\partial y}{\partial \eta} \end{bmatrix} = \mathbf{x}_\eta \quad , \tag{2.65}$$

and the six coefficients P_{11}^1, P_{12}^1, P_{22}^1,P_{11}^2, P_{12}^2, and P_{22}^2 are the so-called control functions, calculated by

$$\begin{pmatrix} P_{11}^1 \\ P_{11}^2 \end{pmatrix} \;=\; -\mathbf{T}^{-1} \begin{pmatrix} s_{\xi\xi} \\ s_{\xi\xi} \end{pmatrix} \quad ,$$

$$\begin{pmatrix} P_{12}^1 \\ P_{12}^2 \end{pmatrix} = -\mathbf{T}^{-1} \begin{pmatrix} s_{\xi\eta} \\ s_{\xi\eta} \end{pmatrix} \quad \text{and}$$
$$\begin{pmatrix} P_{22}^1 \\ P_{22}^2 \end{pmatrix} = -\mathbf{T}^{-1} \begin{pmatrix} s_{\eta\eta} \\ s_{\eta\eta} \end{pmatrix} \quad , \tag{2.66}$$

where the matrix $\mathbf{T}$ is defined as

$$\mathbf{T} = \begin{pmatrix} s_\xi & s_\eta \\ t_\xi & t_\eta \end{pmatrix} \quad . \tag{2.67}$$

While the control functions are explicitly specified in Poisson based grid generation equations, they are calculated only based on the parametric space $\mathcal{P}$ in this procedure. In order to compute the parametric space, it is necessary to first define the values of s and t at all four boundaries. They must satisfy the following restrictions:

- $s \equiv 0$ at the edges E_1 and $s \equiv 1$ at the edges E_2;
- s is the normalized arclength along edges E_3 and E_4;
- $t \equiv 0$ at the edges E_3 and $t \equiv 1$ at the edges E_4;
- t is the normalized arclength along edges E_1 and E_2.

which allows one to solve the system of linear algebraic equations

$$s_{ij} = s_{i0}\,(1 - t_{ij}) + s_{iN_y} t_{ij} \quad \text{and}$$
$$t_{ij} = t_{0j}\,(1 - s_{ij}) + t_{N_x j} s_{ij} \quad , \tag{2.68}$$

for the interior points, since each pair (i, j) represents an interior grid point. This calculation procedure is summarized in algorithm 1. It is important to note that the six control functions are computed once and are not updated again during the iterative process.

Algorithm 1 : Grid generation.

1: Compute an initial grid in the interior of domain $\mathcal{D}$ by a simple algebraic grid generation method using transfinite interpolation.

2: Compute the grid control map (s, t) at the boundaries based on arclength.

3: Compute the grid control map inner points using the linear algebraic equations defined in Eq. (2.68).

4: Compute the six control functions in Eq. (2.66).

5: Solve Eq. (2.64) with an iterative method as well as Direchlet boundary conditions. The initial grid is the initial guess for the iterative process.

The resulting grids obtained from algorithm 1 are usually not orthogonal, specially at the boundaries. However, grid orthogonality is often desired at

some boundaries, since doing so simplifies the implementation of complex boundary conditions. In order to achieve this, the algebraic transformation or control map is modified to redefine the grid as orthogonal at the boundaries. This can be done by first imposing Dirichlet-Neumann boundary conditions for the harmonic map, which is achieved by solving equation

$$a_{22}\mathbf{s}_{\xi\xi} - 2a_{12}\mathbf{s}_{\xi\eta} + a_{11}\mathbf{s}_{\eta\eta} + \Delta\xi\mathbf{s}_{\xi} + \Delta\eta\mathbf{s}_{\eta} = 0 \quad , \tag{2.69}$$

where $\Delta\xi$ and $\Delta\eta$ are respectively obtained from

$$\Delta\xi = \frac{1}{J}\left[(a_{22})_{\xi} - (a_{12})_{\eta}\right] \quad \text{and} \quad \Delta\eta = \frac{1}{J}\left[-(a_{12})_{\xi} + (a_{11})_{\eta}\right] \quad , \tag{2.70}$$

and $J^2 = a_{11}a_{22} - a_{12}^2$. Furthermore, boundary conditions for Eq. (2.64) are

- $s \equiv 0$ at the edges E_1 and $s \equiv 1$ at the edges E_2;
- $\frac{\partial s}{\partial \mathbf{n}} = 0$ along edges E_3 and E_4;
- $t \equiv 0$ at the edges E_3 and $t \equiv 1$ at the edges E_4;
- $\frac{\partial t}{\partial \mathbf{n}} = 0$ along edges E_1 and E_2;

where $\mathbf{n}$ is the outward normal direction of the physical boundaries curves. The Neumann boundary condition at the edges E_3 and E_4 for the parameter s and the edges E_1 and E_2 for t imply that a constant parameter line is a curve in the domain $\mathcal{D}$ which is orthogonal at its respective edges. For the presented proposal, the solution at the boundary of the parametric space is the only important information. Now, the algebraic transformation is redefined into the domain as

$$\begin{aligned} s &= s_{E_3}(\xi)H_0(t) + s_{E_4}(\xi)H_1(t) \quad \text{and} \\ t &= t_{E_1}(\eta)H_0(s) + t_{E_2}(\eta)H_1(s) \end{aligned} \tag{2.71}$$

where s_{E_3}, s_{E_4}, t_{E_1} and t_{E_2} are the new distribution for these parameters at their respective boundaries. Furthermore, H_0 and H_1, defined as

$$H_0(u) = (1+2u)(1-u)^2 \quad \text{and} \quad H_1(u) = (3-2u)u^2 \quad , \tag{2.72}$$

where $0 \leqslant u \leqslant 1$, are cubic Hermite interpolations. It is interesting to note that $H_0(0) = 1$, $H_0'(0) = 0$, $H_0(1) = 0$, $H_0'(1) = 0$, and $H_1(0) = 0$, $H_1'(0) = 0$, $H_1(1) = 1$ and $H_1'(1) = 0$. This means that a constant coordinate line η is mapped into the parameter space as a cubic curve which is orthogonal at both edges E_1 and E_2. A similar conclusion can be made about the a constant coordinate line ξ. This calculation procedure for a grid that is orthogonal at all four boundaries is summarized in algorithm 2. On the other hand, grid orthogonality is often desired at only two or three boundaries. When solving Eq. (2.69) in such cases, it is necessary to replace the Neumann boundary condition by the Dirichlet one where orthogonality is not desired.

Algorithm 2 : Grid orthogonality at all boundaries.

1: Compute an initial boundary conforming grid, using Algorithm 1.

2: Compute grid control map (s, t) at the boundaries based on Eq. (2.69), supplied with Dirichlet-Neumann boundary conditions.

3: Compute inner points of the grid control map (s, t) using cubic Hermite interpolation functions.

4: Compute the six control functions.

5: Solve Eq. (2.64) using an iterative method with the Direchlet boundary conditions. The initial grid is the initial guess for the iteration process.

Furthermore, the cubic Hermite interpolation must be changed rewritten as a quadratic one. Algorithm 2 is the one used to generate grid for 3D4S, with orthogonality imposed at solid walls and at any other boundary where boundary condition quality is important.

Once the grid has been generated, it is necessary to evaluate its properties. Many metrics can be used to do so. In the present case, grid orthogonality is the most important one. In two-dimensional grids, this metric can be calculated by the inner product between the two covariant base vectors for each grid point, as shown in Fig. 2.3. The closer this metric is to zero, the more orthogonal the grid is. However, quantifying orthogonality using radians or degree is preferable. The relative deviation from an orthogonal angle $|(\frac{\pi}{2} - \theta)/\frac{\pi}{2}|$ is used to quantify grid orthogonality, where θ is the angle at the intersection between two grid lines, also shown in Fig. 2.3. This inner product between two covariant vectors, defined in Eq. (2.65), yields

$$\langle \mathbf{x}_\xi, \mathbf{x}_\eta \rangle = \|\mathbf{x}_\xi\| . \|\mathbf{x}_\eta\| \cos[\theta] \quad , \tag{2.73}$$

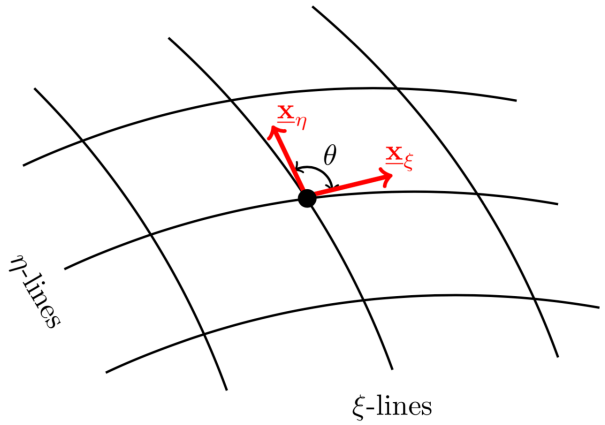

Figure 2.3: A sketch of the intersection between two-dimensional grid lines.

which means θ can be obtained from

$$\theta = \cos^{-1}\left[\frac{\langle \mathbf{x}_\xi, \mathbf{x}_\eta \rangle}{\|\mathbf{x}_\xi\|.\|\mathbf{x}_\eta\|}\right] = \cos^{-1}\left[\frac{(x_\xi x_\eta + y_\xi y_\eta)}{\sqrt{\left(x_\eta^2 + y_\eta^2\right)\left(x_\xi^2 + y_\xi^2\right)}}\right] \quad . \tag{2.74}$$

Finally, all partial derivatives used to compute these grids are calculated using second-order central finite difference schemes for domain points and second-order backward/forward schemes for the boundary points. Such a discretization of the partial derivatives in the Eqs. (2.64) and (2.69) leads to a non-linear system that is solved using a Gauss-Seidel iteration method coupled with the Successive Over-Relaxation method. Furthermore, it is important to point out that the number of desired orthogonal boundaries has a strong effect on the iteration method convergence rate. In other words, requiring more orthogonal boundaries leads to lower convergence rates.

2.2.3 Temporal Discretization

Euler Scheme

Having described in some more detail all the spatial discretization schemes implemented in 3D4S, the same can be done to their time marching counterparts. As explained in the prologue, this particular section focuses on explicit marching schemes, since this part of the report only considers steady-states that are physically stable in a linear and time asymptotic sense. The explicit Euler scheme, which has already been discussed in the prologue as well, is the fundamental explicit marching scheme implemented in 3D4S. All other explicit schemes are extensions of it. However, it is only first-order accurate in time. Hence, multi-step and/or -stage schemes are required for higher-order accuracy. Multi-step schemes have not yet been implemented, only their multi-stage counterparts. They are discussed next. Finally, it should be noted again that implicit multi-step and -stage schemes are discussed in the second part of this report about steady-states that are physically unstable in a linear and time asymptotic sense with a nonzero complex frequency.

Traditional Runge-Kutta Schemes

Before moving on to the explicit multi-stage marching schemes implemented in 3D4S, a brief introduction to Runge-Kutta schemes is required. They advance the non-autonomous version of Eq. (1) forward in time using

$$\mathbf{k}^{(i)} = \mathbf{u}^n + \Delta t \sum_{j=1}^{s} a_{ij}\, \mathbf{f}(t_n + c_j\, \Delta t\,,\, \mathbf{k}^{(j)}) \quad , \tag{2.75}$$

to calculate the i^{th} intermediate stage variables k_i for $i = 1, 2, \ldots, s$, where s is the number of intermediate stages, and then using

$$\mathbf{u}^{n+1} = \mathbf{u}^n + \Delta t \sum_{i=1}^{s} b_i\, \mathbf{f}(t_n + c_i\, \Delta t\,,\, \mathbf{k}^{(i)}) \quad , \tag{2.76}$$

Table 2.2: Butcher tableau format for RK characteristic coefficients.

$$\begin{array}{c|c} \boldsymbol{c} & \boldsymbol{A} \\ \hline & \boldsymbol{b}^T \end{array} \quad \longleftrightarrow \quad \begin{array}{c|cccc} c_1 & a_{11} & a_{12} & \cdots & a_{1s} \\ c_2 & a_{21} & a_{22} & \cdots & a_{2s} \\ \vdots & \vdots & \vdots & \ddots & \vdots \\ c_s & a_{s1} & a_{s2} & \ldots & a_{ss} \\ \hline & b_1 & b_2 & \cdots & b_s \end{array}$$

to obtain the solution $\mathbf{u}$ at the next time step $n+1$, where a_{ij}, b_i and c_i are characteristic coefficients to be determined. They control the accuracy order and numerical stability of the resulting scheme. Furthermore, they are often provided in the form of what is known today as the Butcher tableau shown in Tab. 2.2. Furthermore, it is important to impose relations

$$\sum_{i=1}^{s} b_i = 1 \quad \text{and} \quad c_i = \sum_{j=1}^{s} a_{ij} \quad , \tag{2.77}$$

for $i = 1, 2, \ldots, s$, in order to satisfy consistency requirements. All additional constraints are imposed for these coefficients once the accuracy order and number of stages is specified. Since the focus here is on explicit RK (ERK) schemes, an additional constraint is $a_{ij} = 0$ for $j \geq i$.

The linear and time asymptotic numerical stability analysis of RK schemes can be pursued following the same steps described in the prologue, where an analysis of the homogeneous equation $d\hat{u}_j/dt = \lambda\, \hat{u}_j$ is performed. Applying Eqs. (2.75) and (2.76) to this equation yields

$$\boldsymbol{k} = \hat{u}_j^n\, \boldsymbol{I} + \lambda_j \Delta t\, \boldsymbol{A} \cdot \boldsymbol{k} \quad \text{and} \quad \hat{u}_j^{n+1} = \hat{u}_j^n + \lambda_j \Delta t\, \boldsymbol{b}^T \cdot \boldsymbol{k} \quad , \tag{2.78}$$

respectively, which can be combined to yield

$$G_j = \frac{\hat{u}_j^{n+1}}{\hat{u}_j^n} = 1 + \lambda_j \Delta t \left\{ \boldsymbol{b}^T \cdot (\boldsymbol{I} - \lambda_j \Delta t\, \boldsymbol{A})^{-1} \cdot \boldsymbol{I} \right\} \quad , \tag{2.79}$$

where the stability characteristics of each scheme is still interpreted according to Eqs. (27) and (28) in terms of the gain absolute value α_j and the relative phase speed c_j, defined in Eqs. (26) and (29), respectively.

Strong-Stability-Preserving Runge-Kutta Schemes

When discontinuous solutions such as shock waves are present, however, a linear analysis is not sufficient to determine the range of time steps Δt that lead to numerical stability in high-order accurate marching schemes. This is due to the fact that nonlinear shock capturing schemes, such as TVD and WENO, are employed. These spatial discretization nonlinear properties are only preserved when coupled with monotone marching schemes, such

as the explicit and implicit Euler schemes. However, they are only first-order accurate in time. Hence, extensions to higher-orders for time-accurate simulations must guarantee numerical stability in terms of total variation, or at least non-oscillatory, properties.

Strong stability preserving (SSP) schemes achieve this goal in two steps. In the first one, a spatial discretization with the required nonlinear properties under a given norm, semi-norm or convex function $\|\cdot\|$ is applied to generate Eq. (1), which is then marched forward in time using the explicit Euler scheme under an appropriate time step Δt_{EE}. In other words,

$$\| \mathbf{u}^n + \Delta t\, \mathbf{f}(\mathbf{u}^n) \| \leq \| \mathbf{u}^n \| \quad \text{with} \quad 0 \leqslant \Delta t \leqslant \Delta t_{EE} \quad , \tag{2.80}$$

for all $\mathbf{u}^n$. In the second step, one tries to find a higher-order time marching scheme that maintains these nonlinear stability properties under the same norm, even if a different time step restriction is required. In other words, an SSP scheme with an explicit Euler time step adjustment coefficient $\mathcal{C}$ generates a solution $\mathbf{u}^{n+1}$ that guarantees

$$\| \mathbf{u}^{n+1} \| \leq \| \mathbf{u}^n \| \quad \text{with} \quad \Delta t \leqslant \mathcal{C} \Delta t_{EE} \quad . \tag{2.81}$$

These schemes are not usually written in the traditional Butcher form described in Eqs. (2.75) and (2.76). Since it is more convenient for an SSP analysis, they are quite often presented as

$$\begin{aligned} \mathbf{k}^{(0)} &= \mathbf{u}^n \quad , \\ \mathbf{k}^{(i)} &= \sum_{k=0}^{i-1} \left(\alpha_{i,k}\, \mathbf{k}^{(k)} + \beta_{i,k}\, \Delta t\, \mathbf{f}(\mathbf{k}^{(k)}) \right) \quad \text{for} \quad 1 \leq i \leq s \quad \text{and} \\ \mathbf{u}^{n+1} &= \mathbf{k}^{(s)} \quad , \end{aligned} \tag{2.82}$$

which is known as the Shu-Osher form. Furthermore, these schemes employ more stages than the explicit Euler scheme. Hence, $\mathcal{C}_{eff} = \mathcal{C}/s$ is provided instead to facilitate an efficiency comparison between them. Only SSP-ERK schemes are implemented in 3D4S. Their coefficients have been optimized to provide the largest possible value of $\mathcal{C}$. The second-order accurate version marches the solution forward in time with

$$\begin{aligned} \mathbf{k}^{(1)} &= \mathbf{u}^n + \Delta t\, \mathbf{f}(\mathbf{u}^n) \quad \text{and} \\ \mathbf{u}^{n+1} &= \frac{1}{2}\, \mathbf{u}^n + \frac{1}{2}\, \mathbf{k}^{(1)} + \frac{\Delta t}{2}\, \mathbf{f}(\mathbf{k}^{(1)}) \quad , \end{aligned} \tag{2.83}$$

which has $\mathcal{C}_{eff} = 1/2$, the third-order accurate version does so with

$$\begin{aligned} \mathbf{k}^{(1)} &= \mathbf{u}^n + \Delta t\, \mathbf{f}(\mathbf{u}^n) \quad , \\ \mathbf{k}^{(2)} &= \frac{3}{4}\, \mathbf{u}^n + \frac{1}{4}\, \mathbf{k}^{(1)} + \frac{\Delta t}{4}\, \mathbf{f}(\mathbf{k}^{(1)}) \quad \text{and} \end{aligned}$$

$$\mathbf{u}^{n+1} \;=\; \frac{1}{3}\,\mathbf{u}^{n} + \frac{2}{3}\,\mathbf{k}^{(2)} + \frac{2\,\Delta t}{3}\,\mathbf{f}(\mathbf{k}^{(2)}) \quad , \tag{2.84}$$

which has $\mathcal{C}_{eff} = 1/3$, and the fourth-order accurate version does so with

$$\begin{aligned}
\mathbf{k}^{(1)} &= u^{n} + 0.391752226571890\,\Delta t\,\mathbf{f}(\mathbf{u}^{n}) \quad , \\
\mathbf{k}^{(2)} &= 0.444370493651235\,\mathbf{u}^{n} + 0.555629506348765\,\mathbf{k}^{(1)} \\
&+ 0.368410593050371\,\Delta t\,\mathbf{f}(\mathbf{k}^{(1)}) \quad , \\
\mathbf{k}^{(3)} &= 0.620101851488403\,\mathbf{u}^{n} + 0.379898148511597\,\mathbf{k}^{(2)} \\
&+ 0.251891774271694\,\Delta t\,\mathbf{f}(\mathbf{k}^{(2)}) \quad , \\
\mathbf{k}^{(4)} &= 0.178079954393132\,\mathbf{u}^{n} + 0.821920045606868\,\mathbf{k}^{(3)} \\
&+ 0.544974750228521\,\Delta t\,\mathbf{f}(\mathbf{k}^{(3)}) \quad \text{and} \\
\mathbf{u}^{n+1} &= 0.517231671970585\,\mathbf{u}^{(2)} + 0.096059710526147\,\mathbf{k}^{(3)} \\
&+ 0.386708617503269\,\mathbf{k}^{(4)} + 0.063692468666290\,\Delta t\,\mathbf{f}(\mathbf{k}^{(3)}) \\
&+ 0.226007483236906\,\Delta t\,\mathbf{f}(u^{(4)}) \quad ,
\end{aligned} \tag{2.85}$$

which has $\mathcal{C}_{eff} = 0.302$. All references are provided in subsection 1.2.1.

Chapter 3

Results

3.1 Code Verification

3.1.1 One-Dimensional Models

Most numerical techniques discussed in subsection 1.2.1 were first coded and tested on a scalar model given by Eq. (2.1) before an assessment was made pertaining to their implementation in 3D4S. This model was the viscous and inviscid Burgers equation, defined by their respective fluxes in Eqs. (2.2) and (2.3). The spatial discretization employed for the inviscid fluxes uses the original fifth-order WENO scheme with the Lax-Friedrichs flux-vector splitting for scalar governing equations (Liu et al., 1994) but with the Steger-Warming flux-vector splitting for compressible governing equations (Steger and Warming, 1981). The viscous fluxes, on the other hand, are discretized with a fourth-order central scheme (Santiago and Alves, 2017). Additional tests have also been performed using the original second-order TVD scheme (Harten, 1983) using the Steger-Warming flux-vector splitting and a superbee flux limiter (Roe, 1985) for inviscid fluxes and a second-order central scheme for viscous fluxes (Santiago and Alves, 2017). However, they generate similar results and, hence, are not shown. Optimal second and third-order SSP-RK schemes, respectively from Eqs. (2.83) and (2.84), are employed to generate results. Finally, it should be noted that temporal and spatial numerical accuracy-orders for these schemes in all test cases match their theoretical counterparts. More details are provided by Santos and Alves (2021).

Both inviscid and viscous scenarios are subject to the same initial condition $u(x, t = 0) = \sin[2\,\pi\,x]$ as well as boundary conditions $u(x = 0, t) = u(x = 1, t) = 0$. For these test cases, a banded linear system is solved when implicit and IMEX schemes are applied. The matrix allocation is made in a vector diagonal basis, in order to extract the best efficiency measured in terms of maximum (L_∞) absolute error versus memory and computing (cpu) time. Absolute errors are estimated using the numerical solution generated when halving either the time step Δt, for the constant grid space analysis, or the time step Δt and grid space Δx, for the constant CFL analysis, as a proxy for the exact solution. For all implicit schemes, Newton sub-iterations are

performed for each intermediate stage to achieve accuracy order convergence.

When non-uniform grids are employed, the stretching is accomplished through a transformation (Holst, 1977) given by

$$\frac{x}{x_0} = \frac{\sinh[\,\beta\,(\xi - \xi_0)\,] + \sinh[\,\beta\,\xi_0\,]}{\sinh[\,\beta\,\xi_0\,]} \quad , \tag{3.1}$$

where ξ and x are the uniform computational and non-uniform physical grids, respectively, x_0 is the location in the physical domain where the maximum grid refinement is to occur,

$$\xi_0 = \frac{1}{2\,\beta}\,\ln\left[\,\frac{1 + (e^{\beta} - 1)\,x_0}{1 + (e^{-\beta} - 1)\,x_0}\,\right] \quad , \tag{3.2}$$

and β is a constant that controls the degree of refinement around x_0.

Inviscid Burgers Equation by Santos (2020)

The solution of Eq. (2.1) subject to Eq. (2.2) is shown in Fig. 3.1 for $t = 0.0$ to 0.5 using a uniform grid with $N_x = 251$ points and a time step of $\Delta t = 10^{-3}$. The third-order three-stages ERK time integration is employed to generate solutions with low (TVD) and high (WENO) order schemes. Both are essentially indistinguishable from one another in this figure. Although not show here, it converges to the analytical solution (Benton and Platzman, 1972) as N_x is increased and Δt is decreased. Similar results are obtained for the second and fourth-order ERK schemes as well as nonuniform grids.

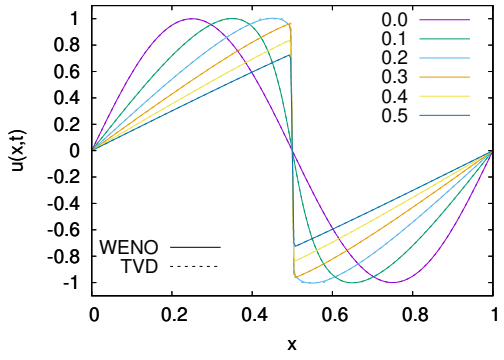

Figure 3.1: Velocity profiles at different times with $N_x = 51$ and $\Delta t = 10^{-3}$.

Viscous Burgers Equation by Santos (2020)

Now the viscous version of the previous test case is analyzed, where Eq. (2.1) is subject to Eq. (2.3) instead. Solutions for this model were generated with the same marching scheme used to generate the solutions shown in Fig. 3.1, as well as low (TVD) and high (WENO) order spatial schemes. Figure 3.2 shows these solutions for $t = 0.0$ to 0.5 using a uniform grid with $N_x = 251$ points and a time step of $\Delta t = 10^{-4}$ for $\mu = 10^{-2}$ (left) and 10^{-3} (right). The latter is similar to the inviscid solution, although discontinuities are

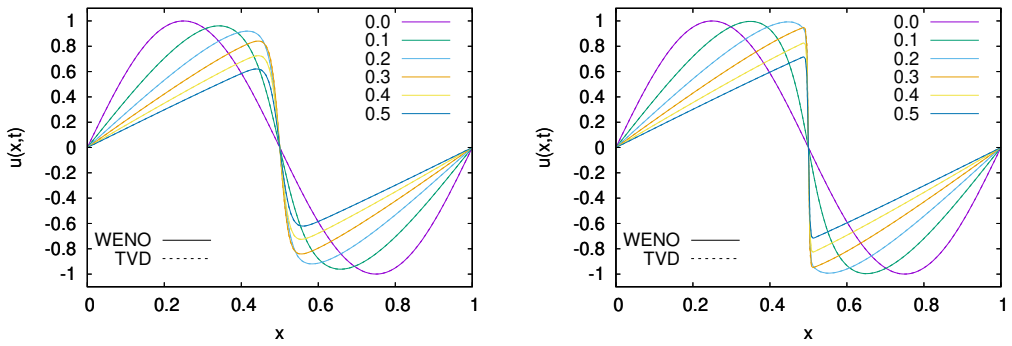

Figure 3.2: Same as Fig. 3.1, but for $\mu = 10^{-2}$ (left) and 10^{-3} (right).

not as strong. Low and high-order solutions are virtually indistinguishable from one another in this figure. Although not show here, both converge to the analytical solution (Alves et al., 2001; Pinheiro et al., 2020) as N_x is increased and Δt is decreased. Similar results are obtained for the second and fourth-order ERK schemes as well as nonuniform grids.

Shock Tube Problem by Santos (2020)

Moving on to a coupled system of equations, the now classical shock tube problem originally devised by Sod (1978) is analyzed. Equation (2.5) is solved with $\mathbf{F} = 0$ and $N = 1$ for initial conditions $\rho = 1$, $u = 0$ and $P = 10^5$ at $x < 0$ and $\rho = 0.125$, $u = 0$ and $P = 10^4$ at $x > 0$ within $-10 < x < +10$ in SI units. Linear extrapolation is used at the boundaries, although all simulations are interrupted before any wave structure reaches them. Figure 3.3 presents the density distribution at $t = 0.01$, marched in time with Eq. (2.83) using the TVD scheme and Eq. (2.84) using the WENO scheme discussed previously, with $N_x = 501$ and $\Delta t = 2 \times 10^{-5}$. The exact solution is also presented, indicating that the latter scheme can generate a solution with less numerical diffusion than the former one, which this figure also shows in greater detail for the contact line discontinuity.

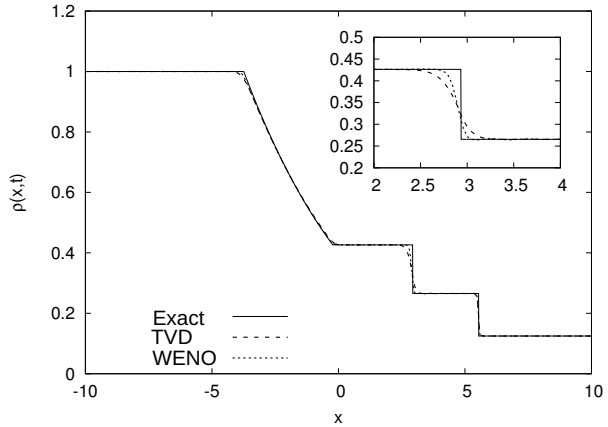

Figure 3.3: Density field with $N_x = 501$ and $\Delta t = 2 \times 10^{-5}$ at $t = 0.01$.

Advection with Strong Heat Release by Santos (2020)

Viscous effects and strong heat release are now included in Eq. (2.5) for the next test case. This is achieved by letting $\mathbf{F}$ be defined by Eq. (2.6) and adding the source term $\mathbf{S} = \{\, 0\,,\, 0\,,\, \beta\, e^{-\alpha\,(x-x_0)^2}\,\}^T$ to the r.h.s. of Eq. (2.5), where α, β and x_0 control the heat source magnitude and distribution within the flow. It considers the behavior of an ideal gas with temperature $T_0 = 300$ and pressure $P_0 = 101325$ advected with a constant Mach number $M = 0.29$ in a domain from $0 \leqslant x \leqslant 1$ when subjected to a localized heat source with $\alpha = -10^5$, $\beta = 10^9$ and $x_0 = 0.5$, all in S.I. units (Merkle and Choi, 1987). Linear extrapolation is used at the boundaries, but no wave structures are allowed to reach them. Figure 3.4 presents the temperature distribution at $t = 10^{-3}$, marched in time with Eq. (2.83) using both TVD and WENO schemes discussed previously with $N_x = 1001$ and $\Delta t = 10^{-7}$. The localized heat release induces a strong gas expansion, generating shock waves in both directions, which are captured with less numerical diffusion by the latter scheme once again.

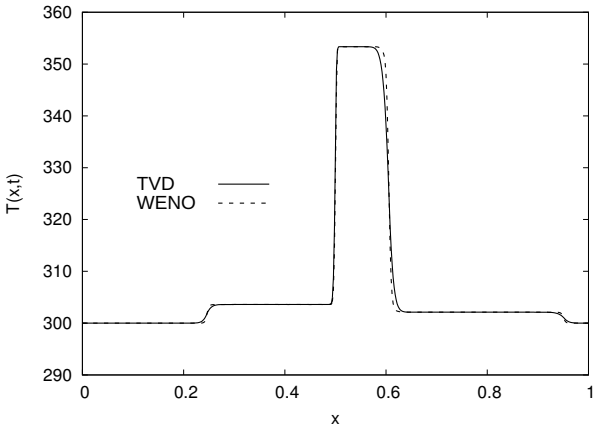

Figure 3.4: Temperature field with $N_x = 1001$ and $\Delta t = 10^{-7}$ at $t = 10^{-3}$.

Thermoacoustic Wave Propagation by Santos (2020)

The final one-dimensional analysis considers the propagation and reflection of thermo-acoustic waves in a closed cavity containing a quiescent ideal gas. The fluid is initially at temperature $T_0 = 300$ and pressure $P_0 = 101325$, has a sound speed of $c_0 \simeq 352.904$ and is confined in a cavity of length $L = 10^{-3}$. Thermoacoustic waves are generated by suddenly increasing the left wall cavity temperature by $\Delta T = 100$. All quantities are provided in S.I. units. At both impermeable walls, the normal pressure derivative is assumed to be zero and density is obtained from a characteristic relation (Poinsot and Lele, 1992). Simulations are based on Eqs. (2.5) and (2.6). Figure 3.5 shows the thermoacoustic wave created by the sudden wall heating at $t/\tau_c = 0.25$, 1, 1.5 and 2, where $\tau_c = L/c_0$. These curves were obtained with WENO and Eq. (2.83). They are in good agreement with experimental data from

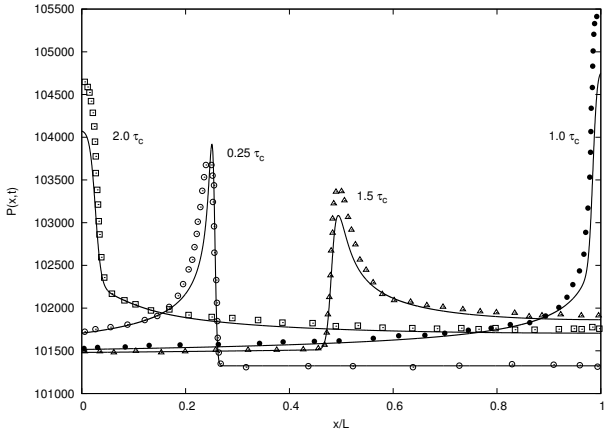

Figure 3.5: Pressure field at $t/\tau_c = 0.25$, 1, 1.5 and 2, where $\tau_c = L/c$, obtained with (lines) $N_x = 1001$ and $\Delta t = 4 \times 10^{-9}$ and (symbols) from the literature (Aktas, 2004).

the literature (Aktas, 2004), where discrepancies observed can be attributed to the difficulty in modeling wall impedance through appropriate boundary conditions (Barros and Alves, 2019). This is an interesting test case since viscous and inviscid fluxes have the same order of magnitude. The former is due to the very thin thermal boundary-layers at these short acoustic time scales, whereas the latter is due to the acoustic convection of energy out of the thermal boundarylayer and into the bulk fluid.

3.1.2 Two-Dimensional Models

Double Mach Reflection by Santos (2020)

The different WENO schemes implemented for unsteady simulations are now verified for the double Mach reflection problem proposed by Woodward and Colella (1984). It is illustrated in Fig. 3.6, which shows what happens after a planar shock wave impinging at an angle on a flat plate at $y = 0$ that is reflective beyond $x \geq 1/6$ but slip otherwise. Pre and post-shock velocities, pressures and densities are also shown in this figure with SI units, as well as dimensionless parameters γ and Ma, where i is the incident shock wave, r is the primary reflected shock wave, m is the primary Mach stem, s is the primary slip line that emanates from the first triple point T, r' is the secondary reflected shock wave, m' is the secondary Mach stem, s' is the secondary slip line that emanates from the first triple point T'. Thick arrows indicate the incident shock wave propagation direction whereas thin arrows indicate the propagation direction of vortical structures produced by the Kelvin-Helmholtz instability associated with the mixing layer across the slip line s, which are eventually pushed downstream along the impermeable wall due the incoming flow. Besides these physical structures, two numerical structures can appear as well. One is the numerical wave b produced by the interaction between the incident shock wave and the inadequately modeled

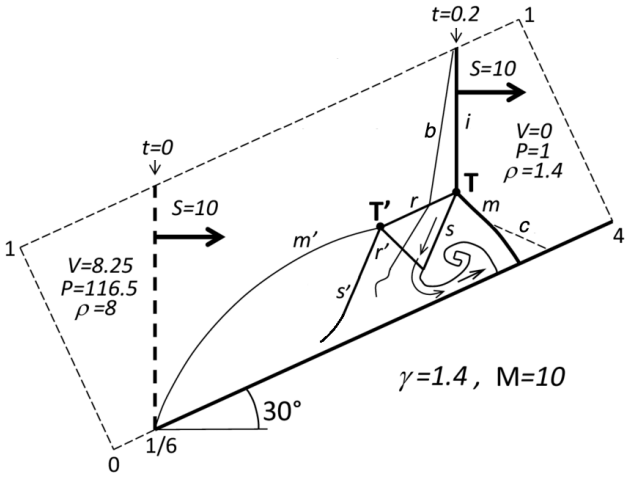

Figure 3.6: Sketch of the initial and final conditions simulated for the double-Mach reflection problem adapted from Zhao (2016).

free stream boundary conditions whereas the other is the carbuncle c, which emanates from the primary Mach stem by inadequate numerical schemes.

All simulations were performed by Santos (2020), who prescribed post-shock conditions at the inlet and free stream but used extrapolation at the outlet. A uniform grid is employed in both directions, with 1601 points in the streamwise direction and 401 points in the wall-normal direction. The third-order accurate three-stage ERK scheme shown in Eq. (2.84) was the one employed in these simulations using $\Delta t = 2 \times 10^{-6}$ to march Eq. (2.5) with $\mathbf{F} = 0$ and $N = 2$ forward in time. The influence of the different WENO schemes implement in 3D4S is discussed below.

Figure 3.7 shows results for density, pressure and velocity components obtained from a simulation using WENO5-JS with the Roe flux-difference splitting based on conservative variables. Their isocontours oscillate quite

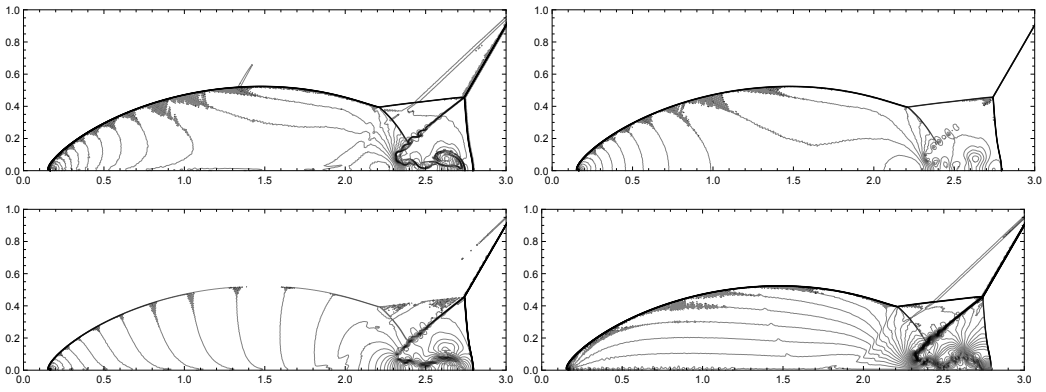

Figure 3.7: Density (top left), pressure (top right), streamwise (bottom left) and wall-normal (bottom right) velocity components at $t = 0.2$ obtained using WENO5-JS with the Roe flux-difference splitting. 44 isocontours were selected between minimum and maximum values.

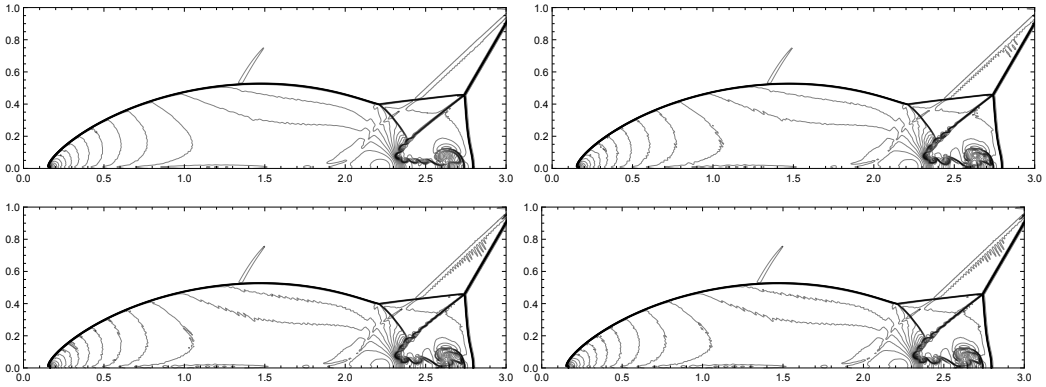

Figure 3.8: 44 density isocontours between 1.41 and 22 at $t = 0.2$ for WENO5-JS (top left), WENO5-M (top right), WENO5-Z (bottom left) and WENO5-Z+ (bottom right) with characteristic-wise flux-vector splitting.

strongly near the secondary Mach stem m'. Hence, the next results were obtained from simulations using different WENO schemes coupled with the characteristic-wise Lax-Friedrichs flux-vector splitting. These density isocontours are shown in Fig. 3.8 for the WENO5-JS, WENO5-M, WENO5-Z and WENO5-Z+ schemes. Despite significant improvements compared to the previous figure, the former scheme is clearly more dissipative whereas the later three ones generate equivalent results between them. In all cases, there is no carbuncle c due to the use of flux-vector splitting. However, there is a numerical wave b propagating downwards from the upper boundary, which is expected since i) this boundary is not orthogonal to the incoming shock i and/or ii) a better free stream boundary condition is not imposed. Similar trends are observed for the pressure as well as velocity components and, hence, they are not shown here.

Flow Over a Blunt Body by Nunes (2021)

WENO schemes developed for unsteady simulations are known to introduce post-shock oscillations with a magnitude proportional to the local truncation error that prevent residue convergence in time towards machine zero (Zhu and Shu, 2017). This issue was overcome with the development of WENO5-ZQ for steady simulations (Zhu and Qiu, 2016; Zhu and Shu, 2018, 2019; Zhang et al., 2019). Its ability to do so is here verified by simulating the hypersonic flow over a blunt body. This problem is also used here to test the grid generation tools developed for 3D4S. A sketch of this geometry is shown in Fig. 3.9, which specifies four boundaries, namely the i) body, ii) symmetry plane, iii) far-field and iv) outlet, based on the work by Cerminara and Sandham (2020). The body is a half-cone with a circular nose that extends up to the connection angle θ, where R is the nose radius, L is the total body length, α is the half-cone angle and $\theta = \pi/2 - \alpha$ in order to guarantee a class C^1 smooth surface. Its geometry is fixed in the present dimensionless simulations by setting $\alpha = 7^o$ and $L/R = 5$. Furthermore, the symmetry plane is a one radius long straight line perpendicular to the body, the far-

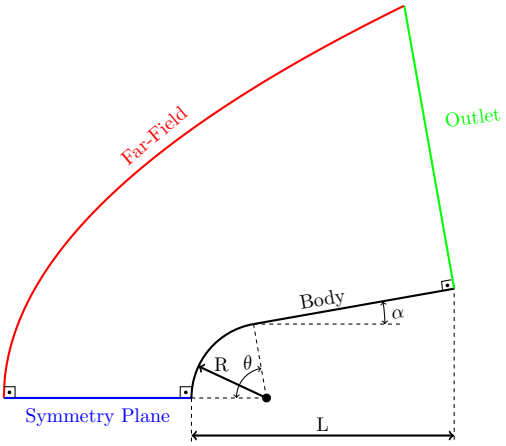

Figure 3.9: Sketch of a two-dimensional blunt body geometry.

field connects to the symmetry plane normal to it, but follows a polynomial function designed to be parallel to the steady shock, approximately, and the outlet is a straight line perpendicularly connected to the body. When imposing orthogonality at the body and symmetry plane with the elliptic grid generation tool from algorithm 2, the maximum relative deviation from orthogonality for $(N_x, N_y) = (151, 101)$, $(301, 201)$, $(601, 401)$, $(901, 601)$, $(1201, 801)$ and $(1501, 1001)$ is 0.108047, 0.0572067, 0.0304814, 0.0211498, 0.0163229, and 0.0133365 percent at these boundaries, respectively. The grid (left) and its relative deviation from orthogonality (right) obtained when using algorithm 2 with $(N_x, N_y) = (76, 51)$ while imposing orthogonality at the body and symmetry plane are shown in Fig. 3.10 over the entire domain. Having set the grid, the hypersonic and symmetric flow can be simulated.

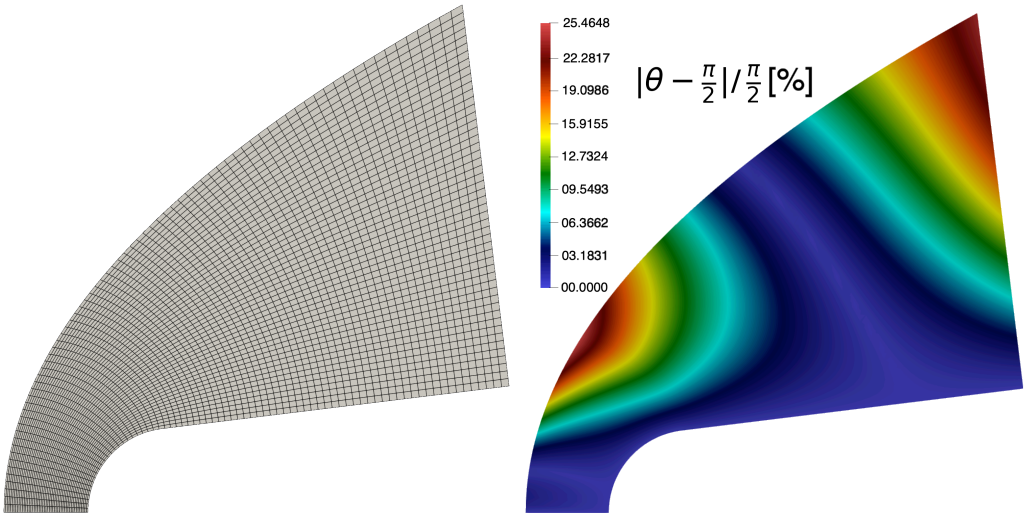

Figure 3.10: Grid (left) and its relative deviation from orthogonality (right) obtained from from algorithm 2 while imposing orthogonality at the body and symmetry plane with $(N_x, N_y) = (76, 51)$ from Nunes (2021).

Flow conditions are set by imposing the free stream Mach number $Ma_\infty = 6$, the Reynolds number based on the nose radius $Re_R = 1000$, the free stream Prandtl number $Pr_\infty = 0.72$, the ratio between constant specific heats $\gamma = 1.4$, the free stream temperature $T_\infty = 200\,K$, the dynamic viscosity defined by Sutherland's law in Eq. (2.25) and the thermal conductivity defined by the constant Prandtl assumption in Eq. (2.26). Grid converged simulations were achieved with $(N_x, N_y) = (1201, 801)$ using a time step of $\Delta t = 5 \times 10^{-6}$. Time integration was performed using the third-order accurate and three-stages ERK scheme in Eq. (2.84) and the viscous luxes were discretized with the fourth-order accurate conservative central-differences scheme.

Two WENO schemes were employed with the characteristic-wise Lax-Friedrichs flux-vector splitting. One is WENO5-JS, originally developed for unsteady simulations, and the other is WENO5-ZQ, recently developed to simulate steady-states. Furthermore, adiabatic, no-slip and impermeable wall boundary conditions were imposed, where the wall-normal pressure derivative was considered zero. Normal derivatives were considered zero on the symmetry plane for all variables, but the normal velocity component, which was assumed zero. Density, temperature and both velocity components were prescribed their free stream values at the far-field boundary. Finally, extrapolation was employed for all variables at the outlet.

Figure 3.11 shows the convergence in time of the L_∞ norm of the residue for the mass, momentum and energy conservation equations using WENO5-JS (dashed) and WENO5-ZQ (solid) schemes. As already expected, post-shock oscillations prevent the maximum residue calculated with the former from converging in time to machine zero. Maximum residues calculated with the latter, on the other hand, decrease 10 orders of magnitude in time, approximately. They are, in fact, located at the shock. Elsewhere, these residues are 2 to 5 orders of magnitude smaller. The steady results obtained using WENO5-ZQ are shown in Fig. 3.12, which include density, pressure, temperature, both velocity components and Mach number isocontours and

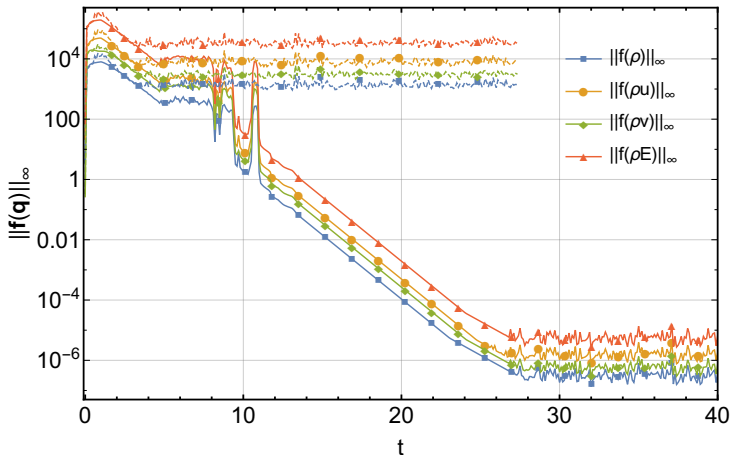

Figure 3.11: Residue time convergence to steady-state for the blunt-body simulation using WENO5-JS (dashed) and WENO5-ZQ (solid) schemes.

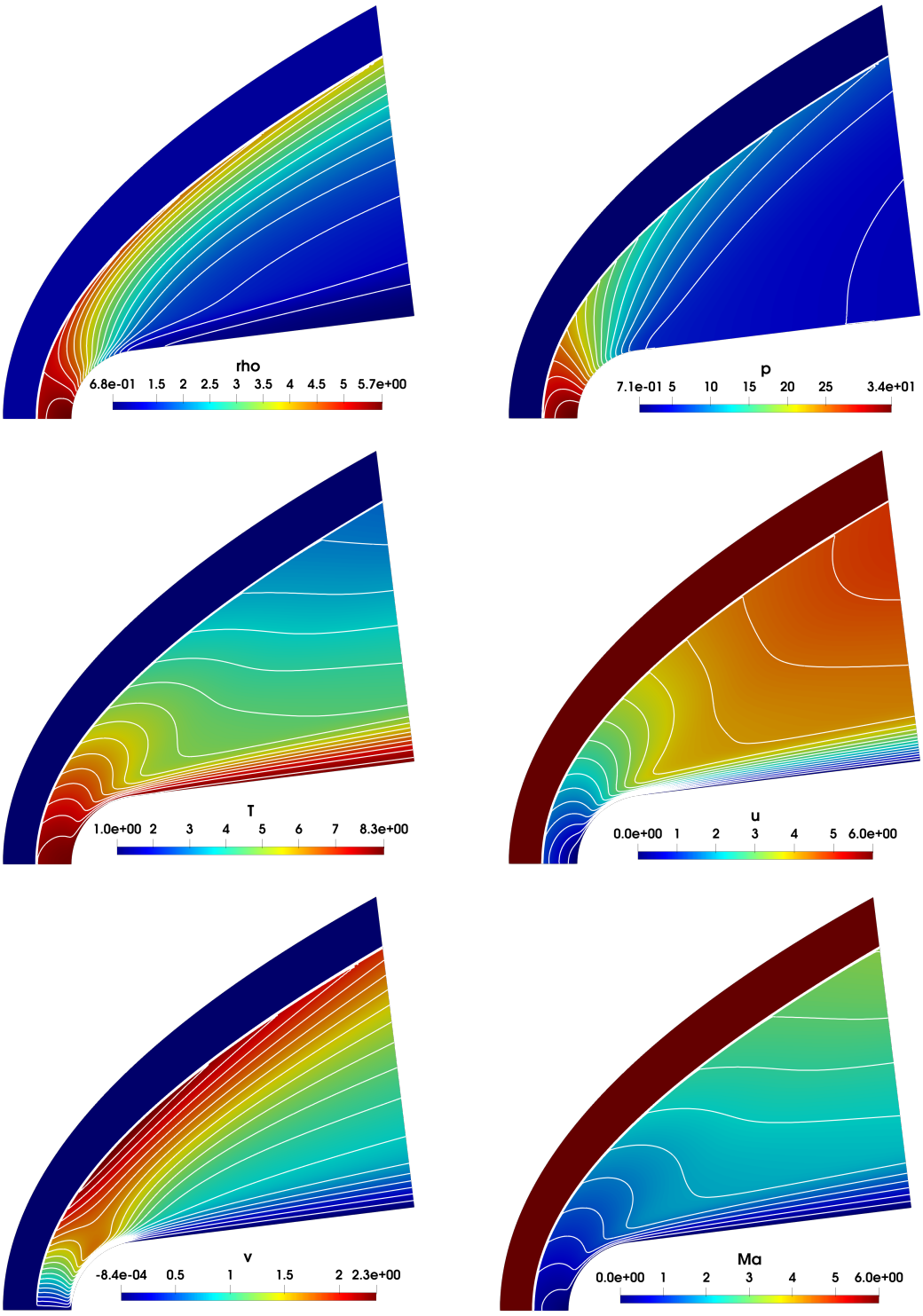

Figure 3.12: Two-dimensional blunt-body steady-state isocontous and isolines for density (top left), pressure (top right), temperature (middle left), streamwise (middle right) and wall-normal (bottom left) velocity components as well as Mach number (bottom right).

isolines. They are in qualitative agreement with literature results for similar parametric conditions and geometry (Cerminara and Sandham, 2020). A key comparative advantage is worth noting. There was no need to either align the grid and the shock or cluster grid points around the shock whenever using WENO. This is in contrast with said literature, which simulated this flow using a second-order TVD-type scheme instead. They spent a large amount of effort trying to improve the alignment between grid and steady shock as well as clustering grid points around this shock due to the strong gradients in the stagnation region. This shows once again the improved ability of WENO schemes with characteristic-wise flux-vector splitting to handle carbuncle.

3.1.3 Three-Dimensional Models

Flow Over a Curved Plate by Santos (2020)

3D4S was programmed in such a way that its extension from two to three-dimensional simulations was straightforward. Hence, the major goal at this point was not necessarily to further verify both temporal integration and spatial discretization schemes already implemented in a three-dimensional setting, but to choose a physically meaningful test case instead. The supersonic flow over a curved plate represents such a test for two reasons. First, its domain is simple enough that a high quality grid can be generated with the tools developed for this report. In other words, there will be no grid induced numerical excitation of physical instabilities. Numerical excitation sources will not come from the spatial discretization either, since it has already been shown that WENO5-ZQ can prevent them from appearing. As discussed in the prologue, being able to eliminate steady numerical excitation sources is key when trying to simulate a flow that is convectively unstable to stationary disturbances. The reason is simple. Being able to do so makes it possible to achieve accurate and disturbance free steady-states. Hence, the present test case will play a relevant role in the third part of this report, where new tools are developed to deal with the opposite scenario, i.e. when it is not possible to eliminate these steady numerical excitation sources.

A sketch of this geometry is shown in Fig. 3.13, which specifies four boundaries, namely the *i*) body, *ii*) inlet, *iii*) far-field and *iv*) outlet. The body is composed of a flat plate located at $0 \leq x \leq L_s + L_f$ smoothly connected to a curved plate whose projection on the x-axis is located at $L_s + L_f \leq x \leq L_s + L_f + L_c$, where $L_s/L_f = 0.2$ and $L_c/L_f = 5$. Smoothly here means that the function describing the body location and its derivative are continuous at the connection point. This function on the curved portion is given by the arc-length of a cylinder centered at $(x, y) = (L_s + L_f, R_c)$ with angle $\alpha = \sin^{-1}[L_f/R_c]$ and radius $R_c/L_f = 20$. The inlet and outlet are $L_i(= L_f)$ and $L_o(= 2\,L_f)$ long straight lines perpendicular to the body at their connection points. The far field connects inlet and outlet edges with the arc-length whose center is at $x = 0$ so that it is perpendicular to the former. The elliptic grid is generated with algorithm 2 imposing orthogonality on the

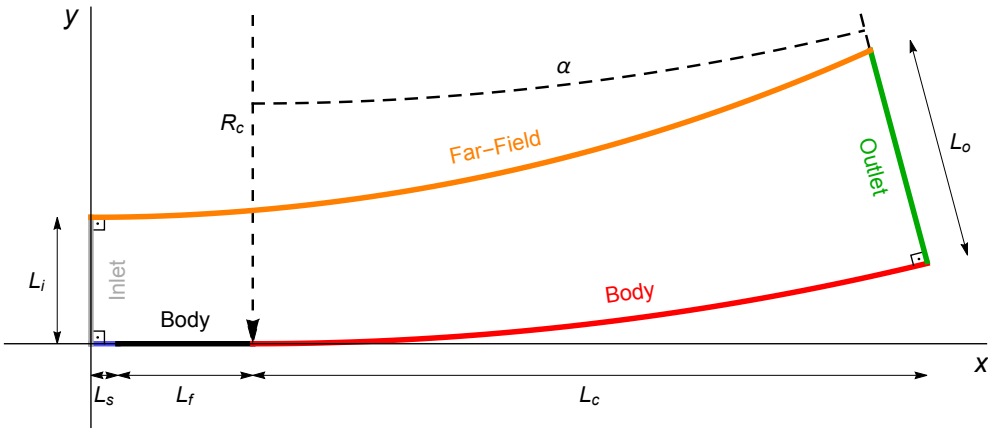

Figure 3.13: Sketch of the two-dimensional version of a curved plate.

inlet and body. Once this two-dimensional grid was generated on the (x, y) plane with near body grid refinement, it was uniformly protruded by $w/L_f = 0.5$ into the z direction to create the three-dimensional grid. Figure 3.14 illustrates this three-dimensional grid as well as its relative deviation from orthogonality on the (x, y) plane for $(N_x, N_y, N_z) = (101, 51, 41)$.

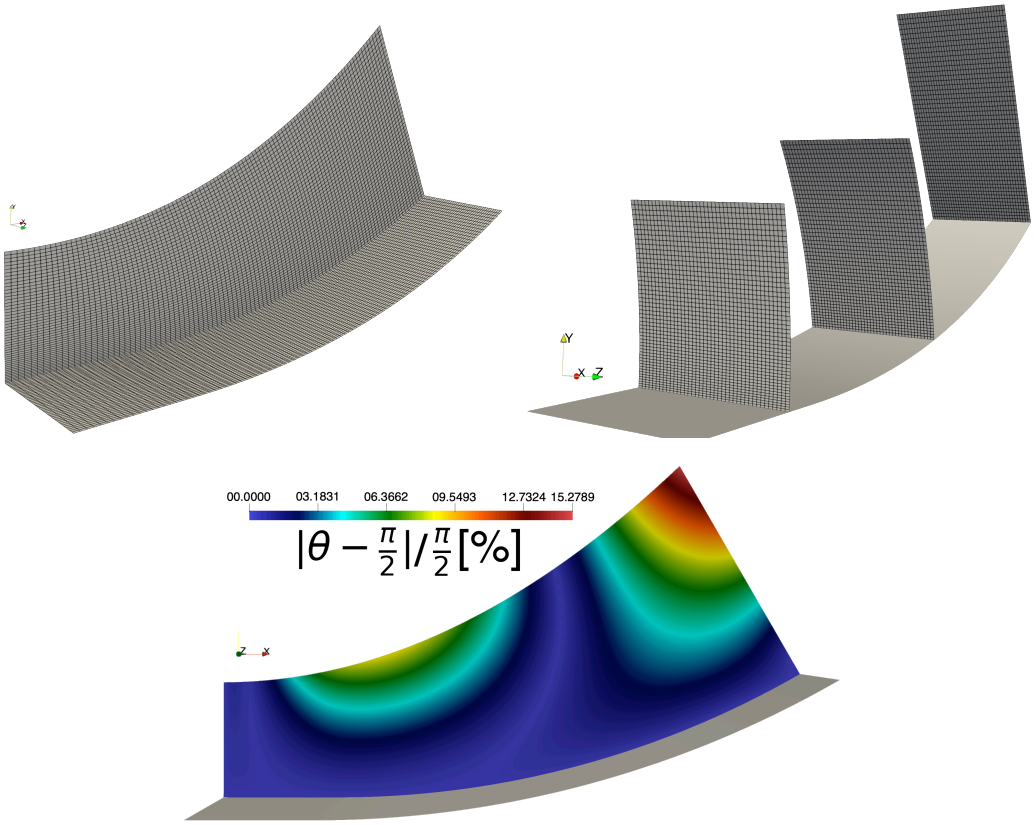

Figure 3.14: Three-dimensional grid (top) and its two-dimensional relative deviation from orthogonality (bottom) from algorithm 2 with orthogonality at the inlet and body with $(N_x, N_y, N_z) = (101, 51, 41)$ by Nunes (2021).

Having set the simulation geometry, the supersonic flow over it can be simulated. Flow conditions follow the guidelines provided by Sescu et al. (2019). They are set by imposing the free stream Mach number $Ma_\infty = 4$, the Reynolds number $Re_{L_f} = 5 \times 10^4$ based on the flat plate length L_f, the free stream Prandtl number $Pr_\infty = 0.72$, the ratio between constant specific heats $\gamma = 1.4$, the free stream temperature $T_\infty = 216.67\,K$, the dynamic viscosity defined by Sutherland's law in Eq. (2.25) and the thermal conductivity defined by the constant Prandtl assumption in Eq. (2.26). These conditions lead to a small enough momentum thickness at $x = L_s + L_f$ such that the Görtler number is always $Go \lesssim 10$. This number commonly leads to the appearance of nonlinear Görtler vortices. Grid converged simulations were achieved with $(N_x, N_y, N_z) = (401, 201, 52)$ using a time step of $\Delta t = 2 \times 10^{-5}$. Time integration was performed using the third-order accurate and three-stages ERK scheme in Eq. (2.84), inviscid fluxes are discretized with the WENO5-ZQ scheme using characteristic-wise Lax-Friedrichs flux-vector splitting and the viscous luxes were discretized with the fourth-order accurate conservative central-differences scheme. Furthermore, free stream conditions are prescribed at the inlet and far-field boundaries whereas all variables are extrapolated at the outlet boundary. Boundary conditions at the body, on the other hand, impose adiabatic walls as well as a zero wall-normal pressure derivative. The velocity boundary conditions, however, are more complex.

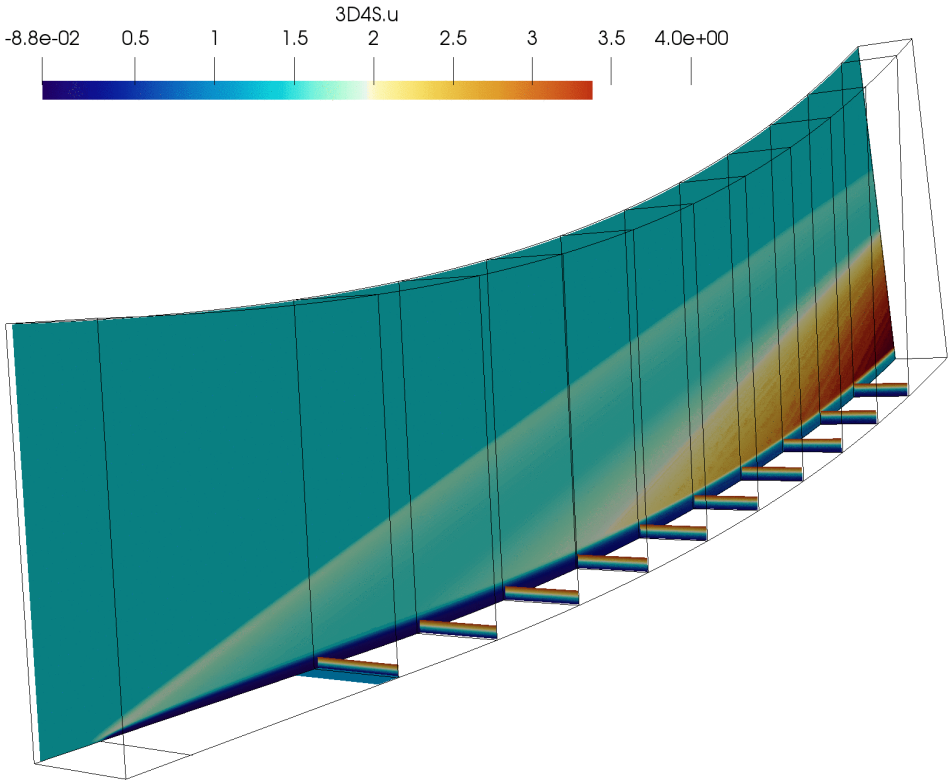

Figure 3.15: Unforced isocontours of the flow over a curved plate. Density on (x, y) plane and streamwise velocity component on (y, z) planes.

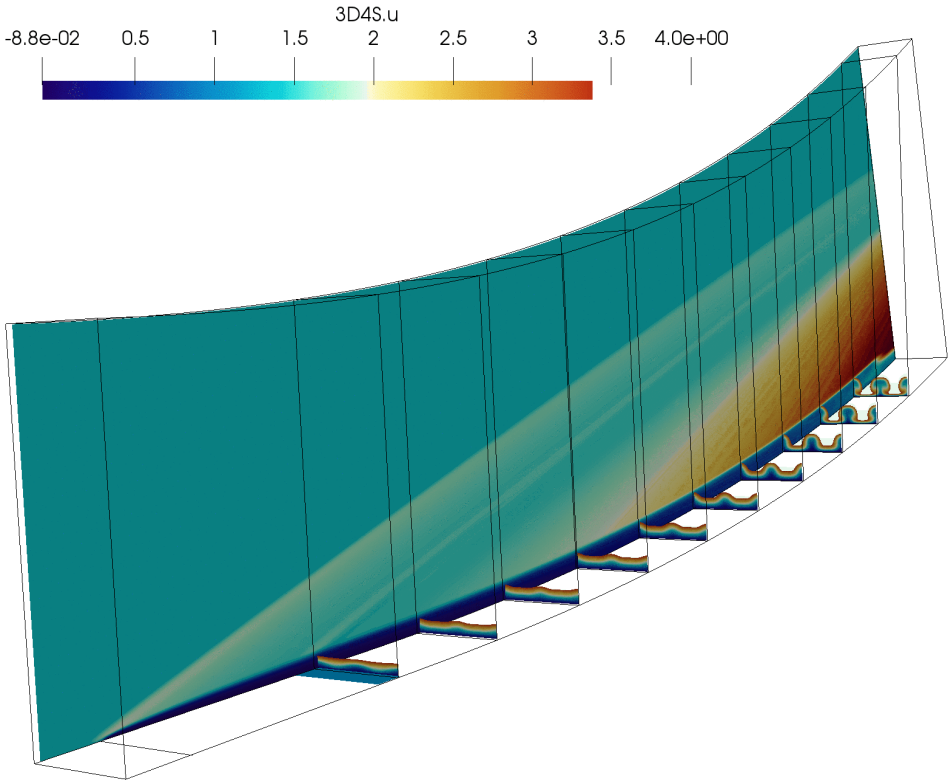

Figure 3.16: Same as Fig. 3.15 but forced with $v_w = 0.15$.

A slip boundary is imposed at $0 \leq x \leq L_s$ and a no-slip one is imposed elsewhere, creating a sharp leading edge at $x = L_s$. Furthermore, the walls are considered impermeable everywhere, except at $x_1 \leq x \leq x_2$ where $x_1 = 0.9$, $x_2 = 1.0$, $\lambda = 3\,(x_2 - x_1)/2$ and $v(x, y = 0, w) = v_w\,\sin^3[\pi\,(x - x_1)/(x_2 - x_1)]\,\cos[2\,\pi\,z/\lambda]$. Doing so creates a steady blowing and suction forcing strip with amplitude v_w just before the curved plate, which excites stationary Görtler vortices with a spanwise wavelength λ. Note that $\lambda \sim O(\theta)$ was chosen because this is commonly done in the literature. Figure 3.15 shows the accurate and disturbance free steady-state obtained in the unforced scenario where $v_w = 0$. On one hand, the (x, y) plane shows density isocontours, which highlight the leading edge shock as well as the curved plate compression fan, both exiting through the outlet boundary. On the other hand, the (y, z) planes show the streamwise velocity component isocontours, which highlight the streamwise thinning of the boundary-layer. Figure 3.16 shows the steady-state contaminated by stationary Görtler vortices due to the forcing having been turned on with $v_w = 0.15$. Noticeable differences include the appearance of a weak shock emanating from the forcing strip and the linear and nonlinear spanwise periodic deformation of the streamwise velocity component just downstream of the excitation location. The same data is shown in Fig. 3.17, but the streamwise disturbance velocity component isocontours appear on the (y, z) planes instead, highlighting the high disturbance amplitudes reached far enough downstream of the excitation location.

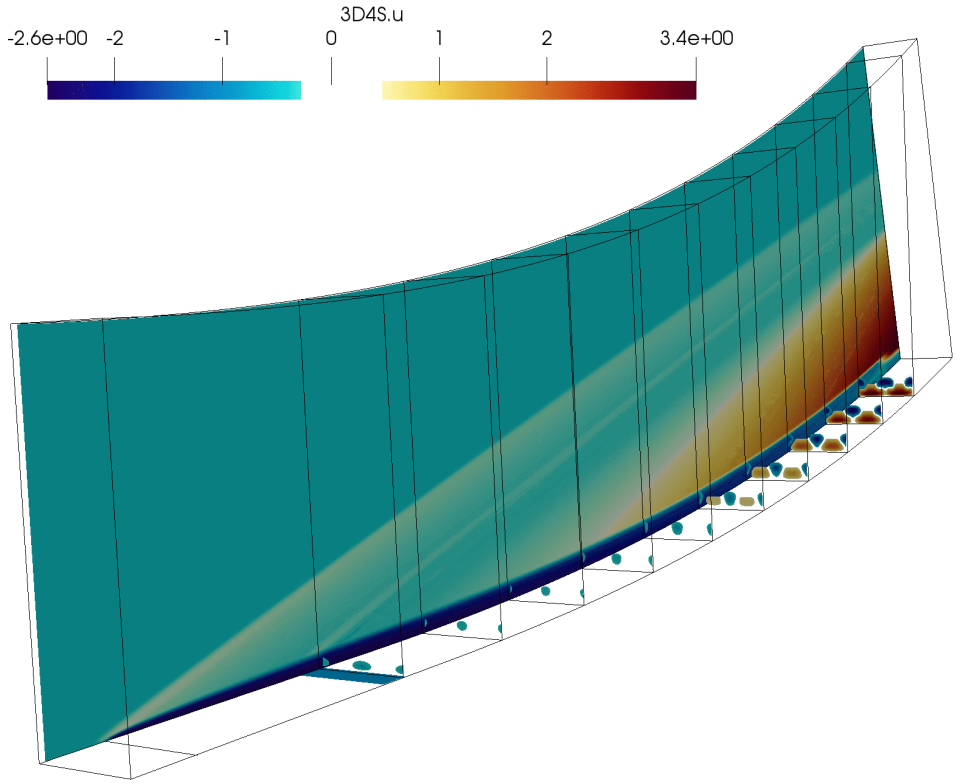

Figure 3.17: Same as Fig. 3.16 but showing disturbance velocity instead.

3.2 Scalability

High-speed flows of interest are usually three-dimensional in nature or, at least, two-dimensional. Furthermore, the goal of this report is to use special time marching and spatial discretization techniques in order to obtain highly accurate and disturbance free steady-states for linear and nonlinear stability analyses. Hence, computational time consuming simulations are practically inevitable. This can be alleviated by parallel computing on high performance computing (HPC) clusters, where many processor are used simultaneously to produce exceptional computational power and, hence, significantly reduce computational time. In order to do so, however, scalability is essential. It indicates the ability of both software and hardware to deliver an increasing amount of computational power as the amount of resources increases. When dealing with software, which is the case here, scalability is also known as parallelization efficiency. It means the ratio between the actual speedup and the ideal speedup obtained when using a certain number of processors. The scalability of 3D4S is discussed next.

3.2.1 Strong Scaling

According to Amdahl (1967), the speedup for a given problem of fixed size is limited by the fraction of the software that is not amenable to parallelization. It can be formulated as

$$speedup = 1 \Big/ \left(s + \frac{p}{N}\right) \quad , \tag{3.3}$$

where s (p) is the time spent on the serial fraction of the software that cannot (can) be parallelized and N is the number of cores. This is known as **Amdahl's law**. Hence, the speedup has an upper limit given by $1/s$ when $N \to \infty$, which is known as **strong scaling**. This means that parallelization efficiency decreases as the amount of resources increases. 3D4S strong scaling was measured on ARCHER, the UK National Supercomputing Service, using the 2D simulations of the compression ramp discussed in section 3.4. These results are shown in Fig. 3.18, where the dashed line represents the optimal linear behavior. They indicate an excellent parallelization efficiency up to $N = 5,000$ cores and a very good one up to $N \simeq 30,000$.

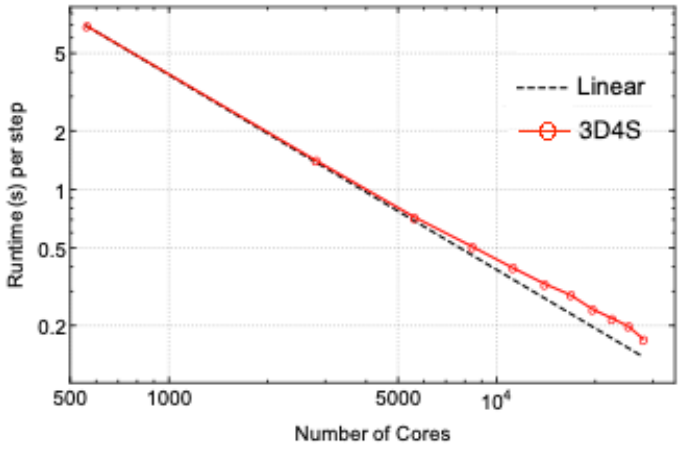

Figure 3.18: 3D4S strong scaling measured on ARCHER, UK.

3.2.2 Weak Scaling

On the other hand, Gustafson (1988) pointed out that, in practical terms, the problem size scales with the amount of resources available. In other words, small (large) problems will be more efficient when using a small (large) amount of resources. A scaled speedup is then formulated as

$$scaled\ speedup = s + p \times N \quad , \tag{3.4}$$

where s, p and N have the same meaning as before. This is known as **Gustafson's law**. Since the scaled speedup increases linearly with respect to the number of cores, it has no upper limit. In other words, the scaled speedup is based on the amount of work done for a scaled problem size

and is known as **weak scaling**. 3D4S strong scaling was also measured on ARCHER, the UK National Supercomputing Service, and also used the 2D simulations of the compression ramp discussed in section 3.4. These results are shown in Fig. 3.19 for $N \geq 5,000$, given the results shown in Fig. 3.18, where the dashed line represents the optimal linear behavior. They indicate a very good parallelization efficiency between $5,000 \leq N \leq 30,000$.

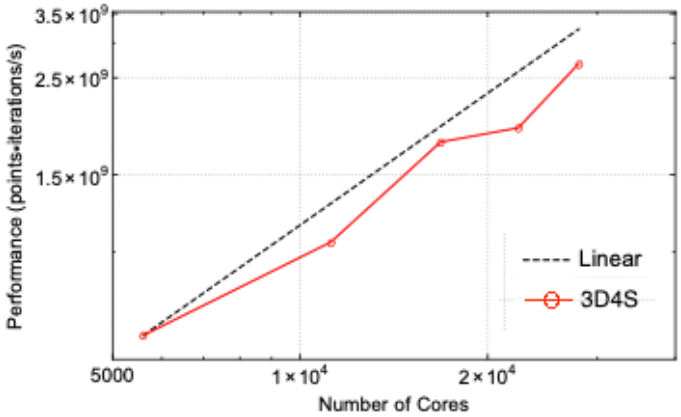

Figure 3.19: 3D4S weak scaling measured on ARCHER, UK.

3.3 2D Cylinder

Having provided evidence in the verification section on the ability of 3D4S to provide accurate and disturbance free steady-states as well as time-accurate unsteady states, an in-depth analysis of the supersonic flow upstream of a two-dimensional cylinder is pursued next. The relevance of this canonical problem comes from the fact that it emulates the flow over an airfoil leading edge. It is simulated here on the same grid used by (Jiang and Shu, 1996), which uses the expressions

$$\begin{aligned} x &= (R_x - (R_x - 1)\,\xi)\cos[\theta\,(2\,\eta - 1)] \quad \text{and} \\ y &= (R_y - (R_y - 1)\,\xi)\sin[\theta\,(2\,\eta - 1)] \quad , \end{aligned} \tag{3.5}$$

to relate the computational domain $(\xi, \eta) \in [0,1] \times [0,1]$ with the Cartesian (x, y) one for a cylinder centered at $(x, y) = (0, 0)$, where $R_x = 3$, $R_y = 6$ and $\theta = 5\,\pi/12$. Hence, the characteristic length scale used to write the equations in dimensionless form is the cylinder radius. This transformation places the four domain boundaries at specific computational grid locations, namely the inlet at $\xi = 0$, the cylinder body at $\xi = 1$ and both outlets at $\eta = 0$ and 1.

All variables are prescribed their free stream values at the inlet whereas extrapolation is employed at both outlets. Both velocity components and the pressure wall-normal derivative are prescribed to zero at the body. Two temperature boundary conditions are considered for the body, namely the body is either adiabatic or isothermal, where its temperature T_w is prescribed

to the free stream value T_∞. Two free stream Mach numbers and three free stream Reynolds numbers are considered as well, namely $Ma_\infty = 4$ and 6 as well as $Re_D = 200$, 1000 and 10000, which is based on the cylinder diameter. Furthermore, the ratio between constant specific heats and the free stream Prandtl number are fixed at $\gamma = 1.4$ and $Pr_\infty = 0.72$, respectively. However, the dynamic viscosity $\mu(T)$ defined by Sutherland's law in Eq. (2.25) and the thermal conductivity $\kappa(T)$ defined by the constant Prandtl assumption in Eq. (2.26) are calculated using two different relevant high altitude hypersonic flight conditions, namely $h_\infty = 40\,km$ and $50\,km$. Their thermodynamic states are defined by the respective free stream temperature and pressure pairs $(T_\infty, P_\infty) = (216.67\,K, 279.74\,Pa)$ and $(271.155\,K, 67.016\,Pa)$. Time steps Δt were chosen close to the maximum CFL limit every time.

3.3.1 Steady-States

Verification

Before describing the accurate and disturbance free steady-states generated by Santos (2020) for the linear and global stability analyses by the UoL group discussed in the next subsections, results obtained by different schemes in 3D4S are verified against those obtained by the rhoCentralFoam solver in

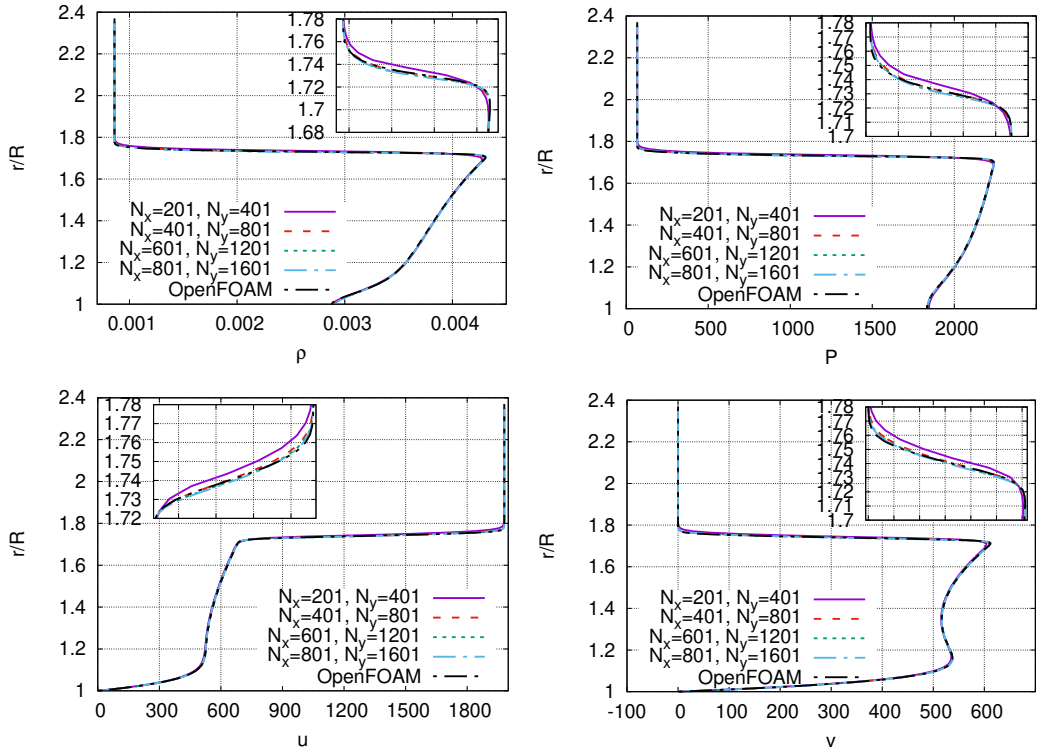

Figure 3.20: Radial profiles for density (top left), pressure (top right), streamwise (bottom left) and vertical (bottom right) velocity components measured at 45 degrees from the stagnation line obtained using the low-order 3D4S and OpenFOAM for $Ma_\infty = 6$, $Re_D = 10^3$, $h_\infty = 40\,km$ and an adiabatic wall.

OpenFOAM (Burtsev et al., 2021), which is a second-order accurate finite-volume code. These comparisons are performed through radial profiles for density, pressure, streamwise and vertical velocity components, which were measured at 45 degrees from the stagnation line. These results are shown in Fig. 3.20 for $Ma_\infty = 6$, $Re_D = 10^3$, $h_\infty = 40\,km$ and an adiabatic wall. Low-order 3D4S results were obtained with an explicit Euler scheme in time as well as a second-order accurate TVD scheme employing a Roe-HLL flux-difference splitting and a conservative second-order accurate central-difference scheme for the spatial discretization of inviscid and viscous fluxes, respectively. The grids points employed, i.e. $(N_x, N_y) = (201, 401)$, $(401, 801)$, $(601, 1201)$ and $(801, 1601)$, indicate spatial profile convergence within graphical error. Also, low-order 3D4S and OpenFOAM grid converged results are in excellent agreement. This analysis is now repeated for the same parameters, except that $Re_D = 10^4$, $h_\infty = 50\,km$ and high-order 3D4S is employed instead. It uses the WENO5-JS scheme with the characteristic-wise Lax-Friedrichs flux-vector splitting and the conservative fourth-order accurate central-difference scheme for the respective spatial discretization of inviscid and viscous fluxes. Once again, spatial profile convergence is within graphical error and 3D4S and OpenFOAM grid converged results are in good agreement. However, it is also possible to notice that OpenFOAM introduces much more numerical diffusion than high-order 3D4S around the bow shock. In any case, this study adds weight to the verification process of 3D4S.

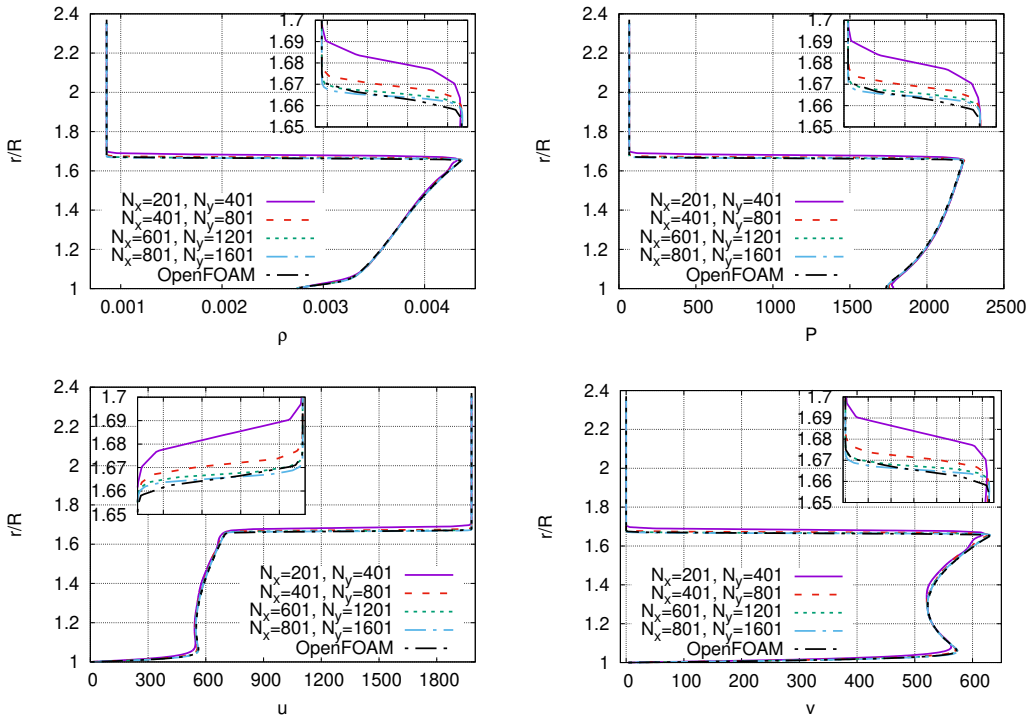

Figure 3.21: Same as Fig. 3.20 but using high-order 3D4S with $Re_D = 10^4$ and $h_\infty = 50\,km$.

Adiabatic Walls

Having gained confidence that 3D4S is capable of providing reliable steady-states for this flow, a more nuanced analysis of these steady-states is provided. Density residue convergence in time of the low-order 3D4S simulations is analyzed in Fig. 3.22 for (left) $Re_D = 10^3$ and (right) $Re_D = 10^4$. No convergence issues were found in the former case, but more refined grids were required for machine zero convergence in the latter case. Insight into

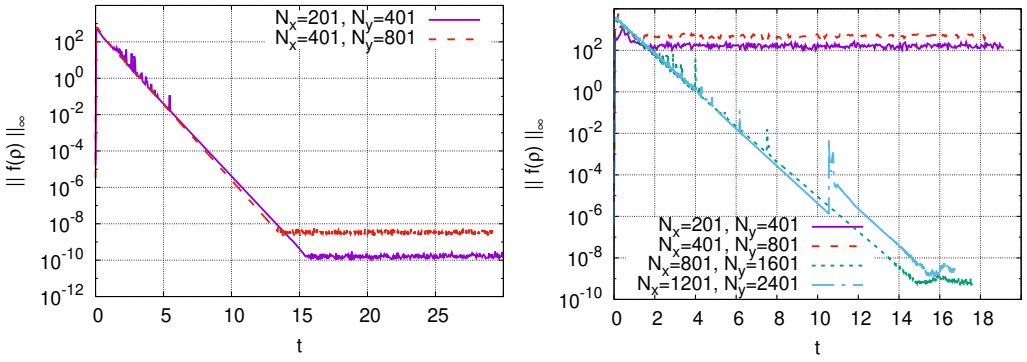

Figure 3.22: Low-order 3D4S density residue infinity norm convergence in time for $Ma_\infty = 6$, $h_\infty = 40\,km$ and an adiabatic wall with (left) $Re_D = 10^3$ and (right) $Re_D = 10^4$.

the reasons for such a behavior con be found by evaluating the synthetic Schlieren images of these steady-states, which are obtained from the density gradients. They are shown in Fig, 3.23. Close inspection reveals that these images are quite clean when $Re_D = 10^3$, but very small striations near the stagnation region that emanate from the bow shock and move downstream of it aligned with the streamlines can be observed when $Re_D = 10^4$. Additional structures away from the stagnation region can also be observed emanating from the shock, but they move towards the wall. Similar structures were observed using OpenFOAM even at $Re_D = 10^3$ (Burtsev et al., 2021).

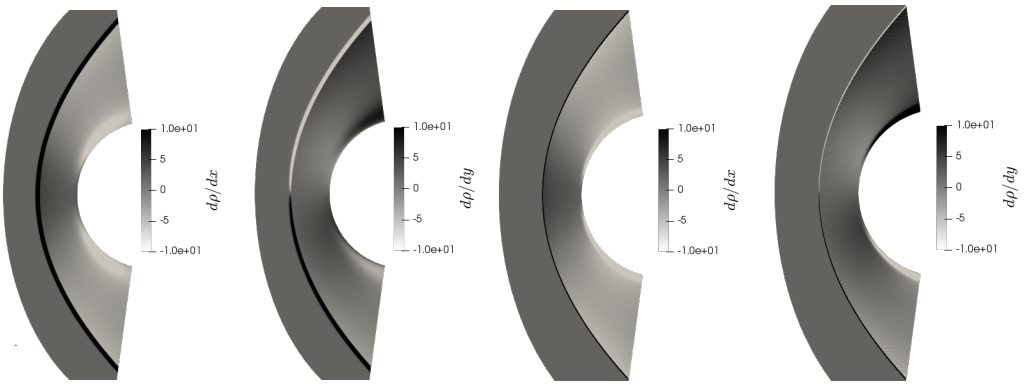

Figure 3.23: Synthetic Schlieren images from the simulation data associated with Fig. 3.22 for (left) $Re_D = 10^3$ and (right) $Re_D = 10^4$.

In order to keep probing into this issue, high-order 3D4S simulation data is analyzed at the same parametric conditions, except for the altitude and Reynolds numbers. Density residue convergence in time is shown in Fig. 3.22 for $h_\infty = 50\,km$ with (left) $Re_D = 200$, (middle) $Re_D = 10^3$ and (right) $Re_D = 10^4$. It is important to note that machine zero was achieved for all grids using WENO5-JS, i.e. WENO5-ZQ was not required. This means there are no significant unsteady post-shock oscillations contaminating these solutions by introducing unsteady disturbances with local truncation error amplitudes, even though there is some evidence that this does happen at much smaller grid sizes (Zhu and Shu, 2019). For the sake the brevity,

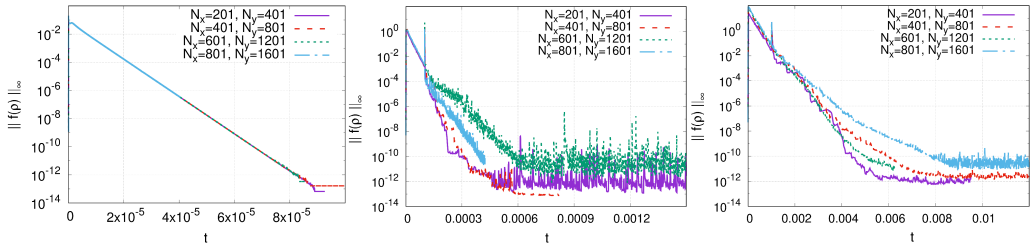

Figure 3.24: Same as Fig. 3.22, but for high-order 3D4S with $h_\infty = 50\,km$ and (left) $Re_D = 200$, (middle) $Re_D = 10^3$ as well as (right) $Re_D = 10^4$.

the same steady radial profiles from Figs. 3.20 and 3.21 are shown again in Fig. 3.25 but only for the vertical velocity component at the parametric conditions associated with Fig. 3.24 for (left) $Re_D = 200$ and (right) $Re_D = 10^3$, since Fig. 3.21 (bottom right) already shows this profile for $Re_D = 10^4$. These latter figures indicate that spatial profiles are grid converged within graphical accuracy and agree with grid converged OpenFOAM results, but the former figures does show non-negligible oscillations between shock and wall for the coarser grids. This implies that the striations observed in Fig. 3.23 (right) based on the TVD scheme data could still be present at $Re_D = 10^4$, but in a much smaller magnitude. Isocontous and isolines for

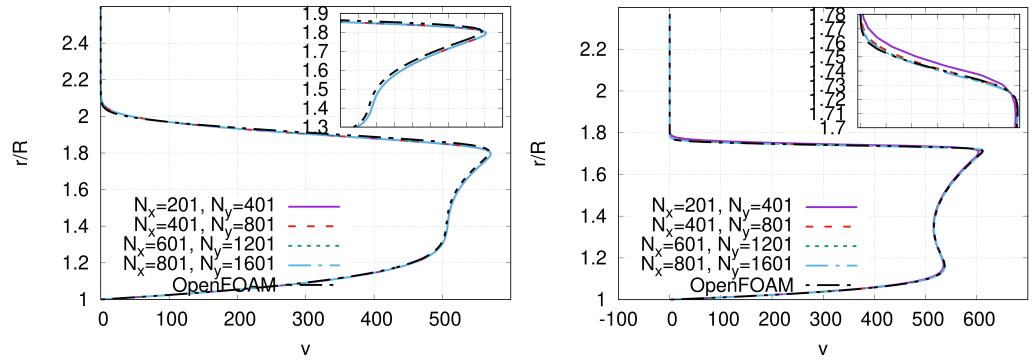

Figure 3.25: Vertical velocity component radial profile measured at 45 degrees from the stagnation line from the high-order 3D4S for $Ma_\infty = 6$, $h_\infty = 50\,km$, an adiabatic wall as well as (left) $Re_D = 200$ and (right) $Re_D = 10^3$.

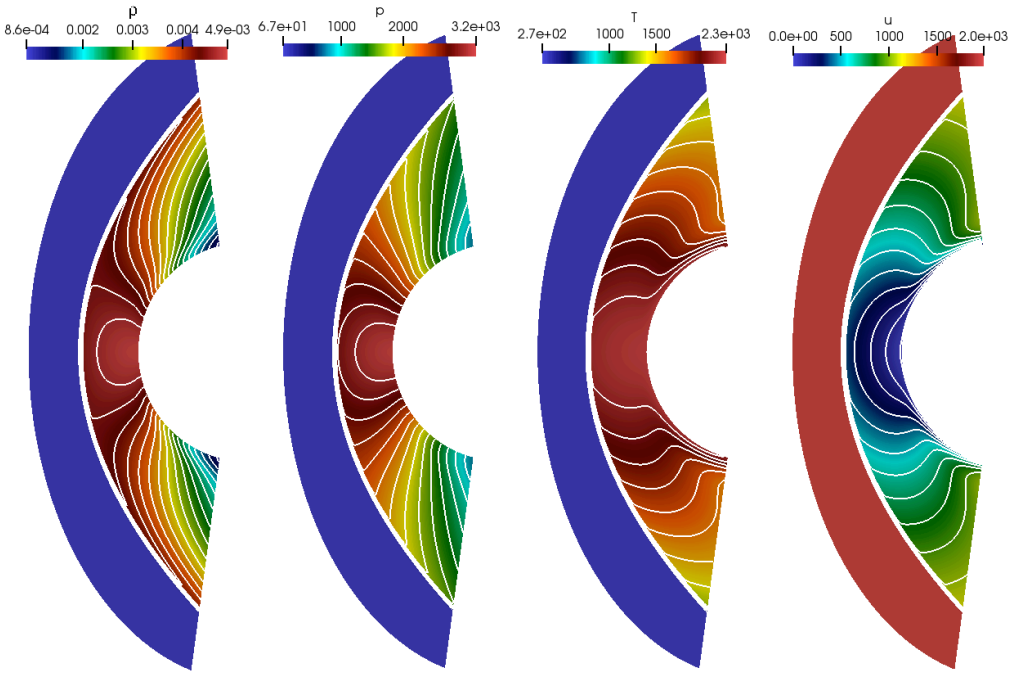

Figure 3.26: 20 isocontous and isolines for density, pressure, temperature and streamwise velocity component obtained from the same $N_x = 801$ and $N_y = 1601$ data shown in Fig. 3.25 (right) when $Re_D = 10^3$.

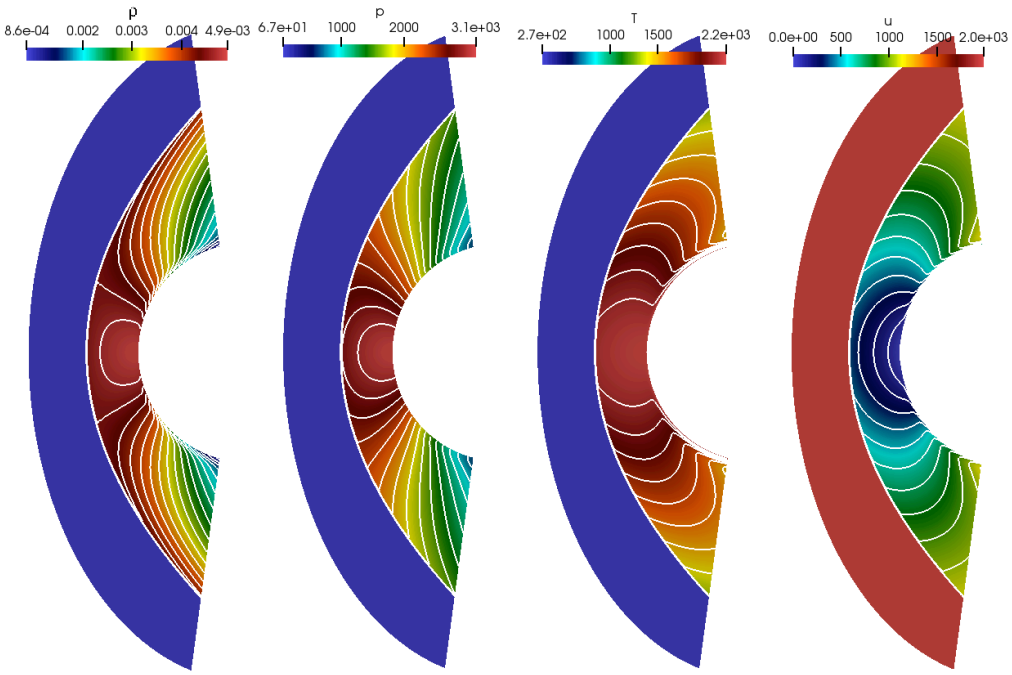

Figure 3.27: Same as Fig. 3.26 but for Fig. 3.21 when $Re_D = 10^4$.

density, pressure, temperature and streamwise velocity component within the entire domain for the same parametric conditions used to generate the $N_x = 801$ and $N_y = 1601$ curves in Fig. 3.25 (right) and Fig. 3.21 are now shown in Figs. 3.26 and 3.27, respectively. The structures are qualitatively quite similar in both cases, although the shock as well as the hydrodynamic and thermal boundary-layers are thinner at the higher Reynolds number. In any case, no striations are apparent in these figures. A more nuanced analysis, such as the one using the density gradients shown in Fig. 3.23, might be required to properly asses the presence of striations. Before doing so, however, the isothermal wall scenario is investigated as well.

Isothermal Walls

High-order 3D4S simulation data is now analyzed for isothermal walls under the parametric conditions given by $T_w = T_\infty$, $Ma_\infty = 6$, $h_\infty = 50\,km$ and different Reynolds numbers. Density residue convergence in time is shown in Fig. 3.28 for (left) $Re_D = 10^3$ and (right) $Re_D = 10^4$. Once again, the use of WENO5-JS did not prevent the residue from reaching machine zero. Hence, significant post-shock oscillations are not present in these results. On the

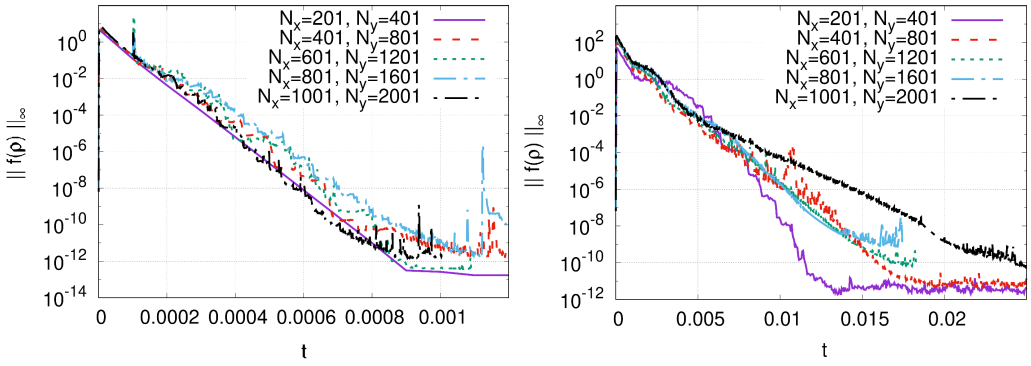

Figure 3.28: High-order 3D4S density residue infinity norm convergence in time for $Ma_\infty = 6$, $h_\infty = 50\,km$ and an isothermal wall with (left) $Re_D = 10^3$ and (right) $Re_D = 10^4$.

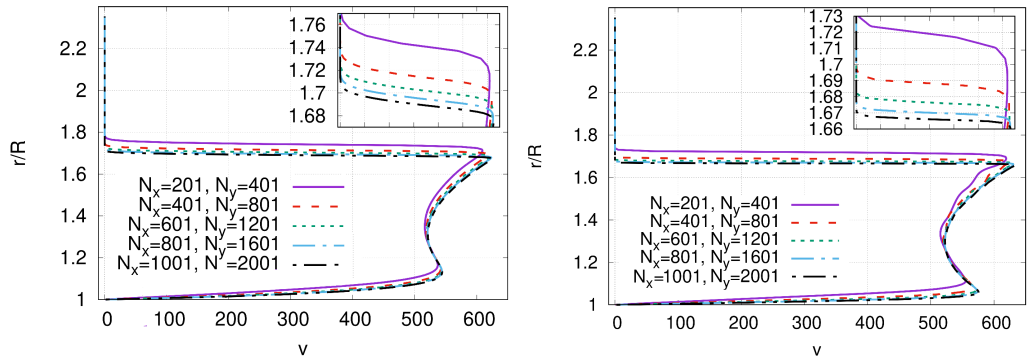

Figure 3.29: Same as Fig. 3.25 but for an isothermal wall with (left) $Re_D = 10^3$ and (right) $Re_D = 10^4$.

other hand, radial profiles for the vertical velocity component measured at 45 degrees from the stagnation line, shown in Fig. 3.29 for (left) $Re_D = 10^3$ and (right) $Re_D = 10^4$, once again indicate the appearance of non-negligible oscillations between shock and wall at the higher Reynolds number. However, they are even stronger than observed for adiabatic walls, since they can still be visualized on the finest grid employed here. Hence, striations are even more likely be present in this case, even if they still have small magnitudes. As in the adiabatic case, on the other hand, they are not easily visualized. Isocontous and isolines for both velocity components within the entire domain are shown in Fig. 3.30 with (left) $Re_D = 10^3$ and (right) $Re_D = 10^4$. They are displayed for the same parametric conditions used to generate the $N_x = 1001$ and $N_y = 2001$ curves in Fig. 3.29. The structures are qualitatively quite similar for both Reynolds numberd, although the shock as well as the hydrodynamic boundary-layer are thinner when $Re_D = 10^4$. Nevertheless, no striations are apparent at either Reynolds number and a more nuanced analysis is required to properly confirm their presence or absence.

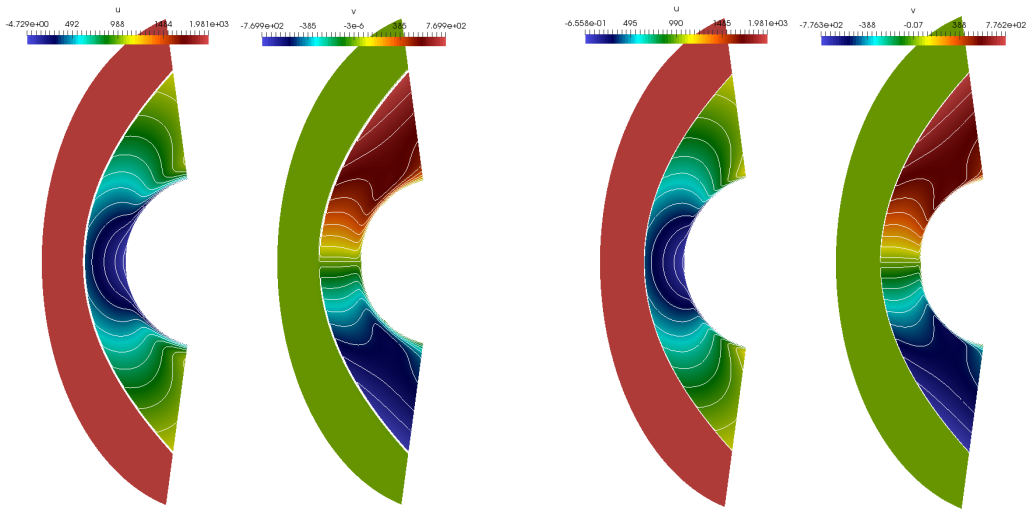

Figure 3.30: 20 isocontous and isolines for both velocity components obtained from the same $N_x = 1001$ and $N_y = 2001$ data shown in Fig. 3.29 when (left) $Re_D = 10^3$ and (right) $Re_D = 10^4$.

3.3.2 Linear and Global Disturbances

Striations

Density gradients evaluated using low-order 3D4S steady-states, shown in Fig. 3.23, revealed the presence of striations at $Re_D = 10^4$ but not at $Re_D = 10^3$. On the other hand, they cannot be observed in the direct visualization of the primitive variables themselves when obtained from high-order 3D4S steady-states at $Re_D = 10^4$, as shown in Figs. 3.27 and 3.30. Nevertheless, their presence can be inferred from the respective coarse grid radial profiles

shown in Figs. 3.21 and 3.29. Hence, it is quite likely that these striations are still present but have small magnitudes.

Since this flow is physically unstable in a linear and time asymptotic sense, one indirect way of quantifying the presence of striations is to evaluate their impact on the least damped mode eigenfunction. This is due to the fact that physical disturbances are strongly influenced by base-flow Jacobians. Hence, striations should have a strong effect on the disturbance that takes the longest to be damped in a simulation marching towards steady-state. In order to evaluate this effect, the residuals algorithm (Theofilis and Colonius, 2003) is employed to extract the least damped from from the 3D4S simulations. It provides simple algebraic formulas to compute the steady-state $\mathbf{Q}_s$, the global disturbance eigenfunction $\mathbf{Q}_n$ and the complex frequency ω of any arbitrary unsteady state $\mathbf{Q}$ obtained from a time marching simulation that is converging towards steady-state, since $\mathbf{Q}$ can then be decomposed as

$$\mathbf{Q}(x,y,t) = \mathbf{Q}_s(x,y) + \epsilon\,\mathbf{Q}_n(x,y)\,e^{-i\,\omega\,t} \quad , \tag{3.6}$$

where $i = \sqrt{-1}$ and ϵ is a small amplitude parameter that quantifies the disturbance amplitude.

Applying this procedure to the isothermal wall simulations that led to the results shown in Fig. 3.30 yields the least damped and stationary disturbance eigenfunctions for both velocity components shown in Fig. 3.31 for (left) $Re_D = 10^3$ and (right) $Re_D = 10^4$. In the former case, the disturbances sit on top of the steady bow shock, having a negligible contribution to the subsonic flow field between shock and wall. It is interesting to note that the streamwise velocity disturbance eigenfunction is positive whereas the vertical one is positive (negative) bellow (above) the stagnation line, which means

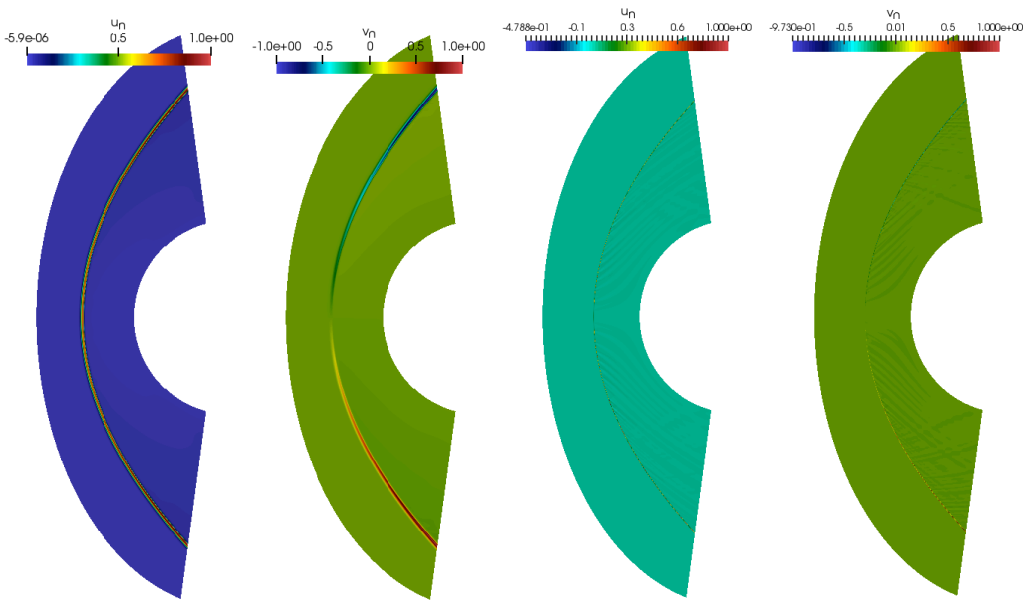

Figure 3.31: Same as Fig. 3.30, but for their respective normalized least damped and stationary disturbance eigenfunctions.

the least damped mode has a tendency of pushing the bow shock against the cylinder wall. In other words, the stand-off distance asymptotically increases towards its final value as the simulation approaches steady-state and this disturbance is damped. In the latter case, however, things are qualitatively different. A significant portion of the disturbances still sits on top of the shock, although these eigenfunctions are much thinner due to the higher Reynolds numbers. However, striations that behave in the same way observed in Fig. 3.23 (right) appear in the subsonic region between shock and wall as well. The same trends are also observed in the adiabatic wall simulations when $Re_D = 10^4$, but they are shown here in yet another way. Absolute values of the disturbance eigenfunctions for temperature, pressure as well as streamwise and vertical velocity components are shown in Fig 3.32. Doing so clearly highlights the striations in the disturbance eigenfunctions.

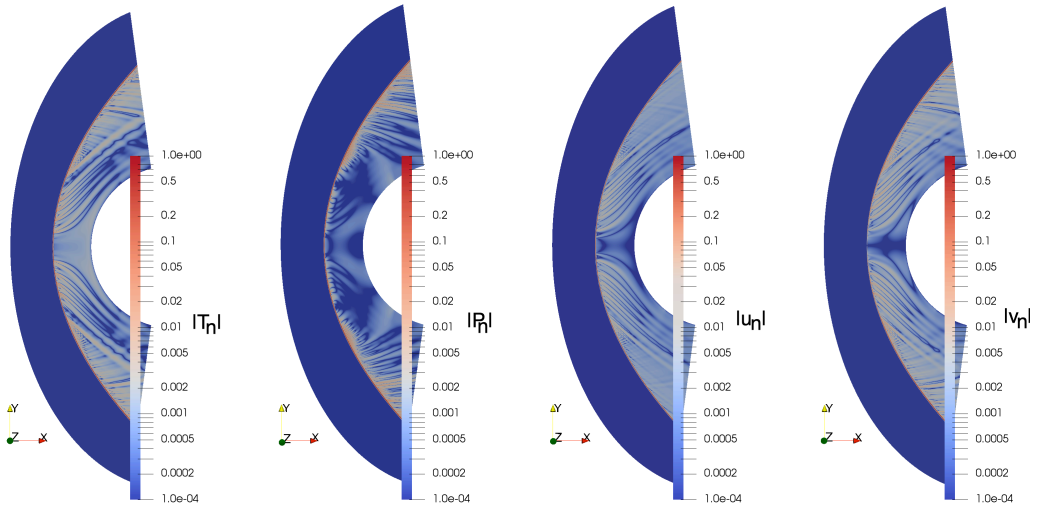

Figure 3.32: Same as Fig. 3.27, but for the normalized absolute value of the least damped and stationary disturbance eigenfunctions.

The analysis performed so far on striations indicates a few relevant things. First, they are present in the steady-state, but only at high enough Reynolds numbers. Second, they are present in the least damped and stationary mode, but only at high enough Reynolds numbers. Third, they appear for both isothermal and adiabatic wall conditions. Fourth, their amplitudes decrease as the grid is refined. These things put together strongly indicate that such striations are in fact due to the carbuncle phenomenon. The fifth thing, however, puts things in perspective. Striations appear in both low-order (TVD with flux-difference splitting) and high-order (WENO5 with characteristic-wise flux-vector splitting) 3D4S simulations, as well as the second-order finite-volume simulations performed with OpenFOAM. If this is indeed carbuncle, such a finding goes against the current understanding in the literature, which states that carbuncle is restricted to spatial discretization schemes that use flux-difference splitting. Additional tests are required, however, before any definitive conclusions can be drawn.

Modal and Non-Modal Analyses

Given the numerical issues likely associated with carbuncle at $Re_D = 10^4$, focus is placed on the $Re_D = 10^3$ case in what follows. A linear and global stability analysis is now pursued based on the steady-state shown in Fig. 3.26, which was obtained from high-order 3D4S for $Ma_\infty = 6$, $h_\infty = 50\,km$, an adiabatic wall and this Reynolds number. This analysis used the LiGHT code developed by Quintanilha Jr et al. (2022) and was performed by graduate student Anton Burtsev from the UoL research group led by prof. Vassilis Theofilis, who collaborated extensively with the UFF research group led by prof. Leo Alves for this part of the project.

The steady-state grid convergence effect on the eigenvalue problem (EVP) spectrum calculated on a fixed grid and domain is shown in Fig. 3.33 (left). Essentially identical results were obtained when either finer grids or larger domains sizes were employed for the EVP. The insert shows the stationary and least damped mode convergence as the steady-state grid resolution is increased. It includes only the three finest grids. When coarser steady-state grids are employed, the correct stationary and least damped mode is not recovered. Furthermore, a stable spectrum is only achieved for steady-state grids with $(N_x, N_y) = (201, 401)$ and above. Figure 3.34 shows a comparison between the stationary and least damped mode amplitude function radial profiles obtained from the LiGHT code and from 3D4S at an angle of 30 degrees from the stagnation line, indicating an excellent agreement.

Figure 3.33 also shows the linear gain as a function of time (right) for the same grids used in the modal analysis (left). Both coarser steady-state grid cases are included to show that the spurious unstable modes they induce in the modal analysis lead to an also spurious exponential growth. As the steady-state grid resolution is increased, however, a $O(10^3)$ transient growth is observed at a small time horizon ($t \sim O(1)$) before the modal decay takes over at larger times ($t \gtrsim 4$). The time asymptotic linear gain slope is shown

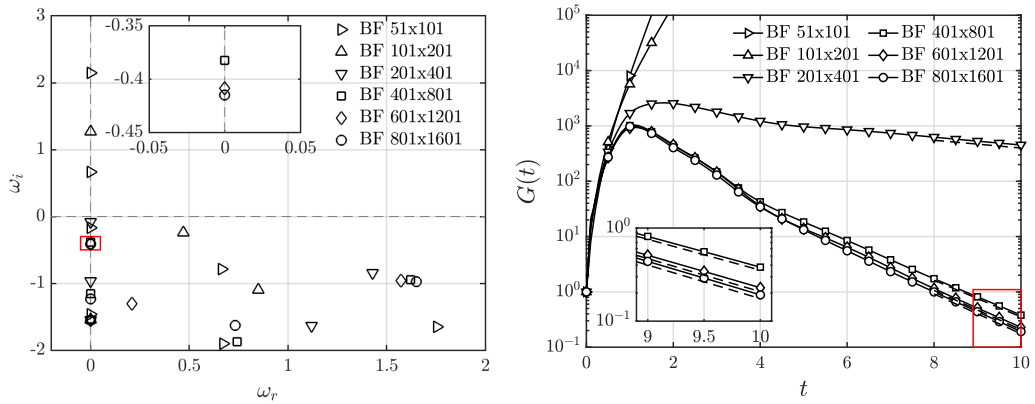

Figure 3.33: Linear spectra (left) and gain over time (right), where both inserts show the convergence of the least damped and stationary mode, for the parametric conditions and steady-state shown in Fig. 3.26.

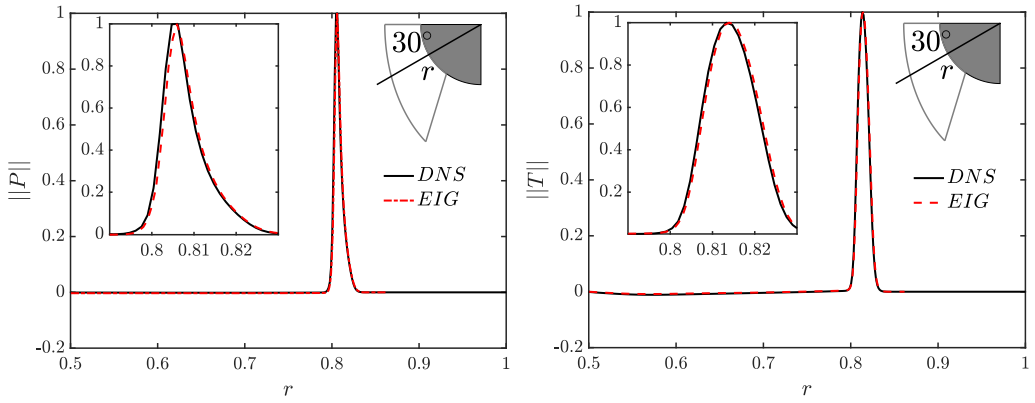

Figure 3.34: Pressure (left) and temperature (right) radial structure of the least damped modes obtained from the residuals algorithm applied to high-order 3D4S (DNS) and the eigenvalue solver in the LiGHT code (EIG).

in the insert, where dashed lines indicate the corresponding damping rate of the least damped mode for each resolution. A very good agreement can be observed between both time asymptotic decay rate calculations for each grid resolution. Furthermore, the maximum linear gain $G_{max} = G(t_{opt})$ has achieved graphical convergence when the steady-state grid is at $(N_x, N_y) = (401, 801)$. Hence, the steady-state grid convergence of the modal analysis is slower than the non-modal one. Initial (left), optimal (middle) and time asymptotic (right) non-modal pressure disturbances are plotted in Fig. 3.35 for $(N_x, N_y) = (801, 1601)$. There are similarities and differences between all three scenarios. On one hand, optimal non-modal disturbances also sit on top of the bow shock, as do modal disturbances. On the other hand, the disturbance eigenfunction magnitude is concentrated at different locations in all three scenarios. It is stronger near the stagnation region for optimal initial

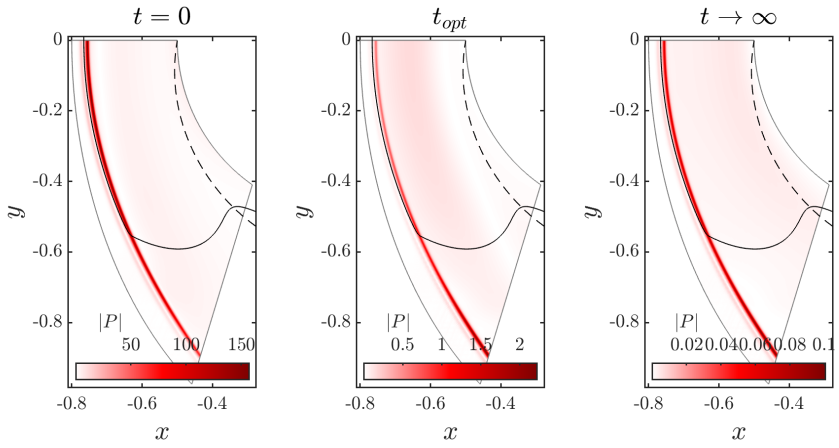

Figure 3.35: Initial (left), optimal (center) and time asymptotic (right) linear pressure disturbances from Fig. 3.33 (right) computed using the $(N_x, N_y) = (801, 1601)$ steady-state shown in Fig. 3.26.

conditions ($t = 0$), but it is weaker there for optimal conditions ($t = t_{opt}$). Finally, the time asymptotic ($t \to \infty$) disturbance eigenfunction magnitude is evenly distributed along the bow shock, being virtually indistinguishable from the spatial structure of the stationary and least damped mode obtained from the EVP modal analysis.

Although they are not shown, it is important to note that preliminary results for the same parametric conditions analyzed here but with $Ma_\infty = 4$ instead were also obtained. They indicate that transient growth is still strong in these conditions, with the optimal linear gain only slightly smaller than its $Ma_\infty = 6$ counterpart. This is true even though the flow is modally quite more stable. Furthermore, the initial, optimal and time asymptotic eigenfunctions are qualitatively very similar as well.

3.3.3 Time-Accurate Unsteady Simulations

Time-accurate simulations are performed using high-order 3D4S to verify the modal and non-modal behaviors identified in the linear and global stability analysis. This is done by interrupting these simulations once the maximum solution increment has decreased below a predefined tolerance, defined here as $||\mathbf{Q}^{n+1} - \mathbf{Q}^n||_\infty \simeq O(10^{-8})$, and re-starting them with a random excitation at the cylinder wall of amplitude $O(10^-7)$. Doing so is equivalent to superposing a random disturbance to the steady-state. This is done deliberately in order to try and trigger a sub-optimal non-modal response, as opposed to superposing the optimal disturbance initial condition from the non-modal stability analysis. Hence, realizability issues are not put into question.

The evolution of this disturbance is presented in Fig. 3.36. Each plot in this figure shows the (left) pressure, temperature and velocity disturbance amplitudes varying with time that were measured by a probe at the shock location on the stagnation line, where the red dots and dashed lines mark the time chosen in each plot to show the (right) respective pressure disturbance spatial structure. This disturbance $\mathbf{Q}_d(\mathbf{x}, t)$ is obtained by post-processing the simulations to extract $\mathbf{Q}_d(\mathbf{x}, t) = \mathbf{Q}(\mathbf{x}, t) - \mathbf{Q}_s(\mathbf{x})$, since the steady-state $\mathbf{Q}_s(\mathbf{x}) = \mathbf{Q}(\mathbf{x}, t \to \infty)$ is already known. The different plots in this figure were chosen to illustrate the disturbance propagation from the wall towards the bow shock, passing through the subsonic region, perturbing the bow shock itself and then dying out at larger times.

Figure 3.36 (top left) shows the disturbance behavior just slightly after the random excitation was introduced at $t = 12$. During this time, the random excitation is evolving into a linear disturbance, which is felt a the probe due to the propagation upstream of the acoustic signal generated at the re-start. The next plot, namely Fig. 3.36 (top right), shows that disturbance is still propagating towards the bow shock when $t \simeq 12.07$, at which time the signal has already passed through the bow shock and disappeared. The disturbance can then be seen hitting the bow shock at $t \simeq 12.14$ in Fig. 3.36 (middle left), but most of the effect of this first impact has already left the stagnation region at $t \simeq 12.2$, as can be seen in Fig. 3.36 (middle right). It is beyond

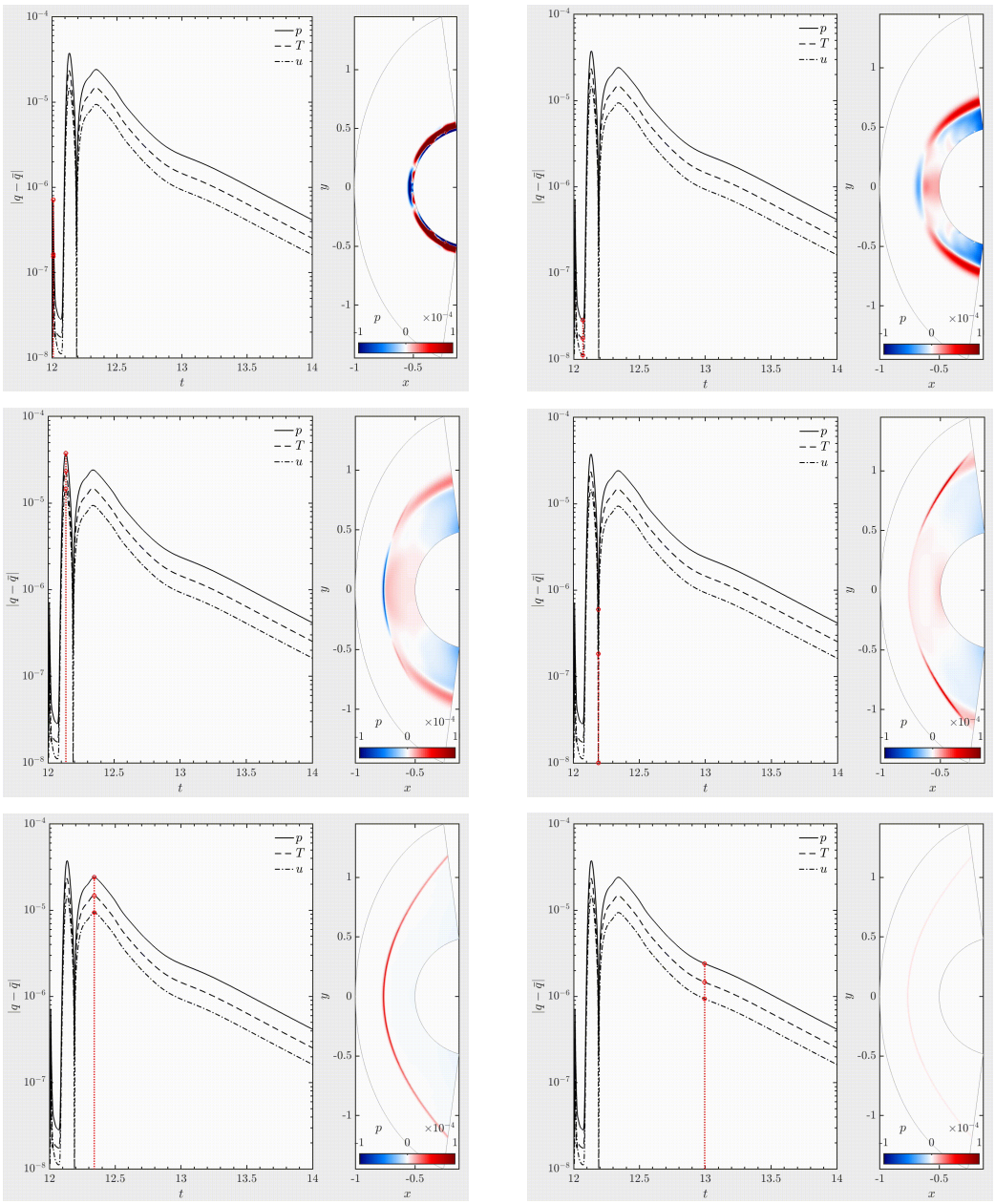

Figure 3.36: Disturbance amplitudes varying with time as measured by a probe at the shock location on the stagnation line, where the red dots and dashed lines mark the respective time chosen in each plot (left) to show the respective pressure disturbance spatial structure (right).

this point in time that the disturbance starts growing again at the shock within the stagnation region, reaching a maximum amplitude at $t \simeq 12.34$ in Fig. 3.36 (bottom left). Furthermore, there is strong evidence this is due to a sub-optimal transient growth. First, the disturbance amplitude is still quite small, i.e. it is still a linear disturbance. Second, the disturbance growth rate in time is not linear in a log plot, i.e. the disturbance growth in time is algebraic and not exponential. Third, the amplitude growth has an

upper bound of $O(10^3)$, measured from the disturbance amplitude baseline at $t = 12$ before the excitation was introduced, making it a close to optimal sub-optimal growth according to Fig. 3.33 (right). The fourth and final evidence is that the pressure disturbance spatial structures during this period resemble the ones shown in Fig. 3.35 for the (left) initial and (middle) optimal non-modal pressure disturbances. At larger times, as shown in Fig. 3.36 (bottom right), the modal behavior takes over and the disturbance amplitude starts decaying exponentially in time. Furthermore, its spatial structure becomes evenly distributed along the bow shock. Both behaviors were predicted by the modal linear and global analysis shown in Figs. 3.33 (right) and 3.35 (right), respectively.

3.4 2D Compression Ramp

Given the evidence provided in the verification and cylinder sections 3.1 and 3.3, respectively, about the ability of 3D4S to provide accurate and disturbance free steady-states, an in-depth analysis of the supersonic flow over a two-dimensional compression ramp is pursued next. Before putting forward a discussion about these steady-states as well as their linear and global instability, some context is required. The difficulty in obtaining steady-states for the compression ramp was brought to our attention by Vassilios Theofilis from UoL, who wanted to perform a linear and global stability analysis of this problem. However, this endeavour could not be adequately pursued because "*it was not possible to reach a true steady-state using OpenFOAM under the temporal and spatial resolutions, as well as parametric conditions, employed*" (Theofilis, 2020). What follows is the product of the joint work that led to us overcoming this challenge, where the UFF research group focussed on the compression ramp steady-states and the UoL group focussed on their linear and global stability.

The relevance of this problem comes from the preponderance of corners is high-speed aerodynamic structures. A sketch of this geometry is shown in Fig. 3.37, taken from the work by Martin et al. (2003). It specifies four boundaries, namely the i) body, including both flat plate and inclined ramp parts, ii) wall-normal inlet, iii) wall-normal outlet and iv) far-field, which is curved to become as close as possible to being normal to both inlet and outlet. Its transformation from the computational domain $(\xi, \eta) \in [0,1] \times [0,1]$ to the physical domain (x, y), passing by the intermediate domain $(s, r) \in [0,1] \times [0,1]$, described by Adams (1998) and Martin et al. (2003), is given by

$$\begin{aligned} x(\xi,\eta) &= \big(1 - r(\eta)\big)\, x_l\big(s(\xi)\big) + r(\eta)\, x_u\big(s(\xi)\big) \quad \text{and} \\ y(\xi,\eta) &= \big(1 - r(\eta)\big)\, y_l\big(s(\xi)\big) + r(\eta)\, y_u\big(s(\xi)\big) \quad , \end{aligned} \tag{3.7}$$

where the subscripts l and u indicate lower and upper boundary values, respectively. On one hand, the lower curve boundary functions are

$$x_l(s) = L_l\, s \quad \text{and}$$

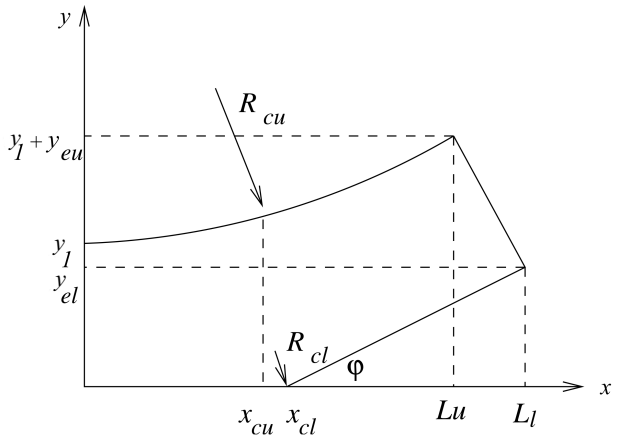

Figure 3.37: Sketch of the compression ramp geometry (Martin et al., 2003).

$$y_l(s) \;=\; d_{2l}\, x_l(s) + \tfrac{d_{2l}}{d_{1l}} \ln\big[\cosh[d_{1l}(x_l(s) - x_{cl})]\big] + d_{2l}\, d_{3l} \quad , \qquad (3.8)$$

with its intermediate variables defined as

$$\begin{aligned} d_{1l} \;&=\; \frac{(1 + d_{2l}^2)^{3/2}}{R_{cl}} \quad , \\ y_l(1) \;&=\; y_{el} \quad \text{and} \\ d_{3l} \;&=\; -\frac{1}{d_{1l}} \ln[\cosh[d_{1l}\, x_{cl}]] \quad , \end{aligned} \qquad (3.9)$$

where R_{cl} is the corner $(x_{cl}, 0)$ radius of curvature, included to prevent the corner singularity in the mapping process, and d_{2l} is obtained from the second equation in (3.9). Furthermore, the upper curve boundary functions are

$$\begin{aligned} x_u(s) \;&=\; L_u\, s \quad \text{and} \\ y_u(s) \;&=\; y_1\, d_{2u}\, x_u(s) + \tfrac{d_{2u}}{d_{1u}} \ln\big[\cosh[d_{1u}(x_u(s) - x_{cu})]\big] + d_{2u}\, d_{3u} \quad , \end{aligned} \qquad (3.10)$$

with its intermediate variables defined as

$$\begin{aligned} d_{1u} \;&=\; \frac{(1 + d_{2u}^2)^{3/2}}{R_{cu}} \quad , \\ y_u(1) \;&=\; y_1 + y_{eu} \quad \text{and} \\ d_{3u} \;&=\; -\frac{1}{d_{1u}} \ln[\cosh[d_{1u}\, x_{cu}]] \quad , \end{aligned} \qquad (3.11)$$

where R_{cu} is the radius of curvature at $x = x_{cu}$ and d_{2u} is obtained from the second equation in (3.11). All other symbols are defined in Fig. 3.37. On the other hand, grid point distribution along parametric $s(\xi)$ lines within the physical domain is given by the function

$$s(\xi) = a\,\xi + b + c_1\, \sinh[g(\xi)] \quad , \qquad (3.12)$$

with its intermediate variables defined as

$$\begin{aligned} g(\xi) &= \frac{\xi - c_2}{c_3} \quad , \\ a &= 1 - c_1 \left(\sinh\left[\frac{c_2}{c_3}\right] + \sinh\left[\frac{1-c_2}{c_3}\right] \right) \quad \text{and} \\ b &= c_1 \sinh\left[\frac{c_2}{c_3}\right] \quad , \end{aligned} \tag{3.13}$$

where increasing c_1 or decreasing c_3 cluster grid points around $\xi = c_2$. Hence, c_2 must be obtained from

$$x_{cl} = x_l\big(s(\xi = c_2)\big) \quad , \tag{3.14}$$

since grid points should be clustered around the corner at $x = x_{cl}$ in the x-direction. Furthermore, the grid point distribution along parametric $r(\eta)$ lines within the physical domain is given by the function

$$r(\eta) = \frac{cc\, h_1(\eta)}{aa + bb\, h_1(\eta)} \quad , \tag{3.15}$$

with its intermediate variables defined as

$$\begin{aligned} h_1(\eta) &= c\,\eta + d + e_1 \sinh[h_2(\eta)] \quad , \\ aa &= h_1(\eta_1)\left(1 - \frac{y_{12}}{y_1}\right) \quad , \\ bb &= \left(\frac{y_{12}}{y_1} - h_1(\eta_1)\right) \quad \text{and} \\ cc &= \frac{y_{12}}{y_1}(1 - h_1(\eta_1)) \quad , \end{aligned} \tag{3.16}$$

which uses the additional intermediate variables

$$\begin{aligned} h_2(\eta) &= \frac{\eta - e_2}{e_3} \quad , \\ c &= 1 - e_1 \left[\sinh\left(\frac{1-e_2}{e3}\right) + \sinh\left(\frac{e_2}{e_3}\right)\right] \quad \text{and} \\ d &= e_1 \sinh\left(\frac{e_2}{e_3}\right) \quad , \end{aligned} \tag{3.17}$$

where increasing e_1 or decreasing e_3 cluster grid points around $\eta = e_2$. Hence, one must set $e_2 = 0$ in order to cluster grid points at the lower boundary. Additionally, η_1 is the percentage of lines within the interval $y \in [0, y_{12}]$ at $x = 0$. It was varied between 0.5 and 0.8 according to the boundarylayer thickness. In all compression ramp simulations performed for this report,

the ramp angle was fixed at $\varphi = 10$ degrees. The characteristic length scale employed is the flat plate length L and the additional parameters required to setup the domain are $c_1 = c_3 = e_3 = 1.0$, $e_1 = 3.0$, $d_3 = 0.5$, $R_{cu} = 1.0$, $R_{cl} = 0.02$, $x_{cu} = x_{cl} = L + x_s$, $L_l = x_{cl}\,(1 + \cos[\varphi])$, $L_u = L_l - x_{cl}\,\tan[\varphi]$, $y_1 = 3.5\,x_{cl}\,\sin[\varphi]$, $y_{12} = y_1/2$ and $y_{eu} = 1.5 - y_1$.

All variables are prescribed their free stream values at the inlet but are extrapolated at the outlet and far-field. Both velocity components and the pressure wall-normal derivative are prescribed to zero at the body, except when $x < x_s$, where slip is enforced to model a sharp leading edge at $x = x_s$. In all compression ramp simulations reported here, $x_s = L/10$. Two temperature boundary conditions are considered for the body, namely the body is either adiabatic or isothermal. In the latter case, its temperature is prescribed to the free stream stagnation temperature, i.e.

$$T_{0,\infty} = \left(1 + \frac{\gamma - 1}{2}\,Ma_\infty^2\right) \Big/ \left((\gamma - 1)\,Ma_\infty^2\right) \quad , \tag{3.18}$$

where the free stream Mach number, temperature and ratio between constant specific heats are respectively fixed at $Ma_\infty = 3$, $T_\infty = 216.67\,K$ and $\gamma = 1.4$. Furthermore, the free stream Prandtl number is fixed at $Pr_\infty = 0.72$. These values were used to set up the dynamic viscosity $\mu(T)$ through Sutherland's law in Eq. (2.25) and the thermal conductivity $\kappa(T)$ through the constant Prandtl assumption in Eq. (2.26). Finally, free stream Reynolds numbers Re_∞ ranging from 5×10^3 to 240×10^3 were simulated using grids (N_x, N_y) ranging from $(601, 201)$ to $(4801, 1601)$. Time steps Δt were chosen close to the maximum CFL limit in each case.

3.4.1 Steady-States

Low-Order 3D4S

First attempts to obtain such steady-states used the low-order 3D4S, here based on the explicit Euler scheme for time integration and a second-order accurate spatial discretization, which employed a TVD scheme with the Roe flux-difference splitting and the SuperBee flux-limiter for inviscid fluxes as well as a conservative central-difference scheme for the viscous fluxes. The density wall-normal profile at the corner (left) and density maximum residue convergence in time (right) obtained for three different free stream Reynolds numbers, namely $Re_\infty = 2{\times}10^3$ (top), $5{\times}10^3$ (middle) and $10{\times}10^3$ (bottom), are show in Fig. 3.38 for the isothermal wall case under different grid sizes. Simulations require an increasingly larger number of grid points for their spatial profiles to converge towards the same tolerances as the free stream Reynolds number increases. Nevertheless, the number of grid points used in this figure do show spatial profiles grid converged to graphical accuracy. On the other hand, residue convergence in time has a much stronger dependence on the free stream Reynolds number. Residue converges in time for all grids employed when $Re_\infty = 2 \times 10^3$, for only the largest four grids employed when

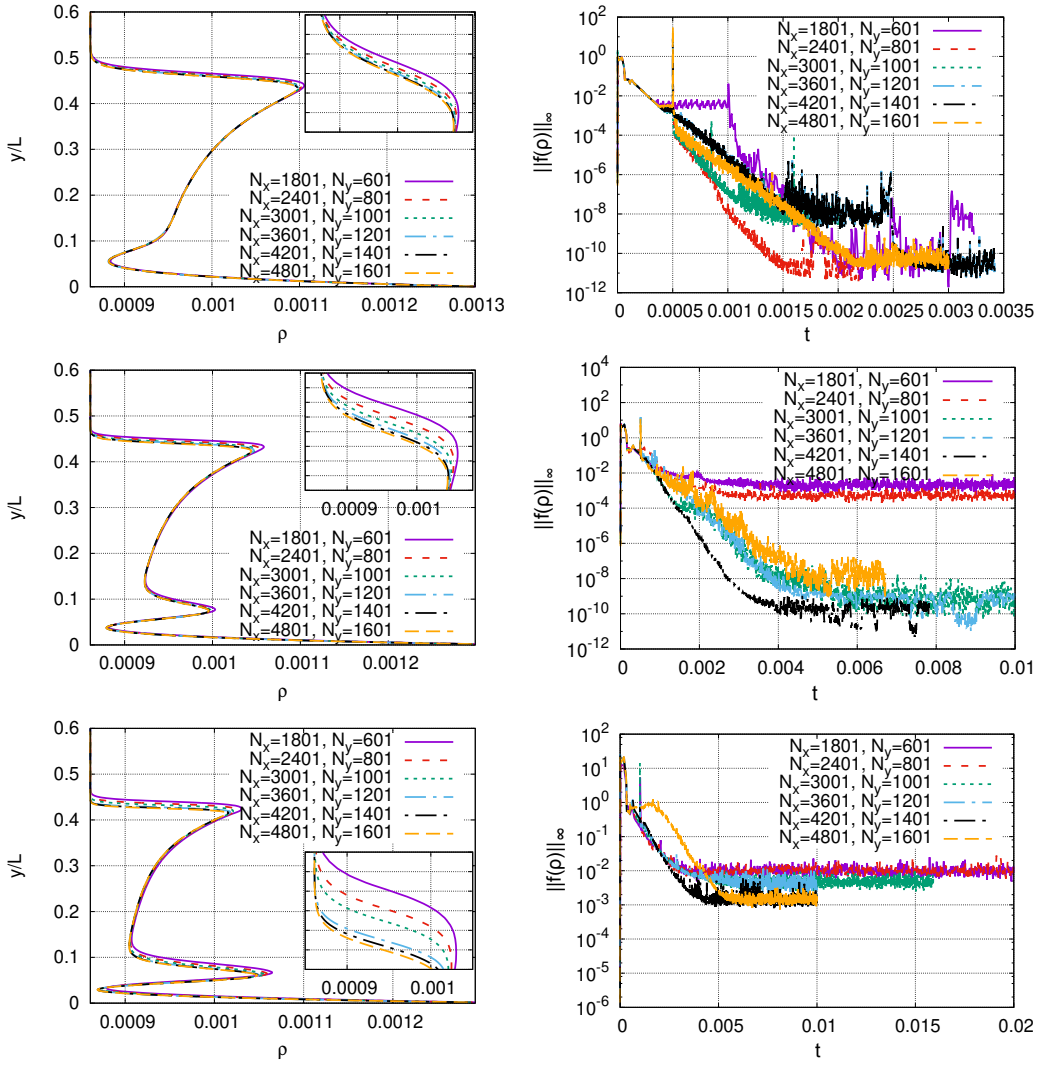

Figure 3.38: Density wall-normal profile at the corner (left) and density maximum residue convergence in time (right) obtained with $Re_\infty = 2 \times 10^3$ (top), 5×10^3 (middle) and 10×10^3 (bottom) from low-order 3D4S for the isothermal wall case under different grid sizes.

$Re_\infty = 5 \times 10^3$ and for none of the grids employed when $Re_\infty = 10 \times 10^3$. Convergence is quantified here by how much the maximum density residue decreases in time. It does so by approximately 10 orders of magnitude in the former two cases. In the latter case, however, it does so by approximately 4 orders of magnitude only, suggesting a 6 digits accuracy loss. These low-order 3D4S trends were also observed when using OpenFOAM, even though its second-order accurate finite-volume solver used approximately 16 million grid points to simulate the $Re_\infty = 10^4$ case (Santos et al., 2019).

In order to better understand what is preventing convergence in time, five probes were placed throughout the domain along the boundary-layer edge to measure the streamwise velocity component behavior in time. This is shown in Fig. 3.39 for the isothermal wall case with $Ma_\infty = 3$, $Re_\infty = 16.8 \times 10^3$,

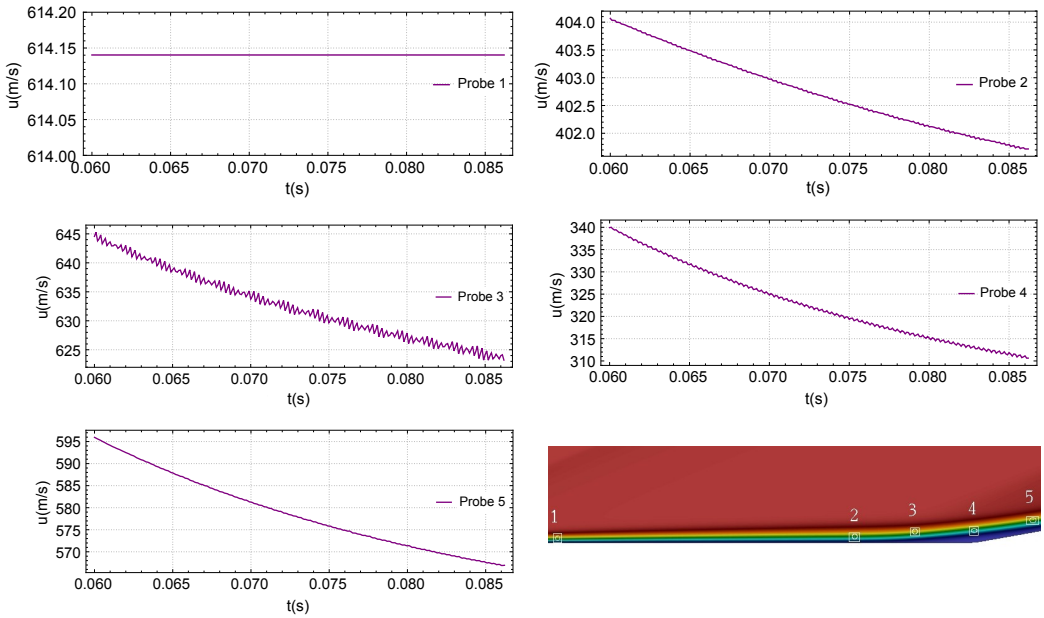

Figure 3.39: Dimensional streamwise velocity component temporal behavior measured by (x, y) probes 1, 2, 3, 4 and 5, respectively placed at $(3.0, 0.1)$, $(8.0, 0.1)$, $(9.0, 0.2)$, $(10.0, 0.2)$ and $(11.0, 0.4)$, from low-order 3D4S for an isothermal wall with $Re_\infty = 16.8 \times 10^3$, $(N_x, N_y) = (3601, 1201)$ and $\eta_1 = 0.6$.

$Pr_\infty = 0.72$ and $T_\infty = 300\,K$, which represents the original OpenFOAM case study (Santos et al., 2019). Probe 1 is placed just downstream of the leading edge (top left), probe 2 is placed just upstream of the separation bubble (top right), probe 3 is placed at the separation region (middle left), probe 4 is placed in the middle of the recirculation bubble (middle right) and probe 5 is placed at the reattachment region (bottom left), as illustrated in Fig. 3.39 (bottom right). No visible unsteadiness was captured by probe 1. This suggests there are no post-leading edge-shock oscillations. However, unsteadiness starts to be observed by probe 2, is the strongest by probe 3, gets weaker by probe 4 and has almost disappeared by probe 5. This suggests the compression fan creates difficulties for the second-order accurate TVD shock-capturing scheme employed.

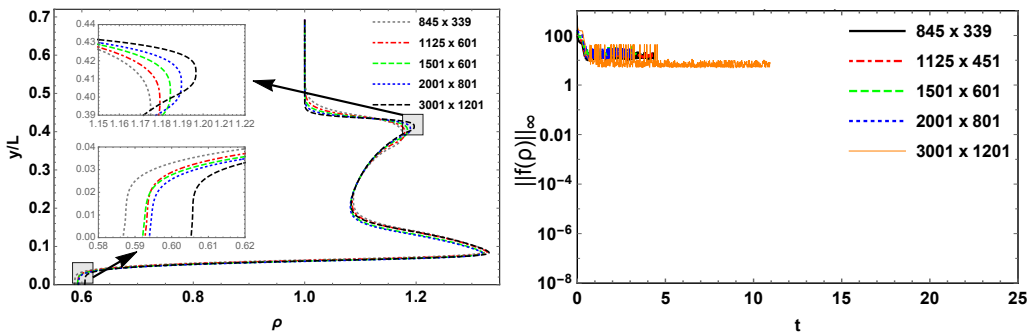

Figure 3.40: Same as Fig. 3.38, but with adiabatic walls and $Re_\infty = 20 \times 10^3$.

The analysis presented in Fig. 3.38 is repeated, but now for low-order 3D4S simulations with an adiabatic wall and $Re_\infty = 20 \times 10^3$ instead, and shown in Fig. 3.40. Once again, the maximum density residue convergence in time (right) did not reach machine zero with the grids employed, even though the density wall-normal profiles at the corner (left) seem reasonably well grid converged everywhere, except at the separation shock due to the excessive numerical diffusion introduced by the shock-capturing scheme employed. In order to try and understand what is preventing convergence in time under these new conditions, an analysis similar to the one presented in Fig. 3.39 is performed and shown in Fig. 3.41. The probes, however, are defined in a different way. Instead of measuring the solution at a point, its maximum value over a region is taken. Three different near wall regions are considered. Probe a contains the leading edge, probe b contains the separation point and probe c contains the reattachment point. Unsteadiness is observed in all three probes, but the former is the dominant one. This suggests that post-leading edge-shock oscillations are now the main culprit. These oscillations most likely survive downstream, since they can be observed in the separation and reattachment regions. Despite the differences in the oscillation origin between isothermal and adiabatic cases, the likely cause in both cases is flickering of the flux-limiter (Hendrickson et al., 2018).

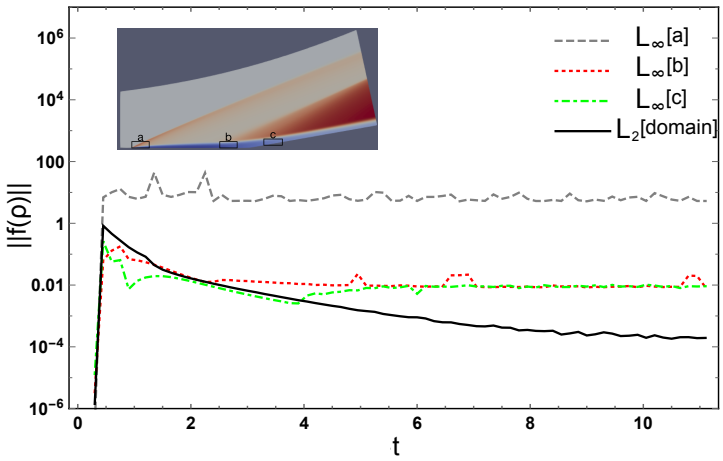

Figure 3.41: Density residue convergence in time for the same conditions used in Fig. 3.40 but $(N_x, N_y) = (3001, 1201)$. Probes measuring the maximum value within leading edge (a), separation (b) and reattachment (c) regions. Euclidean norm over the entire domain presented for comparison purposes.

Finally, it is important to note that the free stream Reynolds numbers analyzed so far are more than 10 orders of magnitude smaller than the ones employed in the recent literature (Chuvakhov et al., 2017; Sidharth et al., 2018; Dwivedi et al., 2019; Hao et al., 2021; Exposito et al., 2021), but the present simulations use similar grid sizes and second-order schemes as well. Since they do not provide any data about residue convergence in time, it is not possible to know if their steady-states are contaminated by temporal content. Given the results analyzed so far, however, this seems likely.

High-Order 3D4S

In order to eliminate these leading-edge shock and separation compression fan related oscillations that prevent residue convergence in time to machine zero when employing low-order 3D4S, the special techniques discussed in the context of the blunt body problem from subsection 3.1.2 are employed by high-order 3D4S. In other words, inviscid fluxes are discretized with WENO5-ZQ and characteristic-wise Lax-Friedrichs flux-vector splitting, viscous fluxes are discretized using the fourth-order accurate conservative central-difference scheme, but time integration does not have to change, i.e. it is still performed with the explicit Euler scheme. The impact of doing so is shown in Fig. 3.42, which reproduces the results shown in Fig. 3.40 but using high-order 3D4S with WENO5-ZQ instead. Now the maximum residue decays in time towards machine zero for the two largest grids employed. Furthermore, comparing both figures indicates that the leading edge shock and the wall temperature are much better resolved using a much smaller grid. Finally, the same three probes a, b and c shown in Fig. 3.40 can be used to analyze the residue in the same three regions involving the leading edge, separation and reattachment points, respectively. This is shown in Fig. 3.43 for high-order 3D4S using $(N_x, N_y) = (2001, 801)$. All residue measures converge in time to machine zero, indicating that numerical unsteadiness has been controlled.

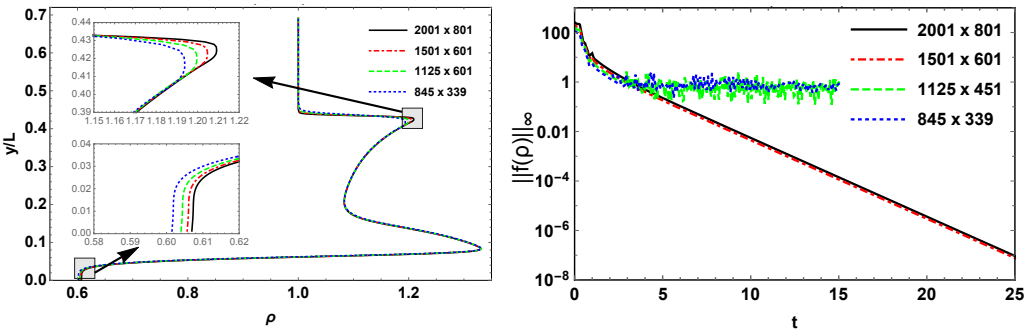

Figure 3.42: Same as Fig. 3.40, but with high-order 3D4S instead.

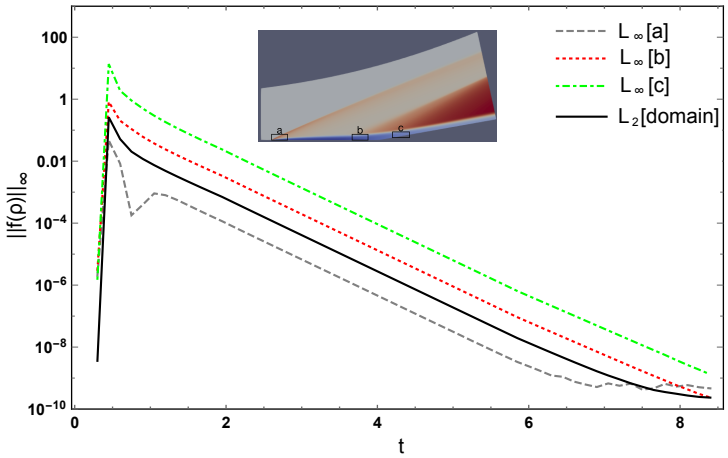

Figure 3.43: Same as Fig. 3.41, but with high-order 3D4S instead.

It turns out the maximum residue convergence in time towards machine zero can be achieved for all free stream Reynolds numbers considered for the compression ramp in this report. In order to provide evidence in favor of this point, Fig. 3.44 presents this data for free stream Reynolds numbers Re_∞ ranging from 20×10^3 to 240×10^3. This figure also provides the respective grid size for each Reynolds number, showing that a reasonable number of grid points was employed to achieve convergence in time for all cases compared to the low-order 3D4S simulations.

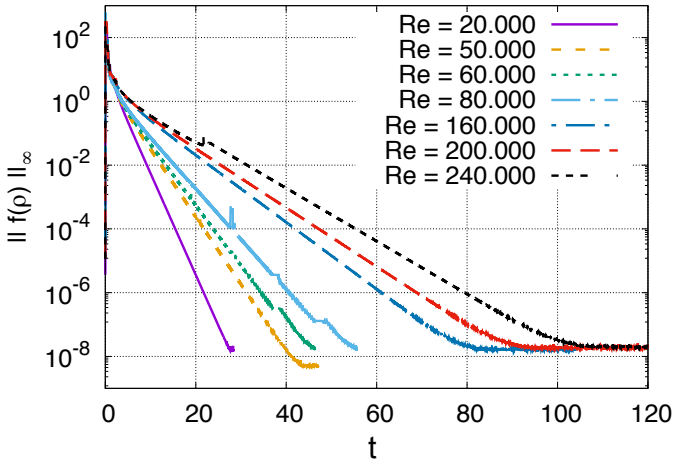

Figure 3.44: Density maximum residue convergence in time for different Reynolds numbers with $(N_x, N_y) = (1801, 601)$, $(2401, 801)$, $(2401, 801)$, $(2401, 801)$, $(3601, 1201)$, $(3601, 1201)$ and $(3601, 1201)$, respectively.

The solution obtained from high-order 3D4S for one of these high Reynolds number cases, namely $Re_\infty = 200 \times 10^3$, is shown in Figure 3.45. It provides isocontours (left column) and wall-normal spatial profiles at the corner (right column) for density (first row), pressure (second row) as well as streamwise (third row) and vertical (last row) velocity components, where isocontours were generated using $(N_x, N_y) = (3001, 1001)$ and profiles were generated using different grids. The former shows the presence of a leading edge shock, recirculation region and both separation and reattachment compression fans and shocks whereas the latter shows that the leading edge shock, compression fan and recirculation region are well resolved. Furthermore, the wall-normal pressure spatial profile at the corner reveals the presence of oscillations close to the wall when the simulation is under-resolved, i.e. $(N_x, N_y) = (901, 301)$, as seen in previous OpenFOAM simulations (Santos et al., 2019). This is also the same reason why the residue of high-order 3D4S simulations using $(N_x, N_y) = (845, 339)$ and $(1125, 451)$ does not converge in time towards machine zero, as seen in Fig. 3.42 (right).

Finally, the recirculation region size can be quantified for each Reynolds number by the distance between reattachment and separation points, where the streamwise velocity component wall-normal derivative is zero. Locating these reattachment (solid diamond) and separation (solid circle) points for all

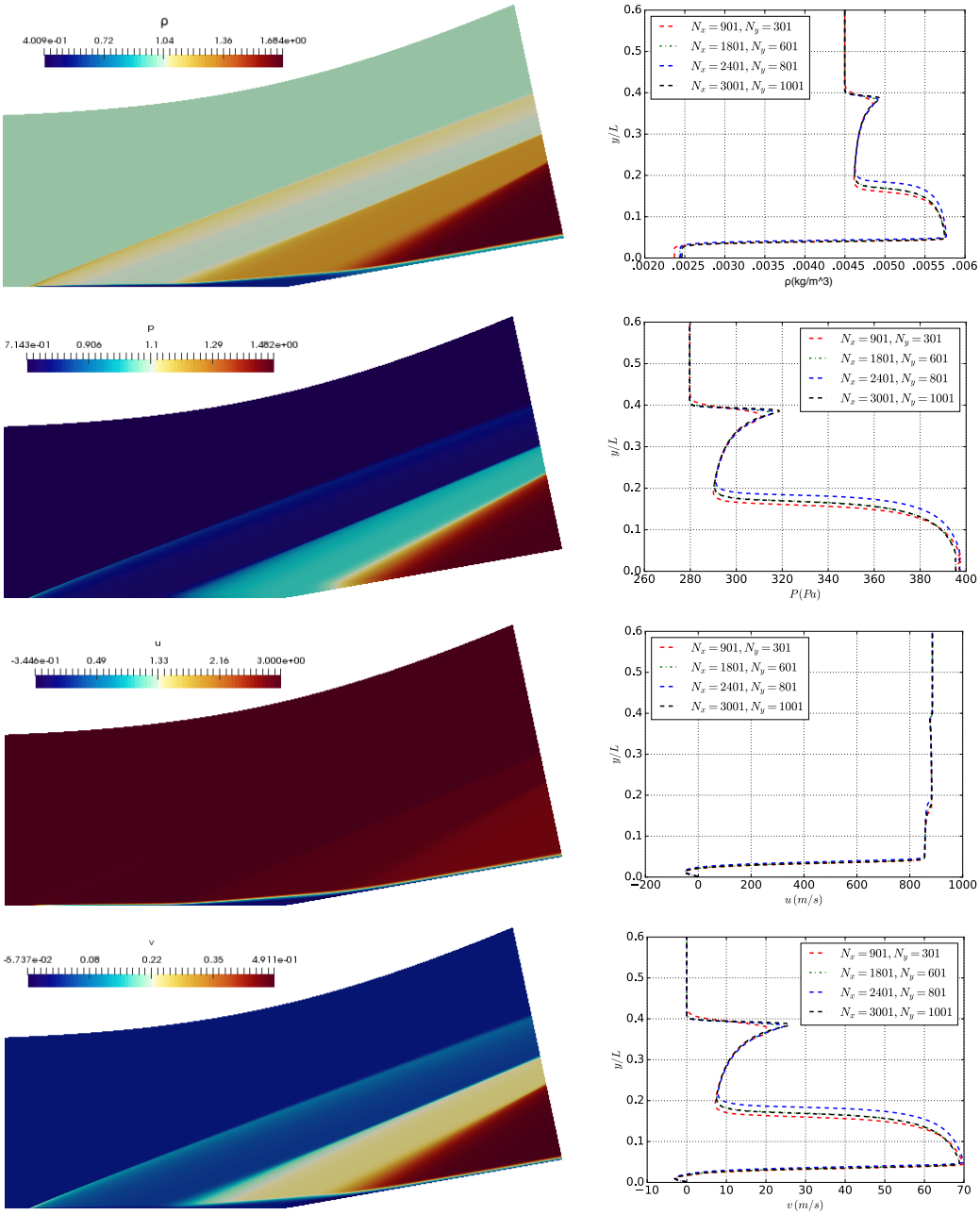

Figure 3.45: Dimensionless isocontours (left) and dimensional wall-normal profiles at the corner (right) for density (first row), pressure (second row), streamwise (third row) and vertical (last row) velocity components from $Re_\infty = 200 \times 10^3$ high-order 3D4S simulations. Isocontours obtained with $(N_x, N_y) = (3001, 1001)$ whereas profiles obtained with different grids.

Reynolds numbers simulated with high-order 3D4S, fitting one curve $f_r(Re_\infty)$ through the reattachment points (blue dash-dot line), and another curve $f_s(Re_\infty)$ through the separation points (red dashed line), using

$$f(Re_\infty) = \sum_{n=0}^{N} a_n\, Re^n + \sum_{m=1}^{M} b_m / Re^m \quad , \tag{3.19}$$

where the incipient separation Reynolds number is defined by equation

$$f_r(Re_{is}) = f_s(Re_{is}) \quad , \tag{3.20}$$

which yields $(N, Re_{is}) = (4, 6870)$, $(3, 6177)$ and $(2, 6451)$ with $M = 1$. It represents the Reynolds number beyond which the recirculation region first appears. All these points and curves are shown in Fig. 3.46 as $x^* - x_c$, i.e. these locations x^* are written relative to the corner location x_c.

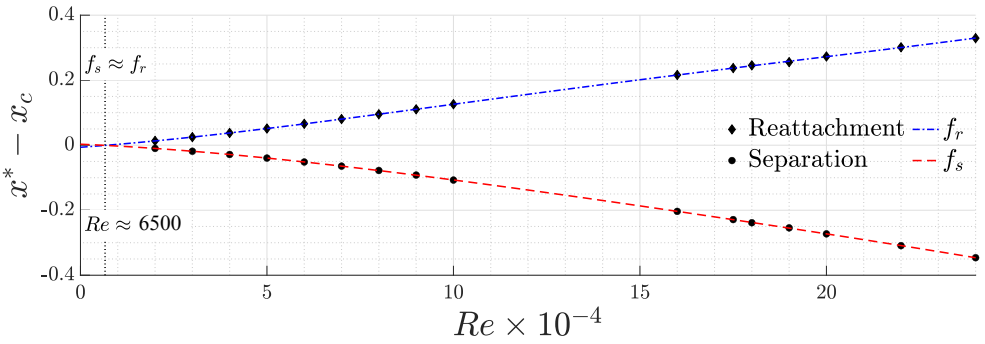

Figure 3.46: Separation and reattachment locations over a range of free stream Reynolds numbers predicting incipient separation at $Re_{is} \approx 6500$, on average. Prepared by Cerulus (2022).

Tripple-Deck Theory

Another important step taken in this study was to compare the accurate and disturbance free steady-states generated by 3D4S with the approximate solutions generated by triple-deck theory. Doing so has two main advantages, namely co-verify both approaches and extrapolate simulation trends beyond the limits of the available data. These approximate solutions were obtained by Cerulus (2022) during his doctorate advised by Vassilios Theofilis at UoL, which was an important part of the collaborative work between UoL and UFF research groups for this project.

The triple deck, as it name suggests, is a theory that separates the flow around a region of self induced separation into three so called "decks", as displayed in Fig. 3.47. The main deck consists of the incoming upstream boundary-layer, which is characterized by an inviscid and rotational flow. Its interaction with the lower deck leads to the vertical displacement of the incoming streamlines. The upper deck, however, consists of the inviscid and irrotational flow outside of the boundary-layer. Its interaction with the main deck leads to the Prandtl-Glauert equations. On the other hand, the lower deck consists of the boundary-layer along the physical wall. It is viscous and incompressible on account of the extremely small wall-normal extent of this region. Under the appropriate scaling, it yields the typical incompressible boundary-layer equations, except with appropriately modified boundary conditions at the top. These upper boundary conditions usually

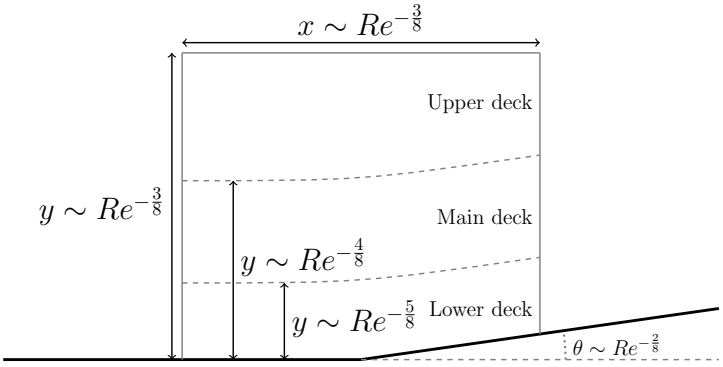

Figure 3.47: Sketch of the triple deck structure on a compression ramp.

come from the inviscid and irrotational external flow in typical boundary-layer problems. However, under the triple deck structure, they are obtained from the inviscid and rotational flow at its interface with the main deck. The interface between main and upper decks are also matched, allowing the streamline displacement from the lower deck to be transmitted into the upper one, while pressure perturbations transmitted in the other direction. Stewartson and Williams (1969) defined the asymptotic equations in the main and upper decks, which could be solved simply and analytically. The fact that the resulting pressure and flow angle in the main deck are independent of the wall-normal coordinate in which they are calculated implies that their values at the bottom of the upper deck can be imposed at the bottom of the main deck as boundary conditions for the lower deck. This approach has been used by Cassel et al. (1995) to calculate compressible flows over compression corners. It is reproduced here, and briefly explained below.

First, the coordinate vector, velocity vector, pressure, density, enthalpy and viscosity are written in the dimensionless form

$$\mathbf{x}' = \frac{\mathbf{x}^*}{L} \quad , \quad \mathbf{v}' = \frac{\mathbf{v}^*}{U_\infty} \quad , \quad p' = \frac{p^*}{\rho_\infty U_\infty^2} \quad , \quad \rho' = \frac{\rho}{\rho_\infty} \quad ,$$
$$h' = \frac{h^*}{h_0} \quad \text{and} \quad \mu' = \frac{\mu^*}{\mu_0} \quad , \tag{3.21}$$

instead of Eqs. (2.15) and (2.20), where $\mathbf{x} = (x, y)^T$,$\mathbf{v} = (u, v)^T$ and the reference viscosity μ_0 is evaluated at the reference dynamic enthalpy $h_0 = U_\infty^2$, which is convenient for high speed boundary-layers and much larger than the typical free stream static temperature. This dynamic viscosity is given by a function of temperature alone through the power law

$$\mu' = (h')^n \quad , \tag{3.22}$$

where n is a positive constant. For air at moderate temperatures, $n = 0.76$. In this case, the Reynolds number Re_0 is evaluated using the reference dynamic viscosity μ_0. The lower deck scales can therefore be defined as

$$x' - 1 \; = \; \rho_w^{-1/2} \mu_w^{-1/4} \lambda^{-5/4} \beta^{-3/4} Re_0^{-3/8} x \quad ,$$

$$
\begin{aligned}
y' &= \rho_w^{-1/2}\mu_w^{1/4}\lambda^{-3/4}\beta^{-1/4}Re_0^{-5/8}(y - f(x)) \quad , \\
u' &= \rho_w^{-1/2}\mu_w^{1/4}\lambda^{1/4}\beta^{-1/4}Re_0^{-1/8}u \quad , \\
v' &= \rho_w^{-1/2}\mu_w^{3/4}\lambda^{3/4}\beta^{1/4}Re_0^{-3/8}(v - f'(x)) \quad , \\
p' - 1 &= \mu_w^{1/2}\lambda^{1/2}\beta^{-1/2}Re_0^{-1/4}p \quad \text{and} \\
t' &= \mu_w^{-1/2}\lambda^{-3/2}\beta^{-1/2}Re_0^{-1/4}t \quad ,
\end{aligned} \tag{3.23}
$$

where, $\beta = (Ma^2 - 1)^{1/2}$, ρ_w and μ_w are the dimensional density and dynamic viscosity at the wall respectively. Finally, λ is a known constant determined by the solution of the upstream boundary-layer. For the Blasius boundary-layer, it is given by $\lambda = 0.33206$. The wall surface, defined by the wall shape function $y|_{x=0} = f(x)$ using the Prandtl transposition theorem, is Incorporated into the scales in Eq. (3.23). For a compression corner, the wall shape function with a continuous corner can be defined as

$$
f(x) = \frac{\alpha}{2}\left(x + \sqrt{x^2 + r^2}\right) \quad , \tag{3.24}
$$

where α is the ramp scaled angle and r is the corner radius. The correct scaling for the ramp angle can now be defined as

$$
\theta = \mu_w^{1/2}\lambda^{1/2}\beta^{1/2}Re_0^{-1/4}\alpha \quad , \tag{3.25}
$$

based on the x and y scales defined above. Following these scales, the lower deck equations are given by

$$
\begin{aligned}
\frac{\partial u}{\partial t} + u\frac{\partial u}{\partial x} + v\frac{\partial u}{\partial y} &= -\frac{\partial p}{\partial x} + \frac{\partial^2 u}{\partial y^2} \quad \text{and} \\
\frac{\partial u}{\partial x} + \frac{\partial v}{\partial y} &= 0 \quad ,
\end{aligned} \tag{3.26}
$$

subject to boundary conditions

$$
\begin{aligned}
u = v = 0 \quad & at \quad y = 0 \quad , \\
u \to y + A(x,t) + ... \quad & as \quad y \to \infty \quad \text{and} \\
u \to y \quad & \text{as} \quad x \to -\infty \quad ,
\end{aligned} \tag{3.27}
$$

where $A(x,t)$ is the displacement thickness of the viscous sublayer. Analyzing the upper deck yields the interaction law given by

$$
p = -\frac{\partial A}{\partial x} + \frac{\partial f}{\partial x} \quad , \tag{3.28}
$$

also known as the Ackeret formula.

This set of equations can now be solved using an appropriate method. Here, the use of second-order accurate finite-difference schemes allows the

use of the Thomas algorithm for the solution of the resulting tridiagonal system, which are described and validated by Cassel et al. (1995). The exact same procedure is also described in detail by Cerulus (2022). In order to validate the present triple deck calculations, its results are compared to the ones obtained by Cassel et al. (1995). Figure 3.48 shows this comparison for the wall shear and wall pressure at $\alpha = 1$ to 3.5 in steps of $\Delta\alpha = 0.5$. A very good agreement can be observed, confirming that the described procedure was correctly implemented.

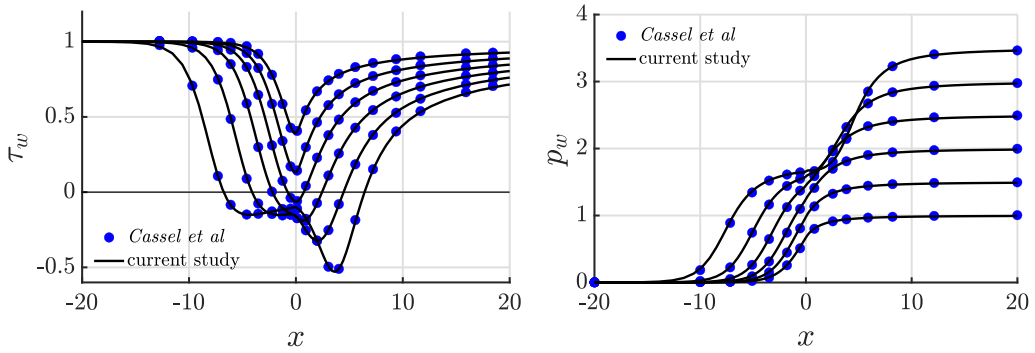

Figure 3.48: Comparison of wall shear stress (left) and wall pressure (right), between the current study and data from Cassel et al. (1995). Curves shown for $\alpha = 1$ to 3.5 in steps of $\Delta\alpha = 0.5$. Incipient separation at $\alpha \simeq 1.8$.

Now that the triple deck approximate solution from Cassel et al. (1995) has been properly reproduced, a comparison with 3D4S can be pursued. Understanding the triple deck scales and their connection to the physical variables is essential in this effort. The independent triple deck variables that must be used to match physical scenarios are the scaled ramp angle (α) and corner radius (r), both of which only affect the wall shape function $f(x)$ in Eq. (3.24). In turn, wall calculations require the wall function derivative, from which the wall shear stress is computed. Several previous studies have used this ramp angle scale to classify characteristics of flows over compression ramp. Early comparisons between experiments and triple deck solutions by Burggraf (1976) showed good agreement, despite a higher wall pressure at the ramp, with the pressure increase occurring further downstream of the plate compared to the triple deck prediction. Egorov and Shvedchenko (2011) later proposed a simplified representation of the scaled angle to classify many previous studies by their defining macro features. Grisham et al. (2018) also compared triple deck theory and second-order accurate compressible Navier-Stokes computations, showing a similar over prediction of the interaction region by the former when measuring separation locations. On the other hand, comparisons have been made for the subsonic flow past a roughness element by Mengaldo et al. (2015), showing an excellent agreement. This latter study has motivated the present pursuit to compare triple deck theory with high-order 3D4S results. If such an agreement can be found here as well, triple deck theory would provide a powerful framework for the validation of high-order DNS methods for high-speed flows.

On one hand, the corner radius impact on separation can be observed in the incipient separation predictions by Cassel et al. (1995) and Rizzetta et al. (1978). The former used the same wall shape function shown in Eq. (3.24), which imposes a finite radius, whereas the latter used a piecewise function instead, which allows the definition of a sharp corner. It turns out that such round corners predict incipient separation at $\alpha = 1.8$ whereas sharp corners do so at $\alpha = 1.57$. Hence, correctly identifying the corner radius of curvature has an impact on the comparison accuracy.

On the other hand, the scaled ramp angle impact on separation is given by Eq. (3.25). Hence, it depends on the non-dimensional wall viscosity, the Mach number, the shape of the incoming boundary-layer, the Reynolds number based on the reference viscosity and the corner angle. Most of these quantities are intrinsic to and directly known from simulations as either input or output values. However, some wall values and reference values defined by the triple deck theory will need to be calculated. For instance, the wall viscosity can be obtained from the wall enthalpy, which is either fixed through a prescribed temperature or can be calculated for adiabatic walls using

$$h_w = h_\infty + r\,\frac{U_\infty^2}{2} \quad , \tag{3.29}$$

where, for supersonic laminar flow, the recovery factor r and the free stream enthalpy h_∞ can be obtained from

$$r = \sqrt{Pr} \quad \text{and} \quad h_\infty = c_p\,T_\infty \quad , \tag{3.30}$$

and the reference viscosity has to be defined based on the reference enthalpy. This can be achieved through Eq. (3.22), i.e.

$$\frac{\mu_\infty}{\mu_0} = \left(\frac{h_\infty}{h_0}\right)^n \quad , \tag{3.31}$$

using the known free stream enthalpy and viscosity.

Once the corner radius and scaled ramp angle are known, the equivalent triple deck calculation can be run to generate the wall pressure and wall shear stress. The former can be obtained directly from Eq. (3.23). On the other hand, the latter require an additional step, which is applying Eq. (3.23) to its definition, i.e. $\tau = \partial u/\partial y$ at the wall. Furthermore, using the chain rule

$$\tau = \frac{\partial u}{\partial y} = L\,U_\infty^{-1}\,\frac{\partial u^*}{\partial y^*}\,\frac{\partial y'}{\partial y}\,\frac{\partial u}{\partial u'} = L\,U_\infty^{-1}\,\lambda^{-1}\,Re_0^{-1/2}\,\frac{\partial u^*}{\partial y^*} \quad , \tag{3.32}$$

provides a way to calculate the wall shear from the high-order 3D4S data through its dimensional velocity derivative, i.e. $\partial u^*/\partial y^*$, in comparable scales to the triple deck solution. The reverse can also be done to both wall pressure and wall shear stress by simply inverting these scaling rules and applying them to the triple deck solution at the wall instead.

Table 3.1 is populated with scaled ramp angles using the aforementioned procedure for different Reynolds numbers, which identifies the appropriate

$Re \times 10^{-3}$	50	160	175	178	180	190	200	220
$Re_0 \times 10^{-3}$	18.92	60.54	66.22	67.36	68.11	71.90	75.68	83.25
α	2.42	3.23	3.30	3.32	3.33	3.37	3.42	3.50

Table 3.1: Scaled ramp angle and reference Reynolds number at $\mu_0 = 3.76 \times 10^{-5}$ for several Reynolds numbers used by high-order 3D4S.

triple deck solutions for comparison purposes. According to the triple deck results in Fig. 3.48 and the high-order 3D4S results in Fig. 3.46, with all cases but $Re = 50k$ showing a double peak in the wall shear stress. Furthermore, Cassel et al. (1995) shows an instability in the separation bubble appearing at $\alpha \geq 3.9$, which is above the highest scaled ramp angle calculated using high-order 3D4S. Using the desired scaled ramp angles, a corner radius of $r = 0.5$ and a resolution of $(N_x, N_y) = (201, 101)$, the triple deck equations are marched in time until the shear stress temporal derivative $\partial\tau/\partial t$ falls below 5×10^{-4}. Following Cassel et al. (1995), the grid clustering values are set to $a = b = 5$ for scaled ramp angles in the range shown in Tab. 3.1.

Having calculated the triple deck solutions, wall shear stresses (left) and wall pressures (right) are compared to the respective high-order 3D4S steady-states in Fig. 3.49 for $Re \times 10^{-3} = 50$ (top), 178 (middle) and 220 (bottom). Their respective scaled ramp angles are shown in Tab. 3.1. Thermodynamic properties as well as velocity components are provided by high-order 3D4S, where the streamwise velocity wall-normal derivative is calculated with a sixth-order one-sided finite differences scheme for a nonuniform stencil. Even though there are large differences upstream of the separation point, likely due to the presence of a leading edge in the 3D4S data, and an undershooting of the wall pressure downstream of the reattachment point, the agreement becomes quite good in the separation region. There is also a slightly steeper wall shear stress decay and wall pressure growth in the high-order 3D4S steady-state as the separation point is approached for all Reynolds numbers. Otherwise, separation and reattachment trends between both solutions match quite well. Furthermore, this agreement improves as the Reynolds number increases, which is expected given the asymptotic nature of the triple deck solution with respect to a negative power of the Reynolds number, as shown in Eq. (3.23). This explains why the triple deck solution cannot capture the 3D4S double peak in the wall shear stress at $Re = 50 \times 10^3$, which is also observed at higher Reynolds numbers. It is important to note that the agreement shown here is comparable to the one observed by Mengaldo et al. (2015) in the subsonic regime. Furthermore, the Reynolds number in the high-order 3D4S simulations is increased by increasing the flat plate length, which impacts the accuracy of the present comparisons as well. Nevertheless, the agreement observed in the present comparison is significantly better than the one observed with the second-order accurate simulations performed by Grisham et al. (2018). This highlights once again the importance of using high-order DNS to obtain accurate and disturbance free steady-states. These results provide even more confidence on the quality of the high-order 3D4S

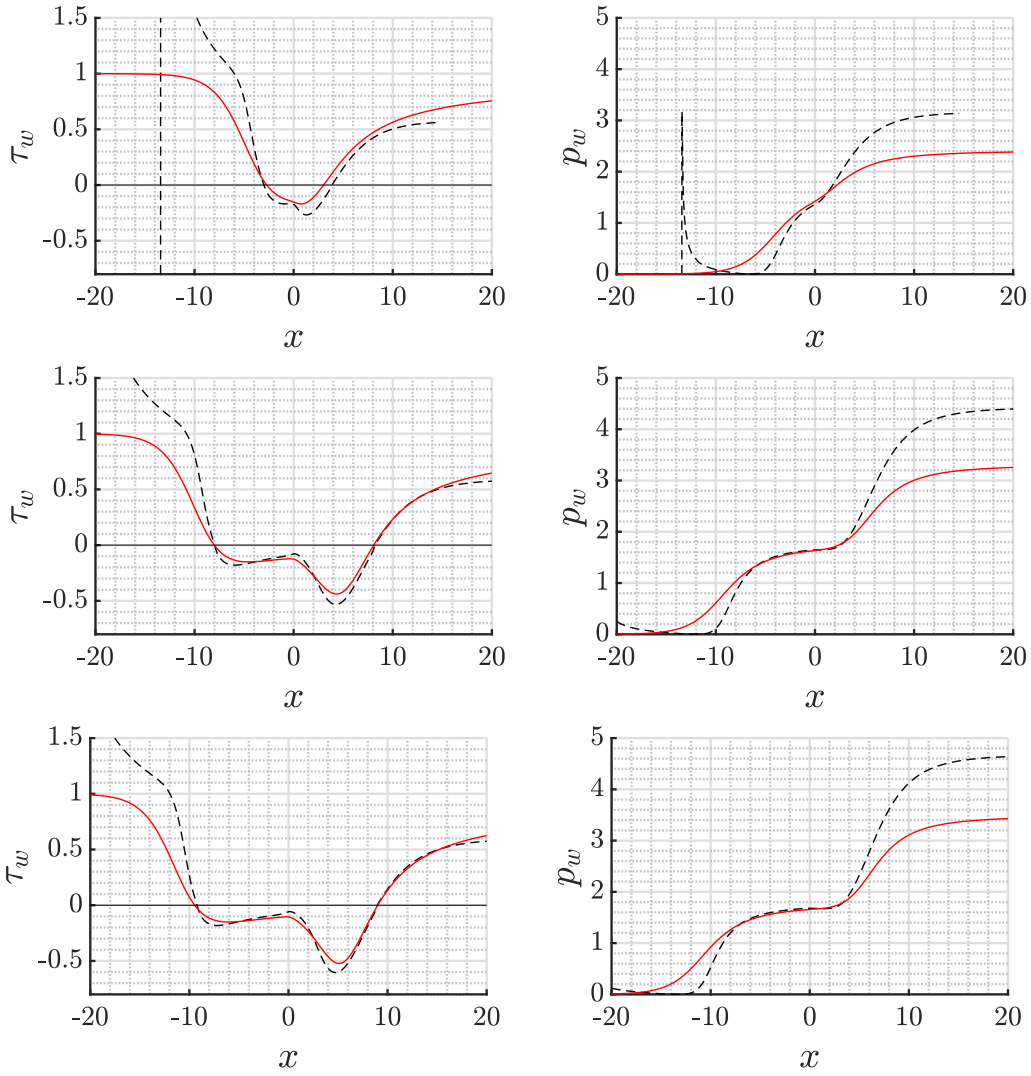

Figure 3.49: Triple deck (solid red) and high-order 3D4S (dashed black) steady-states for wall shear stress (left) and wall pressure (right) for $(Re \times 10^{-3}, \alpha) = (50, 2.42)$ (top), $(178, 3.32)$ (middle) and $(220, 3.50)$ (bottom).

steady-states obtained in this report.

3.4.2 Linear and Global Instabilities

Modal and non-modal stability analyses reported here were performed by Cerulus (2022), using the LiGHT code developed by Quintanilha Jr et al. (2022). Both graduate students obtained their doctorate degrees from UoL during their period at the research group led by prof. Vassilis Theofilis. They collaborated extensively with the UFF research group led by prof. Leo Alves on this part of the project as well. The application of the residual algorithm to high-order 3D4S results was done by Santos (2020).

The forthcoming discussion places a lot of focus on lines composed of generalized inflection points (GIP) in order to guide the data analysis of

such a complex flow. These points satisfy a simple equation given by

$$\frac{\partial}{\partial y}\left(\rho\frac{\partial u}{\partial y}\right) = 0 \quad , \tag{3.33}$$

according to Lees and Lin (1946) and Lees (1947). Doing so is motivated by the recompression shock splitting into separation and reattachment shocks when $Re_\infty > Re_{is}$, which increases the number of such lines. The three major GIP lines that are present in the high-order 3D4S steady-state at $Re_\infty = 220 \times 10^3$ are shown in Fig. 3.50, which also presents isocontours of density gradient magnitude $\sqrt{(\partial\rho/\partial x)^2 + (\partial\rho/\partial y)^2}$. They are related to the shear layer (GIP_1), reattachment (GIP_2) and separation (GIP_3) shocks.

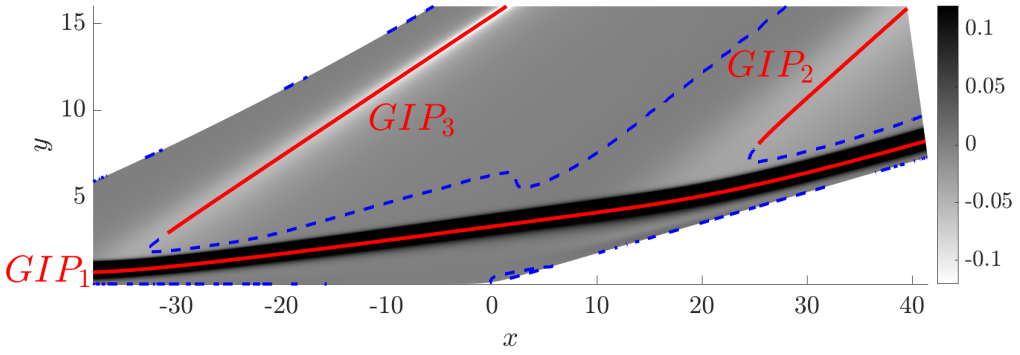

Figure 3.50: Isocontours of density gradient magnitude around the corner region of the $Re_\infty = 220 \times 10^3$ high-order 3D4S steady-state, including also the generalized inflection point lines associated with the shear layer (GIP_1), reattachment shock (GIP_2) and separation shock (GIP_3).

Due to memory constraints, the domain size employed by the LiGHT code is smaller than the one used by high-order 3D4S to minimize the grid sizes required for convergence. This must be done carefully, since the separation region increases as the Reynolds number increases. The same grid generation procedure, illustrated in Fig. 3.37, is employed here as well. However, some parameters are modified to achieve the desired domain reduction for each free stream Reynolds number (Cerulus, 2022). The only other major difference between steady-state and stability domains is that the horizontal axis origin is shifted to the corner to be consistent with Fig. 3.46. Once the domain has been specified, the boundary conditions can be imposed. All disturbances are prescribed to zero at the inlet and far-field, but they are extrapolated at the outlet. Furthermore, all three disturbance velocity components as well as the disturbance pressure and disturbance temperature wall-normal derivatives are prescribed to zero at the body.

Finally, in order to achieve a more consistent comparison between the spectra for different Reynolds numbers, a physically relevant dimensionless frequency is employed instead. It is defined here as

$$St = \frac{f\,\delta^*}{U_\infty} \quad , \tag{3.34}$$

which is also known as Strouhal number, where the disturbance oscillation frequency is $f = \omega_r/(2\pi)$, the angular frequency obtained from the real part of the eigenvalues is ω_r, the free stream velocity is U_∞ and the displacement thickness at the inlet of the stability domain for $Re_\infty = 200 \times 10^3$ is $\delta^* = 0.00933\,m$. It is important to note that this same characteristic length δ^* is employed to write the dimensionless spanwise wavenumber β for the three-dimensional ($\beta \neq 0$) stability analysis.

Verification

Before pursing a detailed modal and non-modal stability analysis, a co-verification process is pursued by comparing modal results from the LiGHT code and the time asymptotic results from the residuals algorithm applied to high-order 3D4S, as discussed in the context of Eq. (3.6). Although both approaches provide a BiGlobal stability analysis, a local spatial analysis is also pursued to connect these results with fundamental phenomena.

First, the residuals algorithm is applied to the high-order 3D4S unsteady simulations near the end of their time asymptotic convergence to machine zero in order to extract the least damped two-dimensional linear and global mode $\mathbf{Q}_n(x, y)$. Figures 3.51 and 3.52 show it at $Re_\infty \times 10^{-3} = 50$ and 200, respectively, for density (top left), temperature (top right), streamwise (bottom left) and vertical (bottom right) velocity component isocontours. The former shows a weak reattachment shock that strongly interacts with the separation shock near the corner region whereas the latter shows a much stronger reattachment shocks does not interact with the separation shock in the same region. Nevertheless, both figures show that the least damped mode eigenfunctions has important spatial structures along all three GPI lines

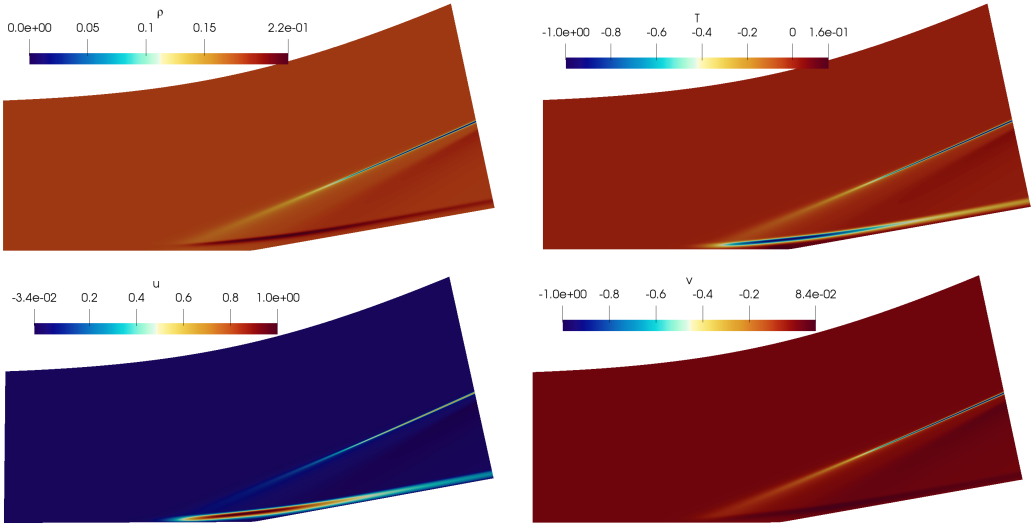

Figure 3.51: High-order 3D4S least damped mode eigenfunction isocontours for density (top left), temperature (top right), streamwise (bottom left) and vertical (bottom right) velocity components with $Re_\infty = 50 \times 10^3$.

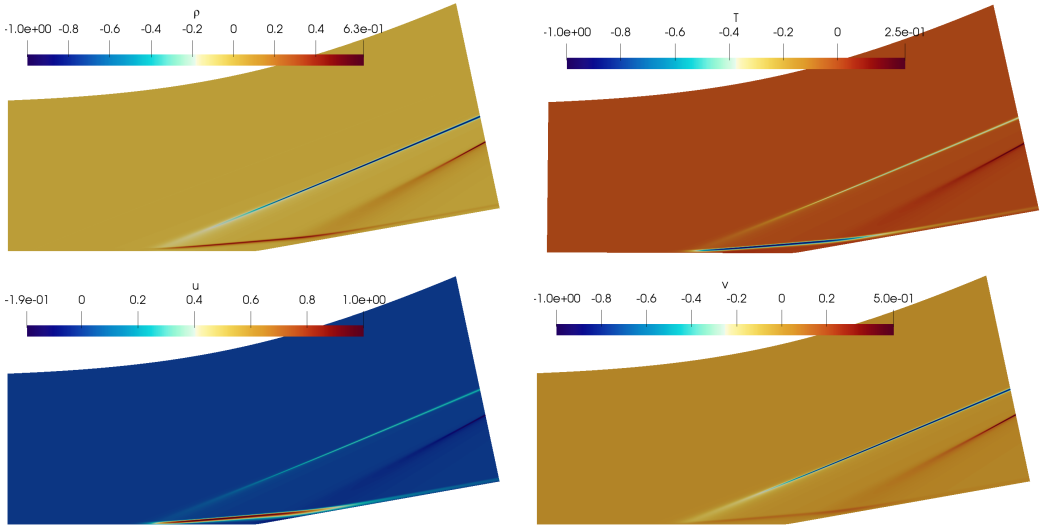

Figure 3.52: Same as Fig. 3.51 but for $Re_\infty = 200 \times 10^3$.

shown in Fig. 3.50. The one near the recirculation region, more specifically along the shear layer, has the largest amplitude. All disturbance structures observed in the literature for this problem are within this region (Chuvakhov et al., 2017; Sidharth et al., 2018; Hao et al., 2021; Cao et al., 2021). In the present results, however, there are additional structures emanating from both separation and reattachment regions. They start at both compression fans and continue throughout their respective shocks, becoming stronger along the way. It is important to emphasize again that this distinct disturbance feature has not been observed in these earlier studies. Finally, the residuals algorithm also provides information about the complex frequency ω of this two-dimensional least damped global mode. It turns out that this mode is stationary, i.e. $\omega_r = 0$. Furthermore, its free stream Reynolds number

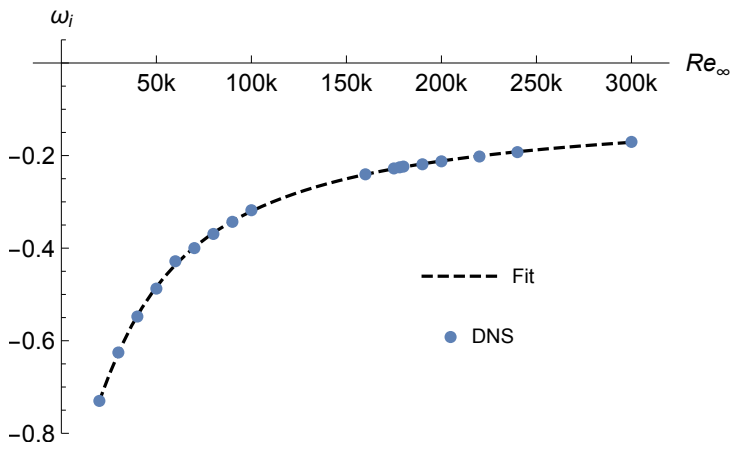

Figure 3.53: Growth rates of the two-dimensional least damped mode as a function of the free stream Reynolds number, obtained by applying the residuals algorithm to high-order 3D4S unsteady data.

dependent decay rates, or negative growth rates ω_i (blue points), are shown in Fig. 3.53. Linear regression based on a third degree polynomial is applied to this data in log form to produce the fitting function shown in this figure (black dashed line). Taking the limit of this fitting function as $Re_\infty \rightarrow \infty$ yields $\omega_i \rightarrow 0$, suggesting two important things about two-dimensional modes: *i*) they are always globally stable in a linear sense, but *ii*) they do become less stable as the Reynolds number increases.

Similar results are obtained when using the LiGHT code with high-order

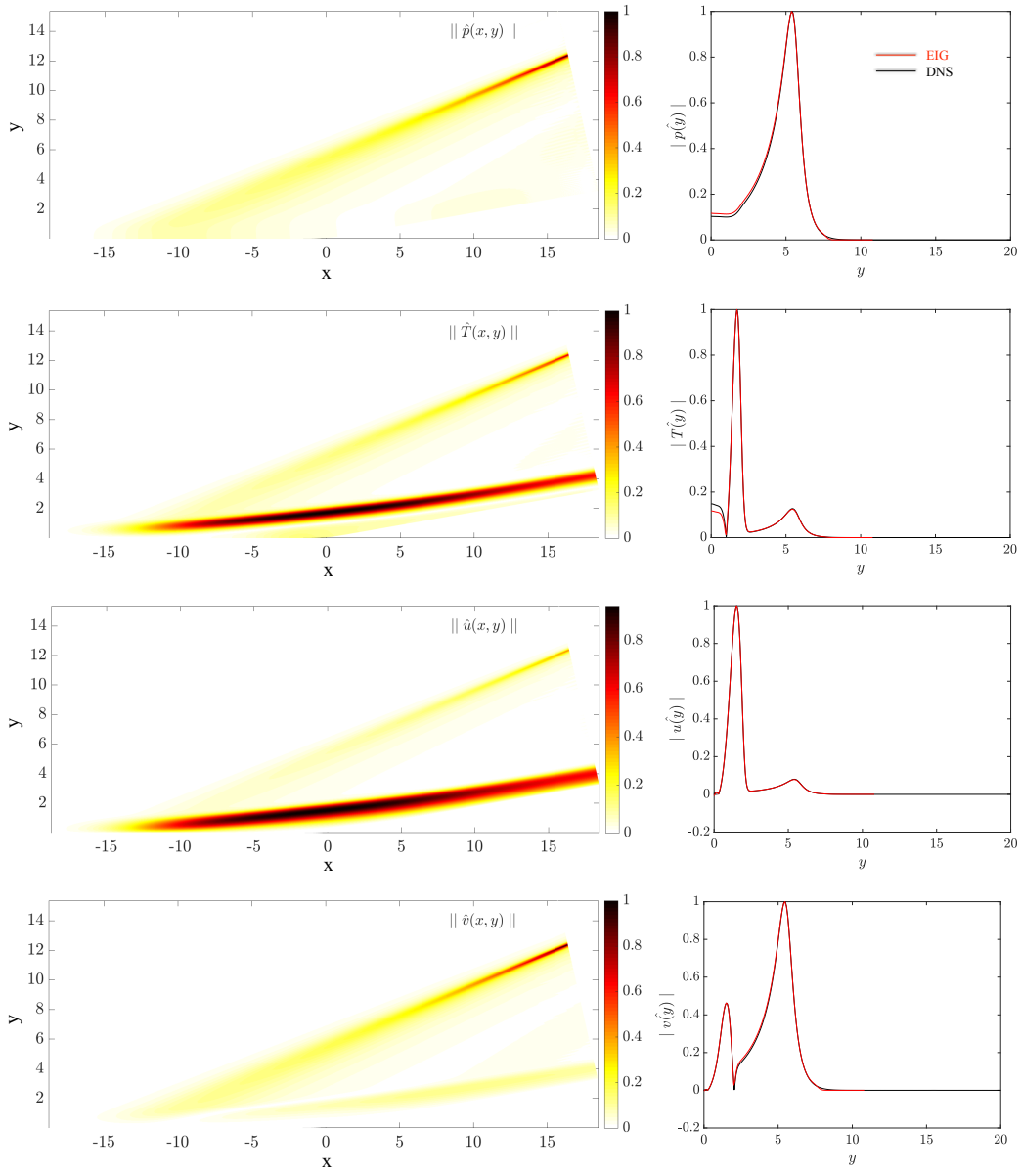

Figure 3.54: LiGHT code least damped mode eigenfunction absolute value isocontours (left) and wall-normal profiles at the corner (right) for pressure (first row), temperature (second row), streamwise (third row) and vertical (last row) velocity components with $Re_\infty = 50 \times 10^3$.

3D4S steady-states by imposing a vanishingly small spanwise wavenumber, i.e. $\beta \to 0$. In order to illustrate this point, the results obtained with $Re_\infty = 50 \times 10^3$, $\beta = 10^{-5}$, $m_{kryl} = 401$ subspaces and a grid resolution of $(N_x, N_y) = (201, 145)$ are presented in Fig. 3.54. This figure (left) shows linear and global two-dimensional eigenfunction absolute value isocontours for pressure (first row), temperature (second row), streamwise (third row) and vertical (last row) velocity components. It is possible to observe once again that these eigenfunctions have dominant structures in two of the three GIP lines discussed earlier, namely along the shear layer as well as the separation compression fan and shock. Only the very beginnings of the structure along the third GIP line, associated with the reattachment region, can be observed due to the reduced domain size used in this stability analysis. This figure (right) also shows a comparison between the wall-normal profiles at the corner obtained by both approaches, i.e. the residuals algorithm applied to unsteady 3D4S data (DNS) and the LiGHT code using high-order 3D4S steady-states (EIG). An excellent agreement can be observed overall, with only minor differences near the wall for the pressure and temperature disturbances. A final analysis is now presented to further co-verify both approaches, based on the spectra associated with Fig. 3.54. It (black points) is shown in Fig. 3.55, which also includes the decay rate of the least damped mode obtained from the residuals algorithm (red point). These decay rates are given by $\omega_i^{(EIG)} = -0.00397$ and $\omega_i^{(DNS)} = -0.00436$, which represents a relative deviation of less than 9%. The agreements observed so far provide confidence on the use of these tools to further investigate this flow field.

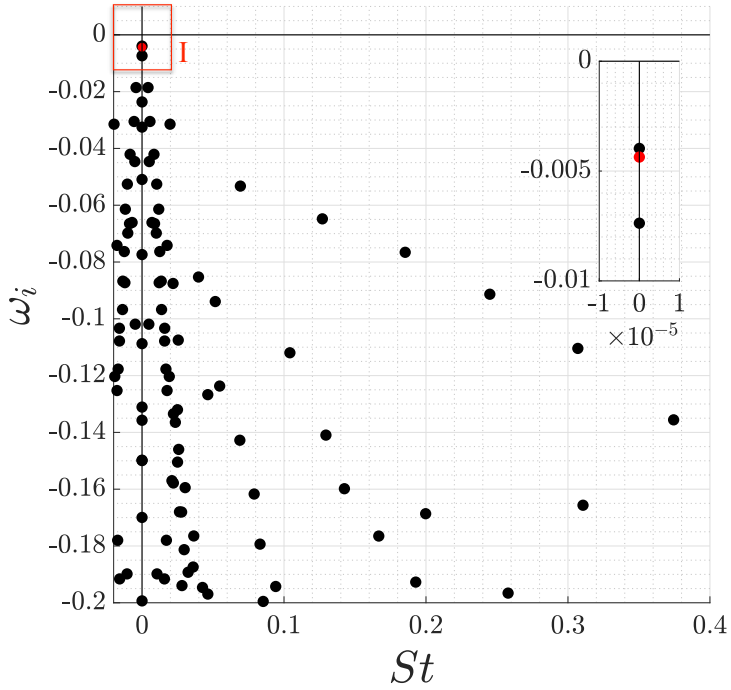

Figure 3.55: Spectra (black points) associated with Fig. 3.54, including the least damped mode decay rate from the residuals algorithm (red point).

Modal Analysis

Having verified the tools developed for the study of the compression ramp stability, the next step is to further investigate region I in Fig. 3.55 to find out what happens to the least damped two-dimensional ($\beta = 0$) mode verified in the previous subsection as it becomes three-dimensional ($\beta > 0$). Before doing so, it is important to make sure that these solutions obtained from the LiGHT code are indeed grid converged for larger Reynolds numbers and spanwise wavenumbers. In order to do so, temporal growth rates are obtained for $Re_\infty = 220 \times 10^3$ and $\beta = 3.0$ employing $(N_x, N_y) = (121, 81)$, $(141, 101)$, $(161, 121)$, $(181, 141)$ and $(191, 151)$. The values (relative errors) found are ω_i ($|\Delta\omega_i/\omega_i|\,\%$) = 6.62249 (0.21056), 6.63411 (0.03554), 6.63638 (0.00134 %), 6.63646 (0.00009 %) and 6.63649 (0 %), respectively. Hence, the grid sizes used in this verification are indeed large enough for the analysis to follow.

This convergence study indicates that three-dimensional stationary modes do become linear and globally unstable. It is then necessary to uncover under which parametric conditions this first occurs. Figure 3.56 shows the temporal growth rate ω_i of these stationary modes ($\omega_r = 0$) for $160 \leqslant Re_\infty \times 10^{-3} \leqslant 220$ and $0 \leqslant \beta \leqslant 0.6$. Empty circles represent the data points calculated whereas their respective curves represent interpolation functions. Furthermore, the maximum temporal growth rate $\omega_{i,peak}$ and the spanwise wavenumber where

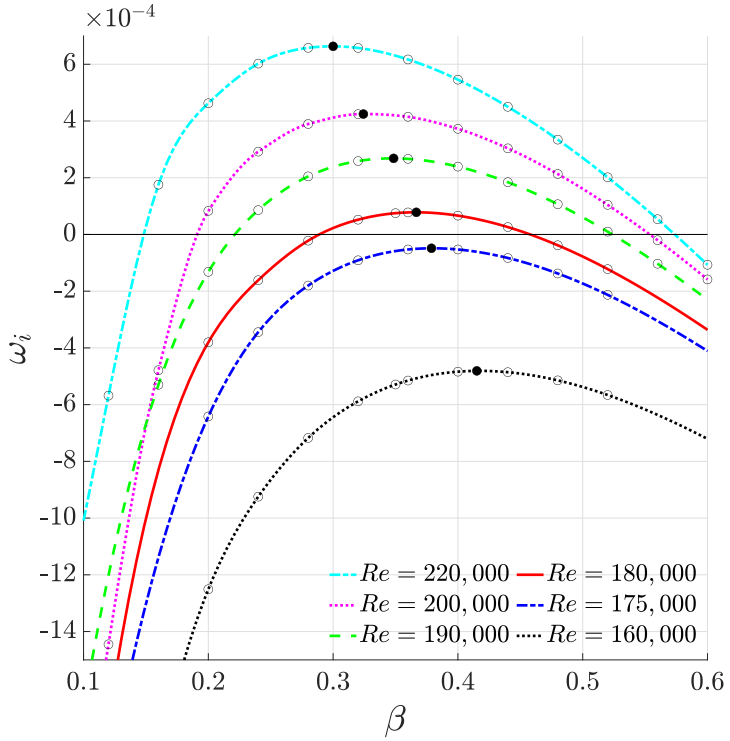

Figure 3.56: Three-dimensional stationary disturbance temporal growth rate (empty circles) for different free stream Reynolds numbers, including the maximum temporal growth rate (filled black circles) in each curve.

it occurs β_{peak} are also shown (filled black circles) for each constant free stream Reynolds number curve. This figure shows that the critical free stream Reynolds number is within $175 < Re_{\infty,c} \times 10^{-3} < 180$. It is also possible to observe the existence of a finite range of unstable wavenumbers when $Re_\infty > Re_{\infty,c}$, namely $\beta_{lower} \leqslant \beta \leqslant \beta_{upper}$. The limits β_{lower} and β_{upper} represent the lower and upper branches of the marginal stability curve, also known as neutral curve, which is defined as the curve $\beta(Re_\infty)$ where $\omega_i = 0$. Nevertheless, these relevant variables are provided in Tab. 3.2 for many free stream Reynolds numbers. It includes data for $Re_\infty = 178 \times 10^3$, not shown in Fig. 3.56 for the sake of clarity, indicating that the critical free stream Reynolds number is actually within $175 < Re_{\infty,c} \times 10^{-3} < 178$. The marginal stability (dashed line) and maximum temporal growth rate (dash dotted line) curves are constructed using this data and shown in Fig. 3.57. The critical point in this figure (filled red circle) was interpolated to $Re_{\infty,c} \simeq 177 \times 10^3$ and $\beta_c \simeq 0.375$. Furthermore, the maximum temporal growth rate of this linear and global three-dimensional disturbance is located at

$$\beta_{peak} \approx -0.001927\, Re_\infty + 0.7166 \quad , \tag{3.35}$$

which is obtained using linear regression with a $r.m.s.$ error of 0.0052. The equivalent wavelength of this disturbance is

$$\lambda_{z,peak} \approx 0.0992\, Re_\infty - 0.7504 \quad , \tag{3.36}$$

since $\lambda_z = 2\pi/\beta$. In other words, the linear and global stability analysis suggests that a three-dimensional steady-state with $\lambda_{z,peak}$ might develop when $Re_\infty \geq Re_{\infty,c}$. Furthermore, generalizing this result using the scaled ramp angle from triple deck theory defined in Eq. (3.25) indicates that a transition to instability occurs when $\alpha_c \approx 3.31$.

The most amplified disturbance has a very similar spatial structure over the entire range of free stream Reynolds numbers investigated here. The real (left) and imaginary (right) parts of its eigenfunctions obtained from the LiGHT code at $Re_\infty = 220 \times 10^3$ and $\beta = 0.28$ are presented in Fig. 3.58,

$Re_\infty \times 10^{-3}$	β_{lower}	β_{peak}	$\omega_{i,peak} \times 10^4$	β_{upper}
160	-	0.4125	−0.4810	-
175	-	0.3788	−0.4877	-
178	0.3279	0.3727	0.2359	0.4217
180	0.2889	0.3667	0.7806	0.4579
190	0.2215	0.3485	2.6826	0.5237
200	0.1910	0.3242	4.2448	0.5538
220	0.1369	0.3000	6.6330	0.5738

Table 3.2: Lower (β_{lower}) and upper (β_{upper}) marginal stability spanwise wavenumber branches as well as maximum temporal growth rate ($\omega_{i,peak}$) and its respective spanwise wavenumber (β_{peak}) for several free stream Reynolds numbers, such as the ones shown in Fig. 3.56.

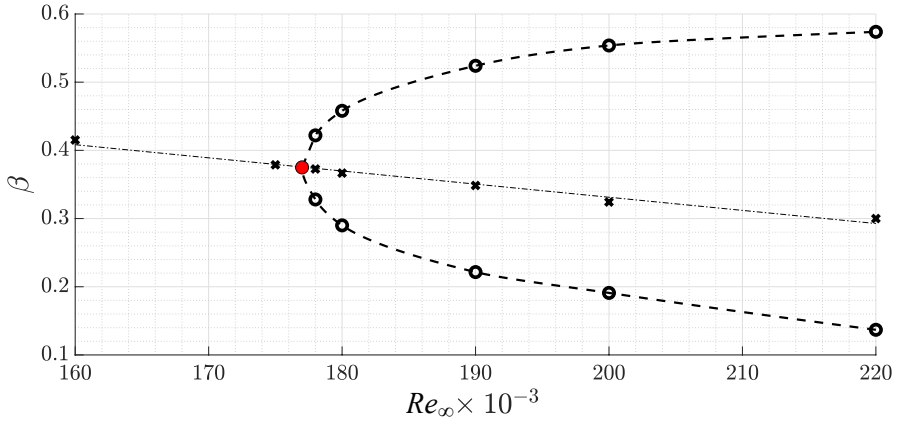

Figure 3.57: Maximum temporal growth rate (dash dotted line) and marginal stability curve (dashed line) using data (symbols) from Fig. 3.56 and Tab. 3.2. Filled red circle represents the critical point $(Re_{\infty,c}, \beta_c) \simeq (177 \times 10^3, 0.375)$.

which shows pressure (first row), temperature (second row), streamwise (third row), vertical (fourth row) and spanwise (last row) velocity components. They are stationary and have a temporal growth rate of $\omega_i = 0.000658$. Its structure is mostly concentrated in the recirculation region, specially along the shear layer, for all variables. This region is depicted by the solid line in this figure ($u = 0$), and the GIP lines play a significant role once again. However, it also appears over this region from separation to reattachment points for the pressure and vertical velocity component. On the other hand, both temperature and streamwise velocity component have structures outside of the recirculation region but only near the reattachment point. Hence, only the spanwise velocity component has its structure entirely concentrated within the recirculation region. It has two distinct peaks, one over the plat and another over the ramp. The structure of this mode is analogous in shape to the unstable stationary mode shown by Sidharth et al. (2018), although it was on a slender double wedge geometry. They also see over lapping peaks either side of the corner for the spanwise velocity component as well as a larger peak in the reattachment shock and a smaller peak in the separation region for the vertical velocity component. It is important to note that the current study shows an unstable mode appearing at a Reynolds number more than three times smaller and a smaller Mach number as well, although the ramp angle is slightly larger. Finally, the spanwise velocity component shown here is in qualitative agreement with the one presented by Hao et al. (2021) for similarly small wavenumbers, where a single unstable stationary mode is observed. They found unstable oscillatory modes for higher wavenumbers as well, which are not present in the current study. However, they considered instead isothermal walls at higher ramp angles as well as Reynolds and Mach numbers. Nevertheless, the onset of instability found in the present study occurs through stationary three-dimensional modes. This suggests that the two-dimensional steady-state will transition to a three-dimensional steady-state. Hence, a secondary stability analysis of the latter should be pursued

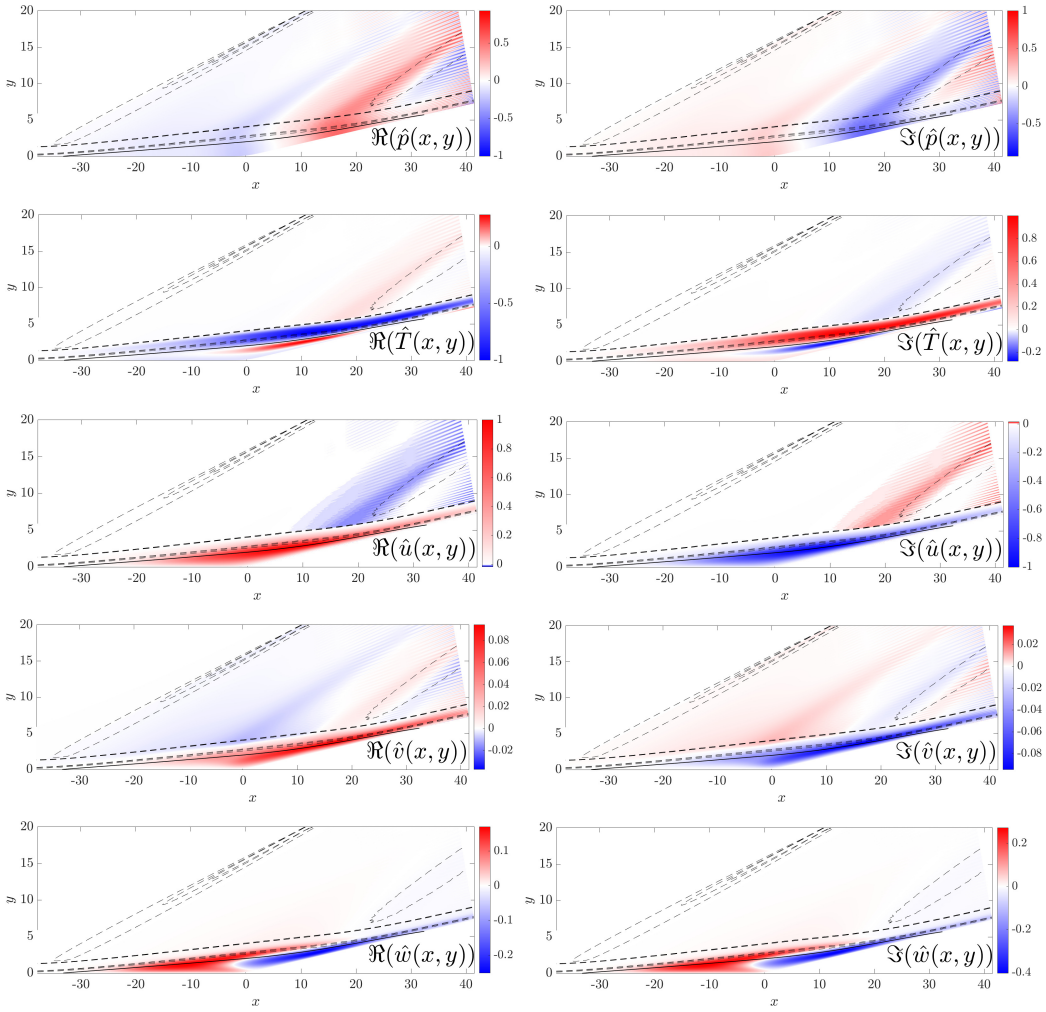

Figure 3.58: Real (left) and imaginary (right) parts of the most amplified disturbance with $(\omega_r, \omega_i) = (0, 0.000658)$ at $Re_\infty = 220\times10^3$ and $\beta = 0.28$ for the pressure (first row), temperature (second row), streamwise (third row), vertical (fourth row) and spanwise (last row) velocity components. Solid line depict the recirculation bubble ($u = 0$) whereas dashed lines are GIP lines.

instead of a higher Reynolds number analysis of the former.

Since these earlier studies indicate that oscillatory modes do eventually become linearly and globally unstable at higher Reynolds numbers, it is worth trying to better understand their behavior near marginal stability conditions. Figure 3.59 presents the spectra within $0.015 \leqslant St \leqslant 0.05$ for $Re_\infty = 220 \times 10^3$, which shows groups of stable coherently organized discrete oscillatory modes in what is called here region II. The least damped mode is located in region II:a, having a temporal growth rate of $\omega_i = -0.0394243$, a Strouhal number of $St = 0.025$ and a spanwise wavenumber of $\beta \simeq 0.75$. All modes in the other regions, namely II:b to II:d, have an increasingly higher damping rate and oscillation frequency. The structure of this least damped mode is presented in Fig. 3.60, which shows pressure (first row),

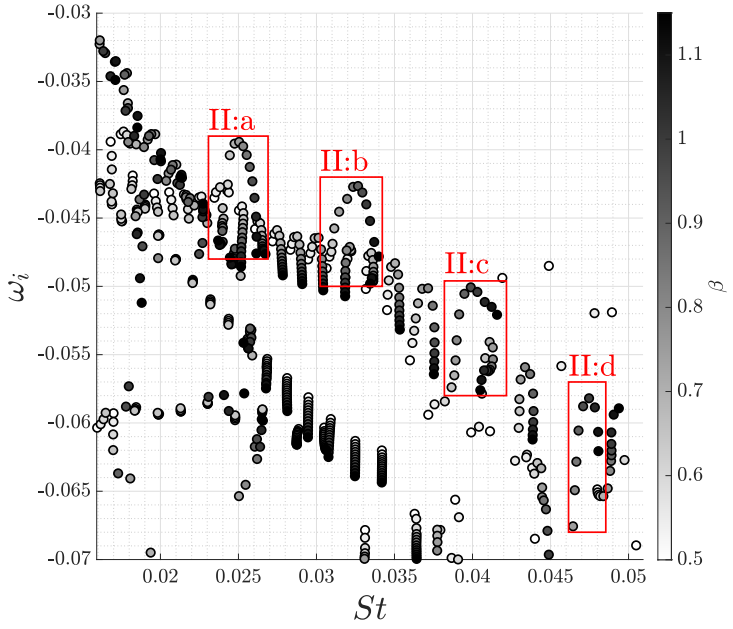

Figure 3.59: Spectra at $Re_\infty = 220 \times 10^3$ for $0.50 \leqslant \beta \leqslant 1.15$.

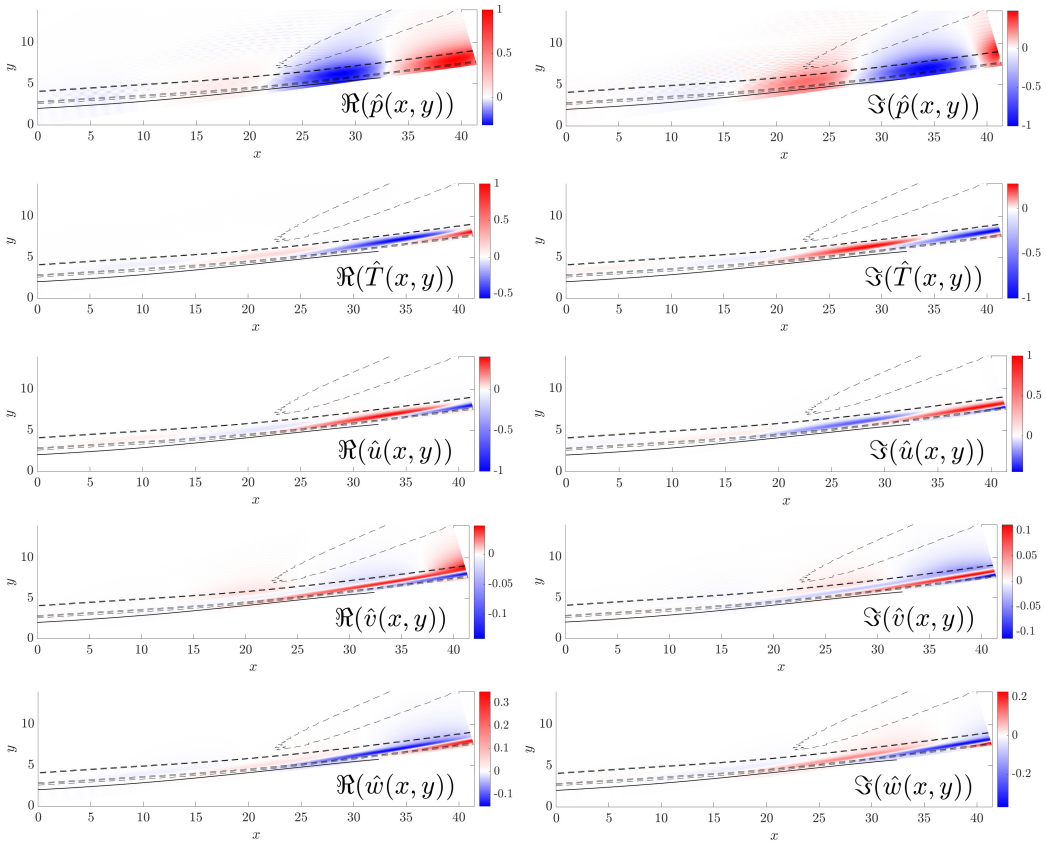

Figure 3.60: Same as Fig. 3.58, but for $(St, \omega_i) = (0.025, -0.0394243)$ at $Re_\infty = 220 \times 10^3$ and $\beta = 0.75$.

temperature (second row), streamwise (third row), vertical (fourth row) and spanwise (last row) velocity components downstream of the corner. They have a few common features. One is the fact they are essentially outside of the recirculation region, marked by the solid line ($u = 0$). Another is the fact their amplitude increases in the streamwise direction, modulated by an oscillation controlled by an apparent positive wavenumber. Furthermore, real and imaginary parts of these disturbances are half a wavelength out of phase. They have a few major differences between them as well. One is that temperature and streamwise velocity component structures remain within the shear layer region whereas all remaining variable structures penetrate the reattachment compression fan. Another is that vertical and spanwise velocity components have a much smaller magnitude compared to the other disturbances. The linear and global disturbance behavior just described is typical of a oscillatory convective instability observed in a linear and local analysis. In order to confirm such a behavior, real (top), imaginary (bottom left) and absolute (bottom right) values of the spanwise velocity component along the line containing shear layer generalized inflection points (GIP_1) are extracted and shown in Fig. 3.61 for the least damped modes from regions II:a to II:d. Top and bottom left plots in this figure not only *i*) confirm the disturbance streamwise oscillations but also *ii*) indicate that their apparent streamwise wavenumber increases from one region to the next, i.e. as the frequency of the least damped mode increases. Despite the differences in wavenumber, there are also similarities. Bottom plots *i*) show a receptivity region that ends at separation, *ii*) leading to a region of exponential growth in space, which confirms the linear disturbance convective instability nature, and *iii*) indicate that the spatial growth rate of the least damped modes from

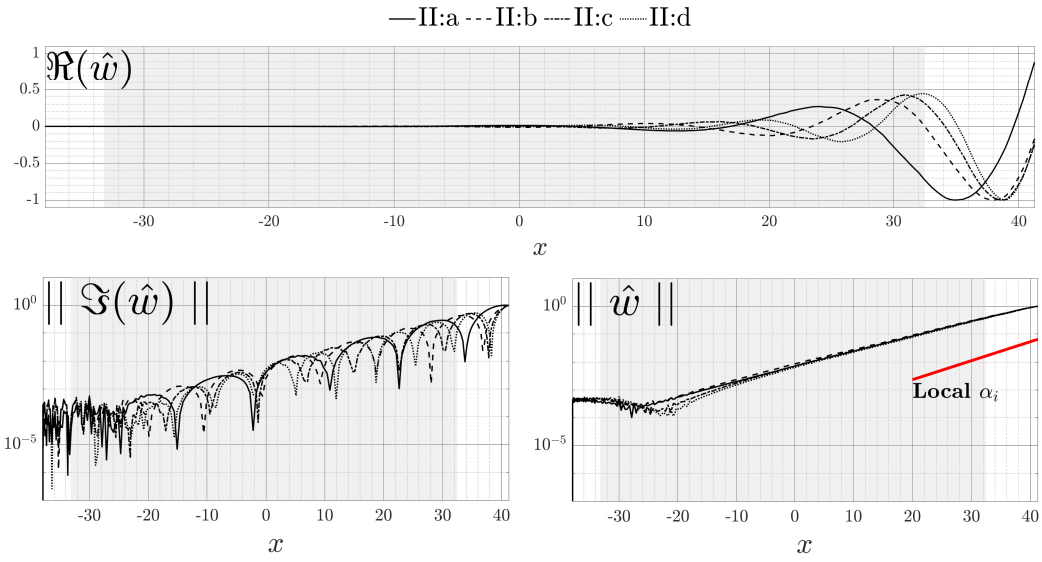

Figure 3.61: Real (top), imaginary (bottom left) and absolute (bottom right) values of the spanwise velocity component from Fig. 3.60 (last row) along the line GIP_1 shown in Fig. 3.50. Red line from a linear and local analysis.

all regions is essentially the same.

A quantitative comparison between the global and local linear analyses can also be performed through their wavelengths as well as spatial growth rates. In order to do so, their values associated with the region II:a least damped mode are first estimated from the linear and global data, yielding $\lambda_{x,BiGlobal} \approx 23.5$ and $-\alpha_{i,BiGlobal} \approx 0.01978$, respectively. Then, a linear and local analysis is performed using the wall-normal steady boundary-layer profiles at $x = 35$, which is a distance of $x_c = 35/\cos[\theta]$ from the corner along the ramp. The velocity vector is also rotated so that its components are parallel and normal to the ramp. Boundary-layer edge Mach and Reynolds numbers at this location are $Ma_e = 2.54$ and $Re_e = 108,698$, respectively. Finally, this analysis is performed at the real frequency of the linear and global mode with $\beta = 0.75$, given by $f_{II:a} = 2,372\,Hz$, yielding $\alpha_{local} = 0.2895 - 0.026\,i$. On one hand, its real part corresponds to a streamwise wavelength of $\lambda_{x,local} = 21.7$, which represents a 8.29% relative deviation from the linear and global wavelength. On the other hand, its imaginary part, also shown in Fig. 3.61 as a red line, represents a 23.9% relative derivation from the linear and global spatial growth rate. Given the approximate nature of this comparison, where the complex global frequency is assumed real in the local analysis, the agreement obtained is actually quite good. Nevertheless, this comparison between global and local linear analyses does not have to be restricted to their eigenvalues. Figure 3.62 shows the ramp wall-normal profile at $x = 35$ of the least damped II:a linear disturbance, from left to right, for pressure, temperature, streamwise, vertical and spanwise velocity components obtained from both local and global analyses. Once again, the agreement is quite good for all variables but the vertical velocity component, which is expected given the approximate nature of this comparison where the local analysis neglects this component of the steady-state.

Finally, it is also interesting to evaluate the phase speed of this localized global mode. It is given by $c_r = \omega_r/\alpha_r = 0.5894$. This value is very close

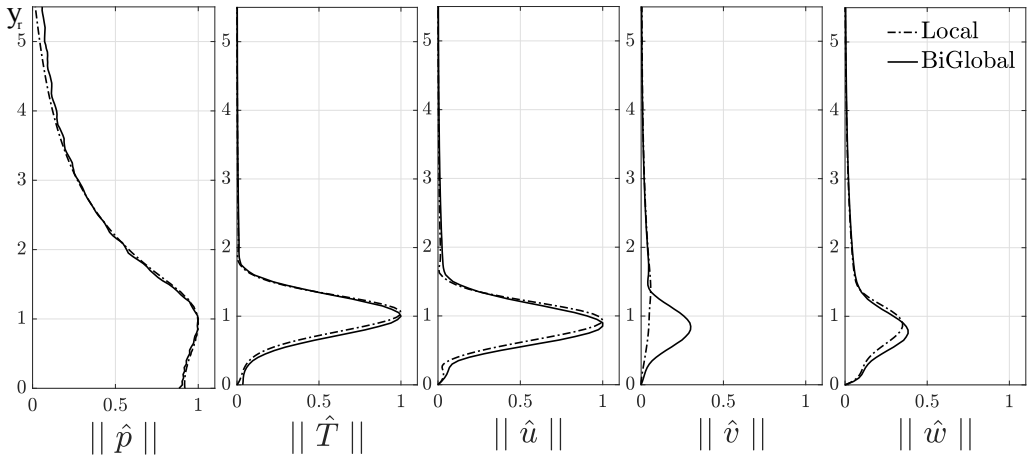

Figure 3.62: Local and global ramp wall-normal linear disturbance profiles at $x = 35$ from the least damped II:a mode.

to the slow acoustic wave speed, namely $1 - 1/Ma_e \approx 0.606$. Although theoretically this mode should not be spatially unstable but neutral, it does eventually become spatially stable at higher frequencies when $f > 6.2\,kHz$. The dependence of both spatial growth rate (red) and phase speed (blue) on frequency are shown in more detail for this mode in Fig. 3.63. Its behavior is very similar to the slow modes observed by both Fedorov and Tumin (2011) as well as Bitter and Shepherd (2015) for the compressible boundary-layer over an adiabatic flat plate.

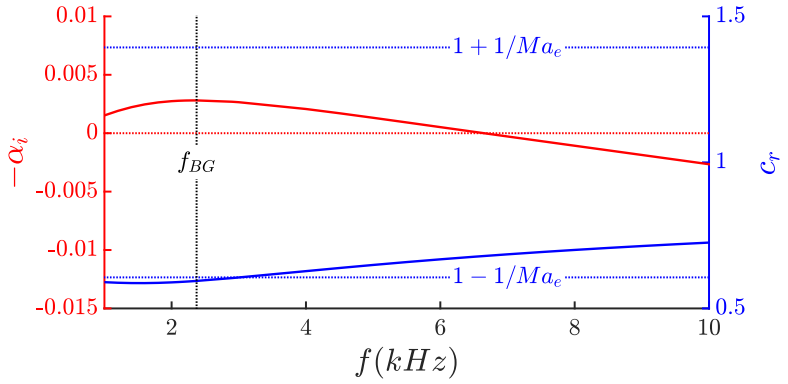

Figure 3.63: Spatial growth (red) rate and phase speed (blue) dependence on frequency associated with the local profiles from Fig. 3.62.

Other relevant groups of oscillatory modes appear at higher frequencies. They belong to what is labelled here region III. The modes in region III:b deserve mention for being locally less damped than surrounding modes with equivalent spanwise wavenumbers. All these groups are shown in Fig. 3.64, which presents the spectra within $0.1 \leqslant St \leqslant 0.16$ for the same Reynolds

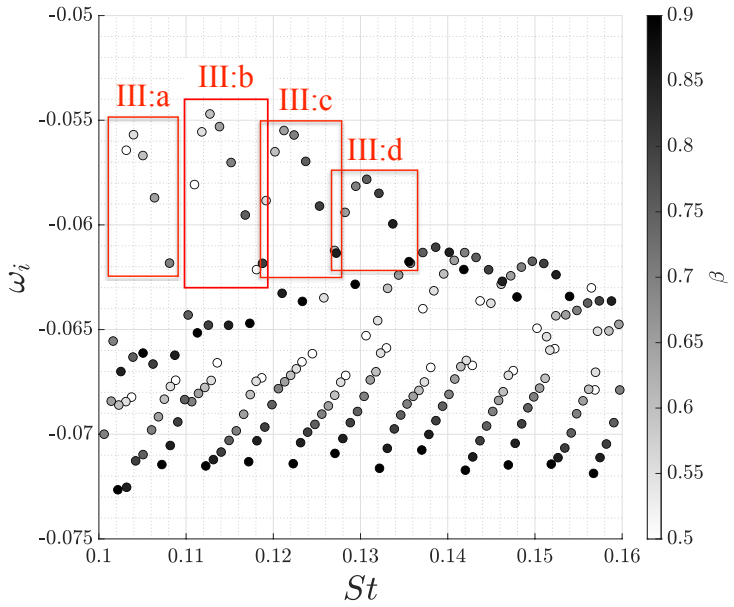

Figure 3.64: Same as Fig. 3.59, but for $0.5 \leqslant \beta \leqslant 0.9$.

number considered in Fig. 3.59. This figure shows that the least damped mode belongs to region III:b and has $\omega_r \approx 0.7$, where the next least damped mode belongs to region III:c and has $\omega_r \approx 1.2$. Focussing on the former, it has a spanwise wanumber of $\beta = 0.6$, a damping rate of $\omega_i = -0.0547$ and a Strouhal number of $St = 0.1127$. It is important to note that, although the least damped modes from regions I and II are less stable, the higher frequency of this mode from region III makes it more susceptible to the incoming free stream high frequency excitation.

Region III:b least damped mode eigenfunctions for pressure (first row), temperature (second row), streamwise (third row), vertical (fourth row) and spanwise (last row) velocity components are displayed in Fig. 3.65. There are a few common features among them. One is their origin, since they appear to emanate from the recirculation region. Their amplitude also increases in the streamwise direction, modulated by an oscillation controlled by an apparent positive wavenumber. Another is their behavior as they exit the recirculation region. Most of their structure remains within the shear layer region, labeled previously as the GIP_1 line. However, part of their structure penetrates the reattachment compression fan. They are upper bounded by the GIP_2 line, being significantly damped away from it. This part is most significant for pressure and vertical velocity components, but it is still non-negligible for the remaining eigenfunctions. The one major difference between them is that

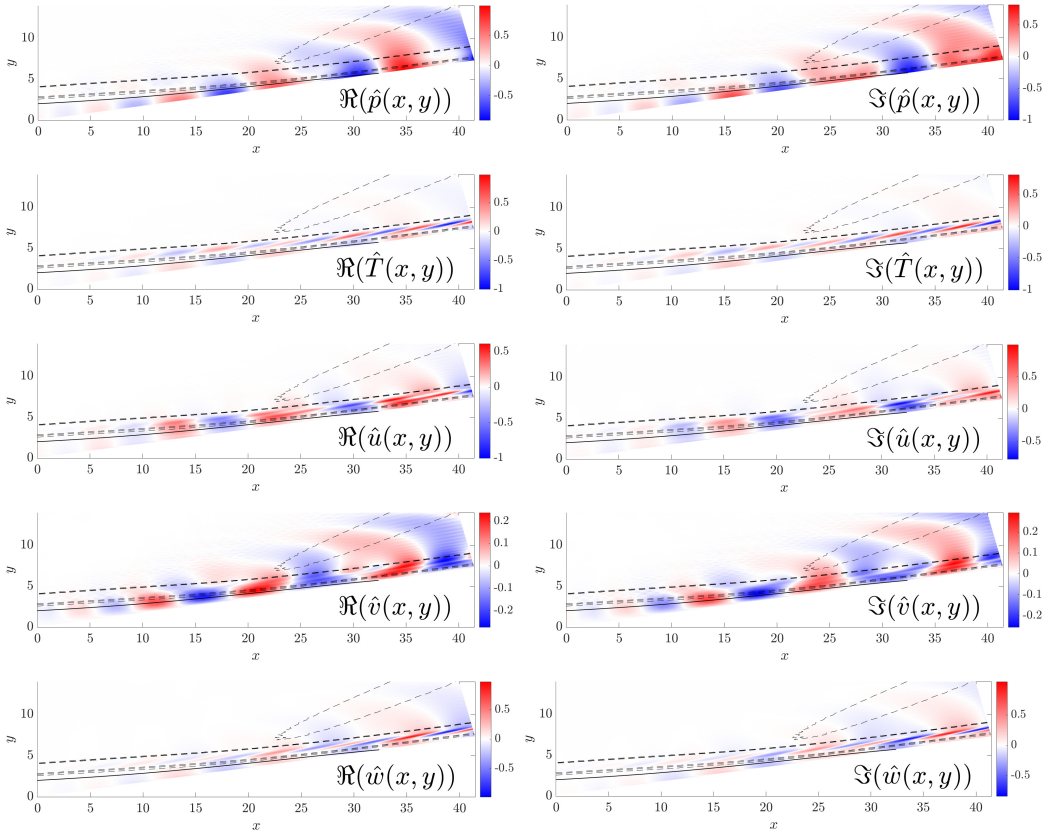

Figure 3.65: Same as Fig. 3.60, but for $\beta = 0.6$ mode from region II:b.

temperate and spanwise velocity component eigenfunctions have a double peak, opposite signed, overlapping rope like structure within the recirculation and shear layer regions. It is reminiscent of the structures observed by Butler and Laurence (2021) in their compression corner experiments. They were performed at a Reynolds number that is one order of magnitude larger and a Mach number that is twice larger, using a cone-flare geometry.

The linear and global disturbance behavior just described once again appears to be that of a oscillatory convective instability, usually observed in a linear and local analysis. In order to verify if this is indeed the case, the real (top), imaginary (middle) and absolute (bottom) disturbance eigenfunction amplitudes along the GIP_1 line defined in Fig. 3.50 is shown in Fig. 3.66 around the entire recirculation (right) and separation (left) regions. There is an exponential growth region in the former region. It starts downstream of the separation compression fan but saturates upstream of the reattachment compression fan for all eigenfunctions, with a common apparent streamwise wavenumber. However, the disturbance behavior in the latter region is quite different. There is an algebraic growth region located within the separation compression fan for all eigenfunctions, the streamwise velocity component being a likely exception, with different streamwise wavenumbers. It must be noted that this growth also saturates before it starts growing again in the subsequent region. Hence, the overall disturbance growth observed within both regions is not monotonic.

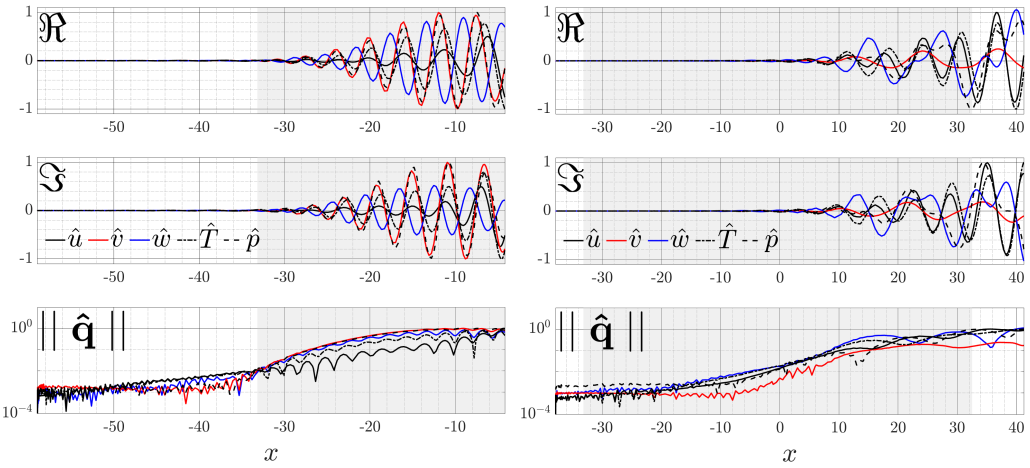

Figure 3.66: Real (top), imaginary (middle) and absolute (bottom) values of the disturbance eigenfunction along GIP_1 line around the separation (left) and recirculation (right) regions from Fig. 3.65.

In order to better understand the behavior displayed by the region III:b least damped mode around the separation region, a new domain is defined on which the analysis is performed. It starts upstream of the separation region and finishes at the corner, including the separation compression fan as well. These results are shown in Fig. 3.67. They suggest that the origin of these disturbances is the separation point, since no discernible structures can be observed upstream of it. Furthermore, all eigenfunctions have a very similar structure downstream of this point. They are perpendicular to the wall below the GIP_1 line, get distorted inside the shear layer region and, above it, they realign themselves to become parallel to the GIP_3 line, which marks the edge of the separation compression fan and shock. The angle of these latter structures is approximately 17.4°, sitting in between the ramp angle $\theta = 10°$ and the Mach angle $\mu_M = \sin^{-1}(1/M) \approx 21.1°$ which, as expected, is very close to the angle of the separation shock itself. Furthermore, their amplitude increases in the streamwise direction, while it oscillates with an apparent streamwise wavenumber below the GIP_1. Above it, however, this wavenumber increases in magnitude and changes direction, so that it now

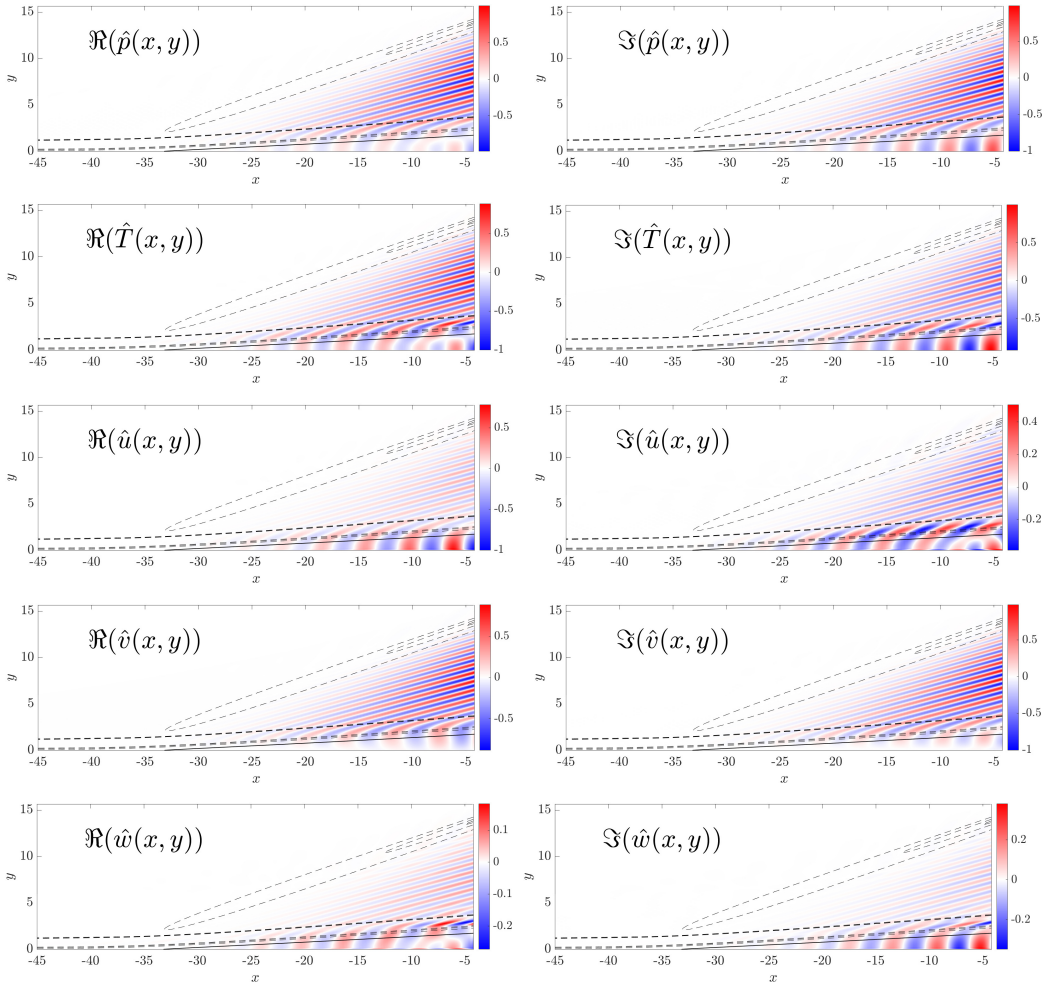

Figure 3.67: Same as Fig. 3.65, but for the flat plate region.

represents the oscillatory behavior in the direction normal to the GIP_3 line. It is also interesting to note that their disturbance amplitudes are strongest for the pressure, temperature and vertical velocity components.

Kuehl (2018) described similar structures in the compressible flow over a flat plate and a flared cone as forced and resonating acoustic waves trapped between inside the boundary-layer due to an acoustic impedance well. The well is maintained between the infinite impedance of the hard wall and the local peak in impedance at the edge of the boundary-layer. When assuming a local steady-state varying only in the wall-normal direction, it is possible to define homogeneous and disturbance impedances as

$$Z_h \sim \sqrt{\rho_s} \quad \text{and} \quad \hat{Z} \sim \frac{p_n}{v_n} \quad , \tag{3.37}$$

respectively, where ρ_s is the local steady density, p_n and v_n are the local pressure and normal velocity disturbances. They are shown in Fig. 3.68 (right), measured along the straight line beginning at $(x, y) = (-10, 0)$ and inclined by an angle of 107.4°, shown in Fig. 3.68 (left). This angle is used to calculate v_n from the streamwise as well as vertical disturbance velocity components. The homogeneous impedance has an inflection point near the GIP_1 line whereas the disturbance impedance has a small amplitude peak near the GIP_1 line. Similar features were observed near the edge of the boundary-layer for the compressible flows over a flat plate as well as a flared cone by Kuehl (2018). Furthermore, Batista and Kuehl (2020) have shown that temperature modulation can either stabilize of destabilize such modes by modifying the acoustic impedance well, which explains why many linear stability analyses and direct numerical simulations have shown these waves escaping the boundary-layer (Bitter and Shepherd, 2015; Chuvakhov and Fedorov, 2016; Salemi and Fasel, 2018; Knisely and Zhong, 2019a,b). On the other hand, there are some distinct features in the present work due to the presence of the corner. Instead of the boundary-layer edge, both inflection point and amplitude peak are better correlated with the GIP_1 line. Furthermore, after the emission process above this line, these waves realigned

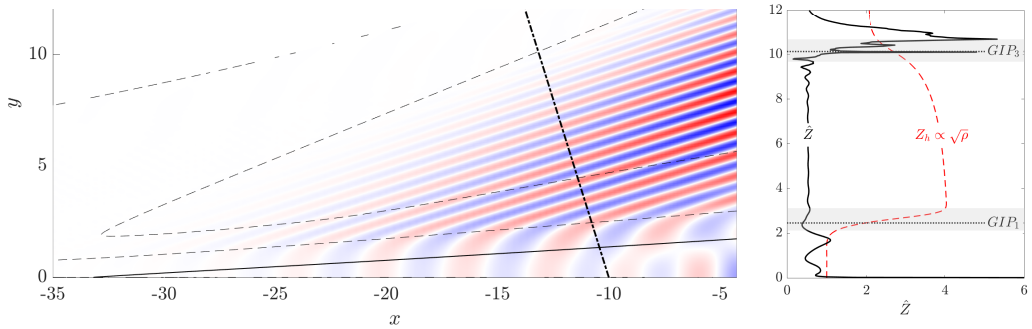

Figure 3.68: Homogeneous and disturbance impedances (right) measured along a straight line starting at $(x, y) = (-10, 0)$ with an angle of 107.4°, shown in the pressure disturbance isocontours (left) by the dash dotted line.

themselves with the GIP_3 line. Nevertheless, while these structures exist on the flat plate, the eigenfunctions including the ramp and reattachment regions clearly show that they are dominated by structures along the ramp instead of the flat plate, as shown in Fig. 3.65. This can be explained by the fact that the damping rate of this mode when the ramp is omitted from the domain is given by $\omega_i \approx -0.112$, which is significant higher than the one including ramp and reattachment regions.

There is still an open question regarding this region III:b least damped mode, pertaining to its origins. Figure 3.66 (right) indicates that it first appears at the separation point, which is confirmed by Fig. 3.67. However, Fig. 3.66 (left) suggests that its origins might be upstream of the separation point. Hence, it is important to verify if the latter behavior is physically relevant. In order to do so, a local analysis is performed on the slowly diverging boundary-layer upstream of separation. It is undertaken at $x = -40$, with $\beta = 0.6$, and $f = 10,694Hz$. The time asymptotic marginally stable mode obtained, which has $\alpha = 0.9346 + 0.0233\,i$, is the compared in Fig. 3.69 to the global mode at the same location, spanwise wavenumber and frequency through pressure, temperature, streamwise, vertical and spanwise velocity component wall-normal profiles, from left to right. The structure of the streamwise disturbance velocity component has three peaks near the wall, unlike the classical two peak structure observed in compressible boundary-layers (Mack, 1984). This difference can be attributed to the adverse pressure gradient experienced by the fluid upstream of the separation point due to the corner. Nevertheless, there are clear discrepancies between the local and global profiles, specially in the pressure and vertical velocity component profiles near the wall as well as away from it. Furthermore, the global mode grows in amplitude in the streamwise direction, but the local mode is being spatially damped. On the other had, it is only marginally so, which suggests

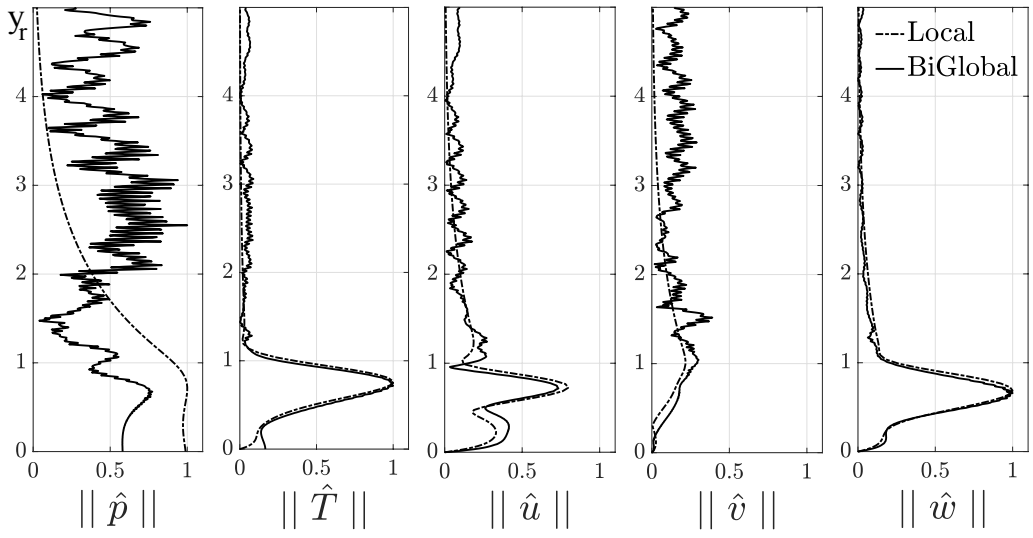

Figure 3.69: Local and global plate wall-normal linear disturbance profiles at $x = -40$ from the least damped III:b mode.

that this local moda could become spatially growing under slightly different parametric conditions than the ones employed here in its calculation. These discrepancies can be explained by the many notable effects neglected in the local analysis, such as *i*) the steady vertical velocity component, *ii*) the steady separation compression fan and *iii*) the temporal damping rate of the original global mode. Despite these issues, there is a good qualitatively agreement between the local and global profiles. They provide confidence that the global structures observed upstream of the separation point are indeed physical.

Moving towards higher frequencies, a new distinct group of modes appear in what is labelled here region IV. They are presented in Fig. 3.70 (left), which shows these modes are locally dominant at higher spanwise wavenumbers. The locally least damped mode in this group is presented in Fig. 3.70 (right). It has $\beta = 2.32$, where its damping rate is $\omega_i = -0.0305$ and frequency is $St = 0.1997$. This leading mode is followed by several other modes with increasingly higher damping but little variation in frequency. However, below $\omega_i = -0.06$, another branch of modes breaks off with a distinct feature, namely their frequency increases as their damping increases. This region

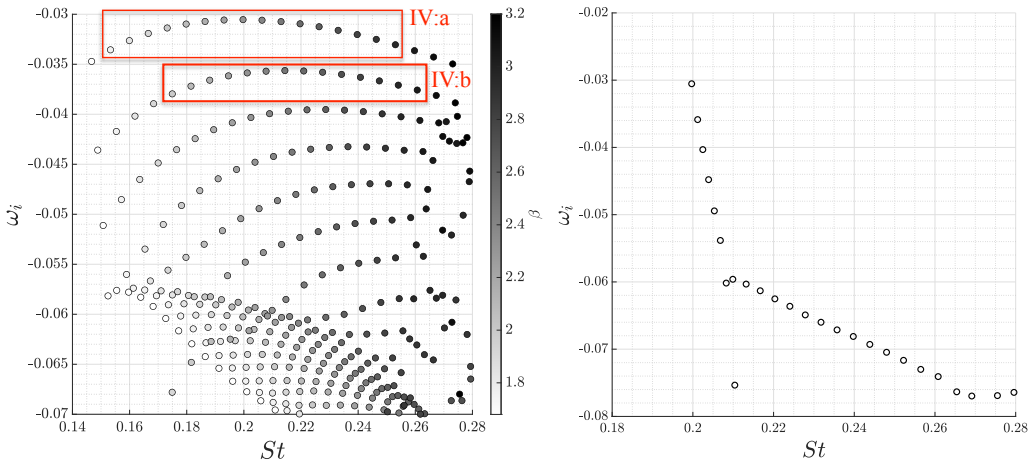

Figure 3.70: Same as Fig. 3.64, but at higher frequencies for $1.9 \leqslant \beta \leqslant 3.2$ (left) and $\beta = 2.32$ (right).

deserves mention because the spatial structure of its modes departs from the one observed in regions II and III. They are presented in Fig. 3.71, which shows real (left column) and imaginary (right column) parts of the region IV:a locally least damped eigenfunctions for pressure (first row), temperature (second row), streamwise (third row), vertical (fourth row) and spanwise (last row) velocity components. The key distinction of this region IV:a mode is the strong importance of the reattachment separation fan observed in the eigenfunctions, which manifests itself as a spatially oscillatory structure that begins at the corner, is basically parallel to the flat plate, has an apparent vertical wavenumber, peaks around the GIP_2 line and damps away before reaching the ramp. Although this structure appears in all eigenfunctions, the dominant amplitudes are found in the pressure and spanwise velocity

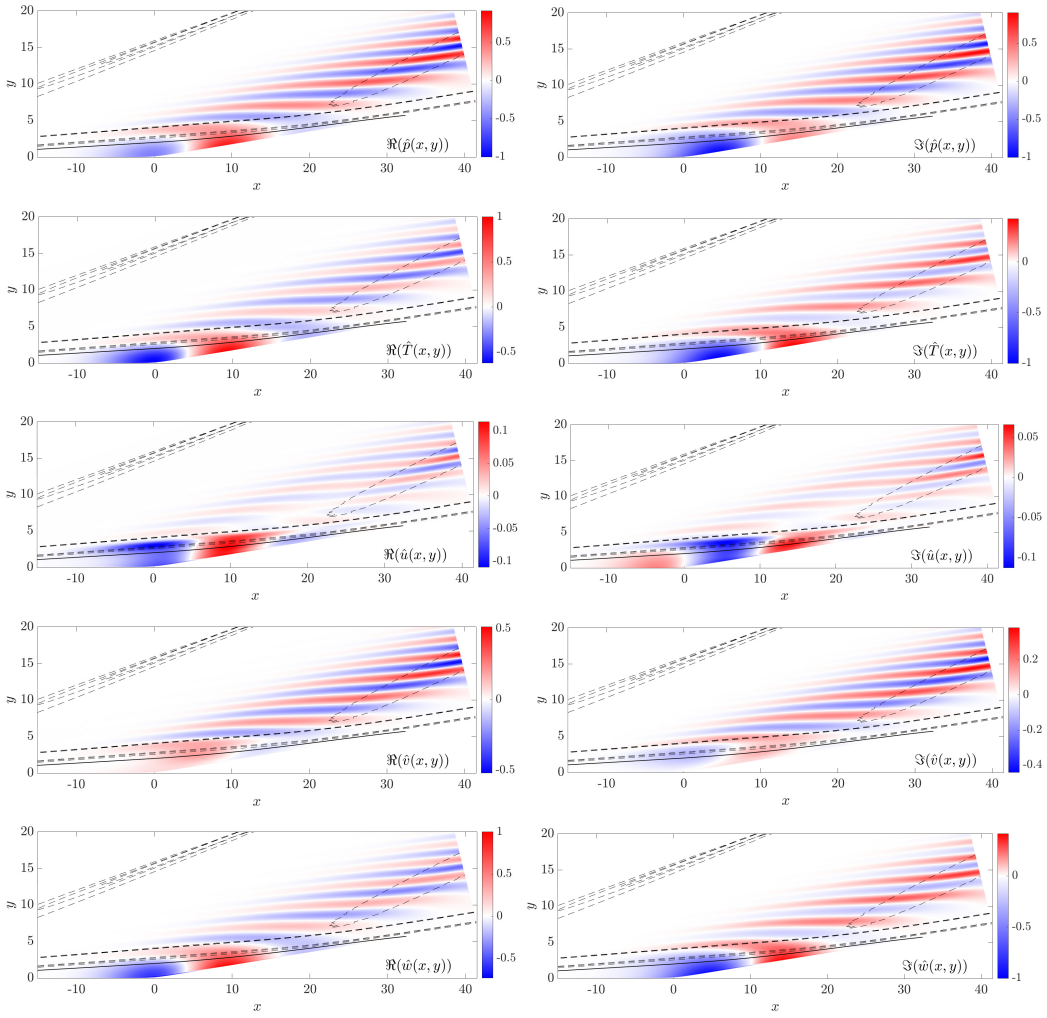

Figure 3.71: Same as Fig. 3.65, but for $\beta = 2.32$ mode from region IV:a.

component disturbances. Furthermore, they come from larger structures that originate in the recirculation region and pass through the GIP_1 line.

More insight about this structure can be gained by evaluating it along the GIP_1 and GIP_2 lines, which represent the shear layer and reattachment compression fan regions, respectively. This is done in Fig. 3.72 (left) and (right), respectively, which shows the real (top), imaginary (middle) and absolute (bottom) values of the disturbance eigenfunctions. In the left figure, there seems to be an algebraic spatial growth starting at the end of the separation compression fan. It reaches a maximum just downstream of the corner and decays up to the reattachment point. There, its behavior changes again. In the right figure, all components show a consistent, phase-locked but small and spatially oscillatory growth pattern. The vertical velocity component is the only exception, having a smaller amplitude and being out of phase with the other eigenfunctions. Hence, this behavior could lead to large disturbance amplitudes much further downstream of the reattachment point than shown here. Confirming this result with a local analysis was not

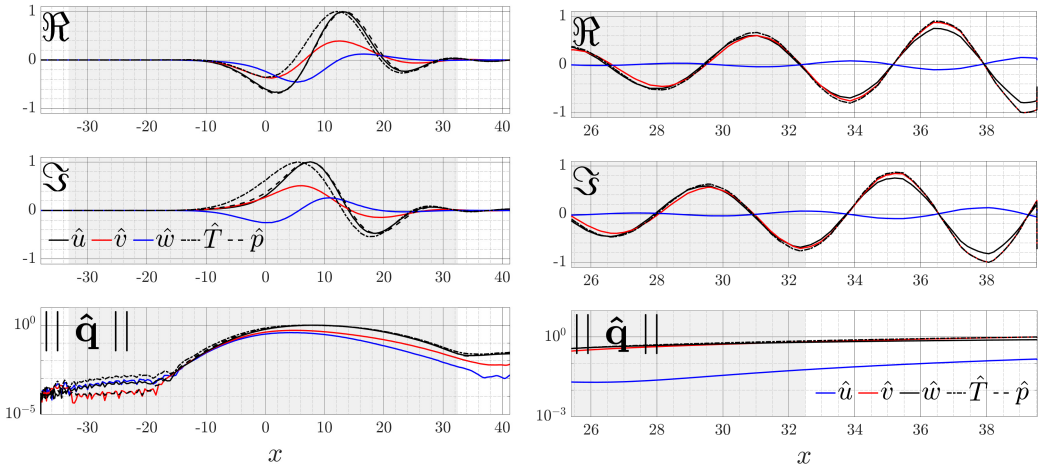

Figure 3.72: Real (top), imaginary (middle) and absolute(bottom) values of the disturbance eigenfunctions along the GIP_1 (left) and GIP_2 (right) lines for the least damped mode from region IV:a.

possible due to the proximity of the reattachment shock.

Non-Modal Analysis

Once the modal analysis has highlighted the possible transition scenarios induced by the time asymptotic disturbance behavior, it is necessary to verify if these scenarios can be bypassed due to the short time disturbance behavior. In order to do so, a non-modal analysis is discussed next. It is more likely to be relevant when the modal behavior, either stable or unstable, is weak. Hence, the following analysis is focused on the free stream Reynolds number range $160,000 \leqslant Re_\infty \leqslant 220,000$. Before proceeding any further, a solution convergence analysis is required. This is done in two steps. The first one is

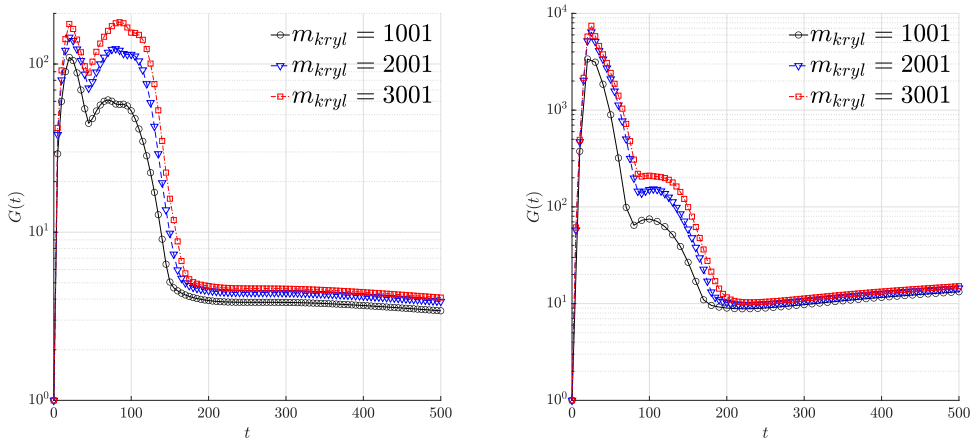

Figure 3.73: Energy gain over time for different number of terms m_{kryl} in the modal matrix with $Re_\infty = 160 \times 10^3$ (left) and 220×10^3 (right).

the convergence of the spectra, which has already been discussed in the modal analysis. The second one involves convergence of the energy gain over time, which is achieved when the correct number of modes m_{kryl} are included in the calculations. Figure 3.73 shows such a convergence for the limiting values of this range, i.e. $Re_\infty \times 10^{-3} = 160$ (left) and 220 (right). This analysis was performed at the spanwise wavenumber closest to the least damped mode of the former and the most unstable mode of the latter. Clearly, the number of Krylov subspaces required for convergence should be $m_{kryl} \geq 3000$. In the present work, $m_{kryl} = 4000$ is employed. Finally, one point must be emphasized. These calculations were performed within a given frequency range in order to remove spurious modes from it. This range moves from $-1.5 - 0.25\,i \leqslant \omega \leqslant 1.5 + 0.00\,i$ to $-1.5 - 0.19\,i \leqslant \omega \leqslant 1.5 + 0.01\,i$ between the free stream Reynolds number limits considered here.

Another relevant metric for verification purposes is to evaluate if the time asymptotic behavior resulting from the transient growth calculation leads to the expected modal result. This is done in Fig. 3.74 (right), which shows the absolute value of the time derivative of the logarithm of the energy gain versus time for different Reynolds numbers (lines) as well as twice the temporal growth rate from the respective modal analysis plotted at $t = 2000$ of the insert (circles). The former converges in time towards the latter since $G(t \to \infty) = e^{2\,\omega_i\,t}$, providing further evidence of the present non-modal calculation accuracy. It is important to mention the existence of a noticeable difference between the two for the $Re_\infty = 180 \times 10^3$ case. This is due to the fact that this value is only slightly above the critical free stream Reynolds number for the onset of instability, namely $Re_{\infty,c} \simeq 177 \times 10^3$. Hence, the temporal growth rate is still quite small and it will take longer for the energy gain to reach its time asymptotic value for this Reynolds number. Such a

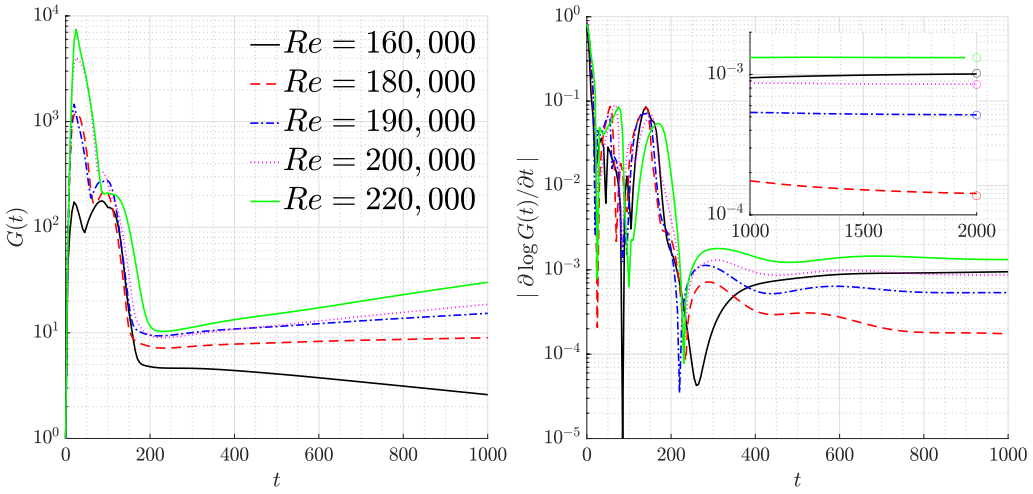

Figure 3.74: Energy gain (left) and the absolute value of the time derivative of its logarithm (right) over time for different free stream Reynolds numbers obtained from the non-modal analysis. Circles on the insert represent twice the respective modal temporal growth rate, where $G(t \to \infty) = e^{2\,\omega_i\,t}$.

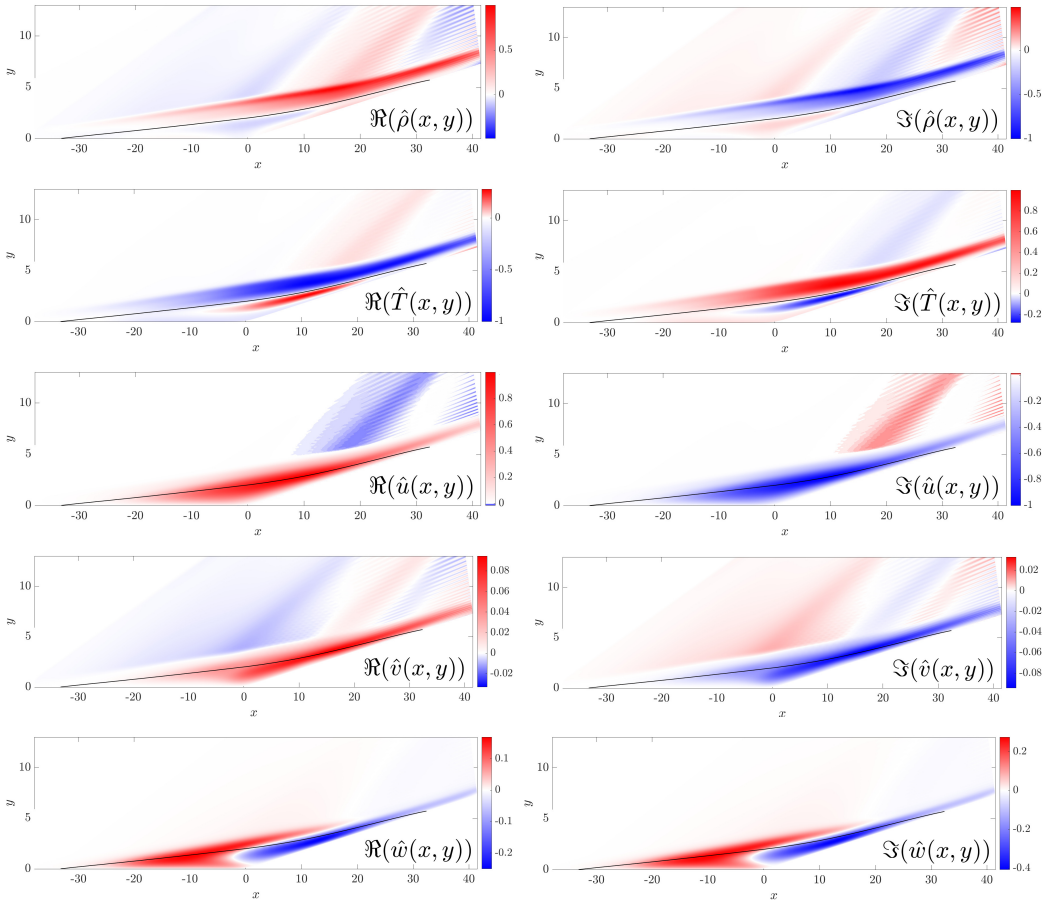

Figure 3.75: Same as Fig. 3.58, except for the pressure, which was replaced by density, but obtained from the time asymptotic non-modal analysis.

modal and time asymptotic non-modal comparison, however, does not have to be restricted to their eigenvalues. Their eigenvectors can be compared as well. Figure 3.75 shows the real (left) and imaginary (right) parts of the time asymptotic non-modal eigenfunctions obtained from the LiGHT code at $Re_\infty = 220 \times 10^3$ and $\beta = 0.28$ for density (first row), temperature (second row), streamwise (third row), vertical (fourth row) and spanwise (last row) velocity components. They are nearly indistinguishable from their counterparts in Fig. 3.58, which were obtained from a modal analysis under the same parametric conditions.

It is important to note the presence of two local peaks in Fig. 3.73, one at $t \approx 25$ and another at $t \approx 100$, which is true independent of the free stream Reynolds number. On the other hand, their relative amplitudes do depend on this number. For this reason, Figure 3.74 (left) compares the energy gain for different free stream Reynolds numbers. Although they have similar magnitudes at $Re_\infty = 160 \times 10^3$, the first peak increases in magnitude significantly more than the second peak as this number increases. This trend suggests that the second peak will eventually disappear within the first one, since it is already barely noticeable at $Re_\infty = 220 \times 10^3$. The maximum

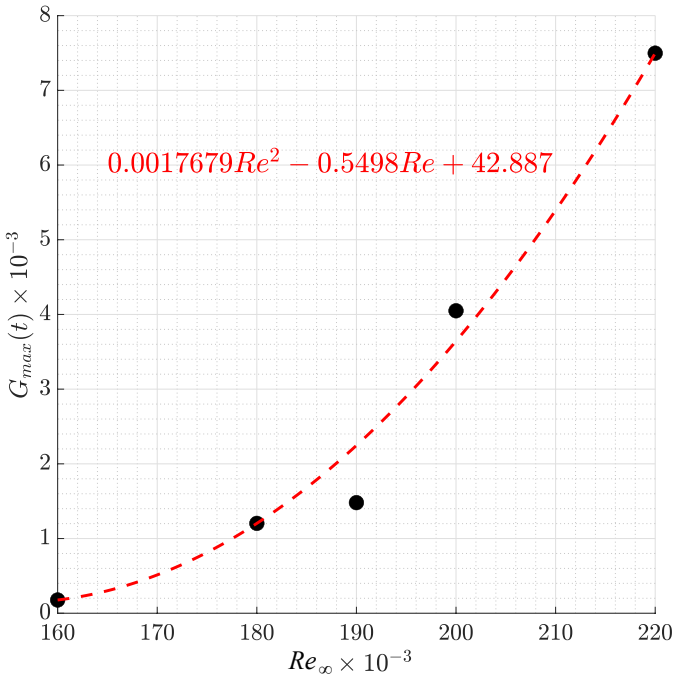

Figure 3.76: Maximum transient energy growth for different free stream Reynolds numbers near the onset of modal instability (points) and a linear regression best fit curve of this data with $R^2 \simeq 0.9784$ (dashed line).

energy gain associated with the first peak for each Reynolds number (points) is presented in Fig. 3.76, which also includes a quadratic polynomial (dashed line) whose coefficients we obtained by linear regression with a coefficient of determination of $R^2 \approx 0.9784$. Its quadratic dependence on the free stream Reynolds number has been suggested as the expected transient growth trend for shear flows by Schmid and Henningson (2001), which has been recently verified by Quintanilha Jr et al. (2022) as well. It is also useful to evaluate the optimal disturbance spatial structure, i.e. the disturbance eigenfunctions, at this first peak. Real (left) and imaginary (right) parts of the optimal non-modal eigenfunctions obtained from the LiGHT code at $Re_\infty = 220 \times 10^3$, $t_{opt} = 25$ and $\beta = 0.6$ for density (first row), temperature (second row), streamwise (third row), vertical (fourth row) and spanwise (last row) velocity components are shown in Fig. 3.77. A common feature of all eigenfunctions is the fact that their structures are associated with the reattachment region. They are mostly located within the boundary-layer, but there are significant contributions inside the compression fan as well, specially for the density and vertical velocity component. This velocity component, however, is the least important one. It turns out the streamwise component is the dominant one, followed by the spanwise component.

The discussion put forward up to this point has been limited to spanwise homogeneous structures with either $\beta = 0.28$ or $\beta = 0.6$, shown in Figs. 3.75 and 3.77, respectively. Hence, it is useful to better understand the disturbance behavior at a variety of spanwise wavenumbers. In order to

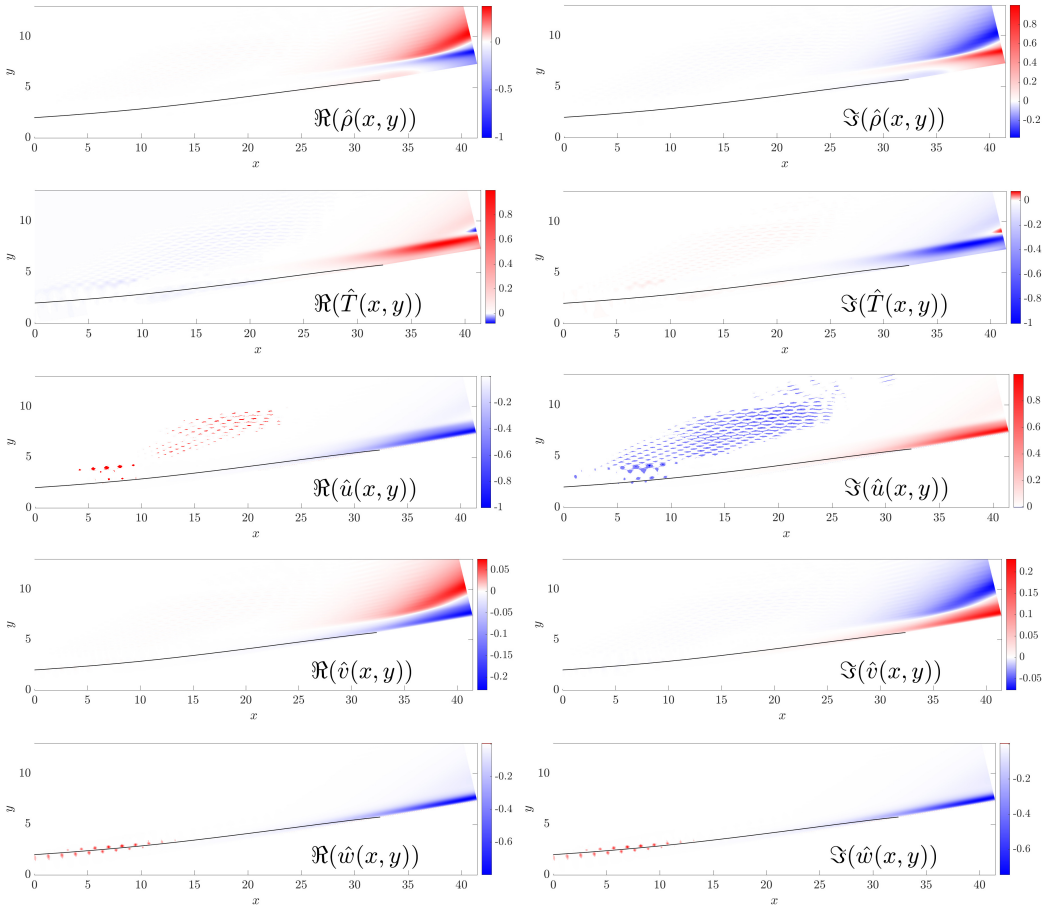

Figure 3.77: Same as Fig. 3.75, but obtained at $t_{opt} = 25$ and $\beta = 0.6$.

do so without exhausting a large number of computational resources, each Reynolds number was simulated for several spanwise wavenumbers using the lowest modal subspace considered in Fig. 3.73, namely $m_{kryl} = 1001$. Such an approach is assumed reasonable since the trends observed in Fig. 3.73 are independent of m_{kryl}. Furthermore, this analysis is performed here only for $Re_\infty = 220 \times 10^3$, since the same trends are observed for the other free stream Reynolds numbers. These results are shown in Fig. 3.78. Two features deserve discussion. On one hand, the magnitude of the first peak monotonically increases as the spanwise wavenumber decreases towards zero. This suggests that the non-modal mechanism possibly responsible for bypass transition most likely involves two-dimensional structures. However, small positive spanwise wavenumbers lead to similar gains, which suggests that this mechanism can also include spanwise elongated three-dimensional structures as well. On the other hand, the second peak also gains in strength as the spanwise wavenumber is decreased towards zero from $\beta = 0.2$. In fact, its amplitude eventually surpasses the one associated with the first peak as β approaches zero. This is consistent with the fact that the two-dimensional steady-state not only is modally stable but also approaches marginal stability as the free stream Reynolds number increases, as shown in Fig. 3.53. Hence,

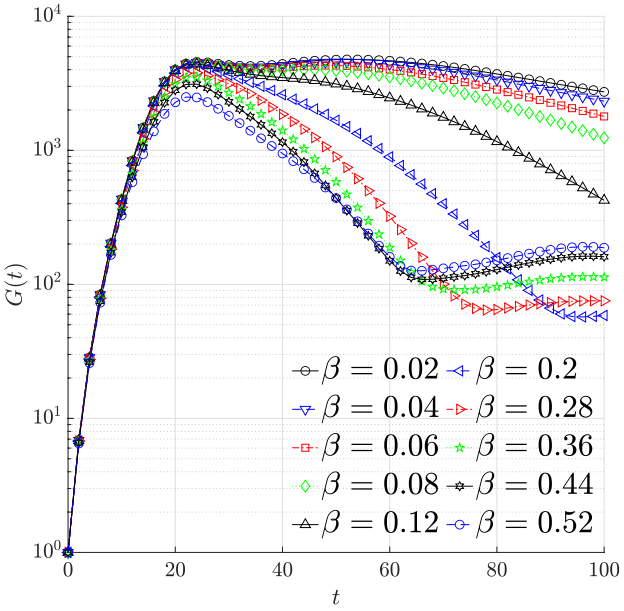

Figure 3.78: Energy gain over time for $Re_\infty = 220 \times 10^3$ using $m_{kryl} = 1001$.

such an increasingly weaker modal stability of two-dimensional disturbances makes them more susceptible to transient growth. The same phenomenon is found is other canonical flows, such as the Couette (Reddy and Henningson, 1993) and Hagen-Poiseuille (Schmid and Henningson, 1994) flows.

Two important conclusions can be drawn from this analysis. The first one pertains to the magnitude of this effect. It turns out that transient energy growth near the onset of modal instability falls within $O(10^2)$ and $O(10^4)$. The second one pertains to the amount of time available for transient growth to take place. Its time horizon, i.e. $t \approx 25$, appears significantly smaller than the modal one. However, it is important to properly quantify the latter. Table 3.3 shows the physical time t_{req} it would take for the modal growth $e^{2\omega_i t_{req}}$ to reach the same maximum energy gain G_{max} induced by non-modal growth at the optimal time t_{opt}. At the higher free stream Reynolds number, namely $Re_\infty = 220 \times 10^3$, t_{req} is two orders of magnitude larger than t_{opt}. This difference increases to three orders of magnitude for the lower Reynolds numbers considered here. Hence, there is ample time for non-modal mechanisms to bypass modal ones and induce transition. A similar scenario was recently observed by Quintanilha Jr et al. (2022) at high altitudes, where Reynolds numbers are smaller due to a decrease in density.

$Re \times 10^{-3}$	$G_{max}(t^*_{opt})$	t^*_{req}	$e^{2\omega_i t_{opt}}$
180	1,203	0.54634	1.004
200	4,049	0.10315	1.021
220	7,498	0.07145	1.034

Table 3.3: Time t_{req} it would take for the modal growth $e^{2\omega_i t_{req}}$ to reach the same non-modal maximum energy gain G_{max} at the optimal time t_{opt}.

Chapter 4

Epilogue

4.1 Conclusions

The main goal of the present report is to use time marching methods to obtain accurate and disturbance free steady-states for high-speed flows in order to provide base flows for linear and nonlinear stability analyses. This chapter concludes the first of its three parts, which focusses on high-speed flows that are physically stable in a linear and time asymptotic sense. In other words, all physically meaningful disturbances should be naturally damped in time-accurate simulations of such flows, rendering special steady-state solvers unnecessary. Doing so allowed this part of the report to focus on the implementation of high accuracy spatial discretization techniques with shock-capturing capabilities on 3D4S. This is the name of the code developed for the work performed in this report, where the acronym stands for *one, two and three-dimensional stable steady-state solver*.

In order to deal with the challenges associated with simulations of high-speed flows imbedded with shocks, special techniques were employed. First, the so-called low-order 3D4S was developed. On one hand, its discretization of the viscous flux derivative uses a second-order accurate conservative central -difference scheme. On the other hand, its discretization of the inviscid flux derivative uses a second-order TVD scheme with classical flux-limiters based on different well-known flux-difference splittings. Many numerical issues, however, made it difficult to reach steady-states with machine zero residues. In general, this issue was caused by flux-limiter flickering around shocks and carbuncle due to the use of flux-difference splitting. This led to the second implementation of 3D4S, which is the so-called high-order version. On one hand, its discretization of the viscous flux derivative uses a fourth-order accurate conservative central-difference scheme. On the other hand, its discretization of the inviscid flux derivative employs different fifth-order WENO schemes, using flux-vector splitting based on either conservative or characteristic-wise variables, for steady and unsteady simulations. Doing so allowed 3D4S to reach steady-states with machine zero residues. It should be noted, however, that similar numerical issues do creep back in at high enough Reynolds numbers, which requires the alignment of the grid with the shock to

be controlled. One, two and three-dimensional steady and unsteady test cases were employed to verify 3D4S. Steady-states are obtained with an explicit Euler scheme whereas unsteady-states are obtained with either second-order or third-order SSP-RK scheme. They generated enough confidence on the ability of 3D4S to deliver accurate and disturbance free steady-states for high-speed flows imbedded with shocks.

Having verified low and high-order 3D4S versions, they are applied to the study of two canonical flows. The first one is the supersonic flow upstream of a two-dimensional cylinder. This is one of the major test cases used to investigate the ability of shock-capturing schemes to prevent carbuncle. Hence, high-order accurate and disturbance free steady-states are available in the literature. However, to the best of our knowledge, all stability analyzes of this problem have been performed using steady-states calculated with low-order accurate schemes instead. This is the reason why a linear and global stability analysis was performed using steady-states generated with high-order 3D4S as base flows. Their results were then verified using time-accurate unsteady simulations, which were performed with high-order 3D4S as well. A few major findings are worth mentioning. First, even fifth-order accurate WENO schemes based on characteristic-wise flux-vector splitting, designed to prevent post-shock oscillations and reach machine zero residues at steady-state, cannot prevent carbuncle at high enough Reynolds numbers when employed on arbitrary grids. Second, although this is a well known modally stable problem, non-modal energy growth has been found for the first time to the best of our knowledge. Gains of three to four orders of magnitude were observed for optimal disturbances located at the shock when $Ma = 6$ and $Re_D = 1000$. Third, time-accurate simulations initialized by an accurate steady-state superposed with random disturbances at the cylinder wall showed the appearance of a similar disturbance structure that underwent algebraic growth to similar magnitudes, which indeed suggests sub-optimal transient growth in this problem.

The second canonical flow studied in this part of the report was the supersonic flow over a compression ramp, which is also physically stable in a linear and time asymptotic sense. On one hand, high-order accurate spatial discretization schemes have been used in time-accurate simulations of this problem. On the other hand, to the best of our knowledge, the base flows employed in its linear stability analyses have been two-dimensional steady-states obtained using second-order accurate TVD-type schemes. Simulations using OpenFOAM and low-order 3D4S discussed here show that such schemes are not capable of achieving machine zero residues due to compression fan and/or shock related oscillations. Hence, temporal content contaminates their steady-states. Since residue convergence in time was not reported in the aforementioned literature, the same cannot be stated about their low-order accurate steady-states. However, it seems likely they suffer from similar convergence issues. Accurate and disturbance free steady-states were then generated for the $Ma = 3$ flow over a $\theta = 10^o$ degrees ramp with adiabatic walls using high-order 3D4S over a wide range of Reynolds numbers. In all

cases, spatially grid converged steady-states with machine zero residues were obtained. In addition, pressure and wall shear stress are in agreement with their triple-deck counterparts within the separation region, which provides further verification. Time-accurate simulations suggest that two-dimensional steady-states are always modally stable, but approach marginal stability as the Reynolds number increases. The least damped mode decay rate as well as eigenfunction were extracted using the residuals methods and agreed well with data obtained from a linear and global stability analysis of the $Re_\infty = 50 \times 10^3$ steady-state. This analysis was then performed at higher Reynolds numbers, which allowed the identification of the neutral curve as well as critical parametric conditions, namely $Re_{\infty,c} \approx 177 \times 10^3$, $\beta_c \approx 0.375$ and $St = 0.0$. It indicates that the onset of instability occurs though three-dimensional and stationary disturbances whose structure is concentrated in the recirculation region to a large extent, although some of it penetrates the reattachment compression fan. Several stable but locally least damped oscillatory modes were also identified. One is a convectively unstable slow acoustic mode excited at the separation region with $St = 0.025$ at $Re_\infty = 220 \times 10^3$. The other goes through a complex spatial growth that seems to involve modal and non-modal mechanisms with $St = 0.1127$ at the same Reynolds number. It appears to be an acoustic wave excited at the separation region with a wall-normal structure. A significant part of it remains trapped inside the impedance well that exists between the wall and the generalized inflection point along the shear layer, but the part released above the shear layer realigns itself parallel to the separation shock. Finally, another spatially amplified oscillatory mode was identified, now with $St = 0.1997$. Its relevance comes from the fact that it is excited at the end of the separation compression fan and remains inside the recirculation region until the corner, when it gets released into the reattachment compression fan with a structure that is parallel to the flat plate. At this stage, it starts spatially growing significantly as it propagates downstream. A linear and global non-modal analysis was also performed around the onset of modal instability. It reveals the potential for transient energy growth of three to four orders of magnitude. Although the optimal disturbance is two-dimensional, sub-optimal elongated three-dimensional structures were found to be relevant as well. Their structures are concentrated within the boundary-layer downstream of the reattachment point but also penetrate the reattachment compression fan. It is important to point out that an equivalent magnitude modal growth would take two to three orders of magnitude longer to manifest. This suggests that there is ample time for this non-modal mechanism to bypass the transition induced by its modal counterpart.

4.2 Future Work

Given the development and the discoveries presented in the first part of this report, which were summarized above, it is important to suggest the next

steps forward. This is done below, segregated by topic of interest.

- **Grid Generation:**

1. Replace the over/under relaxed Gauss-Seidel solver that is currently implemented in the elliptic grid generation tool by the state-of-the-art solvers available in the PETSc library, already used by 3D4S.

2. Develop a procedure to detect the steady shock position, which can then be used as the interface between two elliptic grids orthogonal at this interface and, hence, develop a unified shock aligned grid.

3. Generalize the three-dimensional grid generation tool, currently limited to either rotated or protruded two-dimensional grids, to arbitrary three-dimensional domains in the context of generalized coordinates.

- **3D4S Development:**

4. Extend the two-dimensional formulation of the generalized coordinate framework in which the governing equations were written in order to allow simulations in cylindrical coordinates with axial symmetry.

5. Extend the three-dimensional formulation of the generalized coordinate framework in which the governing equations were written in order to allow simulations in conical coordinates without grid singularities.

6. Extend to three-dimensions the low-order 3D4S spatial discretization schemes currently available only for two-dimensional simulations.

7. Implement the cut-stencil method, which has already been tested in rudimentary in-house codes, to improve the ability of 3D4S to simulate geometries that are too complex for generalized coordinates.

- **Two-Dimensional Cylinder:**

8. Obtain steady-states at higher Reynolds and Mach numbers with high-order 3D4S using a shock aligned grid to remove carbuncle.

9. Use LiGHT code for a linear and global stability analysis to evaluate the bow shock transient growth dependence on both parameters.

10. Confirm optimal and sub-optimal non-modal trends using time-accurate simulations performed with high-order 3D4S.

- **Compression Ramp:**

11. Verify the linear and global stability three-dimensional modal results using time-accurate simulations performed with high-order 3D4S.

12. Verify the linear and global stability two-dimensional non-modal results using time-accurate simulations performed with high-order 3D4S.

13. Investigate the existence of a three-dimensional steady-state induced by stationary and three-dimensional disturbances from linear, global and modal stability theory.

14. Use LiGHT code for a linear and global secondary stability analysis of this new three-dimensional steady-state.

In addition to these short-term goals, there are several other important problems that deserve a brief mention. They are part of the long-term goals of both research groups. The high-speed flow over a blunt body of a more practical shape, such as the one presented in the 3D4S verification studies, is currently being investigate, since it represents a natural extension of the cylinder problem. Furthermore, our groups are also interested on the supersonic flow over a Prandtl-Meyer expansion, which is the natural counterpart to the compression ramp. Finally, all these flows were considered under a planar two-dimensional context and, hence, will also be extended to axially-symmetric cylindrical coordinate context.

Part II

Physically Unstable Flows with $\lambda_j \neq 0$

Chapter 5

Introduction

5.1 Motivation

This project focusses on the use of time-marching schemes for the numerical computation of accurate and disturbance free steady-states of high-speed flows for their use in linear and nonlinear stability analyses. The first part of its report deals with flows that are physically stable under a linear and time asymptotic sense, whereas their unstable counterparts are investigated separately in the present (second) and the next (third) parts of this report. As described in the prologue, unstable flows are placed in each part according to the complex frequency that arises from their linear and time asymptotic physical stability analysis. Its real (imaginary) component describes the physical disturbance oscillation frequency (temporal growth rate). Only the unstable flows whose complex frequency has at least one nonzero component are discussed in the present part. A discussion of the particular case where both complex frequency components are zero is postponed to the third and final part of this report. Nevertheless, the second and present part of this report has two major goals, namely to *i*) investigate the performance of existing steady-state solvers for these flows and *ii*) improve it.

5.2 Literature Review

When such steady-states are required, a wide variety of solvers is available. They generally fall into two broad groups. Solvers in the first group evaluate the steady governing equations using iterative procedures. A vast literature exists on this topic, which is beyond the scope of this report, so only two well known solvers are described here. The first one, and arguably the most used, is known as the Newton method. Modern versions use a matrix-free Newton-Krylov approach that does not require the calculation of Jacobian matrices (Knoll and Keyes, 2004). These solvers are popular due to their quadratic, or at least super-linear, convergence. The Recursive Projection Method (RPM) is the second one (Shroff and Keller, 1993). It uses projection methods to identify the unstable subspace, applying a Newton method on

it and the fixed point iteration on its stable complement. RPM can be effective, but only when the dimension of the unstable subspace is small. Nevertheless, both methods have an important drawback. Their convergence radius is often quite small when the steady-state in unstable. In general terms, convergence depends on the existence of good initial guesses. Hence, parametric continuation techniques are usually employed to minimize this problem (Allgower and Georg, 2003), but they can only find solutions that are parametrically connected by continuity (Brevdo et al., 1999). This can be an issue when multiple and disconnected steady-states exist within a given parametric space of a system undergoing a complex bifurcation pattern. For these reasons, solvers from this group are not implemented in 3D4S.

Solvers in the second group follow a different approach. Steady-states are obtained by marching the unsteady governing equations forward in time until their solution becomes time invariant. Implicit schemes are usually the preferred choice in this scenario, often coupled with multiple convergence acceleration techniques (Mavriplis, 1998). A vast literature on marching schemes exists as well (Butcher, 2008), but once again its review is beyond scope of this report. Nevertheless, the implicit Euler scheme is arguably the most popular one when steady-states are required. This is likely due to the fact that, on a linear basis, it is numerically stable for steady-states that are physically either stable or unstable, as long as the time step can be made large enough. In fact, the nonlinear Newton method is recovered in the infinite time step limit of the implicit Euler scheme (Lomax et al., 2001). There is, however, an important drawback here as well. Stiffness often constrains the maximum time step allowed. This is why different acceleration techniques have to be employed, such as dual-time-stepping (DTS) and low Mach preconditioning (Teixeira and Alves, 2012), to name a few, so larger time-steps can be achieved and enable convergence towards steady-state.

Recently, novel steady-state solvers that fall into the second group have been developed in an attempt to deal with these drawbacks. They generally fall into two different subgroups. The ones in the first subgroup are designed to be easily implemented on top of existing explicit marching schemes, taking advantage of the fact that such schemes are used in most unsteady solvers. Selective Frequency Damping (SFD) is a prime example (Åkervik et al., 2006). It essentially filters the unsteady governing equations to remove the unstable self-excited oscillatory disturbance, allowing convergence towards the otherwise unstable steady-state. Both its control parameters can also be optimized *a priori* (Cunha et al., 2015; Jordi et al., 2015). However, this steady-state solver has its own drawbacks (Jordi et al., 2014). Chief among them is the fact that it cannot damp stationary disturbances. Furthermore, the presence of multiple self-excited frequencies requires the use of multiple filters, which further limits its use. A very recent addition to this subgroup is known as *Boostconv* (Citro et al., 2017). It is an adaptation of RPM designed to avoid the use of Jacobian matrices. The fixed point iteration is replaced by an existing marching scheme to evolve the stable disturbances in time while resolving the unstable ones with residue minimization methods

instead of the Newton method. More testing is required, however, since it might not always be more efficient than RPM (Loiseau et al., 2018). Both SFD and Boostconv have been implemented in 3D4S.

Steady-state solvers in the second subgroup deal with the stiffness issues that hinder convergence of implicit schemes by modifying their linear and numerical stability. Known as Minimal Gain Marching (MGM) schemes, they are also a very recent development (Teixeira and Alves, 2017). The key aspect of their design is to provide the smallest possible linear gains at the smallest possible time steps. Its multi-step version has been able to reach accurate steady-states even when the implicit Euler scheme could not. This ability, however, comes at a price. The implicit Euler scheme is L-stable whereas the multi-step MGM scheme is A-stable. Furthermore, adjusting its control parameter to reduce its numerically unstable region moves the linear gain closer to one for large time-steps. In other words, time asymptotic convergence rates deteriorate.

5.3 Objectives

This second part of the report describes how the convergence rates of MGM schemes can be improved upon. In order to do so, multi-stage MGM schemes are developed. Their control parameters can be monotonically adjusted to significantly reduce the liner gain at small time-steps compared to the implicit Euler scheme while maintaining its L-stability. Doing so greatly improves asymptotic convergence rates. The next chapters pursue this matter by first deriving these schemes and then applying them to a few test cases to show their advantages compared to other steady-state solvers. It is important to emphasize that both multi-step and multi-stage MGM schemes have been implemented in 3D4S, with and without DTS.

Chapter 6

Mathematical Formulation

This chapter briefly describes the steady-state solvers implemented in 3D4S. First, the implementation of well known solvers are discussed. Then, the Minimal Gain Marching (MGM) schemes developed by the UFF research group are discussed, including the multi-stage version developed specifically for this project. All these solvers are based on marching schemes, either explicit or implicit. The schemes employed in the former case have been described in the first part of this report. On the other hand, steady-state solvers using implicit marching schemes require the solution of a nonlinear algebraic system of equations. This is done using the same approach for all such solvers. It is based on the Newton method, where the linear system is solved using MUMPS in PETSc (Balay et al., 1998), with either GMRES or LU decomposition. The Jacobian matrixes are numerically calculated with the graph coloring technique (Coleman and Moré, 1983) and the search procedure is based on the trusted region algorithm (Moré et al., 1984).

6.1 Some Known Steady-State Solvers

6.1.1 Implicit Euler Scheme / Newton Method

Arguably, the most widely used time marching steady-state solver is the implicit Euler scheme. Its marches Eq. (1) in time using Eq. (31). However, $\mathbf{u}^{n+1}$ is not known and $\mathbf{f}(\mathbf{u}^{n+1})$ must be approximated. A typical approach assumes $\mathbf{u}^{n+1} = \mathbf{u}^{k+1}$, where k is an iteration index, re-writes Eq. (31) as

$$\mathbf{u}^{k+1} = \mathbf{u}^n + \Delta t\, \mathbf{f}(\mathbf{u}^{k+1}) \quad , \tag{6.1}$$

and approximates $\mathbf{f}(\mathbf{u}^{k+1})$ using the Taylor series expansion

$$\mathbf{f}(\mathbf{u}^{k+1}) \;=\; \mathbf{f}(\mathbf{u}^k) \;+\; \left.\frac{\partial \mathbf{f}}{\partial \mathbf{u}}\right|^k \Delta\mathbf{u} \;+\; O(\Delta\mathbf{u}^2) \quad , \tag{6.2}$$

where $\Delta\mathbf{u} = \mathbf{u}^{k+1} - \mathbf{u}^k$. Combining these equations leads to

$$\left\{ \frac{\mathbf{I}}{\Delta t} \;-\; \left.\frac{\partial \mathbf{f}}{\partial \mathbf{u}}\right|^k \right\} \cdot \Delta\mathbf{u} \;=\; \mathbf{f}(\mathbf{u}^k) - \frac{\mathbf{u}^k - \mathbf{u}^n}{\Delta t} \quad , \tag{6.3}$$

which can be solved for iteratively using

$$\mathbf{u}^{k+1} = \mathbf{u}^k + \Delta\mathbf{u} \quad , \tag{6.4}$$

for $k = 1, 2, 3, \ldots$, where $\mathbf{u}^k = \mathbf{u}^n$ when $k = 1$. This iterative process is assumed converged when two criteria are satisfied, namely $\Delta\mathbf{u}$ approaches zero and Eq. (6.3) approaches Eq. (31). Together, they imply that

$$\mathbf{u}^{n+1} = \mathbf{u}^{k+1} \quad , \tag{6.5}$$

upon convergence of the iterative process, which means the solution at the unknown time step t_{n+1} has been found. At this point, it is important to emphasize that Eq. (6.3) becomes

$$\left.\frac{\partial \mathbf{f}}{\partial \mathbf{u}}\right|^k \cdot \Delta\mathbf{u} \;=\; -\,\mathbf{f}(\mathbf{u}^k) \quad , \tag{6.6}$$

in the limit as $\Delta t \to \infty$ and, hence, the iterative process becomes the well-known Newton method. This means that Eq. (6.5) becomes

$$\mathbf{u}_s \;=\; \mathbf{u}^{k+1} \quad , \tag{6.7}$$

upon convergence of the iterative process, which means that the unknown steady-state $\mathbf{u}_s = \mathbf{u}(t \to \infty)$ has been found.

There are two major issues associated with the use of the implicit Euler scheme and Newton method to calculate a steady-state $\mathbf{u}_s$. The first one is related to the choice of $\mathbf{u}_0$, i.e. the choice of initial (implicit Euler) condition or (Newton) guess. It should be a good estimate of $\mathbf{u}_s$. This is required to prevent divergence in both cases, although for different reasons. On one hand, the Newton method diverges when the initial guess falls outside its radius of convergence, which is rather small. On the other hand, the implicit Euler scheme diverges when the initial guess generates large nonlinear effects, capable of preventing the time step from being chosen large enough to reach the numerically stable linear region of this scheme shown in Fig. 1 (right). This issue is particularly important in the present context, which considers the behavior of nonzero complex frequency disturbances in flows that are physically unstable in a linear and time asymptotic sense. The second major issue is related to large computational times both implicit Euler scheme and Newton method require. They have two major contributions, which are the calculation of the Jacobian matrix $\partial\mathbf{f}/\partial\mathbf{u}|^k$ and the solution of the resulting linear system. Many attempts have been made to address not only the first (Mavriplis, 1998; Allgower and Georg, 2003) but also the second (Knoll and Keyes, 2004) major issue. This includes the development of new steady-state solvers, some of which are described next.

6.1.2 Selective Frequency Damping

Better known by its acronym SFD, Selective Frequency Damping was first developed for explicit marching schemes as an alternative to the Newton

method (Åkervik et al., 2006). It stabilizes a self-excited dynamical system using special techniques from control theory, namely regularization through proportional feedback. In order to do so, a linear source term is applied to the r.h.s. of Eq. (1), leading to

$$\frac{d\mathbf{u}}{dt} = \mathbf{f}(\mathbf{u}) - \chi\,(\mathbf{u} - \mathbf{y}) \quad , \tag{6.8}$$

which forces the variable $\mathbf{u}$ to approach the target solution $\mathbf{y}$ given enough time, where χ is a positive control parameter. Ideally, the target solution should be the desired steady-state, i.e. $\mathbf{y} = \mathbf{u}_s$. However, $\mathbf{u}_s$ is not known *a priori*. An alternative is to use a version of $\mathbf{u}$ with reduced temporal fluctuations. This can be achieved by a low-pass time filter, such as $\mathbf{y}(t) = H(t;\omega_c)\,\mathbf{u}(t)$. It represents the convolution of $\mathbf{u}$ with the low-pass time filter kernel H, where ω_c represents its cut-off frequency. Asymptotic convergence towards steady-state can be obtained only when the cut-off frequency ω_c used by the kernel H is smaller than all the unstable frequencies of the dynamical system. Since $\mathbf{u}$ is a continuous function of t, the causal low-pass time filter that must be used is defined as

$$\mathbf{y} = \int_{-\infty}^{t} H(\tau - t;\omega_c)\,\mathbf{u}(t)\,d\tau \quad , \tag{6.9}$$

in order for the modified system to return to the original system at steady-state. All that is left now is to define the kernel. Most implementations in the literature employ the exponential filter

$$H(t;\omega_c) = \omega_c\,\exp[\,\omega_c\,t\,] \quad , \tag{6.10}$$

which is not used in practice, however, due to the high cost associated with the temporal integration. Hence, the differential version of this procedure

$$\frac{d\mathbf{y}}{dt} = \omega_c\,(\mathbf{u} - \mathbf{y}) \quad , \tag{6.11}$$

is used instead. It is important to note that a time-accurate marching scheme must be used up to steady-state for the low-pass filter to work.

The implementation of SFD in an existing explicit marching scheme is relatively simple, since only a diagonal source term and a diagonal ODE must be added (Åkervik et al., 2006). This implementation is often done using the encapsulated version instead, which allows the marching scheme to be treated as a black box (Jordi et al., 2014). Furthermore, the arbitrary selection of the control parameters χ and ω_c lead to very low convergence rates towards steady-state, which led to the development of several procedures to optimize them (Jordi et al., 2015; Cunha et al., 2015). They work quite well, except for the particular case where the instability is stationary in nature (Citro et al., 2017). In such cases, the cut-off frequency cannot be smaller than the smallest unstable frequency of the dynamical system. Hence, SFD cannot damp stationary disturbances.

6.1.3 Bootconv

One classical alternative to avoid the high computational costs associated with the Newton method is the fixed point iteration method. It re-writes the steady governing equations $\mathbf{f}(\mathbf{u}) = 0$ as $\mathbf{u} = \mathbf{g}(\mathbf{u})$ and uses this structure to propose the fixed point iteration $\mathbf{u}^{k+1} = \mathbf{g}(\mathbf{u}^k)$, where k is the iteration index. In this sense, it is interesting to note that explicit marching schemes can be understood as fixed point iteration methods. Once convergence is achieved using the usual stoping criteria, such as $||\Delta\mathbf{u}||_p < tol$, where $||\cdot||_p$ is an arbitrary p norm and tol is the absolute error tolerance, the steady-state $\mathbf{u}_s = \mathbf{u}^{k+1}$ is achieved. However, convergence is only achieved when the eigenvalues μ_i associated with the Jacobian matrix $\partial\mathbf{g}/\partial\mathbf{u}$ satisfy the inequality $|\mu_i| < 1$. This creates a major difficulty, since the steady-states of interest in this part of the report are unstable. Hence, there is at least one eigenvalue that does not satisfy this inequality.

On the other hand, there are significantly more stable than unstable eigenvalues in most cases, which led to the development of the Recursive Projection Method (RPM) (Shroff and Keller, 1993). It divides the problem in two subspaces. The first one contains only the unstable eigenvalues, which is solved using the Newton method. The second subspace contains the stable eigenvalues, which is solved using an arbitrary fixed point iteration method. This division guarantees convergence, for an initial guess $\mathbf{u}_0$ sufficiently close to the desired steady-state $\mathbf{u}_s$, and also reduces the computational costs, with respect to the application of the Newton method to the entire subspace. A major disadvantage of RPM, however, is its implementation, which requires significant modifications of an existing fixed point iteration method.

Recently, this implementation issue was overcome by a method known as Boostconv (Citro et al., 2017). It is a modified version of RPM designed to work as a black box that can be applied to a particular family of fixed point iteration methods in the form of

$$\mathbf{u}^{k+1} = \mathbf{u}^k + \mathbf{B} \cdot \mathbf{r}^k \quad , \tag{6.12}$$

where $\mathbf{B}$ is a linear operator describing the iterative method, which could be a marching scheme, and

$$\mathbf{r}^k = \mathbf{f}(\mathbf{u}^k) \quad , \tag{6.13}$$

is the steady residue. It is possible to re-write Eq. (6.12) as

$$\mathbf{r}^{k+1} = \mathbf{r}^k - \mathbf{C} \cdot \mathbf{r}^k \quad , \tag{6.14}$$

which establishes a relationship between the residue at consecutive iteration steps through the problem dependent linear operator $\mathbf{C}$ (Loiseau et al., 2018). Convergence rates can be increased by replacing the original residue $\mathbf{r}$ in Eq. (6.14) by a modified residue $\xi(\mathbf{r})$, leading to

$$\mathbf{r}^{k+1} = \mathbf{r}^k - \mathbf{C} \cdot \xi(\mathbf{r}^k) \quad , \tag{6.15}$$

where the residue modification ξ is designed to guarantee that $\mathbf{r}^{k+1} \simeq 0$, allowing the above equation to be re-written as

$$\mathbf{C} \cdot \xi(\mathbf{r}^k) \;=\; \mathbf{r}^k \quad , \tag{6.16}$$

which eliminates the need for an iterative process at the cost of inverting matrix $\mathbf{C}$. This inversion requires $O(N^3)$ operations (Golub and Loan, 1996), making it a prohibitive calculation when the matrix dimension N is large. In order to avoid this high computational cost, the modified residue is calculated instead by Citro et al. (2017) using a projection method, namely

$$\xi(\mathbf{r}^k) \;=\; \mathbf{r}^k + \sum_{m=1}^{M} c_m \, \tilde{\mathbf{u}}_m - \sum_{m=1}^{M} c_m \, \tilde{\mathbf{v}}_m \quad , \tag{6.17}$$

where $\tilde{\mathbf{u}}_n$ and $\tilde{\mathbf{v}}_n$ are the search and restriction subspace vectors, respectively, c_n are the residue minimization coefficients, obtained from the solution of a least squares problem, and $M \ll N$ is the subspace size. On one hand, choosing $\tilde{\mathbf{u}}_m = \xi(\mathbf{r}^k)$ leads to a projection into Krylov subspaces. Hence, they represent a basis for the first M unstable eigenvalues μ_m. Doing so guarantees that the unstable eigenvalues, which do not satisfy $|\mu_m| < 1$, are damped by the residue modification whereas the stable eigenvalues, which do satisfy $|\mu_m| < 1$, are damped by the original fixed point iteration method. On the other hand, choosing $\tilde{\mathbf{v}}_n = \mathbf{r}^k - \mathbf{r}^{k-1}$ leads to $\tilde{\mathbf{v}}_n = \mathbf{C} \cdot \tilde{\mathbf{u}}_n$. It is important to note that this projection is supposed to represent the subspace of unstable eigenvalues and, hence, M must be larger than the number of unstable eigenvalues to guarantee convergence. Finally, a few additional comments must be made. The subspace bases are initially empty, with new vectors being added at each iteration until they reach the subspace size limit M. Furthermore, the Jacobian varies during the iteration process when the system is nonlinear, which forces the subspace bases to require updating. This is done every K iterations, when the older vectors are discarded and replaced by the most recent ones. When applied to a marching scheme, this black box procedure receives the original residue and delivers the modified residue at each time step.

6.2 Minimal Gain Marching Schemes

As discussed previously, SFD (Åkervik et al., 2006) and Boostconv (Citro et al., 2017) were designed to address two major issues that discourage the use of the Newton method to generate steady-states, namely *i*) its small radius of convergence, which causes a high sensitivity to poorly chosen initial conditions, as well as *ii*) its requirement of a Jacobian matrix, which creates implementation difficulties. They do so by working as black box routines that can be easily attached to an existing explicit marching scheme. There are, however, still some issues associated with the use of these methods, such as the fact that *i*) SFD cannot damp self-excited stationary disturbances,

ii) the selection of adequate values for the Boostconv control parameters is rather difficult and *iii*) neither method can accelerate convergence towards steady-state in the presence of stable but weakly damped disturbances.

An alternative approach is to try and improve the performance of the Newton method itself. A simple step is to switch it back to the implicit Euler scheme and use a large but not infinite time step. Doing so reduces the sensitivity to poorly chosen initial conditions. This can be done even for explicit marching schemes through the use of dual-time-stepping (Teixeira and Alves, 2012). However, limitations placed on the maximum time step size can prevent a time asymptotic physically unstable linear disturbance from being marched in time with a small enough gain. As illustrated in Fig. 6.1, two scenarios then emerge. On one hand, the absolute value of the gain is smaller than one but not close enough to zero. This can significantly decrease the rate with which the marching scheme converges in time towards steady-state. On the other hand, the absolute value of the gain is larger than one. In other words, these limitations prevent such modes from being placed outside of the implicit Euler scheme numerically unstable region, which leads to divergence from the desired steady-state. These limitations can have many causes. Stiffness is a typical one. It is caused by vastly different characteristic time and/or length scales. A typical example of the latter comes from very large or small cell aspect ratios within a given grid whereas a typical example of the former comes from the convective and acoustic time scales in very low

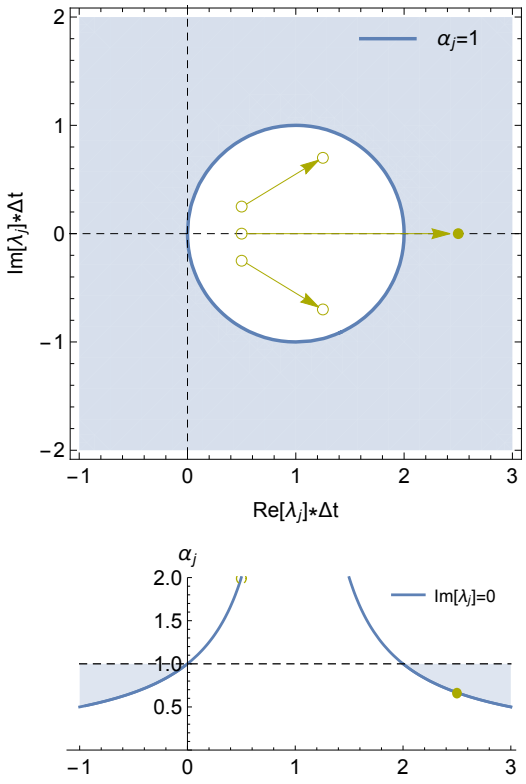

Figure 6.1: Same as Fig. 1 (right), but increasing Δt from Δt_1 to Δt_m.

Mach number flows. Strong nonlinear effects represent another typical cause, where the linear numerical stability analysis presented in this figure is no longer valid for the time step sizes used. Many techniques are available to improve steady-state convergence in this case. Examples include local-time-stepping, multi-grid, preconditioning, dual-time-stepping, continuation, etc. However, their review is beyond the scope of this report.

Recently, a novel methodology was proposed to improve the convergence of implicit marching schemes towards steady-state. The methods derived from it are collectively known as Minimal Gain Marching (MGM) schemes. This methodology solves the problems illustrated in Fig. 6.1 using a rather simple idea. In general, the complex eigenvalue λ_j is fixed by the flow linear physics and the maximum time step allowed Δt_m is restricted by stiffness and/or nonlinearity. Hence, the only alternative left is to move the numerical stability boundary defined by $\alpha_j = 1$. The idea is to place the physically unstable disturbances at $\{\mathrm{Re}[\lambda_j]\,\Delta t_m\,,\,\mathrm{Im}[\lambda_j]\,\Delta t_m\}$ into a numerically stable region with the smallest possible α_j. Convergence in time towards steady-state is then guaranteed as long as these modes are placed outside of the numerically unstable region where $\alpha_j > 1$. This is achieved by modifying the implicit marching scheme coefficients. Doing so, however, is not so easy, since a few constraints still must be satisfied for the resulting scheme to be convergent. This word is used here in its original sense, namely that a discrete governing equation converges towards the differential governing equation it was derived from as the time step goes to zero. Lax's equivalent theorem states that a scheme is convergent if, and only if, it is consistent as well as stable. The restrictions associated with the former come from a truncation error analysis whereas the ones associated with the latter come from a numerical stability analysis. It is important to note that this theorem has a linear basis and its nonlinear counterpart does not exist.

6.2.1 Multi-Step Schemes

When this methodology was first introduced (Teixeira and Alves, 2017), the two-parameter family of multi-step MGM schemes

$$\theta_1\,\frac{\mathbf{u}^{n+1}-\mathbf{u}^{n}}{\Delta t}+(1-\theta_1)\,\frac{\mathbf{u}^{n+1}-\mathbf{u}^{n-1}}{2\,\Delta t}\;=\;\theta_2\,\mathbf{f}(\mathbf{u}^{n+1})+(1-\theta_2)\,\mathbf{f}(\mathbf{u}^{n})\;\;, \tag{6.18}$$

was proposed, which returns to the implicit Euler scheme with $\theta_1 = \theta_2 = 1$ and to the second-order accurate Crank-Nicolson scheme with $\theta_1 = 1$ and $\theta_2 = 1/2$. Its numerical stability boundary, where $\alpha_j = 1$, is defined by

$$\left(\mathrm{Re}[\lambda_j]\,\Delta t-\mathcal{R}_0\right)^2+\left(\mathrm{Im}[\lambda_j]\,\Delta t\right)^2=\mathcal{R}_0^2\quad, \tag{6.19}$$

where $\mathcal{R}_0 = \theta_1/(2\,\theta_2 - 1)$. Furthermore, $\alpha_j = (\theta_2 - 1 + |\theta_2 - 1|)/(2\,\theta_2)$ when $\Delta t \to \infty$, which simplifies to $\alpha_j = (\theta_2 - 1)/\theta_2$ when $\theta_2 \geq 1$ and $\forall\,\theta_1$. These results provide a guideline for the use of this multi-step MGM scheme. Simulations should always be attempted first with $\theta_1 = \theta_2 = 1$, i.e.

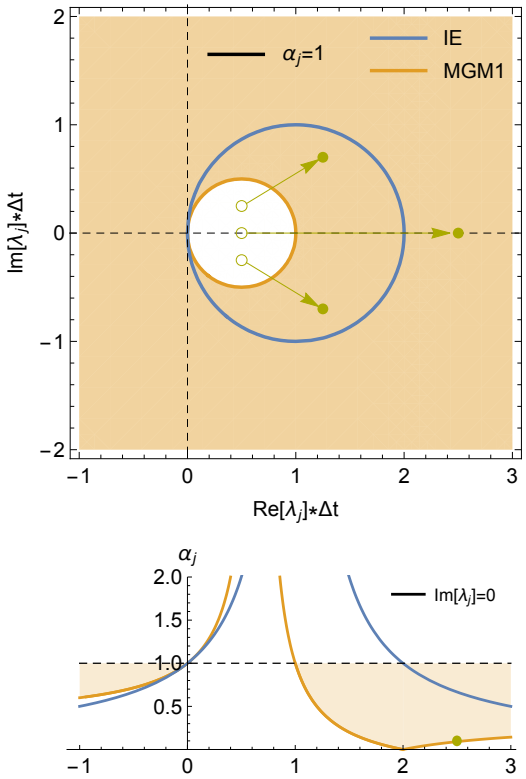

Figure 6.2: Same as Fig. 6.1, but for multi-step MGM scheme in Eq. (6.18) with $\theta_1 = 1$ and $\theta_2 = 3/2$, where $\alpha_j \to 1/3$ as $\Delta t \to \infty$.

the implicit Euler scheme, and the largest possible time step Δt_m. If, and only if, convergence is not achieved, θ_1 should be decreased and/or θ_2 should be increased to reduce the size of the numerically unstable region $\mathcal{R}_0$ until convergence is achieved with Δt_m. This is due to the fact that this MGM scheme is L-stable only when $\theta_1 = \theta_2 = 1$, i.e. the implicit Euler scheme. For every other value of these two parameters, it becomes A-stable. Furthermore, $\alpha_j \to 1$ as $\theta_2 \to \infty$ when $\Delta t \to \infty$. Hence, reducing the numerically unstable region size to enable convergence comes at the cost of reducing the time asymptotic convergence rate. Nevertheless, these points are illustrated by the linear and numerical stability of this multi-step MGM scheme shown in Fig. 6.2 with $\theta_1 = 1$ and $\theta_2 = 3/2$ for the same physically unstable modes from Fig. 6.1. The numerically unstable ones are now numerically stable whereas the numerically stable one is further stabilized.

An iterative version of Eq. (6.18) can also be developed following the same steps described in subsection 6.1.1 to derive Eq. (6.3) from Eq. (31). Applying Eq. (6.2) to and replacing $\mathbf{u}^{n+1}$ by $\mathbf{u}^{k+1}$ in Eq. (6.18) yields

$$\left\{ \frac{\theta_1 + 1}{2\,\Delta t}\,\mathbf{I} - \theta_2 \left.\frac{\partial \mathbf{f}}{\partial \mathbf{u}}\right|^k \right\} \cdot \Delta\mathbf{u} = \theta_2\,\mathbf{f}(\mathbf{u}^k) + (1-\theta_2)\,\mathbf{f}(\mathbf{u}^n) - \left\{ \theta_1 \frac{\mathbf{u}^k - \mathbf{u}^n}{\Delta t} + (1-\theta_1)\frac{\mathbf{u}^k - \mathbf{u}^{n-1}}{2\,\Delta t} \right\} \quad ,(6.20)$$

which becomes, upon replacing n by k,

$$\mathbf{u}^{k+1} \;=\; \mathbf{u}^{k} \;-\; \frac{1}{\theta_2}\,\mathbf{f}(\mathbf{u}^{k}) \Big/ \left.\frac{\partial \mathbf{f}}{\partial \mathbf{u}}\right|^{k} \quad , \tag{6.21}$$

in the limit as $\Delta t \to \infty$ and, hence, the iterative process becomes the well-known under-relaxed Newton method, which is updated with

$$\mathbf{u}^{k+1} \;=\; \omega\,\mathbf{u}^{k+1} \;+\; (1-\omega)\,\mathbf{u}^{k} \quad , \tag{6.22}$$

where $\omega = 1/\theta_2$. This means that imposing $\theta_2 > 1$ is equivalent to under-relaxing ($\omega < 1$) the marching scheme (Newton method).

6.2.2 Multi-Stage Schemes

The above comparison of this multi-step MGM scheme with the implicit Euler scheme revealed a major advantage of the former over the latter, it has a smaller region of numerical instability. However, this comparison also revealed a major disadvantage. The absolute value of its gain approaches one ($\alpha_j \to 1$) as the second control parameter is increased ($\theta_2 \to \infty$) when the time step is large ($\Delta t \to \infty$) for physically stable ($\mathrm{Re}[\lambda_j] < 0$) as well as unstable ($\mathrm{Re}[\lambda_j] > 0$) flows. The same trend is observed when under-relaxing the Newton method. In other words, numerical stabilization reduces the time asymptotic convergence rates. Despite their efforts, Teixeira and Alves (2017) were not able to create an L-stable multi-step MGM scheme.

An obvious alternative is to search for multi-stage schemes whose linear gain can be minimized at small time steps. In order to do so, only a subset of diagonally implicit Runge-Kutta (DIRK) schemes is considered here due to their computational efficiency over fully implicit RK (FIRK) schemes. This is due to the fact that they have $a_{ij} = 0$ for $j > i$, which means each intermediate stage depends on itself and previous intermediate stages but not the following ones. Known as Singly DIRK (SDIRK) schemes, this subset has $a_{ii} = \lambda$ and can be made L-stable through special constraints placed upon their coefficients. Hence, the Butcher tableau in Tab. 2.2 for the two and three-stage SDIRK schemes considered for gain minimization reduce to the respective ones shown in Tab. 6.1. According to Alexander (1977), they can be further reduced to the respective ones shown in Tab. 6.2 by imposing the required S-stability constraints.

Table 6.1: Butcher tableau for two (left) and three (right) stage SDIRK schemes employed for gain minimization.

c_1	λ	0
c_2	a_{21}	λ
	b_1	b_2

and

c_1	λ	0	0
c_2	a_{21}	λ	0
c_3	a_{31}	a_{32}	λ
	b_1	b_2	b_3

Table 6.2: Same as Tab. 6.1, but for S-stable schemes.

$$\begin{array}{c|cc} c_1 & \alpha & 0 \\ 1 & 1-\alpha & \alpha \\ \hline & 1-\alpha & \alpha \end{array} \qquad \text{and} \qquad \begin{array}{c|ccc} c_1 & \alpha & 0 & 0 \\ c_2 & \beta & \alpha & 0 \\ 1 & b_1 & b_2 & \alpha \\ \hline & b_1 & b_2 & \alpha \end{array}$$

Two-Stage MGM Scheme

The two-stage scheme is employed in the literature with $c_1 = \alpha$ and $\alpha = 0.292893$, which is a solution of $\alpha^2 - 2\,\alpha + 1/2 = 0$, because doing so makes it second-order accurate. It is important to note that all problems investigated in this report are governed by autonomous systems of equations and, hence, are independent of c_1 by definition. This scheme can then be written as

$$\begin{aligned} \mathbf{k}^{(1)} &= \mathbf{u}^n + \alpha\,\Delta t\,\mathbf{f}(\mathbf{k}^{(1)}) \quad , \\ \mathbf{k}^{(2)} &= \mathbf{u}^n + (1-\alpha)\,\Delta t\,\mathbf{f}(\mathbf{k}^{(1)}) + \alpha\,\Delta t\,\mathbf{f}(\mathbf{k}^{(2)}) \quad \text{and} \\ \mathbf{u}^{n+1} &= \mathbf{k}^{(2)} \quad , \end{aligned} \tag{6.23}$$

with a linear stability derived from Eq. (2.79) to yield

$$G_j = \frac{(1-2\,\alpha)\,\lambda_j \Delta t + 1}{(\alpha\,\lambda_j \Delta t - 1)^2} \quad , \tag{6.24}$$

when coupled with Tab. 6.2 (left). Based on Eq. (26), it is then possible to say that α_j is controlled exclusively by α and $\lambda_j \Delta t$. The numerical stability boundary of this two-stage scheme cannot be written as Eq. (6.19) when $\alpha > 1$, since it does not have the format of a circle. This is not the case when $\alpha = 1$ because this two-stage MGM scheme reverts back to the implicit Euler scheme. In other words, Eq. (6.23) becomes Eq. (31) and Eq. (6.24) becomes Eq. (35). Nevertheless, Eq. (6.24) reveals that this becomes an MGM scheme when $\alpha > 1$, as shown in Fig. 6.3 when $\alpha = 3$. For instance, physically stable flows ($\mathrm{Re}[\lambda_j] < 0$) have a small region of numerical instability when $\alpha > (2+\sqrt{2})/2$. This numerically unstable region is within

$$-\kappa < \mathrm{Im}[\lambda_j]\Delta t < +\kappa \quad \text{where} \quad \kappa = \frac{\sqrt{2\,(\alpha-2)\,\alpha + 1}}{\alpha^2} \quad , \tag{6.25}$$

when $\mathrm{Re}[\lambda] = 0$. Unfortunately, the value of $\mathrm{Re}[\lambda_j]\,\Delta t$ below which this scheme is always numerically stable ($\alpha_j < 1$) for physically stable flows ($\mathrm{Re}[\lambda_j] < 0$) can only be determined numerically. A similar analysis can be performed for physically unstable flows ($\mathrm{Re}[\lambda_j] > 0$), but when $\mathrm{Im}[\lambda_j] = 0$. They are numerically stable within

$$\mathrm{Re}[\lambda_j]\Delta t > \frac{4\,\alpha - 1 + \sqrt{8\,(\alpha-1)\,\alpha + 1}}{2\,\alpha^2} \quad , \tag{6.26}$$

when $\alpha \geqslant (2+\sqrt{2})/4$. Finally, it is important to point out that $\alpha_j \to 0$ when $\Delta t \to \infty$, i.e. this two-stage MGM scheme is L-stable.

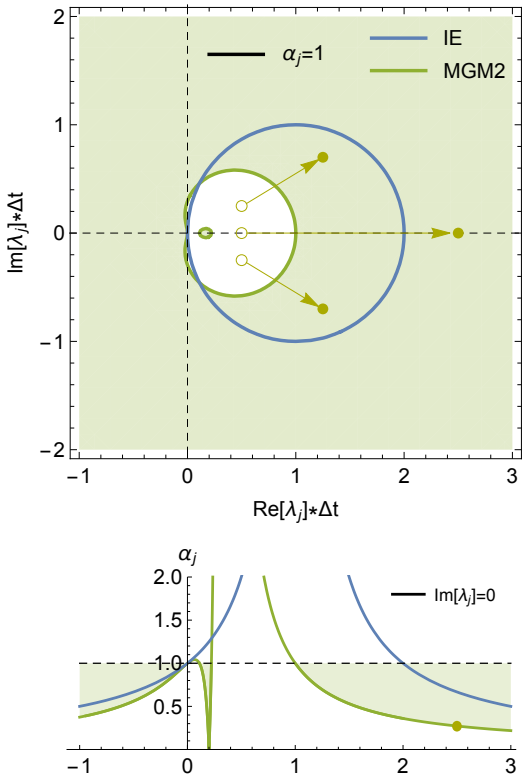

Figure 6.3: Same as Fig. 6.2, but for two-stage MGM scheme in Eq. (6.23) (left) with $\alpha = 3$, where $\alpha_j \to 0$ as $\Delta t \to \infty$.

Three-Stage MGM Scheme

In the previous subsection, it was shown that the two-stage scheme described in Tab. 6.2 (left) becomes a MGM scheme for autonomous systems when $\alpha > 1$, independent of c_1. A similar analysis can be performed for the three-stage scheme described in Tab. 6.2 (right). Applying the consistency requirements defined in Eq. (2.77) leads to

$$c_1 = \alpha \quad , \quad c_2 = \alpha + \beta \quad \text{and} \quad b_1 + b_2 + \alpha = 1 \quad , \tag{6.27}$$

whereas applying the additional constraints required to enforce L-stability from the respective rooted tree sets (Butcher, 2008) leads to

$$b_1\, c_1 + b_2\, c_2 + \alpha = \frac{1}{2} \quad \text{and} \quad b_1\, c_1^2 + b_2\, c_2^2 + \alpha = \frac{1}{3} \quad , \tag{6.28}$$

which can be combined to yield

$$c_1 = \alpha \quad , \quad c_2 = \frac{\alpha\,(\alpha + 4\,b_1 - 1) - b_1}{b_1 + \alpha - 1} \quad ,$$

$$b_2 = 1 - b_1 - \alpha \quad \text{and} \quad \beta = \frac{3\,b_1\,\alpha - b_1}{b_1 + \alpha - 1} \quad , \tag{6.29}$$

reducing the dependence of this three-stage scheme to two parameters, namely b_1 and α. Assuming $\lambda_j \neq 0$, such a scheme generally produces $\alpha_j = 0$ at

a finite and positive Δt. This is in addition to its L-stability, which means that $\alpha_j = 0$ at $\Delta t = \infty$. It is possible to force the absolute value of the linear gain to be zero only at an infinite time step by imposing

$$b_1 = \frac{\alpha\,(2\,\alpha - 1)}{3\,\alpha - 1} \quad , \tag{6.30}$$

reducing the dependence of this three-stage scheme to a single parameter, namely α. It can now be written as

$$\begin{aligned}
\mathbf{k}^{(1)} &= \mathbf{u}^n + \alpha\,\Delta t\,\mathbf{f}(\mathbf{k}^{(1)}) \quad , \\
\mathbf{k}^{(2)} &= \mathbf{u}^n + \beta\,\Delta t\,\mathbf{f}(\mathbf{k}^{(1)}) + \alpha\,\Delta t\,\mathbf{f}(\mathbf{k}^{(2)}) \quad , \\
\mathbf{k}^{(3)} &= \mathbf{u}^n + b_1\,\Delta t\,\mathbf{f}(\mathbf{k}^{(1)}) + b_2\,\Delta t\,\mathbf{f}(\mathbf{k}^{(2)}) + \alpha\,\Delta t\,\mathbf{f}(\mathbf{k}^{(3)}) \quad \text{and} \\
\mathbf{u}^{n+1} &= \mathbf{k}^{(3)} \quad ,
\end{aligned} \tag{6.31}$$

whose a linear stability is governed by

$$G_j = \frac{(3\,\alpha - 1)\,\lambda_j \Delta t - 1}{(\alpha\,\lambda_j \Delta t - 1)^3} \quad , \tag{6.32}$$

derived from Eq. (2.79). Based on Eq. (26), it is then possible to say that α_j is controlled exclusively by α and $\lambda_j \Delta t$. The numerical stability boundary of Eq. (6.31) cannot be written as Eq. (6.19) for any α, since it does not have the format of a circle. Furthermore, it does not reduce to the implicit Euler scheme for a given value of α. Nevertheless, a comparison with the implicit Euler scheme can still be performed for particular cases. For instance, if one imposes $\mathrm{Im}[\lambda_j] = 0$, the above three-stage scheme and the implicit Euler scheme have a similar region of numerical instability when $\alpha = (1 + \sqrt{3})/2$, since it produces $\alpha_j = 1$ at $\mathrm{Re}[\lambda_j]\Delta t = 2$. From this $\mathrm{Im}[\lambda_j] = 0$ perspective, Eq. (6.32) reveals that Eq. (6.31) becomes a MGM scheme when $\alpha > (1 + \sqrt{3})/2$, as shown in Fig. 6.4 when $\alpha = 1 + 2\,\cos[\pi/9]$. This value of α was chosen because it produces $\alpha_j = 1$ at $\mathrm{Re}[\lambda_j]\Delta t = 1$. More information can be extracted from Eq. (6.32). Physically stable flows ($\mathrm{Re}[\lambda_j] < 0$) are always numerically stable when $(3 - \sqrt{3})/6 < \alpha < (3 + \sqrt{3})/6$. Otherwise, there is a region of numerical instability, which is within

$$-\kappa < \mathrm{Im}[\lambda_j]\Delta t < +\kappa \quad \text{where} \quad \kappa = \sqrt{\frac{\sqrt{3\,\alpha\,(11\,\alpha - 8) + 4} - 3\,\alpha}{2\,\alpha^3}} \quad , \tag{6.33}$$

when $\mathrm{Re}[\lambda] = 0$. Unfortunately, the value of $\mathrm{Re}[\lambda_j]\,\Delta t$ below which this scheme is always numerically stable ($\alpha_j < 1$) for physically stable flows ($\mathrm{Re}[\lambda_j] < 0$) can only be determined numerically. A similar analysis can be performed for physically unstable flows ($\mathrm{Re}[\lambda_j] > 0$), but when $\mathrm{Im}[\lambda_j] = 0$. They are numerically stable within

$$\mathrm{Re}[\lambda_j]\Delta t > \frac{3\,\sqrt{\alpha} + \sqrt{9\,\alpha - 4}}{2\,\sqrt{\alpha^3}} \quad , \tag{6.34}$$

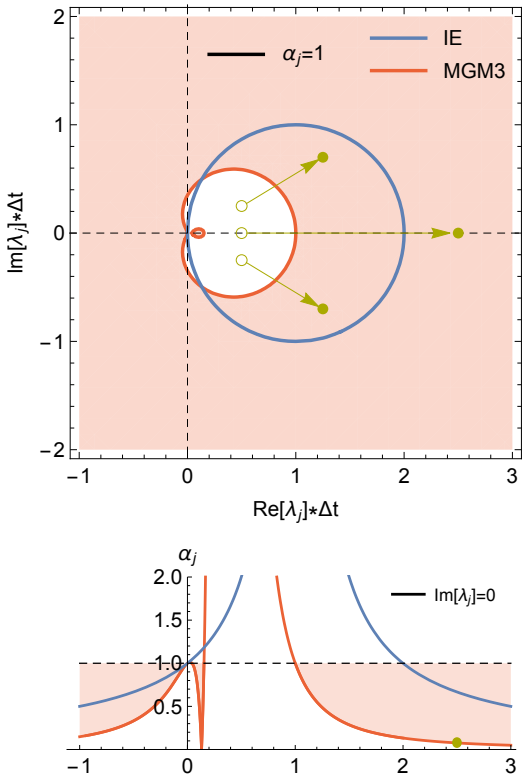

Figure 6.4: Same as Fig. 6.3, but for three-stage MGM scheme in Eq. (6.31) with $\alpha = 1 + 2\cos[\pi/9]$, where $\alpha_j \to 0$ as $\Delta t \to \infty$.

when $\alpha \geqslant 4/9$. Another analytical expression can be derived for smaller values of α. It is not shown here because it is not only too cumbersome but also unnecessary, since the MGM behavior of this three-stage scheme is obtained when $\alpha > (1 + \sqrt{3})/2$.

Comparative Analysis

Having developed these first-order two and three-stage MGM schemes, whose region of numerical instability is smaller than the one of the implicit Euler scheme for a high enough α, a more detailed comparative analysis between these schemes can be performed. Such a comparison is shown in Fig. 6.5, where the multi-step, two and three-stage MGM schemes are plotted with $\text{Im}[\lambda_j] = 0$ and $\alpha_j = 1$ at $\text{Re}[\lambda_j]\Delta t = 1.0$ (top) and 0.5 (bottom). The implicit Euler scheme, where $\alpha_j = 1$ at $\text{Re}[\lambda_j]\Delta t = 2.0$ when $\text{Im}[\lambda_j] = 0$, is also shown for comparison purposes. Physically stable ($\text{Re}[\lambda_j] < 1$) linear gain absolute values (α_j) decrease as one switches from the multis-step MGM scheme to the implicit Euler scheme to the two-stage MGM scheme to the three-stage MGM scheme. A more complex scenario appears for physically unstable ($\text{Re}[\lambda_j] > 1$) flows. Short time step trends, i.e. $\text{Re}[\lambda_j]\Delta t < 2.0$, suggest that MGM1 can have the smallest α_j, since $\alpha_j = 0$ at a finite Δt. Computer times required for residual convergence in time towards machine zero with a given time step, however, show that nonlinearities create an

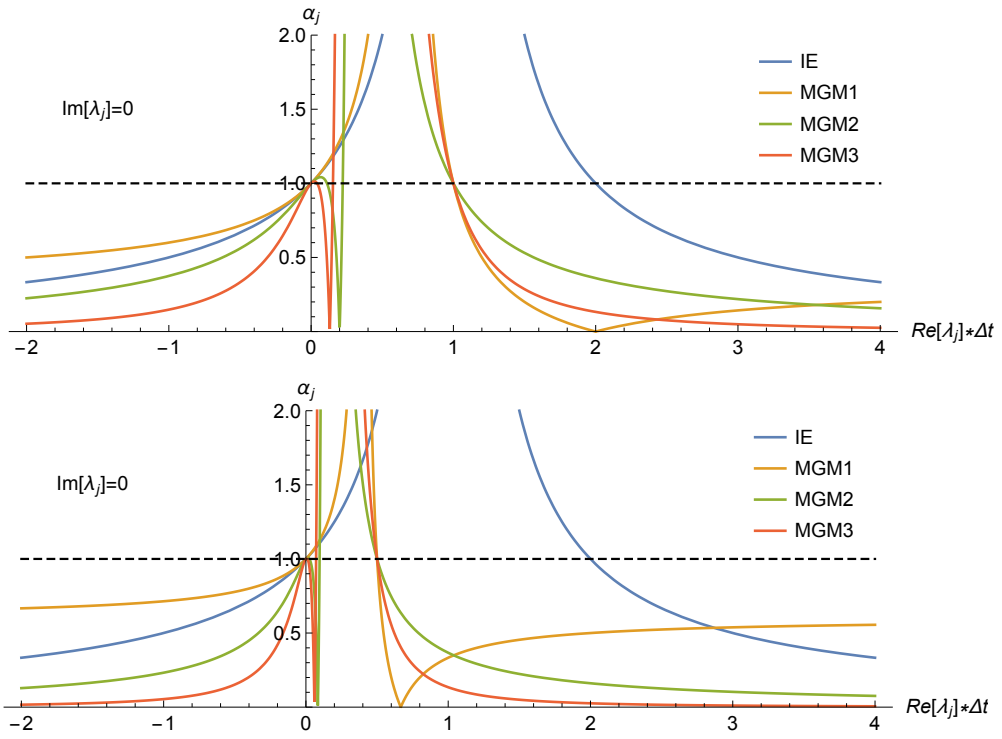

Figure 6.5: Combined results from Figs. 6.1 to 6.4 with $\mathrm{Im}[\lambda_j] = 0$ for the multi-step as well as two and three-stage MGM schemes; labelled MGM1, MGM2 and MGM3; with $\alpha_j = 1$ at $\mathrm{Re}[\lambda_j]\Delta t = 1.0$ (top) and 0.5 (bottom), with the implicit Euler scheme shown for reference purposes.

approximately smooth transition between divergence and time asymptotic convergence as the time step is increased (Teixeira and Alves, 2017). Hence, in practice, the small time step nonlinear gain of the multi-step MGM scheme does not decrease below the large time step linear gain. Large time step trends, i.e. $\mathrm{Re}[\lambda_j]\Delta t \gg 2.0$, suggest that MGM3 has the smallest α_j, followed by MGM2 and the implicit Euler scheme, where the multi-step MGM has the highest α_j. This analysis of physically stable and unstable flows suggests that MGM2 and MGM3 with a high α should outperform the implicit Euler scheme and MGM1 when the maximum time step, limited by stiffness and nonlinearities, is small enough. Otherwise, their linear gain will not be small enough to make up for the additional number of equations they must solve, rendering them less efficient than the implicit Euler scheme. The next chapter provides results for a few test cases that support this statement.

Chapter 7

Results

7.1 Lorenz Equations

7.1.1 Physics

The Lorenz equations are now used to evaluate the performance of the steady-state solvers discussed in the previous chapter. They are given by

$$\begin{aligned} \dot{x}(t) &= \sigma \left(y(t) - x(t) \right) \quad , \\ \dot{y}(t) &= x(t) \left(\rho - z(t) \right) - y(t) \quad \text{and} \\ \dot{z}(t) &= x(t)\, y(t) - \beta\, z(t) \quad , \end{aligned} \tag{7.1}$$

where $\cdot = d/dt$. There is a large literature about the behavior of these equations as a functions of their control parameters (Sparrow, 1982). In the

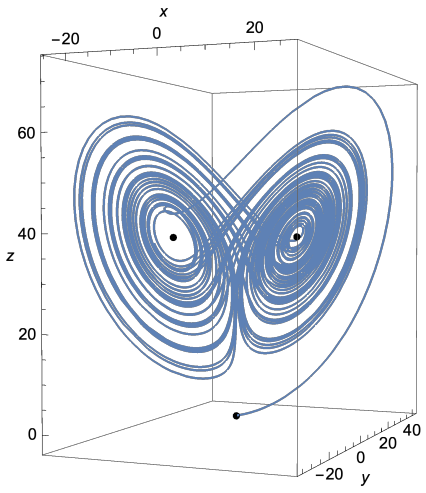

Figure 7.1: Phase portrait of the Lorenz numerical solution for $\sigma = 10$, $\rho = 40$ and $\beta = 8/3$ obtained using **NDSolve** from *Mathematica* 12 with working precision 20 and initial conditions $x(0) = y(0) = z(0) = 0.1$. Solid points represent the three unstable steady-states from Eq. (7.2).

present analysis, they are chosen as $\sigma = 10$, $\rho = 40$ and $\beta = 8/3$. Its time-accurate unsteady behavior is shown in Fig. 7.1, which is a three-dimensional phase portrait of all these variables for $0 < t < 50$. It was obtained using the Crank-Nicolson scheme, which the the multi-step MGM scheme with $\theta_1 = 1$ and $\theta_2 = 1/2$, with a time step of $\Delta t = 10^{-4}$.

Before evaluating the performance of these solvers, the linear and modal stability of this dynamical system around its steady-states is analyzed under the above parametric conditions. Doing so provides information about the temporal behavior of the small amplitude disturbances that must be damped. There are three steady-states, namely

$$x_s = y_s = z_s = 0 \quad \text{and} \quad x_s = y_s = \pm\sqrt{\beta\, z_s} \quad \text{with} \quad z_s = \rho - 1 \quad , \tag{7.2}$$

which do not depend on σ. Applying Eqs. (13) and (18) to Eq. (7.1), where $\mathbf{u} = \{x, y, z\}$ and $\mathbf{v} = \mathbf{u}_n$, leads to the eigenvalue problem

$$\lambda_j \begin{pmatrix} x_n \\ y_n \\ z_n \end{pmatrix} = \begin{pmatrix} -\sigma & \sigma & 0 \\ \rho - z_s & -1 & -x_s \\ y_s & x_s & -\beta \end{pmatrix} \cdot \begin{pmatrix} x_n \\ y_n \\ z_n \end{pmatrix} \quad , \tag{7.3}$$

for an arbitrary steady-state, which depends on all three parameters. Solving this problem for the parametric conditions from Fig. 7.1 and the steady-states in Eq. (7.2) leads to the eigenvalues shown in Fig. 7.2. Many interesting things observed in this figure help explain the unsteady behavior observed in Fig. 7.1. For instance, the trivial steady-state is strongly unstable ($\mathrm{Re}[\lambda_j] \gg 1$) to a stationary disturbance ($\mathrm{Im}[\lambda_j] = 0$) whereas the non-trivial steady-states are weakly unstable ($0 < \mathrm{Re}[\lambda_j] \ll 1$) to oscillatory disturbances ($\mathrm{Im}[\lambda_j] \neq 0$). This explains why the unsteady solution never converges to

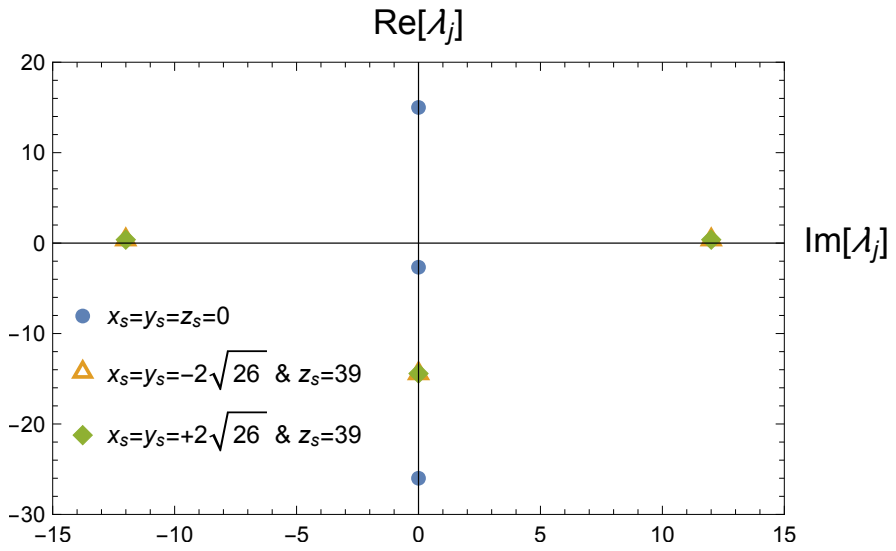

Figure 7.2: Linear and modal spectra of the trivial and non-trivial steady-states of the Lorenz equations for $\sigma = 10$, $\rho = 40$ and $\beta = 8/3$.

any steady-state, oscillating instead around the non-trivial steady-states, but not the trivial one. All other disturbances associated with these steady-states are stable and stationary. Hence, they do not interfere in any significant way with the time asymptotic behavior of this dynamics system.

7.1.2 Numerics

Having understood the physical behavior of the Lorenz equations under the aforementioned parametric conditions, the performance of the different steady-state solvers can be analyzed when applied to this problem. All the simulations employed in this analysis were carried out in a computer with the following configuration: Intel Xeon E5-2670 v2 with 25 Mb of Cache and 2.50 GHz, maximum memory band width of 59,7 GB/s and 128 Gb of RAM. The compiler used is the GNU Fortran (Debian 4.7.2-5) 4.7.2. The code was developed in C++ using the PETSc library.

All three steady-states can be numerically obtained from the available steady-state solvers. In order for a specific steady-state to be obtained, however, the initial condition supplied to the steady-state solver must be close enough to this specific steady-state. This is illustrated in Fig. 7.3 for $y(t)$, where the Crank-Nicolson scheme with $\Delta t = 10^{-3}$ is replaced by the multi-step MGM scheme with $\theta_2 = 2\,\theta_1 = 2$ at $t = 3.0$ (red), $t = 5.4$ (blue) and $t = 7.5$ (yellow) using $\Delta t = 0.05$, 0.05 and 0.20, respectively, which leads to the recovery of all three steady-states described in Eq. (7.2).

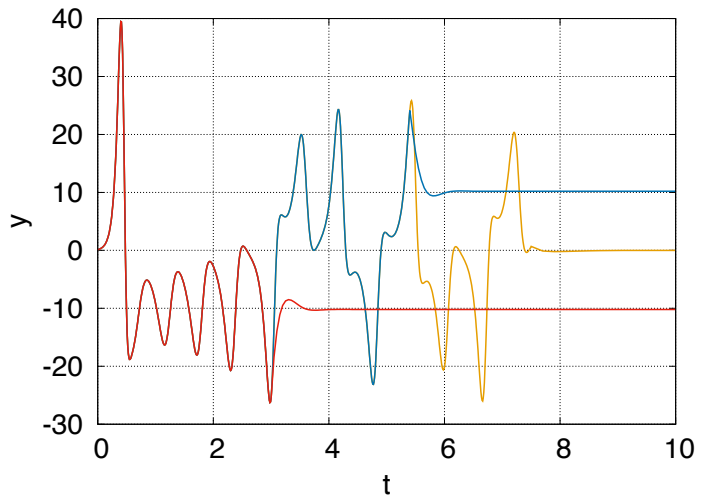

Figure 7.3: Same simulation conditions reported in Fig. 7.1, but switched to the multi-step MGM scheme with $\theta_2 = 2\,\theta_1 = 2$ at $t = 3.0$ (red), $t = 5.4$ (blue) and $t = 7.5$ (yellow) using $\Delta t = 0.05$, 0.05 and 0.20, respectively.

An efficiency analysis is now performed for these steady-state solvers. It considers the computational time CPU_c required by both residue and increment to decrease below a certain tolerance, namely $||f(u)||_\infty < 10^{-8}$ and $||u^{n+1} - u^n||_\infty < 10^{-8}$ with $u = x$, y and z, for a given time step Δt.

These criteria are based on the steady-state accuracy constraints defined in Eqs. (11) and (16). The steady-state simulations employed to measure these quantities use the time-accurate solution from Fig. 7.1 at $t = 1$ as initial condition. Figure 7.4 shows these results for the multi-step, two-stage and three-stage MGM schemes, labelled MGM1, MGM2 and MGM3, respectively. The curve obtained using the implicit Euler scheme is labelled IE. Overall, it is possible to say that the trends predicted by the linear gain analysis from the previous chapter are approximately reproduced here. All schemes eventually diverge for a small enough time step and smoothly reach their smallest computational time at large enough time steps. The only exception for the linear gain predictive capability occurs for the multi-step MGM scheme (MGM1), since its smallest CPU_c is not observed at a finite Δt. In any case, this is an expected behavior caused by nonlinear effects, as already discussed (Teixeira and Alves, 2017). Nevertheless, MGM1 is indeed capable of reducing the numerically unstable region of IE, buts its large time step computational times are larger. Its behavior for different control parameters is qualitatively similar and, hence, is not shown. On the other hand, the numerically unstable regions of MGM2 and MGM3 decrease almost monotonically as their control parameter is increased and their computational times decrease almost monotonically as the time step increases. They are more efficient than IE for small time steps, but less so for large time steps. This is due to the fact that MGM2 and MGM3 have to solve two and three times more equations than IE, respectively, which makes them less efficient when the linear gain difference between these schemes is not large enough.

The previous analysis focused on steady-state solvers based on implicit

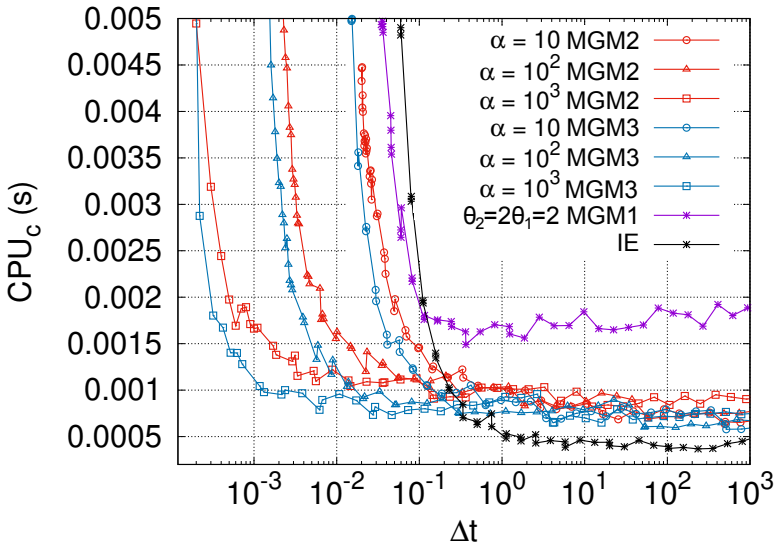

Figure 7.4: Efficiency analysis of the steady-state solvers that employ implicit marching schemes for $\sigma = 10$, $\rho = 40$ and $\beta = 8/3$. The multi-step, two-stage and three-stage MGM schemes are labelled MGM1, MGM2 and MGM3, respectively, where the implicit Euler scheme is labelled IE.

marching schemes, namely MGM schemes and the implicit Euler scheme. They are now compared to steady-state solvers based on explicit marching schemes, namely Boostconv and SFD. In order to perform this comparison, only their respective optimal time steps are employed. All implicit marching schemes use an asymptotically large time step, i.e. $\Delta t = 10^8$. This essentially makes the implicit Euler scheme run as a Newton method. Boostconv and SFD are marched in time using the explicit Euler scheme with $\Delta t = 0.058$ and 0.07, respectively. Furthermore, only their respective optimal control parameters are employed as well. The multi-step MGM scheme used $\theta_2 = 2 \times \theta_1 = 2$ whereas the multi-stage MGM schemes used $\alpha = 10^3$. SFD, on the other hand, used $\Delta = 0.1635$ and $\chi = 6$. Finally, Boostconv used $M = 2$ and $K = 1$. It is important to mention that the search for these optimal parameters was manual. Nevertheless, they are quite easy to find following known guidelines. The only exception was Boostconv, which took significantly longer to optimize. This points to an interesting research topic, namely the development of guidelines for the easy identification of optimal Boostconv parameters, which was not pursued in this work. In any case, these comparisons are provided in Fig. 7.5 for the solution time increment (left) and residue (right) throughout computer time (CPU). The latter is used instead of time because both time step and cost per iteration of each solver are different. This figure shows that both multi-stage MGM schemes as well as Boostconv have an essentially Newton-like asymptotic convergence rate towards steady-state whereas SFD converges to steady-state the slowest, with the multi-step MGM scheme only slightly faster. Nevertheless, all solvers eventually reach approximately the same machine zero residue.

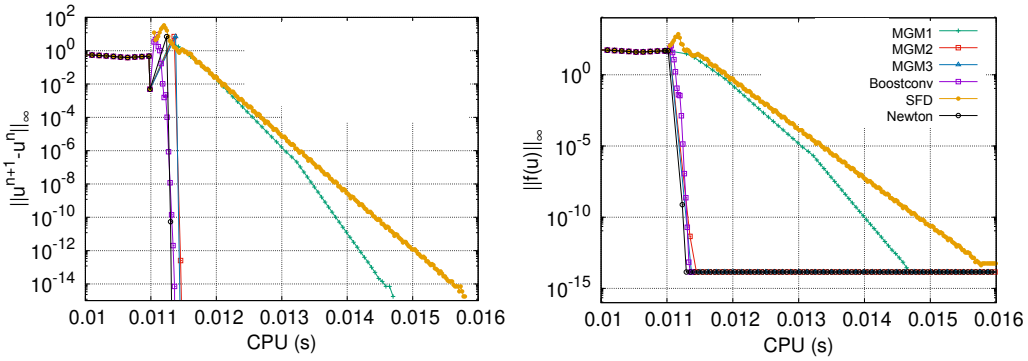

Figure 7.5: Time increment (left) and steady residue (right) as a function of computer time for all steady-state solvers under optimal parameters.

7.2 Modified Burgers Equations

7.2.1 Physics

The modified Burgers' equation is a toy model developed to teach basic concepts about linear absolute instability (Barletta and Alves, 2017). It is

used here to evaluate the performance of the steady-state solvers discussed in the previous chapter. In this toy model, a source term is introduced in the traditional Burgers' equation, modifying it to

$$\frac{\partial u}{\partial t} + u\,\frac{\partial u}{\partial x} = \frac{1}{Re}\,\frac{\partial^2 u}{\partial x^2} - \mathcal{R}\,(u-1) \quad , \tag{7.4}$$

which is written in dimensionless form using the characteristic length and velocity scales U_∞ and L_∞. This leads to the parameters Re and $\mathcal{R}$. The former is the Reynolds number whereas the latter controls the stability of this dynamical system. Imposing

$$u(x=0,t) = 1 \quad \text{and} \quad \left.\frac{\partial u}{\partial x}\right|_{x=\mathcal{L}} = 0 \quad , \tag{7.5}$$

as boundary conditions, where $\mathcal{L}$ is the dimensionless domain size, leads to the uniform dimensionless steady-state

$$u_s = 1 \quad , \tag{7.6}$$

which does not depend on either control parameter. In other words, U_∞ is the dimensional uniform steady-state. L_∞, on the other hand, is just an arbitrary length scale. Two different unsteady physical behaviors can be expected from this model. In order to illustrate them, L_∞ is defined as a viscous length scale, which leads to $Re = 1$. Both behaviors are illustrated in Fig. 7.6, which shows the the unsteady nonlinear disturbance $u_d(x,t) = u(x,t) - u_s$ along the one-dimensional domain $x/\mathcal{L}$ at different times for $\mathcal{R} = 0.24$ and $\mathcal{L} = 250$ (left) and $\mathcal{R} = 2$ and $\mathcal{L} = 200$ (right). Furthermore, both cases were integrated in time using an explicit Euler scheme from the steady-state as initial condition using a time step of $\Delta t = 5 \times 10^{-5}$, with a spatial discretization that employs WENO5-JS with the Lax-Friedrichs flux-vector splitting for the inviscid flux derivative and a fourth-order accurate conservative central-difference scheme for the viscous flux derivative using $N_X = 4001$ grid points. The numerical disturbance was introduced through a Gaussian source term in the governing equation in the form of $A_0\, e^{-B_0\,(x-x_p)^2}$, where $A_0 = 10^{-10}$, $B_0 = 20$ and

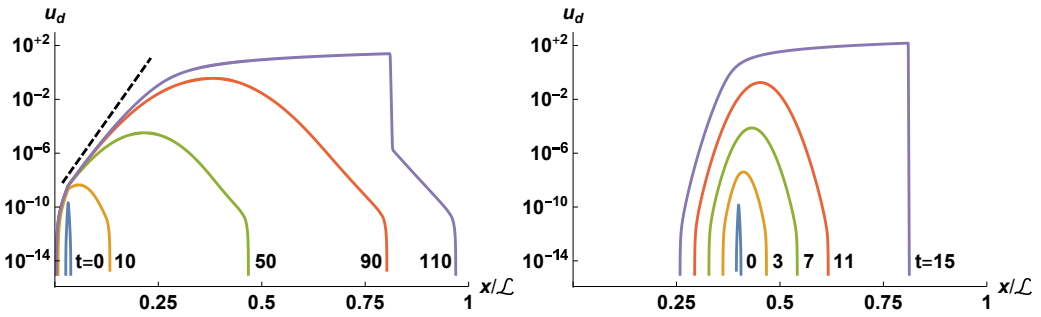

Figure 7.6: Unsteady nonlinear disturbance for $Re = 1$ along the one-dimensional domain at different times for $\mathcal{R} = 0.24$ and $\mathcal{L} = 250$ (left) and $\mathcal{R} = 2$ and $\mathcal{L} = 200$ (right). Dashed line represents linear stability growth.

$x_p = 10$ and 80 for each case. After a long enough time has passed, a linear convectively (left) and absolutely (right) unstable stationary disturbance can be observed to grow from the excitation source location. This manifests as an exponential spatial growth downstream of the source in the former case and it does so as an exponential temporal growth at the source location in the latter case, with a distinct disturbance propagation upstream of the source. Both scenarios occur until the disturbance reaches nonlinear saturation, which leads to the appearance of a shock in the disturbance itself.

In order to better understand the underlying physics associated with the behaviors just presented in Fig. 7.6, the linear and modal stability of this dynamical system around its steady-state is analyzed. This is done here by modifying Eqs. (13) and (18) to use instead

$$u(x,t) = u_s + \epsilon\, u_n\, e^{i\,\alpha\, x + \lambda\, t} + c.c. \quad , \tag{7.7}$$

where $c.c.$ and α mean complex conjugate and wavenumber, respectively. Substituting Eqs. (7.6) and (7.7) into Eq. (7.4) leads to

$$\mathcal{R} - \frac{\alpha^2}{Re} - i\,\alpha - \lambda \,=\, 0 \quad , \tag{7.8}$$

when collecting the terms of $O(\epsilon)$. The above equation is better known as a dispersion relation. It should noted that these equations are often written using the complex frequency ω instead in the context of stability analyses, where $\lambda = -\,i\,\omega$. Both terms are used interchangeably here. Separating real and imaginary parts of Eq. (7.8), one can solve for the parametric conditions bellow which the flow is linearly and modally stable, i.e. disturbances neither grow nor decay in space ($\mathrm{Im}[\alpha] = 0$) and time ($\mathrm{Im}[\omega] = 0$ or $\mathrm{Re}[\lambda] = 0$). Known as marginal stability curve, it is given by

$$\mathrm{Re}[\omega] = \mathrm{Re}[\alpha] \quad \text{and} \quad \mathcal{R} = \frac{\mathrm{Re}[\alpha]^2}{Re} \quad , \tag{7.9}$$

whose critical point, i.e. the minimum point of the second equation above, indicates that this flow first becomes unstable to an uniform ($\mathrm{Re}[\alpha] = 0$) and stationary ($\mathrm{Re}[\omega] = 0$) small amplitude disturbance when $\mathcal{R} > \mathcal{R}_c = 0$. This can be demonstrated by allowing $\mathrm{Im}[\omega] \neq 0$ when analyzing Eq. (7.8), which leads o $\mathrm{Im}[\omega] = \mathcal{R} - \mathrm{Re}[\alpha]^2/Re$. Hence, $\mathrm{Im}[\omega] > 0$ (or $\mathrm{Re}[\lambda] > 0$) when $\mathcal{R} > \mathrm{Re}[\alpha]^2/Re$. The same conclusion can be drawn by allowing $\mathrm{Im}[\alpha] \neq 0$ instead, which results in $-2\,\mathrm{Im}[\alpha] = Re - \{Re^2 - 4\,(\mathcal{R}\,Re - \mathrm{Re}[\alpha]^2)\}^{1/2}$. Hence, $-\mathrm{Im}[\alpha] > 0$ when $\mathcal{R} > \mathrm{Re}[\alpha]^2/Re$. It is worth pointing out that these marginally stable modes represent non-dispersive waves, since their wave speed $\mathrm{Re}[c] = \mathrm{Re}[\omega]/\mathrm{Re}[\alpha] = 1$ does not depend on $\mathrm{Re}[\alpha]$. In other words, modes with different wavenumbers propagate with the same velocity. Hence, a slightly supercritical wave packet does not change its shape as it propagates. This analysis, however, does not inform the nature of the instability beyond the critical point. In order to do so, one must also evaluate the linear onset of absolute instability (Alves et al., 2019). Taking

the derivative of Eq. (7.8) with respect to the wavenumber and imposing the zero group velocity condition yields

$$\frac{2\,\alpha}{Re} + i \;=\; 0 \quad , \tag{7.10}$$

which is an auxiliary dispersion relation. Solving Eqs. (7.8) and (7.10) for the complex wavenumber and frequency yields

$$\begin{aligned} &\mathrm{Re}[\alpha_0] = 0 \quad , \quad \mathrm{Im}[\alpha_0] = -\frac{Re}{2} \quad , \\ &\mathrm{Re}[\omega_0] = 0 \quad \text{and} \quad \mathrm{Im}[\omega_0] = \mathcal{R} - \frac{Re}{4} \quad , \end{aligned} \tag{7.11}$$

where the subscript 0 indicates the above result represents a saddle point. It suggests the flow will become absolutely unstable to a uniform ($\mathrm{Re}[\alpha_0] = 0$) and stationary ($\mathrm{Re}[\omega_0] = 0$) disturbance when $\mathcal{R} > \mathcal{R}_a = Re/4$, since $\mathrm{Im}[\omega_0] > 0$ under these conditions. Before proceeding any further, one must confirm that this saddle point indeed represents an absolute instability. In other words, one must verify it is actually a pinching point, i.e. it is formed by the collision between downstream (α^+) and upstream (α^-) propagating branches on the complex wavenumber plane. This is confirmed using the collision criterion and the steepest descent curve shown in Fig. 7.7, which were constructed using Eq. (7.8) with $\lambda = -i\,\omega$, $Re = 1$ and $\mathcal{R} = \mathcal{R}_a$. The propagation direction of both branches was confirmed from their respective group velocities, calculated from $\mathcal{U} = 1 + 2\,\mathrm{Im}[\alpha]$, when $\mathcal{R} \ll \mathcal{R}_c$. It is now possible to understand what caused the behaviors observed in Fig. 7.6. When choosing $Re = 1$, one obtains $\mathcal{R}_a = 0.25$. Hence, imposing $\mathcal{R} = 0.24$ leads to the convectively unstable behavior shown in Fig. 7.6 (left) whereas imposing $\mathcal{R} = 2$ leads to the absolutely unstable behavior shown in Fig. 7.6 (right), both before the disturbance amplitude grew large enough to reach nonlinear saturation and invalidate the linear stability analysis just described. This was

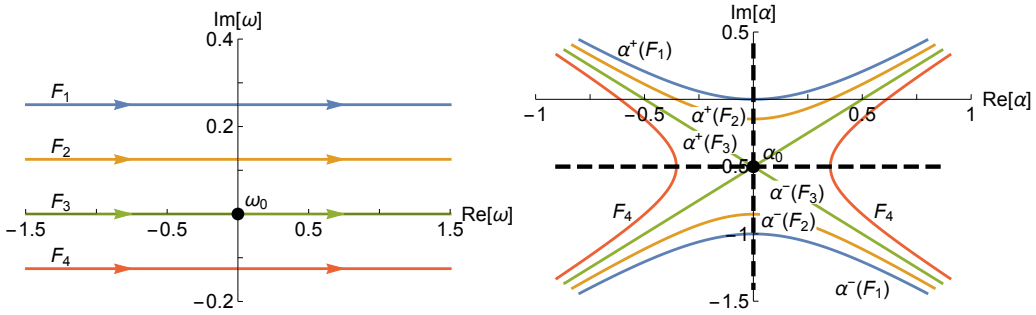

Figure 7.7: Collision criterion constructed using the integration contours $\mathbf{F}$ on the complex frequency plane (left) used to find α_0 on the complex wavenumber plane (right) with $\lambda = -i\,\omega$, $Re = 1$ and $\mathcal{R} = \mathcal{R}_a$. Horizontal and vertical thick dashed lines represent the steepest descent and ascent curves passing by α_0. Solid circles mark the singularity (ω_0,α_0).

quantitatively confirmed by fitting the expected linear stability functions to the numerical simulation data from Fig. 7.6 using nonlinear regression. Doing so led to spatial and temporal growth rates that deviate from their respective values from linear stability theory by only 2 and 3 percent, respectively.

7.2.2 Numerics

Having understood the linear convective/absolute instability nature of the flow modeled by the modified Burgers' equation, which is dominated in both cases by uniform and stationary disturbances, the performance of the steady-state solvers of interest can be analyzed. Note that SFD was not included in this list because it cannot damp stationary disturbances. The convectively unstable case is discussed in detail in the third and final part of this report, since it falls into the zero complex frequency disturbance scenario ($\lambda = 0$). Hence, only the absolutely unstable case is discussed in this subsection. The same computer with the same configuration from the previous section was employed to perform this study.

All simulations were performed using the steady-state defined in Eq. (7.6) as initial condition, where the flow was perturbed using the same source term described in the previous section, now positioned at the middle of the domain. Furthermore, periodic boundary conditions were implemented. However, the domain size is chosen large enough to prevent disturbances from reaching its boundaries within the flow time simulated. Simulations were performed with $Re = 32$, which leads to $\mathcal{R}_a = 8$ according to Eq. (7.11). Additionally, the domain size is $\mathcal{L} = 6$, the number of grid points is $N_x = 701$, the time step is $\Delta t = 10^{-5}$ and stability control parameter is $\mathcal{R} = 3000$. The latter was chosen in such a way as to produce a linear absolute instability whose

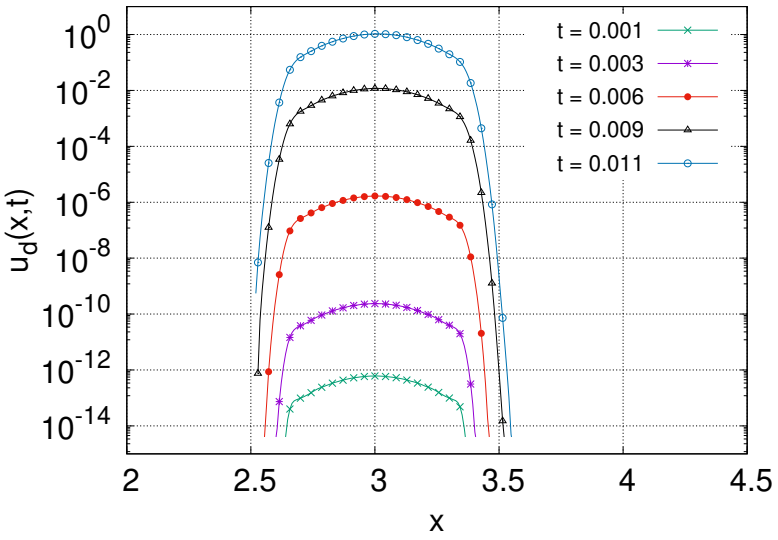

Figure 7.8: Temporal and spatial growth of the nonlinear disturbance of this linear and absolutely unstable flow with $Re = 32$ and $\mathcal{R} = 3000$, simulated with the same methods used to generate the results shown in Fig. 7.6.

dominant uniform and stationary disturbance has a large temporal growth rate. Its temporal growth is shown in Fig. 7.8. The disturbance propagation both upstream and downstream of the source location typical of an absolute instability can be observed as well. Finally, it is important to note that these time-accurate results were obtained using the same numerical methods employed to generate the results shown in Fig. 7.6.

When the maximum disturbance amplitude reaches $||u_d||_\infty = 1$, the time-accurate unsteady simulation is stopped. This occurs at $t = 0.011$, as shown in Fig. 7.8, which is when the steady-state solver is turned on. From this point on, the computational time CPU_c required by both increment and residue to decrease below a certain tolerance, namely $||u^{n+1} - u^n||_\infty < 10^{-8}$ and $||f(u)||_\infty < 10^{-8}$, is measured for different time steps Δt. As done in the previous section, the efficiency of solvers based on implicit marching schemes is compared first. These results are shown in Fig. 7.9, which uses the same legend employed by Fig. 7.4. Both figures present essentially the same trends, in the sense that the current ones also approximately follow the behavior predicted by the linear gain analysis from the previous chapter. They are: *i*) all schemes eventually diverge for a small enough time step, *ii*) all L-stable schemes reach their smallest computational time at large enough time steps in an approximately smooth fashion, *iii*) the MGM1 scheme is slower than the IE scheme at large time steps but is convergent at smaller time steps, having a minimum close to the divergence point, *iv*) increasing the time step makes the computational times of the IE, MGM2 and MGM3 decrease towards their smallest values, which are approximately the same, in an approximate smooth fashion, but *v*) the MGM2 and MGM3 are significantly more efficient than IE at smaller time steps, where *vi*) how small depends on how large is the control parameter α.

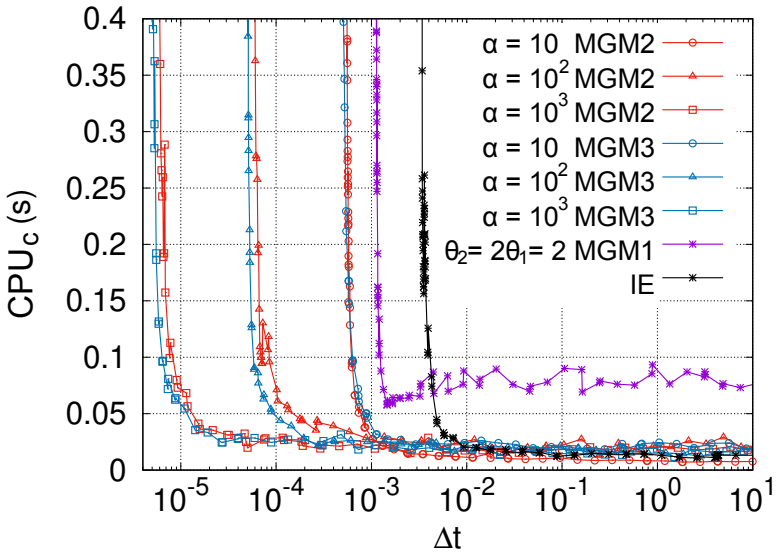

Figure 7.9: Same as Fig. 7.4, but for absolutely unstable modified Burgers' equation with $Re = 32$ and $\mathcal{R} = 3000$.

These steady-state solvers based on implicit marching schemes are now compared to their counterparts based on explicit marching schemes, which includes only Boostconv, since SFD cannot damp stationary disturbances. This is done under their respective optimal control parameters, which were obtained manually. All implicit marching schemes use the asymptotically large time step of $\Delta t = 10^8$ whereas Boostconv is applied to the explicit Euler scheme with $\Delta t = 1.3 \times 10^{-5}$. Furthermore, the optimal control parameters are $\theta_2 = 2 \times \theta_1 = 2$ for the multi-step MGM scheme, $\alpha = 10^3$ for the multi-stage MGM schemes as well as $M = 7$ and $K = 1$ for Boostconv. Once again, it was significantly more difficult to perform this optimization for Boostconv. These results are shown in Fig. 7.10, which is analogous to Fig. 7.5, showing the solution time increment (left) and residue (right) throughout computer time (CPU). As expected, both multi-stage MGM schemes as well as Boostconv have an essentially Newton-like asymptotic convergence rate towards a steady-state with a machine zero residue whereas the multi-step MGM scheme converges the slowest to it.

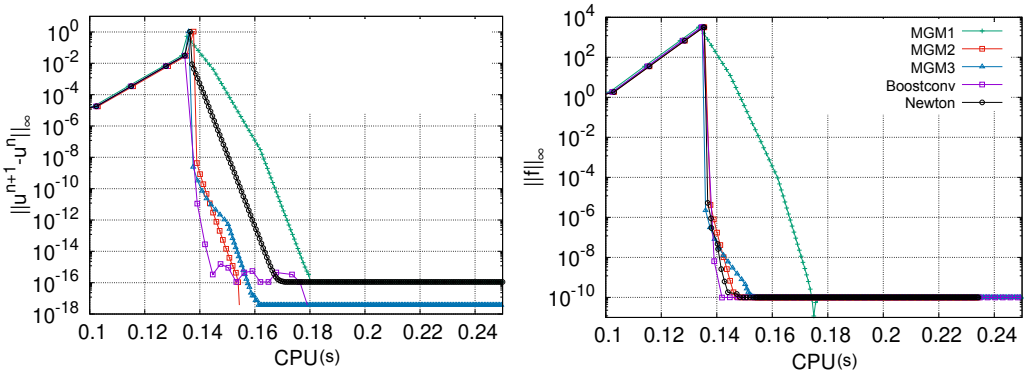

Figure 7.10: Same as Fig. 7.5, but for the modified Burgers' equation.

7.3 Modified 1D Navier-Stokes Equations

7.3.1 Physics

The third and final test case employed in this second part of the report is based on the classical problem used to verify compressible flow codes, known as the advection of an entropy disturbances (Alves et al., 2021). However, a modified version is used instead to evaluate the performance of the steady-state solvers being analyzed here. This new version of the model is given by Eqs. (2.5) to (2.14) with $N = 1$, but written as

$$\frac{\partial \mathbf{Q}}{\partial t} + \frac{\partial \mathbf{E}}{\partial x} = \frac{\partial \mathbf{F}}{\partial x} + \mathbf{S} \quad , \tag{7.12}$$

where the source term that modifies the classical model is defined as

$$\mathbf{S} = \mathcal{R} \left\{ \begin{array}{c} \rho - 1 \\ \rho\, u - 1 \\ (\rho\, E - 1) + \frac{1}{2}\,(u-1)^2 \end{array} \right\} \quad , \tag{7.13}$$

and $\mathcal{R}$ is the new parameter that controls the flow stability, where all fluid properties are assumed constant for this particular study. It is written in dimensionless form using the free stream conditions defined in Eq. (2.21), leading to the other parameter definitions in Eq. (2.22). Imposing periodic boundary conditions within the dimensionless domain $0 \leq x \leq 1$ leads to the control parameter free, uniform and dimensionless steady-state

$$\rho_s = 1 \quad , \quad u_s = 1 \quad \text{and} \quad T_s = 1 \quad , \tag{7.14}$$

which means $p_s = 1/(\gamma\, Ma_\infty^2)$, based on Eq. (2.18). In other words, ρ_∞, U_∞ and T_∞ are the dimensional uniform steady-states. Due to the spatial periodicity of this problem, a temporally evolving flow is expected. In order to control this evolution, the initial condition is defined as

$$\rho(x,0) = 1 + A_0\, \cos[\,\alpha_0\, x\,] \quad \text{and} \quad u(x,0) = T(x,0) = 1 \quad , \tag{7.15}$$

where $A_0 = 10^{-4}$ and $\alpha_0 = 2\,\pi\, m$ are the amplitude and wavenumber of the initial disturbance, with $m = 3$ chosen in the present study. Furthermore, $Re_\infty = \infty$, $Pr_\infty = 0.72$, $Ma_\infty = 0.5$ and $\gamma = 1.4$ are imposed. Additionally imposing $\mathcal{R} = 0$ leads to the classical behavior where small amplitude entropy disturbances are advected downstream with constant amplitude and wave speed. When $\mathcal{R} > 0$, on the other hand, the amplitude of these disturbances grows exponentially in time. This can be observed in Fig. 7.11, which shows

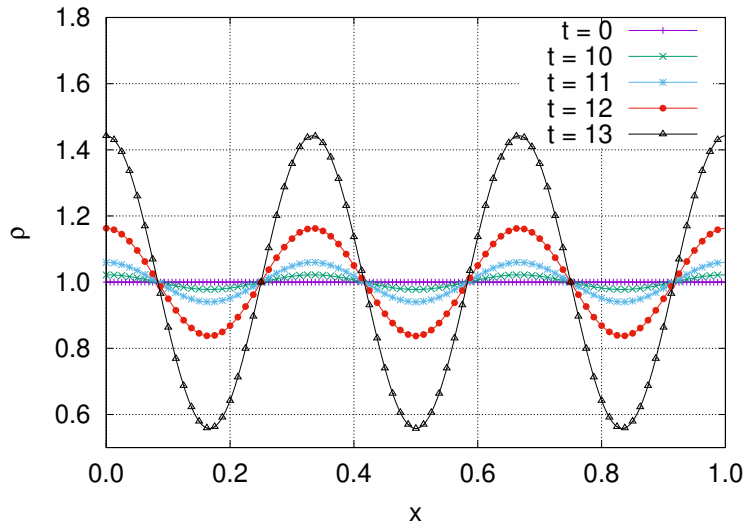

Figure 7.11: Temporally unstable density spatial profile at different times with $\mathcal{R} = 1$, $Re_\infty = \infty$, $Pr_\infty = 0.72$, $Ma_\infty = 0.5$ and $\gamma = 1.4$.

the density spatial profile at different times. These results were integrated in time using a fourth-order accurate explicit Runge-Kutta scheme from the initial condition in Eq. (7.15) using a time step of $\Delta t = 10^{-5}$, with a spatial discretization that employs the WENO5-JS scheme with the characteristic-wise Lax-Friedrichs flux-vector splitting using $N_X = 805$ grid points.

In order to clarify the effect of the stability control parameter $\mathcal{R}$, the linear and modal stability of this dynamical system around its steady-state is analyzed. This analysis was not performed on Eq. (7.12), but on its version written in primitive variables instead. They are composed of

$$\begin{aligned} \frac{D\rho}{Dt} &= -\rho \frac{\partial u}{\partial x} \quad , \\ \rho \frac{Du}{Dt} &= -\frac{\partial p}{\partial x} + \frac{4}{3} \frac{1}{Re_\infty} \frac{\partial^2 u}{\partial x^2} \quad \text{and} \\ \rho \frac{DT}{Dt} + \rho T (\gamma - 1) \frac{\partial u}{\partial x} &= \frac{\gamma}{Re_\infty Pr_\infty} \frac{\partial^2 T}{\partial x^2} + \frac{4}{3} \frac{\gamma (\gamma - 1) Ma_\infty^2}{Re_\infty} \left(\frac{\partial u}{\partial x} \right)^2 \quad , \end{aligned} \tag{7.16}$$

coupled with the equation of state

$$p = \frac{1}{\gamma Ma_\infty^2} \rho T \quad , \tag{7.17}$$

for perfect gases. The modal linearization for this problem is

$$\begin{Bmatrix} \rho \\ u \\ T \\ p \end{Bmatrix} (x,t) = \begin{Bmatrix} \rho_s \\ u_s \\ T_s \\ p_s \end{Bmatrix} + \epsilon \begin{Bmatrix} \rho_n \\ u_n \\ T_n \\ p_n \end{Bmatrix} e^{i\alpha x + \lambda t} + c.c. \quad , \tag{7.18}$$

which is analogous to Eq. (7.7). Substituting Eqs. (7.14) and (7.18) into Eqs. (7.16) and (7.17) leads to the dispersion relation

$$\begin{aligned} &\left\{ \frac{\alpha^2}{\gamma Ma_{\infty^2}} + (i(\alpha - \omega) - \mathcal{R}) \left(i(\alpha - \omega) + \frac{4\alpha^2}{3 Re_\infty} - \mathcal{R} \right) \right\} \times \\ &\left(i(\alpha - \omega) + \frac{\gamma \alpha^2}{Re_\infty Pr_\infty} - \mathcal{R} \right) + \frac{(\gamma - 1)\alpha^2}{\gamma Ma_\infty^2} (i(\alpha - \omega) - \mathcal{R}) = 0 \quad , \end{aligned} \tag{7.19}$$

when collecting the terms of $O(\epsilon)$ and using ω instead of λ. Separating real and imaginary parts of this equation in a temporal analysis, where α is real number and ω is a complex number, and solving for ω yields

$$\omega = \mathrm{Re}[\alpha] + i\mathcal{R} \quad \text{and} \quad \omega = \left(\frac{Ma_\infty \pm 1}{Ma_\infty} \right) \mathrm{Re}[\alpha] + i\mathcal{R} \quad , \tag{7.20}$$

in the infinite Reynolds number limit. This result confirms that all small amplitude disturbances in this $Re_\infty = \infty$ flow have a constant amplitude when $\mathcal{R} = 0$ and a constant phase speed, since $\mathrm{Re}[c] = \mathrm{Re}[\omega]/\mathrm{Re}[\alpha] = 1$

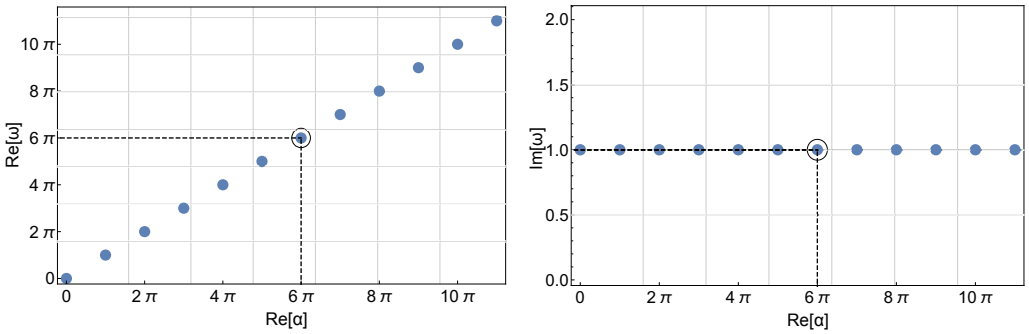

Figure 7.12: Linear and modal oscillation frequency (left) and temporal growth rate (right) versus wavenumber for the one-dimensional advection of entropy waves modified with $\mathcal{R} = 1$ when $Re_\infty = \infty$. Dashed lines indicate the ω values of the $\mathrm{Re}[\alpha] = \alpha_0$ initial disturbance.

and $(Ma_\infty \pm 1)/Ma_\infty$. Furthermore, they grow exponentially in time when $\mathcal{R} > 0$. The behavior of the entropy disturbance in Eq. (7.20) is visualized in Fig. 7.12, which shows the oscillation frequency (left) and temporal growth rate (right) as a function of the wavenumber for $\mathcal{R} = 1$. Their values when $\mathrm{Re}[\alpha] = \alpha_0$, used in the initial condition defined in Eq. (7.15), is highlighted by dashed lines. One characteristic in particular makes this test case unique. As shown in Eq. (7.20) and Fig. 7.12, all linear and modal disturbances have the same temporal growth rate $\mathcal{R}$ independent of their wavenumber $\mathrm{Re}[\alpha]$. This means that any numerical disturbance introduced by an inadequate spatial discretization will be amplified. Hence, this model problem represents a stringent test case for any code. Finally, the numerical and theoretical results from Figs. 7.11 and 7.12 (right), respectively, are now compared. This is done by fitting the expected linear and modal theoretical disturbance behavior to the numerical data using nonlinear regression. Doing so shows that the temporal growth rate relative error obtained with high-order 3D4S is approximately 0.014 %, indicating an excellent agreement.

7.3.2 Numerics

Having understood the unstable model behavior that the steady-state solvers must damp as well as verified code accuracy on this model, a comparative analysis of the efficiency of these solvers can be performed. This was done on the same computer with the same configuration from the previous sections. Only steady-state solvers based on implicit marching schemes are compared in this subsection. In other words, SFD and Boostconv are not included. The former is not competitive with the other solvers whereas the latter is too cumbersome to optimize. Nevertheless, these particular simulations were performed with $\mathcal{R} = 10$ and $Ma_\infty = 2$, with all other parameters being the same as in Fig. 7.11. Once the density residue reaches $||f(\rho)||_\infty = 1$, the steady-state solvers considered here were turned on. The computational time CPU_c required by both increment and residue to decrease eight orders

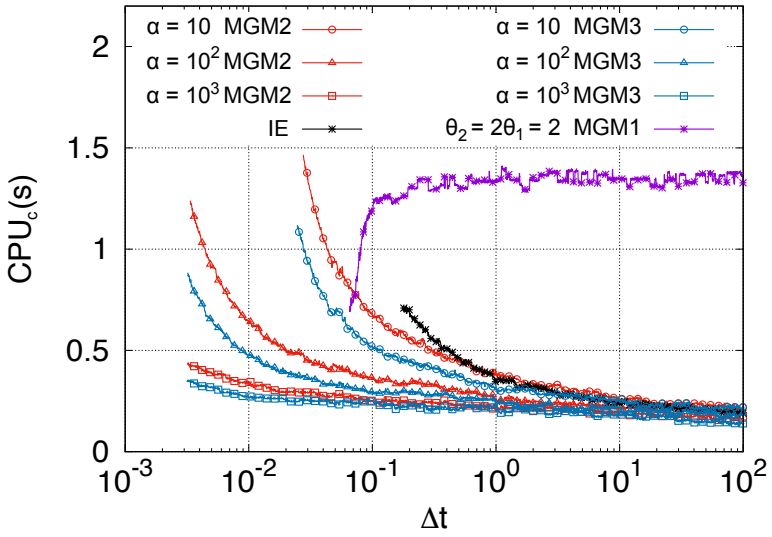

Figure 7.13: Same as Figs. 7.4 and 7.9, but for the temporally unstable advection of one-dimensional entropy disturbances with $\mathcal{R} = 10$, $Re_\infty = \infty$, $Pr_\infty = 0.72$, $Ma_\infty = 2$ and $\gamma = 1.4$.

of magnitude, i.e. $||\rho^{n+1} - \rho^n||_\infty < 10^{-8}$ and $||f(\rho)||_\infty < 10^{-8}$, was measured for different time steps Δt. These results are shown in Fig. 7.13, which is analogous to Figs. 7.4 and 7.9, i.e. the legends in all three figures represent the same schemes. At medium and large time steps, the trends are essentially the same. However, there are qualitative differences in the small time step limit. The approximately smooth and monotonic trend towards divergence that occurred in Figs. 7.4 and 7.9 as the time step was decreased is no longer observed in Fig. 7.13. This is true for all schemes and all parametric combinations evaluated. All schemes abruptly diverge below a certain scheme dependent time step, which is the reason why these curves suddenly stop.

Two analyses are performed to uncover the reason for this behavior. The first one involves the density temporal behavior in terms of both maximum disturbance amplitude (left) and maximum residue amplitude (right), which are shown in Fig. 7.14. It contains four sets of curves with different colors, namely blue, orange, green and red. They represent different stages of the entire simulation. The second analysis involves the absolute value of the density disturbance spatial profile at different times within each stage from Fig. 7.14, which are shown in Fig. 7.15 (top left), (top right), (bottom left) and (bottom right), respectively. Combined, Figs. 7.14 and 7.15 provide evidence that better explains the odd behavior observed in Fig. 7.13. The blue curves represent the initial time-accurate behavior, which shows the physically correct disturbance propagation and growth. They are followed by three sets of curves, obtained with the implicit Euler scheme using as time step the first one that lead to divergence in Fig. 7.13. The first one contains the orange curves in both figures. They indicate convergence towards the disturbance free and accurate steady-state, since the disturbance amplitude

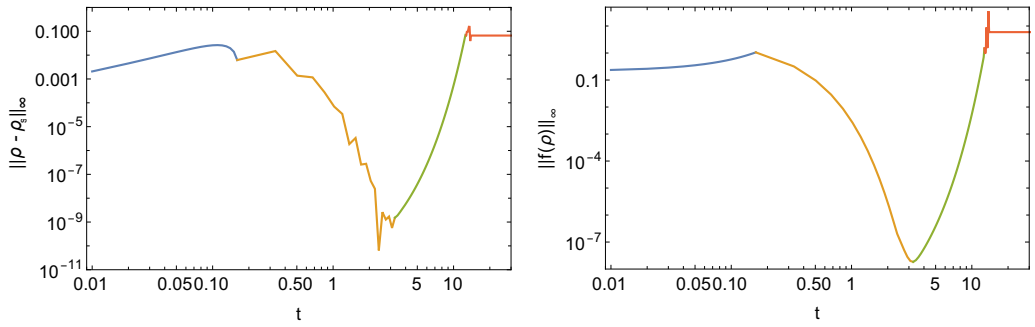

Figure 7.14: Maximum amplitude of the density disturbance (left) and residue (right) versus time. They are calculated using a time-accurate time step (blue) and the first time step that diverges in the implicit Euler scheme simulation from Fig. 7.13 (orange, green and red).

(left) and residue (right) converge towards machine zero in Fig. 7.14 as the implicit Euler scheme is damping this temporally ($\mathrm{Re}[\omega] \neq 0$) and spatially ($\mathrm{Re}[\alpha] \neq 0$) oscillatory disturbance in Fig. 7.15 (top right). At the end of this process, however, this disturbance becomes uniform in time ($\mathrm{Re}[\omega] = 0$) and space ($\mathrm{Re}[\alpha] = 0$). This is when the third stage starts, represented by the second set of curves obtained with the implicit Euler scheme. They are the green curves shown in both figures. Fitting the numerical data in Fig. 7.15 (bottom left) to the expected theoretical linear and modal behavior and using nonlinear regression yields $\mathrm{Im}[\omega] \simeq 1.89$. This is not an accurate

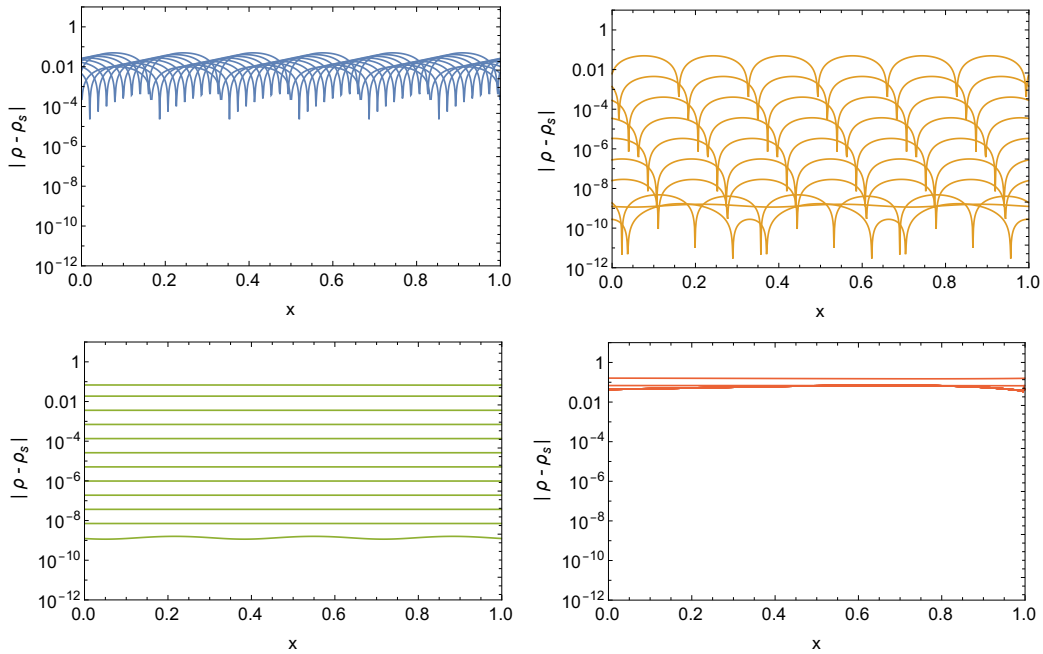

Figure 7.15: Absolute value of the density disturbance spatial profiles at different times within each stage shown in Fig. 7.14, namely blue (top left), orange (top right), green (bottom left) and red (bottom right).

result because the corresponding simulation was performed using a first-order accurate scheme with a large time step. In any case, a stationary and exponential growth in time is observed, which agrees with the expected linear and modal behavior from Eq. (7.20). The fourth stage begins at the end of this process, when nonlinear saturations occurs. This behavior is represented by the third set of curves in both figures, which are colored red.

The main question that must be answered now is why an oscillatory disturbance (orange) is damped but a stationary one (green) is not. In order to do so, the numerical stability of the implicit Euler scheme is invoked. Figure 7.16 shows its linear and time asymptotic numerical stability region, originally presented in Fig. 1 (right), as a background to illustrate the linear and modal physically unstable ($\mathrm{Re}[\lambda_j]\,\Delta t > 0$) disturbance as it transitions from oscillatory ($\mathrm{Im}[\lambda_j]\,\Delta t > 0$) to stationary ($\mathrm{Im}[\lambda_j]\,\Delta t = 0$) for two time step scenarios. At the larger one, the physically unstable disturbance remains within the numerically stable region during this transition. At the smaller time step, however, it moves from the numerically stable region into the numerically unstable one during this transition. The latter scenario is the one that explains why the solution obtained using the implicit Euler scheme transitions from the behavior shown in Fig. 7.15 (top right) to the behavior shown in Fig. 7.15 (bottom left). A similar thing is observed for all steady-state solvers, which explains why Fig. 7.13 is qualitatively different from Figs. 7.4 and 7.9 within the low time step range.

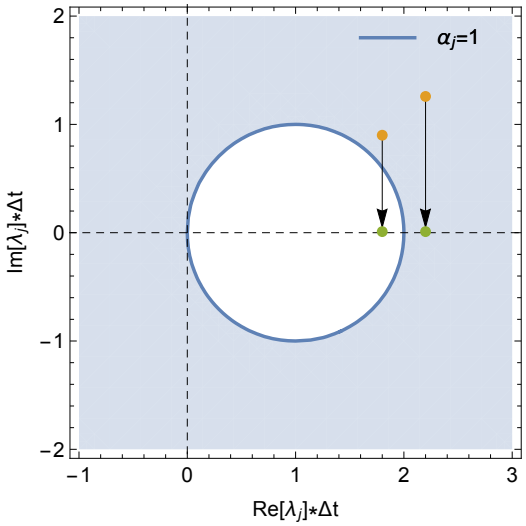

Figure 7.16: Linear and time asymptotic numerical stability region of the implicit Euler scheme, showing the numerically neutral contour line ($\alpha_j = 1$), in the complex and physical dimensionless eigenvalue ($\lambda_j\,\Delta t$) plane. Symbols show a physically unstable (filled) disturbance as it transitions (arrows) from oscillatory (orange) to stationary (green).

Chapter 8

Epilogue

8.1 Conclusions

The main goal of the present report is to use time marching methods to obtain accurate and disturbance free steady-states for high-speed flows in order to provide base flows for linear and nonlinear stability analyses. This chapter concludes the second of its three parts, which focusses on flows that are physically unstable to disturbances with a nonzero complex frequency in a linear and time asymptotic sense. In other words, special steady-state solvers are necessary to damp all physically meaningful disturbances, which oscillate and/or grow in time, since they will not be naturally damped in time-accurate simulations of such flows. The report then focusses on two fronts. On one end, new steady-state solvers based on implicit marching schemes were developed. On the other end, the performance of a few selected steady-state solvers based on explicit and implicit marching schemes is compared.

Within its category of steady-state solvers, the implicit Euler scheme is arguably the most well known. Its L-stability implies that faster convergence towards steady-state is achieved as the time step is increased. In fact, the Newton method is recovered in the infinite time step limit. However, a region of numerical instability does exist at small time steps for flows that are physically unstable in a linear and time-asymptotic sense. In other words, convergence towards steady-state can only be achieved for large enough time steps. This might pose a serious challenge, if the maximum time step allowed due to stiffness and/or nonlinearity prevents a time asymptotic physically unstable linear disturbance from being marched in time with a gain that is smaller than one. In order to circumvent this difficulty, multi-step Minimal Gain Marching (MGM) schemes were developed. The coefficients of this implicit marching scheme are chosen in such a way as to reduce its linear and time asymptotic numerical stability region until the gain at the maximum time step allowed becomes smaller than one. L-stability is lost, however, when doing so. Furthermore, the gain at large time steps becomes closer to one as the numerically unstable region is reduced. Hence, convergence rates toward steady-state at large time steps become smaller. In order to overcome this issue, multi-stage MGM schemes were developed for this project. They

are the subject of the second part of this report. The coefficients of this implicit marching scheme are also chosen in order to reduce its linear and time asymptotic numerical stability region until the gain at the maximum time step allowed becomes smaller than one. However, contrary to their multi-step counterpart, L-stability is maintained. Two and three-stage MGM schemes were developed and evaluated for three different test cases, where they proved to be more efficient than both the implicit Euler scheme and multi-step MGM schemes at small time steps.

All these steady-state solvers based on implicit marching schemes, namely implicit Euler as well as multi-step and multi-stage MGM schemes, were then compared to their counterparts based on explicit marching schemes. This comparison was performed in terms of the computational time required to reach machine zero residue and solution increment for the first two test-cases. Selective frequency damping (SFD) proved to be the least efficient, followed by the multi-step MGM scheme. Boostconv as well as both multi-stage MGM schemes proved to be as efficient as the Newton method. The control parameters of the former, however, were significantly more difficult to optimize in comparison with all other schemes.

8.2 Future Work

Given the development and the discoveries presented in the second part of this report, which were summarized above, it is important to suggest the next steps forward. This is done below, segregated by topic of interest.

- **Efficiency Analysis:**

  1. Evaluate the optimal computational time it takes both Boostconv and SFD to generate a machine zero steady-state for the one-dimensional advection and growth of entropy waves, in order to compare them to the other steady-state solvers and confirm the trends observed in the first two test cases.

  2. Use the compressible flow around a two-dimensional cylinder as another test case representing a complex physically unstable steady-state, since it contains both convectively and absolutely unstable regions.

  3. Use the compressible flow over a backwards facing step as test case, since it represents a complex physically stable steady-state, in order to confirm the advantage that multi-stage MGM schemes have over other steady-state solvers based on implicit marching schemes, as implied by the linear and time asymptotic numerical stability analysis.

- **SSP MGM schemes:**

  1. Evaluate the effect of the time step restriction imposed by the nonlinear numerical stability properties of these steady-state solvers based on

implicit and explicit marching schemes in order to asses their ability to efficiently obtain steady-states associated with supersonic flows that are embedded with shock waves.

2. Develop a new family of multi-stage MGM schemes without the time step restriction required by the nonlinear numerical stability property known as strong stability preserving by basing them on diagonally split Runge-Kutta schemes.

Part III

Physically Unstable Flows with $\lambda_j = 0$

Chapter 9

Introduction

9.1 Motivation

This project focusses on the use of special spatial discretization and time-marching schemes for the numerical computation of accurate and disturbance free steady-states to be used as base flows in linear and nonlinear stability analyses. It is divided in three parts according to the flow physical stability under a linear and time asymptotic sense. The first part only considered physically stable flows whereas the second one only considered flows that are physically unstable to nonzero complex frequency disturbances. On the other hand, the third and final part of this report only considers flows that are physically unstable to disturbances with a zero complex frequency. As was described in the prologue, these real and imaginary frequency components describe the physical disturbance oscillation frequency and temporal growth rate, respectively. Hence, spatially developing flows studied in the present part of this report are convectively unstable to stationary disturbances. As such, they present unique numerical challenges to the calculation of steady-states that are explored next due to their importance to the three-dimensional transition scenarios found in high-speed boundary-layers.

9.2 Literature Review

The reason for this importance comes from the fact that these accurate and disturbance free steady-states can be employed as reliable base flows for both linear and nonlinear stability analyses, which are some of the most used tools employed to understand these transition scenarios. When it comes to three-dimensional high-speed boundary-layers, the possible paths that a flow can take during transition have been identified as a function of the environmental disturbance levels (Morkovin et al., 1994). These paths to transition are illustrated in Fig. 9.1, which includes new terminology that is defined here. Receptivity is the response of the flow to external forcing, which provides initial conditions for the disturbance amplitudes, frequencies, growth rates and phases (Zhong and Wang, 2012). Asymptotic and transient

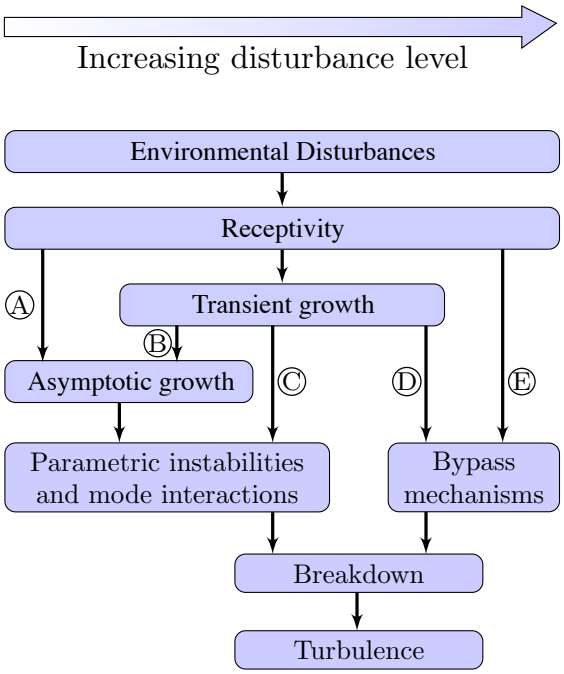

Figure 9.1: Different paths to transition in high-speed boundary-layers adapted from Morkovin et al. (1994).

growths have already been discussed. The former represents the large time exponential disturbance growth described by a linear and modal stability analysis (Huerre and Monkewitz, 1990; Theofilis, 2011) whereas the latter represents the initial temporary algebraic disturbance growth described by a linear and non-modal stability analysis (Schmid, 2007; Theofilis, 2011). Parametric instabilities (Kachanov and Levchenko, 1984) as well as mode interactions (Zaki and Durbin, 2005) represent disturbance growth due to external excitation and mode coupling, respectively. When the amplitude of the environmental disturbances is high enough, the aforementioned primary transition mechanisms can be circumvented in many different ways. These nonlinear transition scenarios are known as bypass mechanisms (Jovanović, 2021). Breakdown is eventually reached independent of the transition path followed, which is characterized by a violent onset of small-scale secondary disturbances that develop on top of large-scale primary ones. Beyond this point, turbulence ensues (Landahl, 1975).

Flows that are convectively unstable to stationary disturbances fall on path A from Fig. 9.1. The toy problem studied in section 7.2, called modified Burgers' equation, provides an interesting example of such flows. However, this is true only when $0 < \mathcal{R} < Re/4$, as illustrated in Fig. 7.6 (left). It is absolutely unstable otherwise, as illustrated in Fig. 7.6 (right), which is the parametric condition actually studied in that section. One of the best known examples of such a stationary and convective instability in high-speed boundary-layers is the one induced by wall curvature, which produces the well known Görtler vortices (Floryan, 1991; Saric, 1994). In other words, they are

steady and longitudinal counter-rotating vortices induced by a centrifugal instability. A lot of work has been done on this problem. Although the early ones focussed on its linear instability (Floryan and Saric, 1984; Hall, 1985), the nonlinear mechanisms associated with its transition process have been extensively studied as well (Tandiono et al., 2008; Li et al., 2010b; Chen et al., 2019). A vast literature exists on Görtler vortices but its review is beyond the scope of this report. Only a couple of papers are mentioned here, since they highlight the role played by these vortices on compression corners (Martinez and Tutty, 2005) and flared cones (Chen et al., 2017).

More complex flow topologies are capable of producing another quite well known example of a convective instability in high-speed boundary-layers, known as crossflow instability (Saric et al., 2003). It is an inviscid instability caused by the inflection point introduced by the secondary flow generated within three-dimensional boundary-layers by an imbalance between pressure and centrifugal forces. This instability can be either stationary or oscillatory, depending on the flow receptivity to free-stream disturbances and surface roughness (Bippes, 1999). For instance, a low (high) amplitude disturbance environment favors stationary (oscillatory) crossflows. The former appears as steady and co-rotating vortices approximately aligned with the local inviscid streamlines that distort the original disturbance free steady-state. This, in turn, leads to secondary instabilities that are responsible for the transition to turbulence, as illustrated in Fig. 9.2 for a swept wing (Serpieri and Kotsonis, 2016). There are several studies examining the flow over swept wings, from

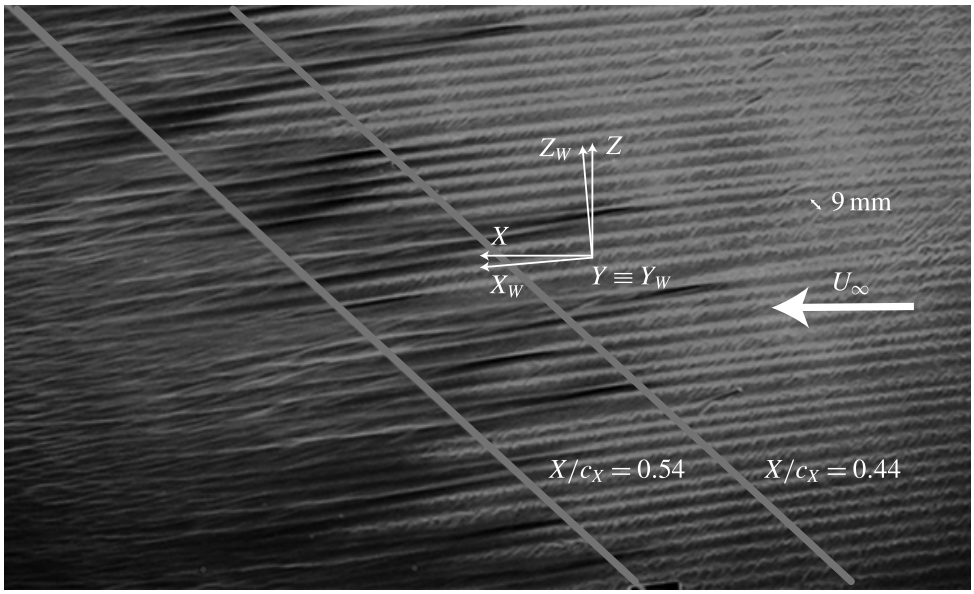

Figure 9.2: Fluorescent oil visualization of the transition region induced by spanwise uniform forcing through discrete roughness elements in a swept wing taken from Serpieri and Kotsonis (2016). White streaks indicate stationary crossflow vortices, darker region suggests the flow is turbulent and inclined straight white lines indicate the mean transition region.

both stability analysis and direct numerical simulation perspectives (Fischer and Dailmann, 1991; Joslin and Streett, 1994; Malike et al., 1999; Janke and Balakumar, 2000; Koch et al., 2000; Koch, 2002; Wassermann and Kloker, 2002; Li et al., 2016). Secondary instability comparisons between the two, however, often reveal significant deviations in the amplification rates. This was originally assumed to be due to the lack of non-parallel effects in a local analysis (Högberg and Henningson, 1998), which was later generalized to a necessarily simplified representation of the primary state (Bonfigli and Kloker, 2007). In the context of the present work, a primary state means a disturbance free steady-state superposed by a spatially growing stationary crossflow instability. Nevertheless, these authors extracted it from direct numerical simulation data, where their difficulty came from the fact that there is no unique way to impose a local approximation. This is simply a new look at the age old problem this report is trying to address, inaccurate base flows lead to inaccurate stability analyses.

Similar issues can also be found in more complex geometries. The three-dimensional boundary-layers that are formed during the hypersonic flow over circular (Kimmel et al., 2007) and elliptic (Kimmel et al., 2010) cones studied under the Hypersonic International Flight Research Experimentation (HiFIRE) program (Barnstorff, 2012) provide yet another well known example. An extensive literature exists on these two problems, trying to understand them using stability analysis and direct numerical simulations. Only a brief review is reported here, focusing on the particular studies that highlight the difficulties faced when trying to obtain converged base flows due in large part to the presence of a stationary crossflow instability. Li et al. (2010a) investigated the circular cone problem with a Mach number of $Ma = 6$, a unit Reynolds number of $Re = 10.8 \times 10^6/m$, a half angle of 7 degrees and angles of attack of 3 and 6 degrees. Their transition investigation employed linear and local stability theory, both in one and two-dimensions as well as linear and nonlinear parabolized stability equations. The base flow used was obtained from VULCAN (NASA, 2009). However, grid convergence studies were not possible due to an extreme sensitivity to grid resolution. In fact, these base flows were recently sent to the UFF research group to aid in our analysis (Choudhari, 2020). Similar studies of the elliptic cone presented the same issues. To the best of our knowledge, Dinzl and Candler (2015) provided the most detailed description to date of the numerical difficulties associated with obtaining base flows for this problem. They did so for the geometry provided by Juliano and Schneider (2010) with a Mach number of $Ma = 6$, a unit Reynolds number of $Re = 11.8 \times 10^6/m$ and a zero angle of attack. A high sensitivity to numerical diffusion and grid resolution levels was observed when attempting to grid converge their base flow using US3D (Subbareddy and Candler, 2009). This is illustrated in Fig. 9.3, using data from Dinzl and Candler (2015). It shows steady wall-normal density isocontours at different locations downstream of the cone nose obtained from a second-order accurate simulation using three different number of grid points. As this number increases, the centerline vortex becomes better resolved but

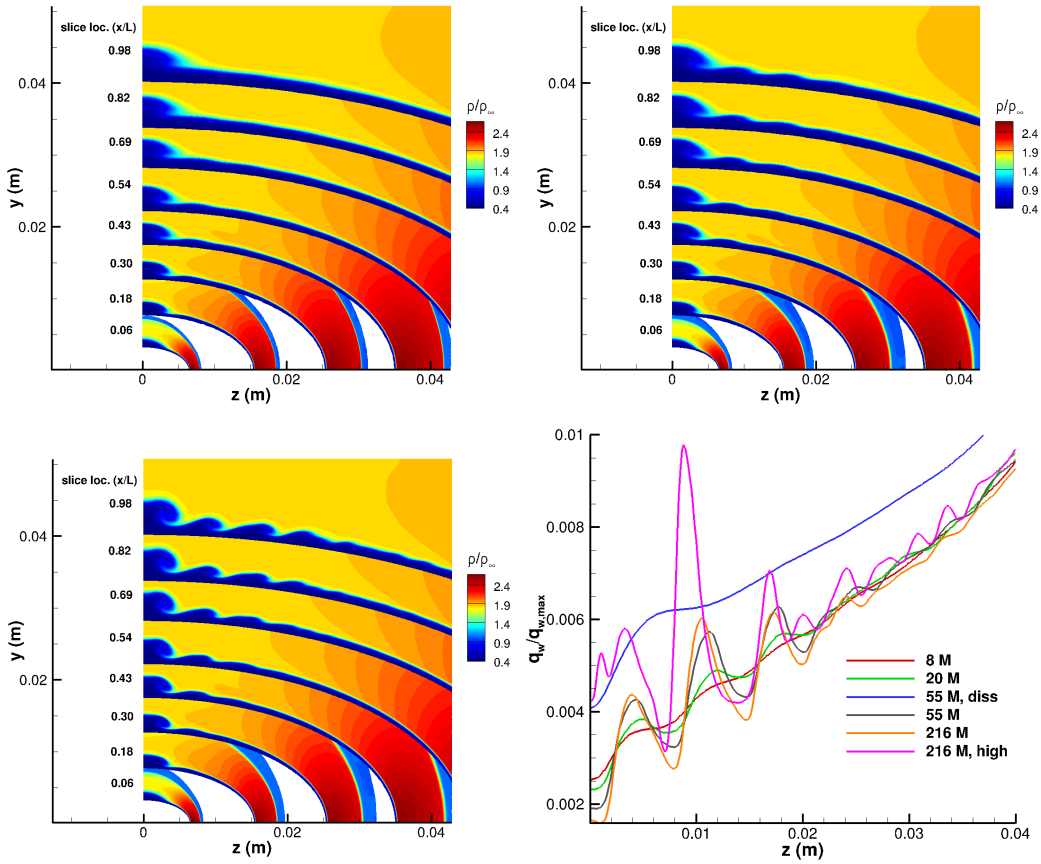

Figure 9.3: Wall-normal density isocontours at different streamwise locations for 3 different grids, i.e. 8 million elements (top left), 20 million elements (top right) and 216 million elements (bottom left) as well as normalized wall heat flux as a function of distance from the centerline at a fixed downstream location (bottom right). All figures taken from Dinzl and Candler (2015).

the number of steady crossflow vortices emanating from it increases, reaching significant amplitudes further downstream due to the spatial growth of this linear convective instability. Figure 9.3 also shows the normalized wall heat flux at a fixed downstream location along a distance normal from the centerline, using four different number of grids points and three different numerical diffusion levels. All six solutions are different from each other, with spatial oscillations increasing in magnitude as the former increases and the latter decreases. This extreme difficulty in spatially resolving the steady crossflow vortices is proposed as the major cause for the inability to grid converge the base flow. Similar conclusions were reached by Porter et al. (2017) when studying the flow over a $2:1$ elliptic cone with a Mach number of $Ma = 7.7$, a unit Reynolds number of $Re = 5 \times 10^6/m$, an angle of attack of 2 degrees, a yaw angle of 2 degrees and a half angle on the minor axis of 7 degrees. A high sensitivity of the base flow to grid resolution was observed when using OVERFLOW (NASA, 2017). This is shown in Fig. 9.4 employing data from the aforementioned paper. It shows the Stanton number as a function of

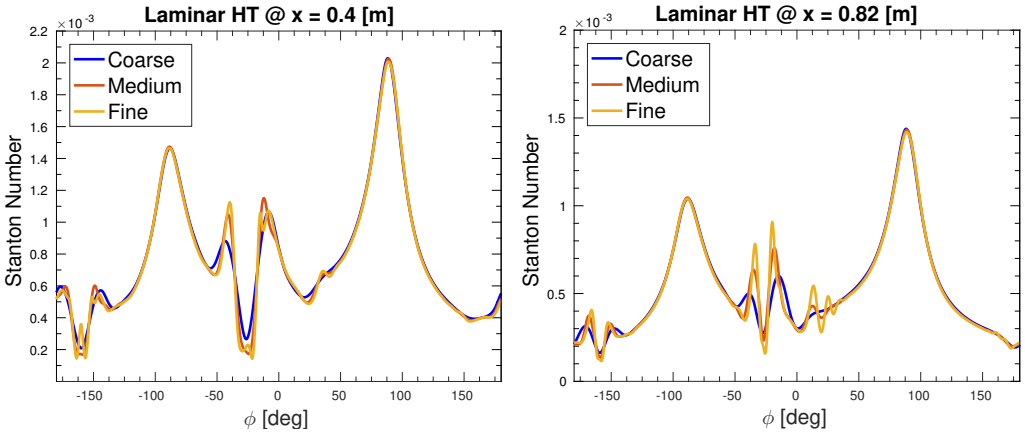

Figure 9.4: Grid convergence analysis of the laminar flow simulations using the Stanton number azimuthal profile at (left) $x = 0.4\,m$ and (right) $x = 0.82\,m$ downstream of the nose tip taken from Porter et al. (2017).

the azimuthal angle, calculated at two different distances downstream of the nose tip under three different number of grid points. The grid convergence issues appear where the stationary linear instabilities are located, becoming stronger downstream due to their exponential spatial growth. This problem was not present when turbulence models were employed instead, since these instabilities were no longer present. Nevertheless, their inability to achieve grid convergence led them to make a striking statement, namely that "*it may not be possible to obtain a strictly laminar basic state on a very fine grid*".

This steady-state sensitivity to grid and/or numerical diffusion induced by stationary crossflow vortices is felt the strongest when considering smooth surfaces. For this reason, roughness has been used to try and suppress it. One example comes from Dinzl and Candler (2017), who introduced surface roughness to their elliptic cone simulations. This significantly reduced their steady-state grid sensitivity and localized the stationary crossflow origin, enabling a better comparison with experiments. The success achieved with this approach led to an input/output analysis of the surface roughness effect on other complex geometries, such as a sharp cone (Cook et al., 2018) and BOLT (Cook et al., 2019). Some groups have not reported any steady-state grid convergence issues in the presence of smooth surfaces (Moyes et al., 2017). However, comparisons with experiments were only performed after adding the effects of surface and discrete roughnesses. This was done by superposing these steady-states with stationary crossflow vortices obtained from nonlinear parabolized stability equations to construct the primary base flow and then performing a secondary stability analysis on it using spatial Bi-Global theory. Nevertheless, the importance of properly grid converging base flows as well as the difficulty in doing so due to an extreme sensitivity to stationary crossflow vortices has been highlighted by this group in both previous (Reed et al., 2015) and following (Kocian et al., 2019) studies.

9.3 Objectives

This third and final part of the report discusses in depth the steady-state convergence issues associated stationary crossflow vortices. It is divided in four steps discussed within the next two chapters. First, a hypothesis is put forward to explain the origin of this issue based on a mixture of physical and numerical stability theories. Second, a toy problem is employed to provide evidence in favor of this hypothesis. Third, a novel procedure is proposed to try and constrain the development of this instability. These three steps are discussed in the next chapter. In the fourth and final step, discussed in the third chapter, preliminary results are shown for a few toy problems and for the Görtler instability problem. Conclusions and the future work still required are presented in the fourth and final chapter.

Chapter 10

Mathematical Formulation

10.1 A Hypothesis

Such a difficulty in the numerical calculation of disturbance free steady-states for the aforementioned problems, namely the *i*) modified Burgers' equation, *ii*) Görtler vortices and *iii*) stationary crossflow vortices, has a cause that can be found in the similarities between them. It lies within their linear instability, both physical as well as numerical, which have already been briefly described in this report. Both in its prologue and the former in the introduction of its third part as well. Nevertheless, each type of linear instability is reviewed separately in one of the two following paragraphs, before the final hypothesis combining both arguments is put forward.

The time asymptotic behavior of all three dynamical systems around their respective accurate steady-states is convectively unstable to small amplitude stationary disturbances. There are two aspects of these steady-states that must be clearly understood. The first one is related to their linear and modal onset of instability, which is convective. All flows with such characteristics are known as noise amplifiers (Huerre and Monkewitz, 1990). They are either local or slowly diverging with respect to their main propagation direction. The latter can also be understood as weakly global, in order to highlight its contrast with flows that vary strongly in their main propagation direction and, hence, are truly global (Theofilis, 2011). Unsteady dynamical systems prone to such an instability display an extrinsic dynamics. In other words, their downstream spatial evolution is determined in large part by how they are excited by an upstream source. Control strategies can then be devised by tailoring the excitation character to meet the desired goals. Figure 10.1 illustrates this convective instability concept in two scenarios. Both present the expected behavior after an initial ($t = 0$) impulse excitation at the origin ($x = 0$) triggered the propagation of unstable disturbances, known as wave packet, downstream of the excitation source. The difference between them accounts for the particular cases where dominant disturbances are oscillatory (left) and stationary (right), noting the latter represents the same behavior displayed by all three aforementioned problems. In other words, they can be physically understood from a time asymptotic point of view as steady flows

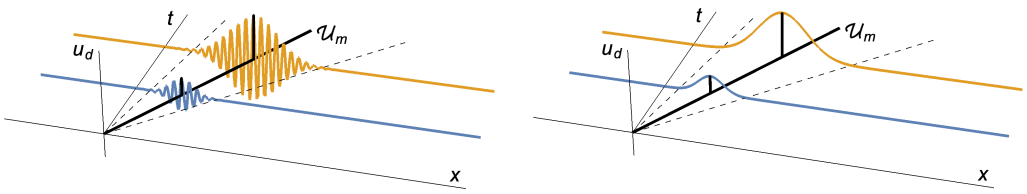

Figure 10.1: Illustration of the convective instability of an unsteady and one-dimensional disturbance wave packet impulsively excited by a source located at the origin propagating downstream of it. The dominant disturbance can be either oscillatory (left) or stationary (right). Dashed lines represent the wave packet boundaries whereas solid line represents the wave packet characteristic propagation direction $x/t = \mathcal{U}_m$.

linearly, and quite often also nonlinearly, modified by steady disturbances that grow spatially downstream of their steady excitation sources.

Having understood the physical instability aspects of this problem, their numerical counterparts can now be discussed. Some fundamental aspects have already been rigorously presented from a mathematical point of view in the prologue, focussing on the specific cases of the explicit and implicit Euler schemes for illustration purposes. Hence, this prologue serves as a reference to the simplified discussion that follows. A similar analysis to what follows can be found elsewhere (Teixeira and Alves, 2017). It starts with the generic linear and homogeneous conservation equation

$$\frac{du}{dt} = \lambda\, u \quad , \tag{10.1}$$

the scalar version of Eq. (21), where λ is a complex eigenvalue. A marching scheme must now be chosen to advance Eq. (10.1) forward in time. For the sake of simplicity, this is done here with a time step Δt using

$$\frac{a_{+1}\, u^{n+1} + a_0\, u^n + a_{-1}\, u^{n-1}}{\Delta t} = \lambda \left(b_{+1}\, u^{n+1} + b_0\, u^n + b_{-1}\, u^{n-1} \right) \quad , \tag{10.2}$$

which is a generic six coefficient multi-step scheme. This analysis could have been done with any other multi-step or multi-stage scheme instead. The above one is only used here because several well known multi-step schemes can be derived from it, such as the explicit ($a_{+1} = b_0 = 1$, $a_0 = -1$, $a_{-1} = b_{+1} = b_{-1} = 0$) and implicit ($a_{+1} = b_{+1} = 1$, $a_0 = -1$, $a_{-1} = b_0 = b_{-1} = 0$) Euler schemes, the second-order Crank-Nicolson scheme ($a_{+1} = 1$, $a_0 = -1$, $b_{+1} = b_0 = 1/2$, $a_{-1} = b_{-1} = 0$) and the second-order backwards-difference-formula ($a_{+1} = 3/2$, $a_0 = -2$, $a_{-1} = 1/2$, $b_{+1} = 1$, $b_0 = b_{-1} = 0$). Nevertheless, according to Lax's equivalence theorem (Lax and Richtmyer, 1956), any discrete algebraic equation can only converge to the continuous linear differential equation it represents, as the time step goes to zero, if it is consistent and stable. In other words, Eq. (10.2) converges back to Eq. (10.1) in the limit when $\Delta t \to 0$ if Eq. (10.2) is a consistent and stable representation of Eq. (10.1). The former property is evaluated first. Using

the Taylor series expansions of u^{n+1} and u^{n-1} with respect to u^n, it is possible to re-write Eq. (10.2) as

$$\begin{aligned}(a_{+1} - a_{-1}) \left.\frac{du}{dt}\right|^n &= (b_{+1} + b_0 + b_{-1})\,\lambda\, u^n \;-\; (a_{+1} + a_0 + a_{-1})\,\frac{u^n}{\Delta t} \\ &+ \Delta t \left\{ (b_{+1} - b_{-1})\,\lambda \left.\frac{du}{dt}\right|^n - \frac{a_{+1} + a_{-1}}{2} \left.\frac{d^2u}{dt^2}\right|^n \right\} \\ &+ O\big(\Delta t^2\big) \quad , \end{aligned} \tag{10.3}$$

also known as a modified equation. It is Eq. (10.1), evaluated at $t = t_n$, plus an additional term known as truncation error. Hence, consistency requires that the truncation error must go to zero as the time step goes to zero. In order to satisfy this property, it is necessary to impose

$$a_{+1} + a_0 + a_{-1} \;=\; 0 \quad , \tag{10.4}$$

which guarantees that the discrete time derivative in Eq. (10.2) goes to zero when the solution becomes time invariant, i.e. $u^{n+1} = u^n = u^{n-1} = cte$. It is important to note that consistency also requires that

$$a_{+1} - a_{-1} \;=\; b_{+1} + b_0 + b_{-1} \quad , \tag{10.5}$$

otherwise Eq. (10.3) would result in a time re-scaled version of Eq. (10.1) in the limit when $\Delta t \to 0$. With these results at hand, it is now possible to evaluate the numerical stability of Eq. (10.2). Based on the same linear gain definition provided in Eq. (24), it is possible to write

$$G = \frac{u^{n+1}}{u^n} = e^{\lambda\,\Delta t} \quad , \tag{10.6}$$

since $t_{n+1} = t_n + \Delta t$, $u(0) = u_0$ and $u(t_n) = u_0\, e^{\lambda\, t_n}$, which is the solution of Eq. (10.1). Since λ is complex in general, the stability of this physical solution is still dictated by Eqs. (19) and (20), with λ_j replaced by λ. The stability of the numerical solution of Eq. (10.3), on the other hand, is found by first substituting Eq. (10.6) into this equation, which yields

$$(a_{+1} - b_{+1}\,\lambda\Delta t)\,G^2 + (a_0 - b_0\,\lambda\Delta t)\,G + (a_{-1} - b_{-1}\,\lambda\Delta t) = 0 \quad , \tag{10.7}$$

whose solution is given by

$$G(\lambda = 0) = \left(-a_0 \pm \sqrt{a_0^2 - 4\,a_{+1}\,a_{-1}} \right) \Big/ \left(2\,a_{+1}\right) \quad , \tag{10.8}$$

for $\lambda = 0$, which is the correct parametric condition to impose when the flow is convectively unstable ($\mathrm{Re}[\lambda] = 0$) to stationary disturbances ($\mathrm{Im}[\lambda] = 0$). Imposing the consistency condition in Eq. (10.4), done here by eliminating a_0 from Eq. (10.8), simplifies this solution to

$$G(\lambda = 0) = 1 \quad \text{and} \quad G(\lambda = 0) = \frac{a_{-1}}{a_{+1}} \quad , \tag{10.9}$$

where $a_{+1} > a_{-1}$. Since the maximum value is the only one observed in a numerical simulation, it is possible to say that $G(\lambda = 0) = 1$. Hence, any consistent multi-step marching scheme that is a subset of Eq. (10.2) is neutrally stable ($G = 1$) towards stationary and convectively unstable disturbances ($\lambda = 0$) in a linear and time asymptotic sense, independent of the time step (Δt) employed. Two examples are provided in Fig. 1 for particular cases of the explicit (left) and implicit (right) Euler schemes, where the empty red squares at the origin illustrate the stationary and convectively unstable disturbances ($\lambda = 0$). Although this result could not be generalized to an arbitrary marching scheme, we were unable to derive a single multi-step or multi-stage scheme for which this result does not hold.

Both physical and numerical linear and time asymptotic stability aspects associated with the use of time marching schemes, and by extension their iterative counterparts, to calculate steady-states of dynamical systems that are convectively unstable to stationary disturbances have now been clarified. A hypothesis is then proposed to explain the reason why grid convergence of the steady-state of such flows can be quite difficult:

1. The simulation of complex flows often requires *i*) artificial inlet and outlet (e.g. when truncating either semi-infinite or infinite domains), *ii*) approximate initial conditions (e.g. when the steady-state is unknown), *iii*) variable numerical diffusion (e.g. for shock capturing), *iv*) low quality grids due to poorly distributed points (e.g. for complex geometries), *v*) and so on.

2. Any single one of these issues, or several of them occurring at the same time, almost unavoidably leads to a steady spatial error distribution that is not smooth. Its error peaks, in turn, can often act as steady excitation sources that are purely numerical in nature.

3. When the flow in question is physically unstable in a linear and time asymptotic sense to stationary small amplitude disturbances, the steady nature of these numerical excitation sources triggers their growth.

4. Furthermore, when this physical instability is also convective in a local or weakly global sense, all these numerically triggered linear and time asymptotic stationary disturbances will grow spatially downstream of these steady sources, eventually to such a large amplitude that they nonlinearly distort the original steady-state.

5. On the other hand, all time marching schemes, and by extension any iterative method based on them, used to calculate these steady-states must satisfy the linear consistency requirement from Lax's equivalence theorem. Otherwise, time step convergence is not guaranteed.

6. Imposing this requirement, however, forces their linear gain to be one when the disturbance complex frequency is zero, i.e. in the case of stationary and convectively unstable disturbances. Hence, they are

not capable of changing the linear and time asymptotic amplitude of such disturbances, independent of the time step used.

7. As a consequence, all steady-states obtained under these circumstances are contaminated by stationary and convectively unstable disturbances with a physically consistent behavior downstream of their excitation, even though this excitation is purely numerical and not physical.

8. Any attempts to modify artificial boundary conditions, approximate initial conditions, numerical diffusion and/or grids, in order to resolve this issue will likely only change the numerical excitation character, e.g. its location, amplitude and shape.

9. Doing so, however, not only reduces the steady-state accuracy but also changes how the stationary and convectively unstable disturbances grow spatially downstream of their numerical excitation source and, eventually, modify this now inaccurate steady-state.

10. Using any of these contaminated and inaccurate steady-states as base flows then leads to an *ad hoc* secondary stability analysis, and not an accurate primary one. The latter can only be performed when using as base flow an accurate and disturbance free steady-state.

10.2 Some Additional Evidence

The effect of both numerical diffusion and grid resolution on the behavior of stationary and convectively unstable flows has already been throughly investigated (Dinzl and Candler, 2015; Porter et al., 2017). More evidence in favor of the hypothesis put forward in the previous section is provided here by showing the effect of both artificial boundaries and approximate initial conditions on the behavior of the toy problem described in section 7.2, which is governed by the modified Burgers' equation provided in Eq. (7.4). It is convectively unstable to stationary disturbances when $0 < \mathcal{R} < Re/4$, as discussed by Barletta and Alves (2017) and illustrated in Fig. 7.6 (left), and numerically simulated here by imposing,

$$u(0,t) = 1 \quad \text{and} \quad \left.\frac{\partial^2 u}{\partial x^2}\right|_{x=\mathcal{L}} = 0 \quad , \tag{10.10}$$

as local boundary conditions, which can be coupled with buffer layers at the inlet and/or outlet (Bodony, 2006). In order to do so, the source term $\sigma(x)\,(u(x,t) - u_s)$ is subtracted from the r.h.s. of Eq. (7.4), where

$$\sigma(x) = \begin{cases} \mathcal{B}_0 \left(\frac{\mathcal{B}_1 - x}{\mathcal{B}_1}\right)^3 & \text{for } x < \mathcal{B}_1 \\ \mathcal{B}_2 \left(\frac{x - \mathcal{B}_3}{\mathcal{L} - \mathcal{B}_3}\right)^3 & \text{for } x > \mathcal{B}_3 \\ 0 & \text{otherwise} \end{cases} \quad , \tag{10.11}$$

and $\mathcal{B}_i$ are user defined parameters. When correctly choosing their values, this global boundary condition will push the disturbance amplitude to zero through the governing equation. Furthermore,

$$u(x,0) = 1 + \mathcal{A}_0 \left(\exp\left[-\mathcal{A}_1 \left(x - x_1 \right)^2 \right] + \exp\left[-\mathcal{A}_2 \left(x - x_2 \right)^2 \right] \right) \ , \quad (10.12)$$

is imposed as initial condition, where $\mathcal{A}_i$ and x_i are used defined parameters. In this section, the control parameters are chosen as $\mathcal{L} = 24$, $Re = 10$ and $\mathcal{R} = 1$ whereas the chosen numerical schemes are the explicit Euler scheme for time integration and central-difference schemes for the spatial discretization of first and second derivatives. This is done to eliminate the effect of numerical diffusion. A uniform grid with $N_x = 241$, which leads to $\Delta x = \mathcal{L}/(N_x - 1)$, is employed to eliminate the effect of grid resolution. Finally, time integration is performed with $\Delta t = CFL\, \Delta x / u_s$, where u_s is defined by Eq. (7.6) and $CFL = 10^{-2}$ for time accuracy.

A baseline simulation is setup first for comparison purposes. It does not use buffer layers ($\mathcal{B}_0 = 0$) and uses the steady-state as initial condition ($\mathcal{A}_0 = 0$). Furthermore, it employs second-order schemes for its spatial discretization, which removes the need for biased schemes near the artificial boundaries. Such a numerical simulation reveals that the velocity profile remains at its initial value as time advances, i.e. $u(x, t > 0) = u(x, t = 0)$ when $u(x, t = 0) = u_s$. In other words, $u_d(x, t > 0) = 0$. Hence, there is no numerical excitation triggering the convective growth of this stationary instability when the spatial error distribution is smooth. The second step is to change this baseline setup in a number of ways to illustrate the effect of artificial boundaries and approximate initial conditions. Results from the numerical simulation of these novel scenarios are provided in Fig. 10.2, which shows disturbance spatial profiles at different times $t_n = n\, \Delta t$, where $n = 1$ (blue), 11 (orange), 101 (green) and 301 (red).

The first three scenarios modify this baseline to evaluate the effect of artificial boundaries. Its first scenario does so by employing fourth-order schemes instead for the spatial discretization, which means biased schemes must be employed on the first point into the domain coming off of each boundary. Since biased schemes have different properties when compared to central-difference schemes, e.g. modified wavenumber and truncation error, the spatial error distribution will no longer be smooth near each boundary. Figure 10.2 (first row) shows the consequences of this change in accuracy-order. A stationary disturbance is numerically excited near the inlet. It grows spatially downstream of this numerical source in a physically consistent manner, as confirmed by the linear stability growth rate shown as a dashed black line. As time passes, it reaches further into the domain until it arrives at a time invariant solution within the simulated domain. This solution is the steady contamination, i.e. the contaminated steady-state is given by $u(x, t \to \infty) = u_s + u_d(x, t \to \infty)$. In the next scenario, the first one is modified by introducing a buffer layer near the inlet with $\mathcal{B}_0 = 10^3$, $\mathcal{B}_1 = 2$ and $\mathcal{B}_2 = 0$. Figure 10.2 (second row) shows that doing so does not prevent the numerical excitation of the stationary disturbance, but only modifies it

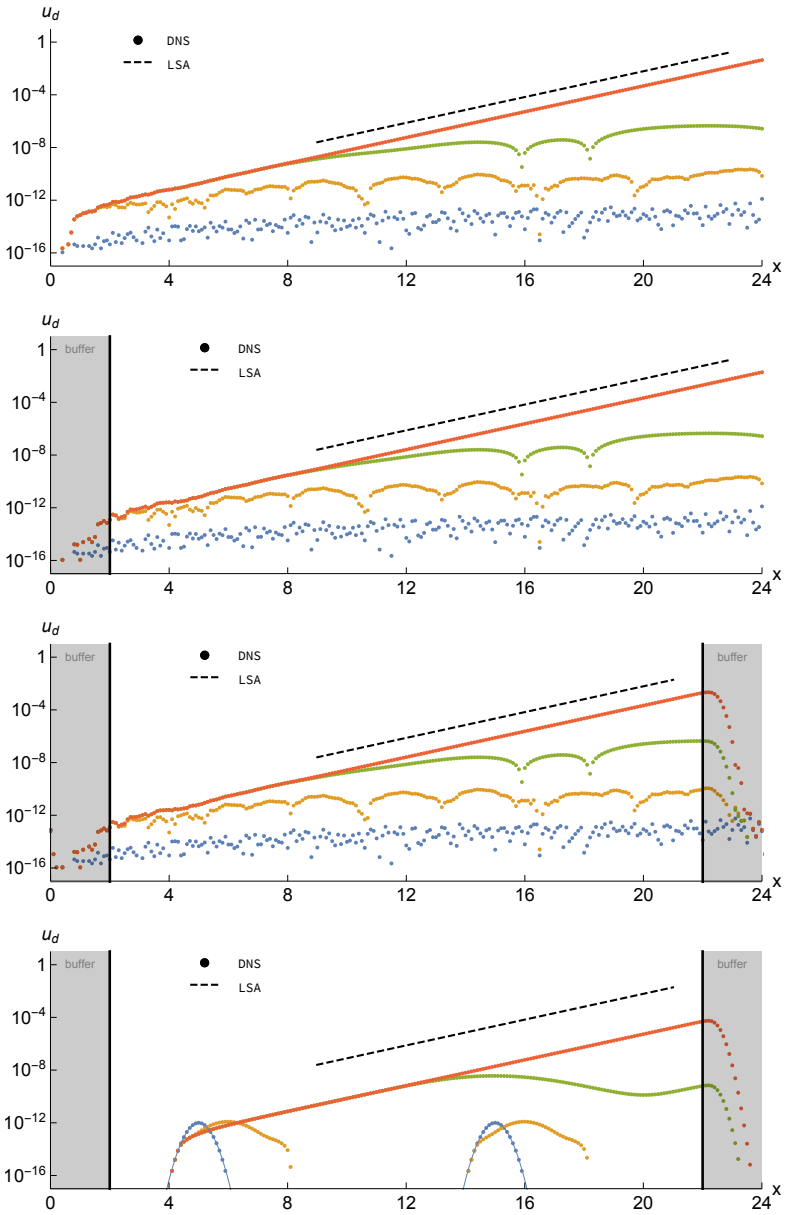

Figure 10.2: Disturbance spatial profiles obtained from numerical simulations of Eq. (7.4) subject to Eq. (10.10) measured at iterations $n = t_n/\Delta t = 1$ (blue), 11 (orange), 101 (green) and 301 (red) using $\mathcal{L} = 24$, $Re = 10$, $\mathcal{R} = 1$, $CFL = 10^{-2}$, $N_x = 241$, $\Delta x = \mathcal{L}/(N_x - 1)$ and $\Delta t = CFL\,\Delta x/u_s$, with $u_s = 1$, $\mathcal{R}_c = 0$ and $\mathcal{R}_a = 2.5$. Time integration performed with the explicit Euler scheme and spatial discretization performed using central-difference schemes with (first row) fourth-order accuracy without buffer, (second row) fourth-order accuracy with buffer at the inlet, (third row) with buffer at the inlet as well as outlet and (fourth row) second-order accuracy without buffer. The former three rows used $\mathcal{A}_0 = 0$ whereas the latter row used $\mathcal{A}_0 = 10^{-12}$, $\mathcal{A}_1 = \mathcal{A}_2 = 10$, $x_1 = 5$ and $x_2 = 15$ when imposing the initial condition in Eq. (10.12). Buffer layers use $\mathcal{B}_0 = 10^3$, $\mathcal{B}_1 = 2$ and/or $\mathcal{B}_2 = \mathcal{B}_0$, $\mathcal{B}_3 = \mathcal{L} - \mathcal{B}_1$. Dashed lines show the spatial growth rate from linear stability analysis (LSA) whereas points show direct numerical simulation (DNS) data.

slightly. This can be inferred from the fact that the steady contamination is further away from the dashed black line than in Fig. 10.2 (first row). It is important to note that this qualitative behavior does not change for other values of the buffer layer parameters. In the next scenario, the second one is modified by also introducing a buffer layer near the outlet, with $\mathcal{B}_2 = \mathcal{B}_0$ and $\mathcal{B}_3 = \mathcal{L} - \mathcal{B}_1$, as well as switching to periodic boundary conditions, i.e. $u(0,t) = u(\mathcal{L},t)$ or $u_d(0,t) = u_d(\mathcal{L},t)$. This was done to eliminate the need to bias the scheme near the boundaries while enforcing the correct inlet condition and minimizing numerical wave reflection at the outlet. As shown in Fig. 10.2 (third row), second and third scenarios are very similar.

The fourth and final scenario is now employed to evaluate the effect of approximate initial conditions. This is done here by employing $\mathcal{A}_0 = 10^{-12}$, $\mathcal{A}_1 = \mathcal{A}_2 = 10$, $x_1 = 5$ and $x_2 = 15$ instead of $\mathcal{A}_0 = 0$. In order to evaluate this effect, however, the inlet cannot be allowed to act as a numerical excitation source. Hence, the spatial discretization is returned to second-order accuracy to eliminate the need for biased schemes. Both buffer layers are still used because they do not act as a numerical excitation source on their own. This is the case because the reference solution they employ is the accurate and disturbance free steady-state defined in Eq. (7.6). Figure 10.2 (fourth row) shows the consequences of this change in initial condition. Two stationary disturbances are numerically excited, near x_1 and x_2. They grow spatially downstream of their respective numerical sources in a physically consistent manner, as confirmed by the linear stability growth rate shown as a dashed black line. As time passes, both reach further into the domain until the former overtakes the latter and arrives at a time invariant solution within the simulated domain. This solution is the steady contamination, i.e. the contaminated steady-state is given by $u(x, t \to \infty) = u_s + u_d(x, t \to \infty)$. Such a result is quite surprising, since one usually expects convectively unstable flows to propagate disturbances in the initial condition out of the finite domain in the absence of a continuous excitation source (Huerre and Monkewitz, 1990). It turns out this only true for oscillatory disturbances, since they travel at positive phase speeds. Stationary disturbances in the initial condition, however, remain at the same location because they have a zero phase speed. In other words, initial conditions that have been disturbed by either numerical or physical mechanisms can create continuous steady excitation sources when they trigger the growth of stationary disturbances.

These results, both from the literature and presented here for the first time, clearly indicate that unstable stationary disturbances can be easily excited by different steady numerical excitation sources. Furthermore, there is strong theoretical evidence in section 10.1 that none of the time marching schemes available in the literature, and the iterative methods derived from them, are capable of damping these disturbances once they have been excited. Numerical evidence in favor of this latter statement can be provided as well. Figure 10.3 shows that neither the solution increment (left) nor the residue (right) maximum absolute values converge in time to machine precision when simulating the same toy model discussed in this section with the Newton

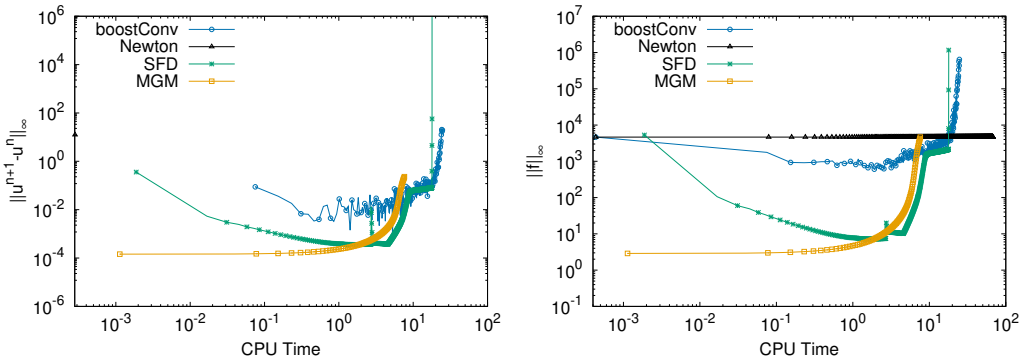

Figure 10.3: Solution increment (left) and density residue (right) maximum absolute values versus CPU time for the simulation of Eqs. (7.4) and (7.5). The initial condition was taken from Fig. 7.6 (left) at $t = 100$. The curves in these plots were generated by time marching from it using the implicit Euler scheme with a large time step, the multi-step MGM scheme as well as the explicit Euler scheme with SFD and Boostconv. A very large selection of numerical parameters was tested in each case, but none led to convergence.

method, i.e. the implicit Euler scheme with $\Delta t \to \infty$, the multi-step MGM scheme as well as the explicit Euler scheme with SFD and Boostconv (Veloso et al., 2019). Even though $||u^{n+1} - u^n||_\infty$ does decay between two and three orders of magnitude, $||f(u^n)||_\infty$ decays only one order of magnitude at most. In other words, there is strong evidence that existing steady-state solvers are not capable of damping (physically consistent) stationary disturbances once they have been numerically excited. All this evidence suggests that a novel steady-state solver should be developed for the computation of accurate and disturbance free steady-states of complex flows that are convectively unstable to stationary disturbances.

10.3 The Frequency Displacement Procedure

The present derivation starts from Eq. (1), i.e.

$$\frac{\partial \mathbf{u}}{\partial t} = \mathbf{f}\big(\mathbf{u}(\mathbf{x}, t)\big) \quad , \tag{10.13}$$

with a steady-state $\mathbf{u}_s$ that must yield a null residue, i.e.

$$\mathbf{f}\big(\mathbf{u}_s(\mathbf{x})\big) = 0 \quad , \tag{10.14}$$

as well as satisfy time invariance, i.e.

$$\frac{\partial \mathbf{u}_s}{\partial t} = 0 \quad , \tag{10.15}$$

which were originally written in Eqs. (2) and (3), respectively. Furthermore, all small amplitude stationary disturbances superposed to this steady-state

are assumed to be convectively unstable under the linear and local version of Eq. (10.13). Hence, the time asymptotic relations

$$\mathbf{f}\big(\mathbf{u}(\mathbf{x}, t \to \infty)\big) \,=\, \mathbf{f}\big(\mathbf{u}_s(\mathbf{x})\big) \,=\, 0 \quad \text{and} \quad \mathbf{u}(\mathbf{x}, t \to \infty) \,=\, \mathbf{u}_s(\mathbf{x}) \quad , \tag{10.16}$$

are satisfied in the absence of steady excitation sources.

As discussed in previous sections, however, numerically induced steady excitation sources are quite often unavoidable. Furthermore, steady-state solvers cannot be used to obtain time invariant solutions that are convectively unstable to stationary disturbances, if they have been numerically excited, because of the consistency requirement. Since this numerical requirement guarantees the existence of a steady-state, it cannot be removed. Hence, the dynamical system physical instability must be modified instead. However, its governing equations must be modified without changing its steady-state. The approach taken here to do so is motivated by the classical linear and homogeneous mass-damper-spring model, which is defined by

$$\frac{d^2x}{dt^2} \,+\, 2\,\zeta\,\omega_n\,\frac{dx}{dt} \,+\, \omega_n^2\,x \,=\, 0 \quad , \tag{10.17}$$

where ζ is the damping ratio and ω_n is the natural frequency, which leads to oscillatory solutions when $\zeta < 1$. Subtracting its steady version from the above equation and integrating the result in time yields

$$\frac{dx}{dt} \,+\, 2\,\zeta\,\omega_n\,(x - x_s) \,+\, \omega_n^2 \int_0^t (x - x_s)\,d\tau \,=\, 0 \quad , \tag{10.18}$$

whose second term is analogous to the scalar version of the source term added by SFD to Eq. (6.8) with $\chi = 2\,\zeta\,\omega_n$. This suggests a reason why such a source term *i*) has a damping effect on oscillatory ($\omega_n \neq 0$) disturbances but *ii*) does not work on stationary ($\omega_n = 0$) disturbances. On the other hand, the third term of the above equation suggests that the natural frequency associated with Eq. (10.13) can be modified by re-writing it as

$$\frac{\partial \mathbf{u}}{\partial t} \,=\, \mathbf{f}\big(\mathbf{u}(\mathbf{x}, t)\big) \,-\, \Omega^2 \int_0^t \big(\mathbf{u}(\mathbf{x}, \tau) - \mathbf{u}_s(\mathbf{x})\big)\,d\tau \quad , \tag{10.19}$$

where Ω is the frequency imposed on the otherwise stationary model, i.e. the frequency displacement away from zero. For this reason, it is labelled here the Frequency Displacement Procedure (FDP). The addition of this term does not affect the requirements in Eqs. (10.14) and (10.15) for the steady-state $\mathbf{u}_s$ since the relations defined in Eq. (10.16) are now satisfied in the absence of oscillatory excitation sources instead, which can be easily removed from any given numerical simulation. Steady-state solvers that did not work when applied to Eq. (10.13) should now work when applied to Eq. (10.19).

Solving this integral-differential model as defined by Eq. (10.19) requires a time integration that becomes an increasingly more expensive numerical task as time evolves. Hence, its differential version, given by

$$\frac{\partial \mathbf{u}}{\partial t} \quad = \quad \mathbf{f}\big(\mathbf{u}(\mathbf{x}, t)\big) \,-\, \Omega^2\,\mathbf{v}(\mathbf{x}, t) \quad \text{and}$$

$$\frac{\partial \mathbf{v}}{\partial t} \;=\; \mathbf{u}(\mathbf{x},t) - \mathbf{u}_s(\mathbf{x}) \quad \text{with} \quad \mathbf{v}(\mathbf{x},t=0) = 0 \quad , \tag{10.20}$$

is solved instead, which is a significantly less expensive numerical task.

Two additional steps in this derivation are now required. First, it must be formally demonstrated that the introduction of this source term makes the flow convectively unstable to oscillatory disturbances but not stationary ones. In other words, all linear and originally stationary disturbances have their frequencies moved away from zero. This is labelled here the exact FDP. Second, $\mathbf{u}_s$ must be removed from this term. Since it is the still unknown and yet to be determined steady-state, it cannot be a variable in the modified governing equations. This is labelled here the approximate FDP. Both steps are respectively taken in the following two subsections.

10.3.1 Exact FDP

A linear and global stability analysis of an arbitrary steady-state $u_s(x)$ can now be performed. Following the discussion presented in the prologue, the first step to do so is proposing the following decomposition

$$\mathbf{u}(\mathbf{x},t) \;=\; \mathbf{u}_s(\mathbf{x}) \;+\; \epsilon\, \mathbf{u}_n(\mathbf{x})\, e^{-\,i\,\omega_{\text{FD}}\,t} \;+\; O(\epsilon^2) \quad , \tag{10.21}$$

where $\epsilon \ll 1$ is a small amplitude parameter, $\mathbf{u}_n(x)$ is the global eigenfunction and ω_{FD} is the complex eigenvalue describing the time asymptotic oscillation frequency $\text{Re}[\omega_{\text{FD}}]$ and temporal growth rate $\text{Im}[\omega_{\text{FD}}]$, with $i = \sqrt{-1}$. The second step is to linearize the residue using the Taylor series expansion

$$\mathbf{f}\big(\mathbf{u}(\mathbf{x},t)\big) \;=\; \mathbf{f}\big(\mathbf{u}_s(\mathbf{x})\big) \;+\; \left.\frac{\partial \mathbf{f}}{\partial \mathbf{u}}\right|_{\mathbf{u}_s} \big(\mathbf{u}(\mathbf{x},t) - \mathbf{u}_s(\mathbf{x})\big) \;+\; O(\epsilon^2) \quad , \tag{10.22}$$

around the steady-state. Applying Eqs. (10.21) and (10.22) to Eq. (10.19) and collecting the $O(\epsilon)$ terms yields

$$-\,i\left(\frac{\omega_{\text{FD}}^2 - \Omega^2}{\omega_{\text{FD}}}\right)\mathbf{u}_n \;=\; \left.\frac{\partial \mathbf{f}}{\partial \mathbf{u}}\right|_{\mathbf{u}_s} \mathbf{u}_n \quad , \tag{10.23}$$

which returns the eigenvalues ω of the original generalized eigenvalue problem when $\Omega = 0$. Since both problems can be formulated in the exact same way, i.e. $\omega \leftrightarrow (\omega_{\text{FD}}^2 - \Omega^2)/\omega_{\text{FD}}$, it is possible to say that

$$\omega_{\text{FD}} = \frac{1}{2}\left(\,\omega \,\pm\, \sqrt{\omega^2 + 4\,\Omega^2}\,\right) \quad . \tag{10.24}$$

Some important conclusions can be drawn from Eq. (10.24). Since the original flow of interest is convectively unstable, i.e. $\text{Im}[\omega] = 0$, the exactly frequency displaced flow will remain convectively unstable, i.e. $\text{Im}[\omega_{\text{FD}}] = 0$, when $\text{Im}[\Omega] = 0$. Under these conditions, the frequencies of all disturbances are forced to be nonzero by the exact FDP, i.e. imposing $\text{Re}[\Omega] \neq 0$ in Eq. (10.24) forces $\text{Re}[\omega_{\text{FD}}] \neq 0$. Furthermore, the exact FDP forces originally

stationary disturbances in a convectively unstable flow to oscillate according to the frequency displacement, since $\mathrm{Re}[\omega_{\mathrm{FD}}] = \pm\,\mathrm{Re}[\Omega]$ whenever $\mathrm{Re}[\omega] = 0$. Finally, it is important to note that Eq. (10.24) also predicts the appearance of a temporally unstable mode when $\mathrm{Im}[\Omega] \neq 0$, which is another reason for Ω to be a real parameter in the simulation of convectively unstable flows ($\mathrm{Im}[\omega] = 0$) to stationary disturbances ($\mathrm{Re}[\omega] = 0$). It is now clear that the exact FDP guarantees there will be no more stationary disturbances growing spatially due to steady excitation sources. Since unsteady excitation sources can usually be removed from numerical simulations, traditional steady-state solvers can now be employed for the calculation of accurate and disturbance free steady-states. These ideas are illustrated in Fig. 10.4, in the context of the explicit (left) and implicit (right) Euler schemes. When $\Omega = 0$, the stationary and convectively unstable mode at the origin ($\omega = 0$) has $\alpha = 1$ for both schemes, i.e. it is numerically marginally stable for any time step Δt. When $\Omega \neq 0$, however, the former becomes numerically unstable ($\alpha > 1$) whereas the latter becomes numerically stable ($\alpha < 1$) for any Δt. Hence, the implicit Euler scheme became an acceptable steady-state solver for the frequency displaced version of the original problem. The same is true for its time asymptotic ($\Delta t \to \infty$) extension, i.e. the Newton method.

A more specific example can be discussed now by applying the above general analysis to the toy model discussed in the previous section. Since its steady-state defined in Eq. (7.6) is fully developed, a linear and local stability analysis can be pursued instead. Hence, Eq. (10.21) can be re-written as

$$u(x,t) \;=\; u_s \;+\; \epsilon\, u_n\, e^{i\,(\alpha\, x\,-\,\omega_{\mathrm{FD}}\, t)} \;+\; O(\epsilon^2) \quad , \tag{10.25}$$

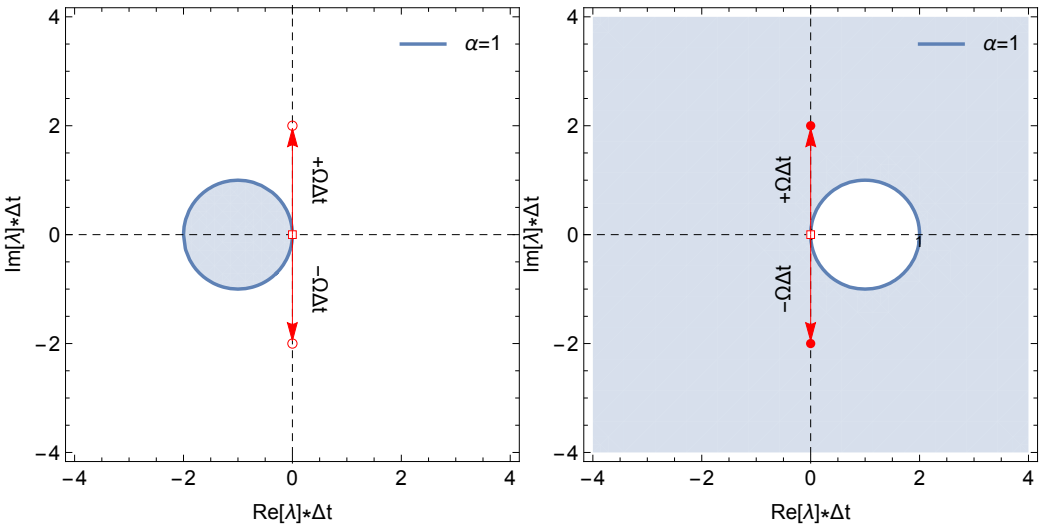

Figure 10.4: Similar to Fig. 1 (top row), where red symbols show the effect of the exact FDP on the originally stationary (square, $\mathrm{Re}[\omega] = 0$) that are now oscillatory (circles, $\mathrm{Re}[\omega] = \pm\,\Omega$) convectively unstable disturbances ($\mathrm{Im}[\omega] = 0$), where $\lambda = -\,i\,\omega$, $\alpha = \mathrm{abs}[G]$ and $G = e^{\lambda \Delta t}$.

where α is the complex eigenvalue describing the time asymptotic oscillation wavenumber Re[α] and spatial growth rate -Im[α]. It is equivalent to Eq. (7.7) with $\lambda = -i\,\omega$. Substituting Eq. (10.25) into Eq. (7.4) and collecting the $O(\epsilon)$ terms leads to the dispersion relation

$$\mathcal{R} - \frac{\alpha^2}{Re} - i\,\alpha + i\left(\frac{\omega_{\text{FD}}^2 - \Omega^2}{\omega_{\text{FD}}}\right) = 0 \quad , \tag{10.26}$$

for non-trivial disturbances, i.e. $u_n \neq 0$, which can be formulated in the same way as Eq. (7.8) using $\omega \leftrightarrow (\omega_{\text{FD}}^2 - \Omega^2)/\omega_{\text{FD}}$. Hence, the complex wavenumber map shown in Fig. 7.7 is not altered by the exact FDP, although the real frequency ω_{FD} associated with each complex wavenumber α does depend on the real frequency displacement Ω. This can be observed in Fig. 10.5, which shows the oscillation wavenumber (left) and spatial growth rate (right) as a function of the displaced frequency for different values of the frequency displacement parameter, i.e. $\Omega = 0$ (blue), 1 (red) and 2 (yellow), when $Re = 10$ and $\mathcal{R} = 1$. As expected from section 7.2, the most convectively unstable disturbance (max[$-$Im[α]]) is stationary (Re[ω_{FD}] = 0) and uniform (Re[α] = 0) when $\Omega = 0$. Some important characteristics change when this parameter is increased to $\Omega = 1$. Although the most convectively unstable disturbance (max[$-$Im[α]]) is still uniform (Re[α] = 0), it is no longer stationary but oscillatory instead (Re[ω_{FD}] = $\pm$1). Furthermore, it is also interesting to note that the stationary disturbance (Re[ω_{FD}] = 0) is no longer convectively unstable but stable instead ($-$Im[α] < 0). Finally, Eq. (10.26) can be used to show that the most convectively unstable disturbance oscillates according to the frequency displacement parameter in general, i.e. Re[ω_{FD}] = $\pm\,\Omega$. It can also be used to show that the stationary disturbance spatial growth rate, i.e. $-\text{Im}[\alpha] \simeq -\Omega\sqrt{Re/(2\,\text{Re}[\omega_{\text{FD}}])}$, becomes increasingly more stable as Re[ω_{FD}] $\to$ 0. Hence, steady excitation sources are innocuous when $\Omega > 0$.

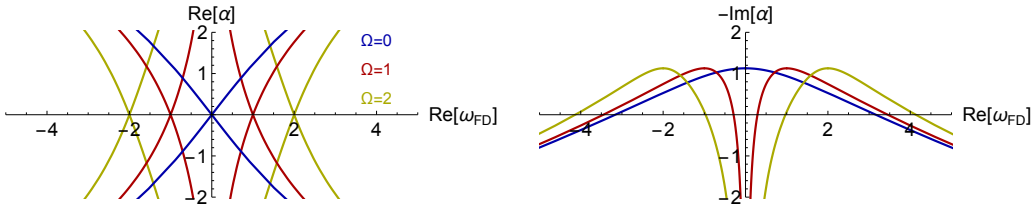

Figure 10.5: Oscillation wavenumber (left) and spatial growth rate (right) as functions of the real frequency for Im[ω_{FD}] = 0, $Re = 10$ and $\mathcal{R} = 1$ with $\Omega = 0$ (blue), 1 (red) and 2 (yellow), noting that Im[Ω] = 0.

10.3.2 Approximate FDP

An important issue still remains though, which is the fact that $\mathbf{u}_s$ in Eq. (10.20) is not known *a priori* and must be removed. A few different approximations can be employed to do so. Usually, a Taylor-series expansion is employed to

approximate $\mathbf{f}\big(\mathbf{u}(\mathbf{x},t)\big)$ in the neighborhood of $\mathbf{f}\big(\mathbf{u}_s(\mathbf{x})\big)$, as in Eq. (10.22). The approximation considered here does the opposite, i.e.

$$\mathbf{f}\big(\mathbf{u}_s(\mathbf{x})\big) \;=\; \mathbf{f}\big(\mathbf{u}(\mathbf{x},t)\big) \;-\; \mathbf{J}\cdot\Delta\mathbf{u} + \; O\big((\Delta\mathbf{u})^2\big) \quad , \tag{10.27}$$

where $\mathbf{J} = (\partial\mathbf{f}/\partial\mathbf{u})_{\mathbf{u}}$ is the Jacobian matrix and $\Delta\mathbf{u} = \mathbf{u}(\mathbf{x},t) - \mathbf{u}_s(\mathbf{x})$ is the steady-state deviation vector. It can be re-written as

$$\mathbf{J}\cdot\Delta\mathbf{u} \;=\; \mathbf{f}\big(\mathbf{u}(\mathbf{x},t)\big) + \; O\big((\Delta\mathbf{u})^2\big) \quad , \tag{10.28}$$

since $\mathbf{f}\big(\mathbf{u}_s(\mathbf{x})\big) = 0$. Hence, Eq. (10.20) can be approximated by

$$\begin{aligned} \frac{\partial\mathbf{u}}{\partial t} \;&=\; \mathbf{f}\big(\mathbf{u}(\mathbf{x},t)\big) \;-\; \Omega^2\,\mathbf{v}(\mathbf{x},t) \quad \text{and} \\ \mathbf{J}\cdot\frac{\partial\mathbf{v}}{\partial t} \;&\simeq\; \mathbf{f}\big(\mathbf{u}(\mathbf{x},t)\big) \quad \text{with} \quad \mathbf{v}(\mathbf{x},t=0) = 0 \quad , \end{aligned} \tag{10.29}$$

where the Jacobian matrix can be evaluated numerically instead in order to facilitate the simulation of Eq. (10.29).

Chapter 11

Results

11.1 Exact FDP

11.1.1 Modified Burgers' Equation

Applying the exact version of the efficient frequency displacement procedure to the modified Burgers's equation given by Eq. (7.4), and subject to the boundary conditions in Eq. (10.10), means applying the scalar version of Eq. (10.20) with the residue defined as

$$f\big(u(x,t)\big) = \frac{1}{Re}\frac{\partial^2 u}{\partial x^2} - \mathcal{R}\,(u-1) - u\,\frac{\partial u}{\partial x} \quad , \tag{11.1}$$

and the steady-state u_s defined as Eq. (7.6). Following section 10.2, the physical control parameters are chosen as $\mathcal{L} = 24$, $Re = 10$ and $\mathcal{R} = 1$. Furthermore, the explicit Euler scheme is used for time integration with $\Delta t = CFL\,\Delta x/u_s$ and fourth-order central difference schemes are used for the spatial discretization of first and second derivatives. This is done while using $CFL = 10^{-2}$ and a uniform grid with $N_x = 241$, where $\Delta x = \mathcal{L}/(N_x - 1)$, to guarantee sufficient temporal and spatial accuracy. Finally, no buffer zones are used and the initial condition is the disturbance free steady-state u_s.

When imposing $\Omega = 0$, the original modified Burgers's equation defined in Eq. (7.4) is recovered. Hence, according to the linear and local stability analysis shown in Fig. 10.5, stationary disturbances are the most unstable in this convectively unstable flow. Although not shown here, the numerical simulation under this parametric setup reproduces the solutions shown in Fig. 10.2 (first row). When imposing $\Omega > 0$, however, a qualitative change in the solution behavior is observed. This is shown in Fig. 11.1 for the particular case where $\Omega = 1$. Steady numerical excitation sources no longer promote the time asymptotic spatial growth of stationary disturbances. This is due to the fact that such disturbances are now convectively stable according to the linear and local stability analysis shown in Fig. 10.5. The initial impulse excitation due to numerical error, however, still promotes the spatial growth of oscillatory disturbances. Since the convectively unstable wave packet has a positive group velocity, with all disturbances in it having positive

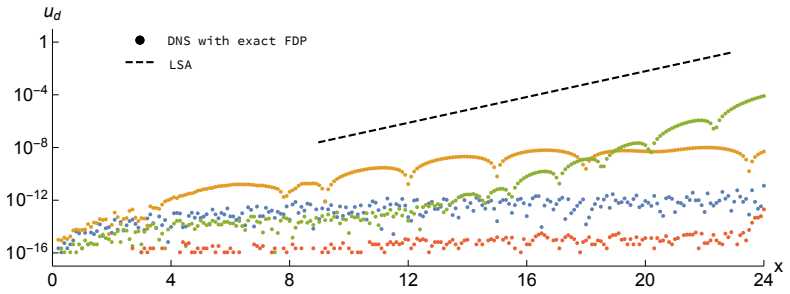

Figure 11.1: Same as Fig. 10.2 (first row), except with disturbance spatial profiles obtained instead from the numerical simulations of Eq. (10.20) with $\Omega = 1$, the residue in Eq. (11.1) and the steady-state in Eq. (7.6).

phase speeds, such oscillatory disturbances do eventually propagate out of the domain. Furthermore, new oscillatory disturbances are not excited because there are no oscillatory numerical excitation sources, which means that the disturbance field eventually decays to machine zero. Hence, the disturbance free steady-state u_s is reached.

Having better understood the frequency displacement effect on the flow dynamics that allows convergence to the disturbance free steady-state, it can now be quantified. In order to do so, the temporal variation of the infinity norm of the (left) disturbance amplitude and the (right) residue are shown in Fig. 11.2 for $\Omega = 0.5$, 1.0 and 2.0, where all other physical and numerical parameters are provided in Fig. 11.1. Their temporal behavior is essentially the same up until they reach their respective maximum values. Beyond this point in time, namely a single peak at $t \sim 58$ for the former and a double peak at $t \sim 41$ and 77 for the latter, increasing Ω means speeding up the damping process. This is likely due to the fact that an increase in Ω also increases the range of convectively stable low frequency disturbances, as shown in Fig. 10.5. Finally, it is important to note that even though the disturbance amplitude maximum norm decays approximately 12 orders

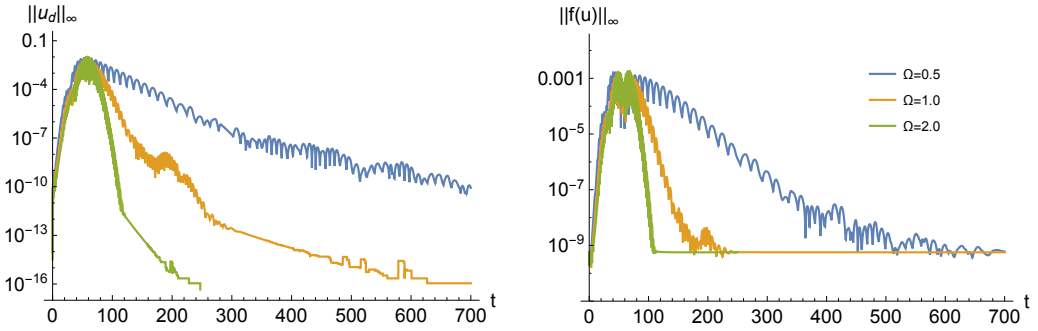

Figure 11.2: Infinity norm of the (left) disturbance amplitude and the (right) residue behavior in time when applied the exact FDP to the modified Burger's equation for $\Omega = 0.5$, 1.0 and 2.0. All additional physical and numerical parameters are the same ones used to generate the data shown in Fig. 11.1.

of magnitude towards essentially machine zero, the residue maximum norm only decays approximately 6 orders of magnitude. As originally pointed out by Teixeira and Alves (2017), this worse residue convergence is an issue with solvers that require source terms to drive the marching scheme towards steady-state, such as FDP or Selective Frequency Damping (or SFD), since these very same source terms must eventually vanish in time for the correct steady-state to be reached. Some evidence for this issue is shown in Fig. 11.2 as well. A qualitative change in the disturbance amplitude maximum norm convergence rate can be observed at the same time beyond which the residue maximum norm ceases to converge for $\Omega = 0.5$ and 1.

11.1.2 Modified 1D Navier-Stokes' Equations

Having verified in the previous subsection that the exact FDP as defined in Eq. (10.19), or its more efficient version in Eq. (10.20), works as designed for flows that are convectively unstable to stationary disturbances when governed by a scalar conservation law, the same must be done for flows governed by a system of equations as well. The first step towards doing so uses the modified version of the one-dimensional Navier-Stokes equations that was originally defined in subsection 7.3.1. Its steady-state is still given by Eq. (7.14) and its linear and local stability is still governed by Eq. (7.19). In this analysis, however, spatial periodicity is removed in order to allow the existence of a convectively unstable parametric conditions. Furthermore, one must also identify the parametric conditions under which the flow instability transitions from convective to absolute. Hence, the temporal stability analysis performed in subsection 7.3.1 is no longer valid and new analyses are required for both parameter sets. Finally, all three types of linear stability disturbances present in this flow must be considered when performing these analyses. The first one includes entropy disturbances, whose phase speed is equal to the steady velocity, whereas the second (third) one includes instead fast (slow) acoustic disturbances, whose phase speed is equal to the steady velocity superposed to (subtracted by) the speed of sound.

All results presented in this subsection focussed on the pair $\mathcal{R}$ and Ma_∞ while fixing the remaining physical parameters, i.e. $Re_\infty = 100$, $Pr_\infty = 0.72$ and $\gamma = 1.4$. As was the case in subsection 7.3.1, imposing $\mathcal{R} = 0$ recovers the original one-dimensional Navier-Stokes equations and makes the steady-state defined in Eq. (7.14) marginally stable for any Ma_∞. In other words, the onset of convective instability still occurs at $\mathcal{R}_c = 0$. When $\mathcal{R} > \mathcal{R}_c$, a spatial stability analysis yields the disturbance wavenumber (Re[α]) and spatial growth rate (- Im[α]) for a prescribed disturbance frequency (Re[ω]), while imposing Im[ω] = 0. These results are shown in Figs. 11.3 and 11.4 for $Ma_\infty = 0.5$ and 2.0, respectively, which include data for $\mathcal{R} = 0$ (lines) and 1 (symbols). They confirm the flow is marginally stable when $\mathcal{R} = 0$, with the stationary mode of the entropy, fast and slow acoustic disturbances being the least stable one, where the latter propagates upstream (downstream) when $Ma_\infty = 0.5$ (2.0). All three disturbances have a finite range of convectively

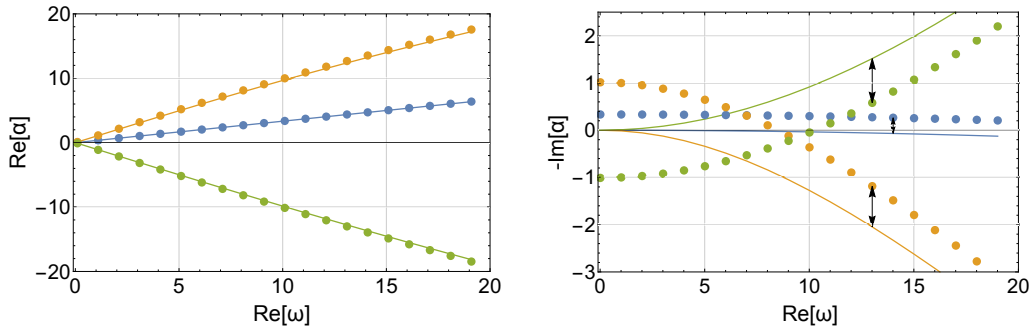

Figure 11.3: Disturbance (left) wavenumber and (right) spatial growth rate versus frequency for $Ma_\infty = 0.5$ as well as $\mathcal{R} = 0$ (lines) and 1 (symbols). Yellow represents entropy disturbances whereas blue and green represent fast and slow acoustic disturbances, respectively.

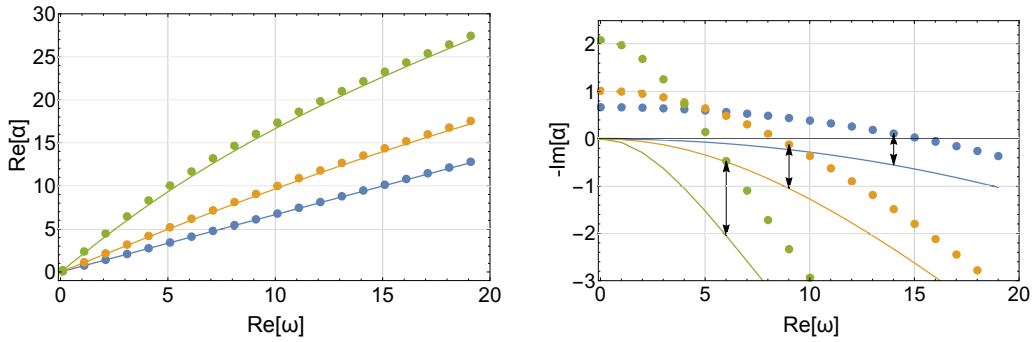

Figure 11.4: Same as Fig. 11.3 but for $Ma_\infty = 2.0$.

unstable frequencies when $\mathcal{R} = 1$, with the stationary mode now becoming the most unstable one for each disturbance. Finally, it should be noted that their wavenumbers and, hence, phase speeds, do not depend on $\mathcal{R}$.

The qualitative behavior just described does not occur for any $\mathcal{R} > \mathcal{R}_c$ because the flow does transition to absolute instability at $\mathcal{R} = \mathcal{R}_a$. Hence, it is important to guarantee that $\mathcal{R}_c < \mathcal{R} < \mathcal{R}_a$ in order to maintain a convectively unstable flow. This new critical parameter can be evaluated using Eq. (7.19) and following the same procedure used for the modified Burgers' equation in subsection 7.2.1 and described in detail by Alves et al. (2019). Doing so yields the values of $\mathcal{R}$ that lead to the saddle points shown in Fig. 11.5 as solid symbols for different Ma_∞. The open symbols in this figure, on the other hand, indicate which saddle points are also pinching points, i.e. also satisfy the collision criterion. In other words, they indicate the onset of absolute instability $\mathcal{R}_a$ for different Ma_∞. It turns out $\mathcal{R}_a$ depends on Ma_∞. Furthermore, three distinct Mach number ranges can be observed in this figure, differing by which disturbance first becomes absolutely unstable. This onset occurs through the entropy disturbance when $Ma_\infty \lesssim 0.6$, which starts to propagate upstream as well for $\mathcal{R} > \mathcal{R}_a$. Otherwise, it occurs through the slow acoustic disturbance, which also starts to propagate downstream when $0.6 \lesssim Ma_\infty < 1.0$ and upstream when $Ma_\infty > 1.0$, for $\mathcal{R} > \mathcal{R}_a$. Finally,

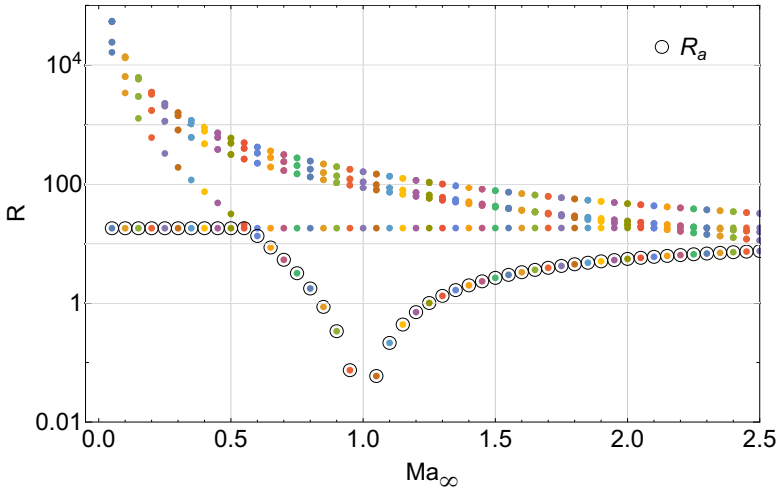

Figure 11.5: Values of the critical control parameters $\mathcal{R}$ that lead to saddle points (solid symbols) for different Mach numbers Ma_∞ for $Re_\infty = 100$, $Pr_\infty = 0.72$ and $\gamma = 1.4$. Pinching points (open symbols) are the saddle points that also satisfy the collision criterion (Alves et al., 2019).

$\mathcal{R}_a = \mathcal{R}_c$ when $Ma_\infty = 1$. In other words, there is no region of convective instability in this scenario, which means the flow transitions directly from stable to absolutely unstable when $\mathcal{R} > 0$.

Now that the physical behavior of this toy model for a system of equations has been clarified, numerical simulations can be performed using 3D4S. These particular simulations were performed using the optimal third-order SSP RK scheme (Shu and Osher, 1988) for temporal integration with a $\Delta t = 10^{-5}$ time step, the WENO5-JS scheme coupled with a global Lax-Friedrichs flux splitting (Jiang and Shu, 1996) for the inviscid flux discretization as well as the fourth-order conservative central-difference scheme for the viscous fluxes with $N_x = 505$ grid points. Furthermore, periodic boundary conditions were imposed with buffer zones at the inlet and outlet (Bodony, 2006) in order to eliminate the need to bias the scheme near the boundaries while enforcing the correct inlet condition and minimizing numerical wave reflection at the outlet. Contrary to the previous test case, however, steady excitation sources are not artificially created by the numerics implemented to simulate the present test case. Hence, convectively unstable stationary disturbances are never excited. This is likely due to the innate ability of WENO schemes to smooth out the spatial error distribution. Such a hypothesis comes from the fact that stationary disturbances were not excited either when WENO schemes were employed to simulate the toy model for a scalar conservation law studied in the previous test case. In order to circumvent this issue and excite stationary disturbances in the present test case, the steady Gaussian source term $\mathcal{S}(x) = \mathcal{A}_0 \exp[-\theta_0 (x - x_0)^2]$ was added to the mass conservation equation at $x_0 = 8$ with amplitude $\mathcal{A}_0 = 10^{-8}$ and intensity $\theta_0 = 10$. It can also be understood as a means to emulate the effect of alternative numerical excitation sources, such as ones that are internal to the model.

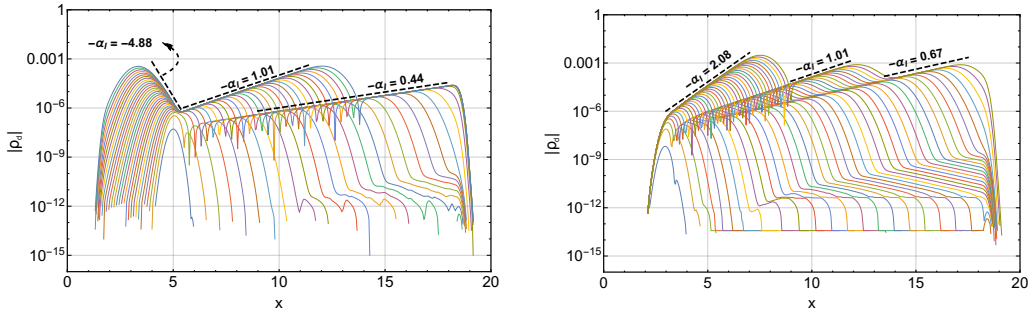

Figure 11.6: Absolute value of the density disturbance spatial profiles at different times taken from numerical simulations of the modified one-dimensional Navier-Stokes equations with $\mathcal{L} = 20$, $Re_\infty = 100$, $Pr_\infty = 0.72$, $\gamma = 1.4$, (left) $x_0 = 5$, $Ma_\infty = 0.2$ and $\mathcal{R} = 5$ as well as (right) $x_0 = 3$, $Ma_\infty = 2.0$ and $\mathcal{R} = 1$. Dashed lines show the spatial growth rates of the entropy as well as slow and fast acoustic disturbances stationary modes obtained from the linear and local stability analysis.

Some results from these direct numerical simulations (DNS) are shown in Fig. 11.6, namely the absolute density profile over the entire domain for different times using (left) $x_0 = 5$, $Ma_\infty = 0.2$ and $\mathcal{R} = 5$ as well as (right) $x_0 = 3$, $Ma_\infty = 2.0$ and $\mathcal{R} = 1$. This figure also shows (dashed lines) the linear and local stability (LSA) spatial growth rates for all three disturbances. In both cases, the mass conservation equation low amplitude and steady source term excitation triggers the spatial growth of the stationary modes from entropy as well as slow and fast acoustic disturbances. As expected, the spatial growth observed in the DNS follows the predicted LSA trends. For instance, the convectively unstable stationary slow acoustic disturbance propagates upstream when $Ma_\infty = 0.2$ but downstream when $Ma_\infty = 2.0$. Furthermore, the slow acoustic disturbance grows the most, followed by the entropy and fast acoustic disturbances, among all three excited stationary modes. Although not shown here, similar agreements were observed under other parametric conditions, including absolutely unstable ones. This DNS data generated when using the one-dimensional version of 3D4S confirmed the LSA prediction that this toy model can indeed be convectively unstable to stationary disturbances under the appropriate parametric conditions.

It is now time to evaluate the inability of traditional steady-state solvers to obtain a disturbance free steady-state for this toy model. This is shown in Fig. 11.7, which presents the density residue maximum norm over time when the time-accurate marching scheme is switched to different steady-state solvers at $t \simeq 2.1$. These solvers are the implicit Euler scheme, the multi-step MGM scheme (MGM1), both multi-stage MGM schemes (MGM2 and MGM3) and boostConv. In all cases, the maximum norm of the density residue does not decay significantly once the steady-state solver is turned on. For instance, it diverges with the MGM1 scheme. Furthermore, it stagnates with the implicit Euler, MGM2 and MGM3 schemes. Finally, it only decays approximately one order of magnitude with boostConv. This is yet

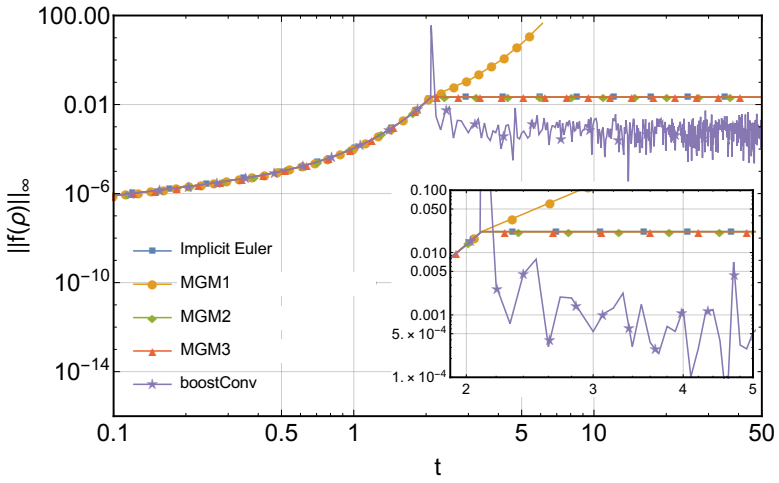

Figure 11.7: Maximum norm of the density residue obtained using a time-accurate marching scheme from Fig. 11.6 (left) up to $t \simeq 2.1$ and five different steady-state solvers beyond this point, i.e. the implicit Euler scheme ($\Delta t = 0.5$), multi-step (MGM1 with $\Delta t = 0.5$, $\theta_1 = 1$ and $\theta_2 = 1.5$), two-stage (MGM2 with $\Delta t = 0.5$ and $\alpha = 10$) and three-stage (MGM3 with $\Delta t = 0.5$ and $\alpha = 10$) MGM schemes and boostConv ($\Delta t = 10^{-5}$, $M = 2$ and $K = 1$).

another strong evidence that traditional steady-state solvers are not capable of damping stationary disturbances in convectively unstable flows once they have been excited.

It is important to emphasize, however, that this lack of convergence might remain hidden depending on which metric is used to evaluate steady-state convergence. In order to illustrate this issue, the two most relevant metrics are shown in Fig. 11.8 when applying the implicit Euler scheme from Fig. 11.7 as steady-state solver, but now with different time steps. These metrics are the maximum norm of (left) the density residue and (right) the solution increment in time, where $\Delta\rho = \rho^{n+1} - \rho^n$ and n is the time step index. This figure shows that the former stagnates for all time steps tested but the latter

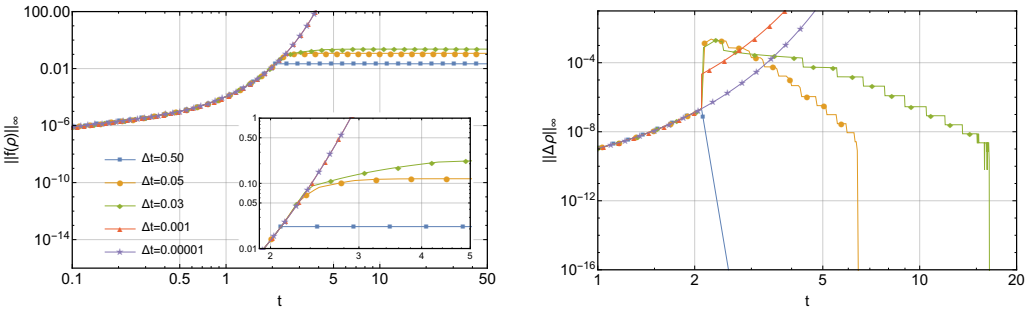

Figure 11.8: Maximum norm of (left) the density residue as well as (right) the density solution increment versus time, obtained using a time-accurate marching scheme (Fig. 11.6) up to $t \simeq 2.1$ and the implicit Euler scheme with different time steps beyond this point.

converges to machine zero once the time step is chosen large enough. Such a discrepancy between both metrics is observed for all steady-state solvers show in Fig. 11.7. It arises from the large condition number of the implicit matrix used in each solver. Hence, employing the solution increment alone as a convergence metric when performing numerical simulations of flows that are convectively unstable to stationary disturbances will likely lead to steady-states that are still contaminated with temporal content.

So the next step is to verify that the exact FDP works as designed when applied to this toy model for systems of equations. Figure 11.9 presents strong evidence that it does so using data obtained from DNS with $Ma_\infty = 0.8$, $\mathcal{R} = 1$ and measured at $x_0 = 5$ for different frequency displacements, namely $\Omega = 0$ (blue), 5 (oriange), 10 (green) and 20 (red). A time-accurate simulation with the exact FDP turned off (on) is shown in the first (second) stage. This is done using the density absolute value temporal behavior (left), which indicates that dominant disturbances in this convectively unstable flow go from stationary to oscillatory when the exact FDP is turned on at $t = 3$. Furthermore, (right) its respective normalized spectra suggests that their oscillation frequency is indeed $\omega_{\text{FD}} \simeq \Omega$, as was originally implied by Eq. (10.24) for flows that are convectively unstable ($\text{Im}[\omega] = 0$) to stationary disturbances ($\text{Re}[\omega] = 0$). Finally, it is important to mention that the same results were obtained with several other Ma_∞ and $\mathcal{R}$ combinations.

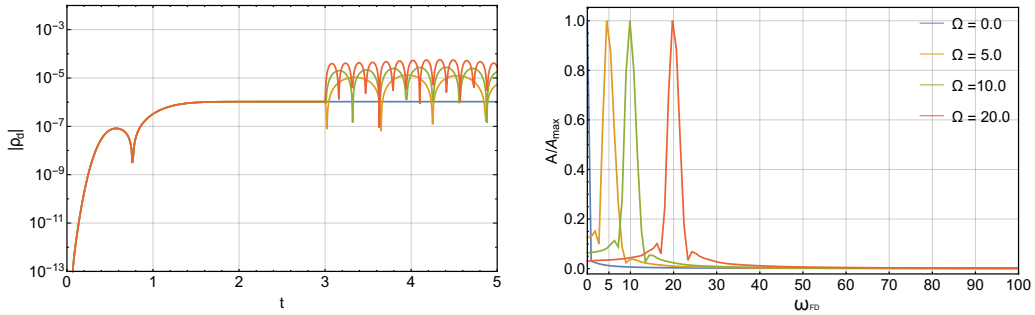

Figure 11.9: Density disturbance absolute value (left) temporal behavior measured at x_0 and (right) its respective normalized spectra for different Ω when $x_0 = 5$, $Ma_\infty = 0.8$ and $\mathcal{R} = 1$. Exact FDP turned on when $t \geq 3$.

In the present test case, however, a disturbance free steady-state is not eventually reached when the time-accurate marching scheme coupled with the exact FDP is run for large enough times. This is likely due to the fact that disturbances were introduced through a steady source term added to the mass conservation equation, in contrast to the previous test case where disturbances were introduced through initial and/or boundary conditions. Hence, the exact FDP must be coupled with a steady-state solver instead of a time-accurate marching scheme. Figure 11.10 shows the effect of doing so in three stages. In the first stage, the same time-accurate simulation used to generate the data shown in Fig. 11.6 (right) is presented up to $t \simeq 8.7$. Both residue and solution increment increase in time in a non-oscillatory

fashion due to the dominant stationary disturbance spatial growth within the domain during this period of time. The exact FDP is turned on after $t \simeq 8.7$ with $\Omega = 10$, characterizing the second stage shown in this figure. Both residue and solution increment start oscillating in time as expected, since the dominant disturbance is now oscillatory. This second stage is brief, however, since the marching scheme is switched from the time-accurate one to a steady-state solver after $t \simeq 9.7$. Five different solvers were tested, namely the implicit Euler scheme, the multi-step MGM scheme (MGM1), both multi-stage MGM schemes (MGM2 and MGM3) and boostConv. In all cases, both residue and solution increment eventually decay to machine zero. It is important to emphasize here that these solvers were not optimized. In other words, comparisons between their efficiencies should not be pursued using this data. The point here is to show that a disturbance free steady-state can be obtained for this toy problem when the exact FDP is coupled with any of the traditional steady-state solvers tested here. Finally, the same results were obtained with several other parametric combinations.

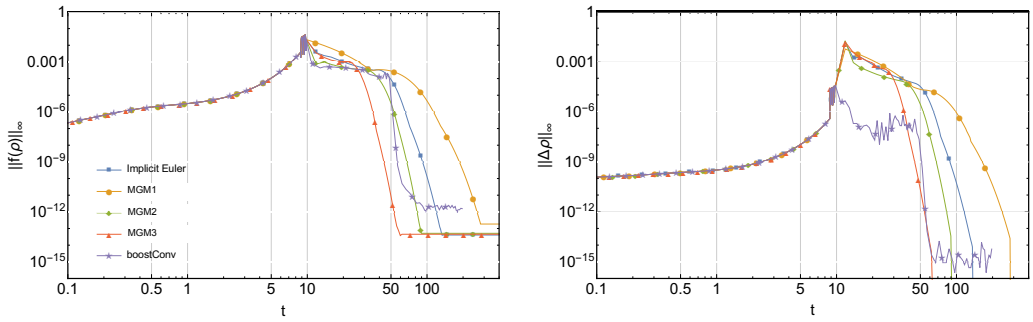

Figure 11.10: Maximum norm of the (left) density residue as well as the (right) density solution increment versus time, obtained using a time-accurate marching scheme from Fig. 11.6 (right) up to $t \simeq 9.7$, but switching to five different steady-state solvers beyond this point, namely the implicit Euler scheme ($\Delta t = 0.5$), multi-step (MGM1 with $\Delta t = 0.5$, $\theta_1 = 1$ and $\theta_2 = 2.5$), two-stage (MGM2 with $\Delta t = 0.5$ and $\alpha = 2$) and three-stage (MGM3 with $\Delta t = 0.5$ and $\alpha = 2$) MGM schemes and boostConv ($\Delta t = 10^{-5}$, $M = 2$ and $K = 1$). The exact FDP was only turned on after $t \simeq 8.7$ with $\Omega = 10$.

11.1.3 Modified 2D Navier-Stokes' Equations

One additional toy model was created and tested during this project with the intent of extending the analysis performed in the previous subsection to two-dimensional flows. The original problem is the compressible flow over a flat plate, including a sharp leading edge, which leads to the appearance of a leading edge shock upstream of the boundary layer when the free-stream is supersonic. Although this flow is convectively unstable beyond a critical Reynolds number, two-dimensional stationary disturbances are stable. In other words, the introduction of a steady blowing and suction strip at the

wall to produce a small amplitude excitation downstream of the leading edge does not lead to boundary-layer instabilities under supercritical parametric conditions. Hence, an artificial source term is added to the original problem in order to create a toy model with the same steady-state which is unstable to stationary disturbances. It is important to note, however, that they were not always dominant, contrary to the previous one-dimensional toy model. On the other had, this has no relevance to the issues discussed in this third part of the report. It turns out the results obtained with this two-dimensional toy model were essentially the same as the ones shown and discussed in the previous subsection. For this reason, they are not going to be shown and discussed here. Only one point deserves special mention, which is the fact that the presence of a leading edge shock has no effect on the exact FDP.

11.1.4 3D Navier-Stokes' Equations

Before moving on with the present analysis, it is important to justify the use of toy models up to this point. Reduced order models are very important because, among other things, they provide a computationally inexpensive means to study the flow physics of interest. On the other hand, real fluid flow models that are relevant to high-speed aerodynamics and also convectively unstable to stationary disturbances are always three-dimensional, as far as the authors are aware. This is the main reason why a few specially designed one and two-dimensional toy models were developed and employed on all the tests discussed so far.

Having made this disclaimer, the final test case of this section presented now is based on a real fluid flow model. It is the unsteady, three-dimensional and compressible flow over a curved surface already used for code verification purposes in subsection 3.1.3. Since such a flow is convectively unstable to stationary disturbances, as already discussed at length in other parts of the present report, the use of steady excitation strips at the wall leads to the appearance of steady structures known as Görtler vortices. For instance, these structures can be observed in Figs. 3.16 and 3.17. In the absence of external excitation, on the other hand, these structures should not appear, leaving the boundary-layer undisturbed. This is the main reason why such structures cannot be observed in Fig. 3.15.

The effect of the exact FDP on this real fluid flow model is tested here by applying it to a problem similar to the former example, where the steady excitation strip is turned on. In other words, a contaminated steady-state, such as the one presented in Fig. 3.16, is employed as initial condition to a new simulation that uses the same numerical methods already discussed in subsection 3.1.3, but now coupled with the exact FDP. This is shown in Fig. 11.11, where the steady forcing amplitude is $v_w = 0.01$ and the frequency displacement is $\Omega = 100$. This figure contains several plots, each one focusing on the same last four (y, z) planes containing isocontours of the streamwise velocity disturbance component, but measured at different consecutive and equidistant times. The velocity disturbance isocontour color change observed

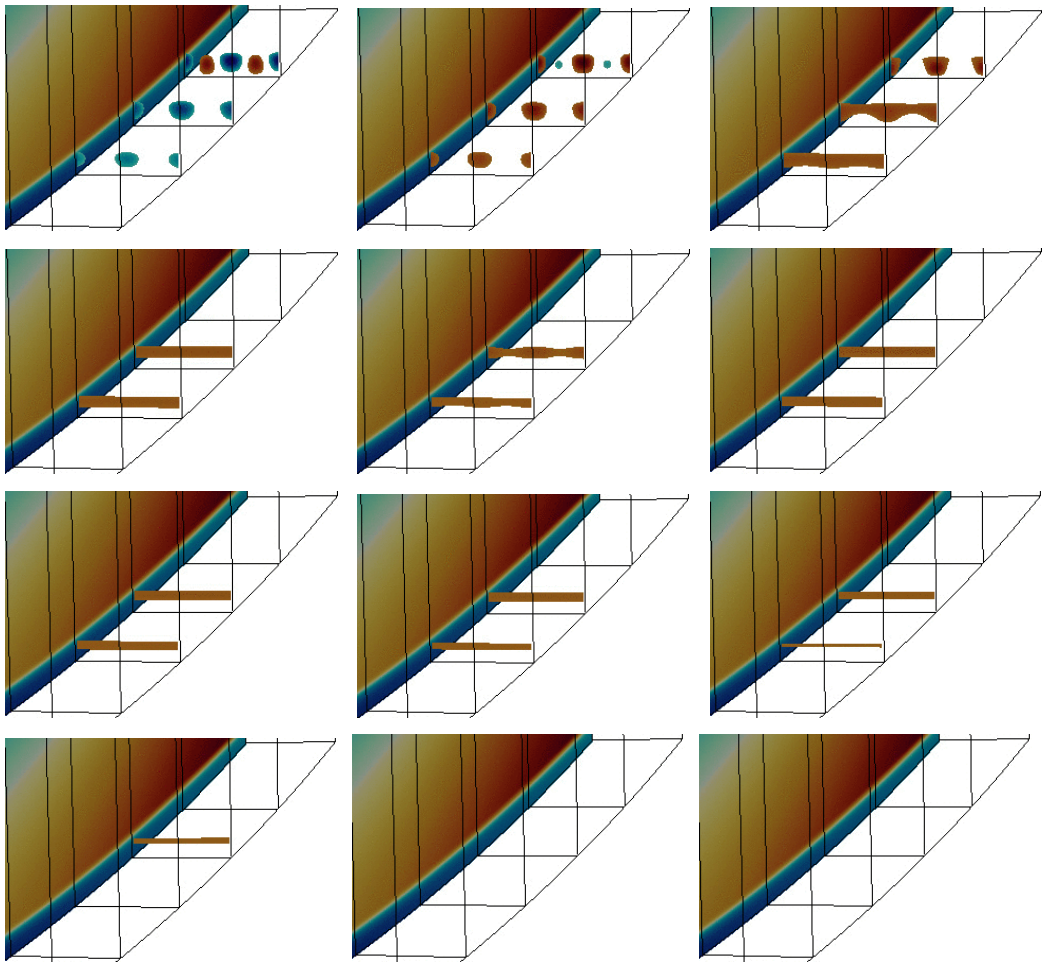

Figure 11.11: Plots showing a version of Fig. 3.17 at consecutive equidistant times (left to right, top to bottom), but obtained using the exact FDP with $\Omega = 100$ and a forcing of $v_w = 0.01$. The same last four (y, z) isocontour planes of the streamwise velocity disturbance component are shown.

in the first two plots (top left and top middle) indicates that the dominant instability became oscillatory, as expected. Since there are no oscillatory excitation sources, this oscillatory disturbance is eventually convected out of the domain due to its positive phase velocity. Furthermore, the small amplitude steady excitation strip can no longer trigger instabilities, since the exact FDP turned stationary disturbances into convectively stable. This is the reason why it is also possible to observe that the velocity disturbances decay in time until they vanish in the last two plots (bottom middle and bottom right). In other words, a disturbance free steady-state is eventually reached. As was the case of the first toy model studied in subsection 11.1.1, there is no need to couple the exact FDP with a steady-state solver.

This section ends with an important note of caution. The exact FDP does not work when the forcing amplitude v_w is too high. This problem was identified when trying to run the very same simulations previously discussed once again, but now with $v_w = 0.15$. Figure 11.12 shows these results, but

for the streamwise velocity component instead. It is quite clear that the high forcing amplitude triggers strong nonlinear unsteady effects. The exact FDP, however, was designed to control the behavior of linear disturbances. Hence, it is not surprising that these nonlinear unsteady effects become self-sustaining and a steady-state cannot be achieved. Nevertheless, the message here is clear. The exact FDP can only be expected to control the growth of stationary disturbances in a convectively unstable flow when their (numerical or physical) excitation sources have a small amplitude.

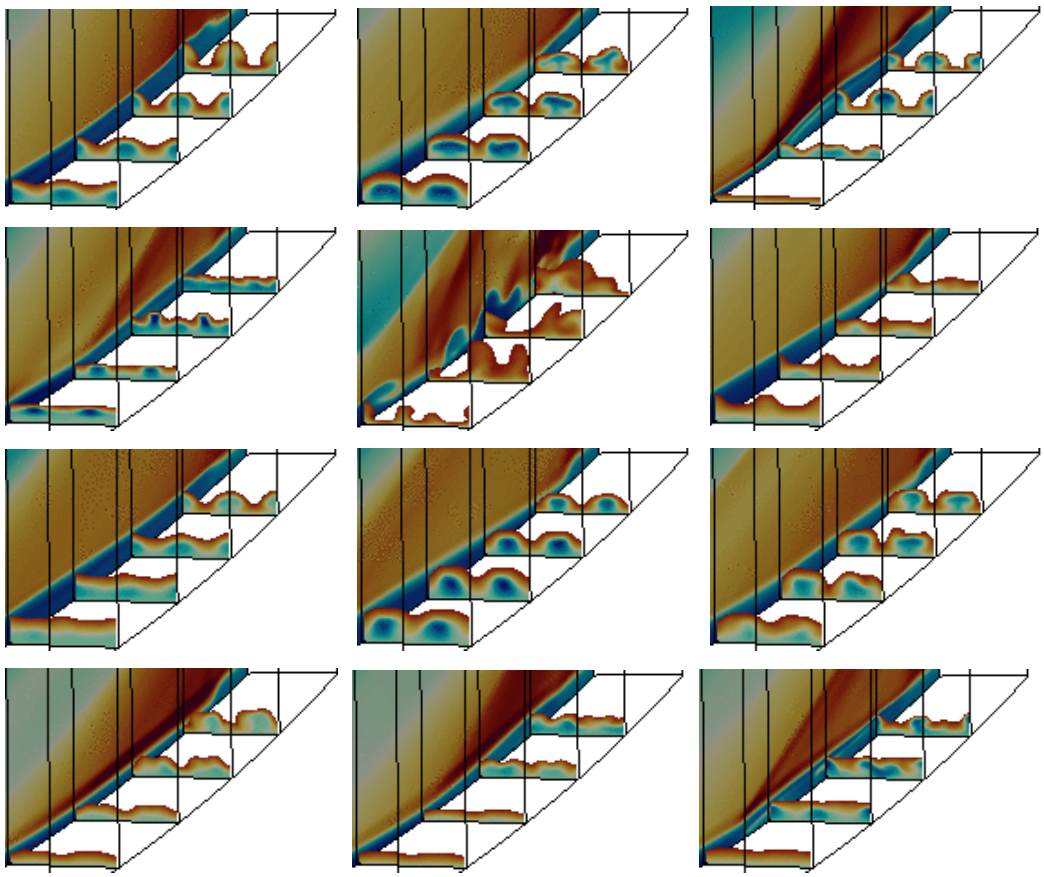

Figure 11.12: Same as Fig. 11.11, but showing instead the streamwise velocity component obtained with $v_w = 0.15$, as done in Fig. 3.16.

11.2 Approximate FDP

11.2.1 Modified Burgers' Equation

Having analyzed in great detail the exact FDP defined in Eq. (10.20), it is time to evaluate its approximate version defined in Eq. (10.29). The latter is the present attempt to develop a steady-state solver for convectively unstable flows that can prevent the growth of stationary disturbances whose numerical excitation one cannot avoid. In order to do so, the residue defined

in Eq. (11.1) is applied to the scalar version of Eq. (10.29), subject to the steady-state superposed by a disturbance, namely

$$u(x,0) = 1 + \mathcal{A}\,\exp\big[\,-\theta\,x^2\,\big] \quad , \tag{11.2}$$

as initial condition, where $\mathcal{A}$ and θ control the disturbance amplitude and spatial distribution, respectively. Hence, the left boundary condition defined in Eq. (10.10) is modified accordingly, whereas the one on the right remains unaltered in the present study. All simulation results presented here were obtained using an explicit Euler scheme for time integration and fourth-order central-difference schemes for spatial discretization. Furthermore, the physical and numerical control parameters imposed are $\theta = 10$, $\mathcal{L} = 20$, $N_x = 201$, $\Delta x = \mathcal{L}/(N_x - 1)$, $Re = 10$ and $\mathcal{R} = 1$.

In the present analysis, a numerical Jacobian is employed to facilitate the simulation of the scalar version of Eq. (10.29). It is given by

$$\left.\frac{\partial f}{\partial u}\right|_u = \frac{f\big(u^n\big) - f\big(u^{n-1}\big)}{u^n - u^{n-1}} + O\big(\Delta u\big) \quad , \tag{11.3}$$

leading to, when applying an explicit marching scheme,

$$\begin{aligned} v^{n+1} &\simeq v^n + \Delta t\left(\frac{\mathcal{F}^n}{\Delta\mathcal{F}^n}\left(u^n - u^{n-1}\right)\right) \quad \text{and} \\ u^{n+1} &= u^n + \Delta t\left(\mathcal{F}^n - \Omega^2\,v^{n+1}\right) \quad , \end{aligned} \tag{11.4}$$

where the above notation means $u^n = u(x,t_n)$, $v^n = v(x,t_n)$, $\mathcal{F}^n = \mathcal{F}\big(u^n\big)$ and $\Delta\mathcal{F}^n = \max[\,\mathcal{F}^n - \mathcal{F}^{n-1}\,,\,\delta\,]$, with the parameter δ being introduced to prevent a singular behavior. In general, δ must be a small number, but still larger than $||\mathcal{F}^\infty||_\infty$. Finally, $\mathcal{F}$ is used in Eq. (11.4) instead of f from Eq. (10.29) to represent a generic explicit time integration scheme.

The behavior of this dynamical system under the approximate FDP just described is presented in Fig. 11.13, which shows the disturbance spatial profiles at different times until steady-state is reached. Unlike the results shown in Fig. 11.1, a disturbance free steady-state is not reached. However, a sizable amount of damping is actually achieved, since the steady disturbance amplitude only grows in space downstream from the inlet approximately four orders of magnitude, being eventually constrained to $O(10^{-6})$. This is an important achievement by the approximate FDP, as the results it generates are in stark contrast to the expected behavior of the original system where disturbances can grow in ampltude up to nonlinear saturation at $O(1)$, as illustrated in Fig. 10.2 (top).

In order to better understand this dynamical system, a series of numerical experiments were performed under different parametric conditions. These results are shown in Fig. 11.14. Figure 11.14 (top left) that the downstream disturbance amplitude in the contaminated steady-state is not affected by the disturbance amplitude at the inlet. This robustness with respect to the inlet disturbance amplitude is a desired attribute in a steady-state solver, since

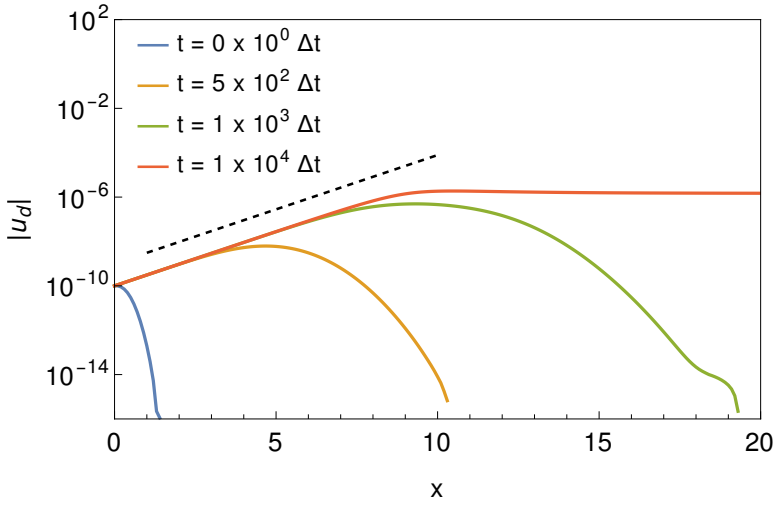

Figure 11.13: Similar to Fig. 11.1, but using the setup described in this subsection with $\Delta t = 0.01$, $\mathcal{A} = 10^{-10}$ and $\delta = 10^{-8}$.

this parameter cannot usually be controlled. On the other hand, the inlet disturbance amplitude cannot be significantly higher than the downstream disturbance amplitude, otherwise convergence issues appear. This figure also shows an accurate marching scheme is not important, since increasing the time step reduces the downstream disturbance amplitude (top right), likely

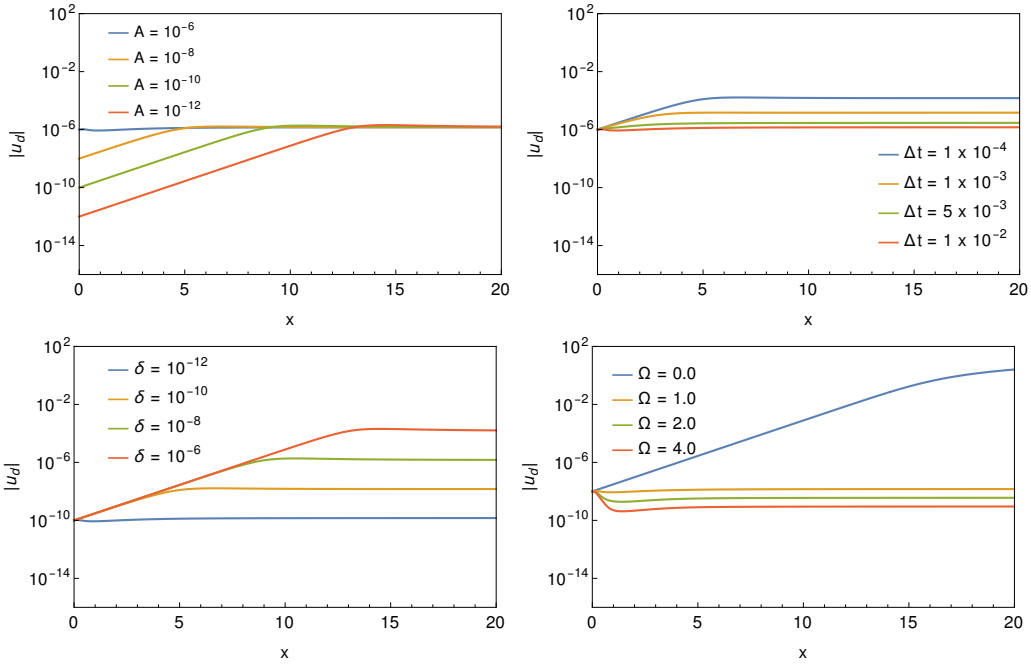

Figure 11.14: Ability of the approximate FDP to generate a disturbance free steady-state under different parameters, namely (top left) inlet disturbance amplitude $\mathcal{A}$, (top right) time step Δt, (bottom left) numerical parameter δ and (bottom right) frequency displacement Ω.

due to the larger numerical diffusion introduced. An opposite behavior is observed with respect to the numerical parameter δ (bottom left). Hence, an accurate numerical Jacobian is important for the approximate FDP. Finally, as one would expect, increasing the frequency displacement Ω reduces the downstream disturbance amplitude (bottom right).

A careful analyses of Eq. 11.4, while also taking into account the results shown in Fig. 11.14, suggests that the downstream disturbance amplitude is proportional to $O(\delta/(\Delta t\,\Omega^2))$. This effect is confirmed in Fig. 11.15, which shows results obtained under different control parameters that were chosen in a such way to keep the ratio $\delta/(\Delta t\,\Omega^2) = 1\times10^{-7}$. In all cases, the maximum downstream disturbance amplitude is proportional to this ratio, even when varying the inlet disturbance amplitude.

These results allow us to define a good strategy for selecting the control parameters. In other words, one must try and satisfy the ratio $\delta/(\Delta t\,\Omega^2) \simeq \mathcal{A}$ to constrain the spatial growth of stationary disturbances in convectively unstable flows. However, the maximum time step is limited by the CFL condition, and often by nonlinear restrictions as well, and δ is limited by the inlet disturbance amplitude. Hence, the procedure developed for selecting the control parameters starts by choosing an appropriate Δt for the marching scheme, then selecting δ at most two orders of magnitude smaller than $\mathcal{A}$, and finally imposing Ω to guarantee that the ratio is satisfied.

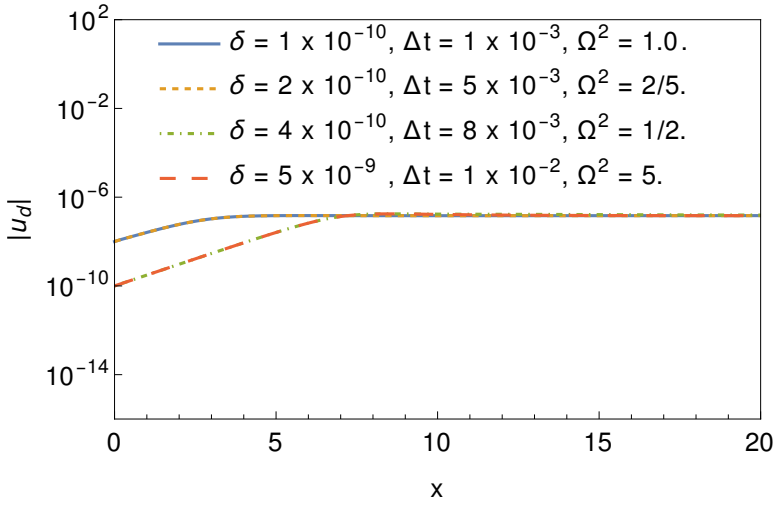

Figure 11.15: Steady disturbance amplitude spatial distribution for different control parameters, selected by satisfying the ratio $\delta/(\Delta t\,\Omega^2) = 1\times10^{-7}$.

Chapter 12

Epilogue

12.1 Conclusions

The main goal of the present report is to use time marching methods to obtain accurate and disturbance free steady-states for high-speed flows in order to provide base flows for linear and nonlinear stability analyses. This chapter concludes the third and final of its three parts, which focusses on flows that are physically unstable to disturbances with a zero complex frequency in a linear and time asymptotic sense. In order words, flows that are convectively unstable to stationary disturbances. Both numerical and physical steady excitation sources are capable of triggering the time asymptotic and spatial growth of these small amplitude disturbances, which occurs downstream of this source and is time independent as well. This final part of the report then focusses on two fronts. On one hand, rigorous numerical and physical stability analyses are employed to explain why traditional steady-state solvers cannot generate accurate and disturbance free steady-states when steady sources excite stationary disturbances in convectively unstable flows. On the other hand, a novel filter that can be coupled with existing steady-state solvers to generate accurate and disturbance free steady-states is developed and tested, with some success.

Convectively unstable flows are usually described as noise amplifiers, i.e. they enable the downstream spatial growth of small amplitude disturbances that originate from an upstream source and fall within a certain range of unstable frequencies. In most scenarios, the stationary limit of this range is either stable or marginally stable. Hence, oscillatory excitation sources are required to trigger this growth. These sources often have a physical origin included by design, since it is fairly straightforward to avoid their numerical counterparts in a code. This means that one should be able to easily prevent their excitation if so desired. In some scenarios, however, the stationary limit of this frequency range is unstable. Hence, steady excitation sources are required to trigger the growth of these stationary disturbances. They can certainly also have a physical origin but, contrary to the previous scenarios, steady numerical excitation sources can be quite difficult to remove from a code. The reason is the fact that anything preventing the spatial

error distribution from being smooth can act as a steady excitation source, such as inaccurate initial and inlet conditions, any number of grid issues, inadequate variable numerical diffusion schemes, and so on. Once stationary disturbances have been excited by whatever means in a convectively unstable flow, existing steady-state solvers are not capable of preventing their time asymptotic spatial growth downstream of their source. This is due to the consistency requirement for any convergent discrete numerical scheme, which forces their linear gain to be one whenever the complex disturbance frequency is zero. In other words, steady-state solvers cannot modify the stationary disturbance amplitude in time, allowing them to grow in space. Finally, it is important to note that, although this discussion focussed on solvers that employ marching schemes, the same is true for their iterative counterparts.

In order to try and overcome this issue, a novel filter is developed to change the angular frequency of linear disturbances in a given model without changing its steady-state. Named here Frequency Displacement Procedure, or FDP, this filter can be added to any steady-state solver. Its exact version was capable of recovering accurate and disturbance free steady-states for a wide range of problems, such as the modified Burgers' equation, the modified entropy disturbance advection using the 1D and compressible Navier-Stokes equations, the modified boundary-layer over a flat plate using the 2D and compressible Navier-Stokes equations, and the Görtler problem using the 3D and compressible Navier-Stokes equations. The term modified refers to the introduction of a special source term in the original model that renders it convectively unstable to stationary disturbances. A major drawback of the exact FDP, however, is the fact that its filter requires knowledge of the steady-state. For this reason, the approximate FDP was developed to remove the steady-state from its filter. This approximate version was only tested on the modified Burgers' equation. Nevertheless, it was capable of constraining the time asymptotic spatial growth of stationary disturbances, but only when the deviation from the disturbance free steady-state is small. When the fully contaminated steady-state is employed as initial condition, on the other hand, the approximate FDP developed here does not work.

12.2 Future Work

Given the results discussed in the third and final part of this report, which were summarized above, one must consider the next steps forward to continue the FDP development. This is done below.

1. Improve the accuracy of the numerical Jacobian $\mathbf{J}$ employed with the approximate FDP in Eq. (10.29).

2. Improve the accuracy of the Taylor-series expansion in Eq. (10.27) used to derive the approximate FDP in Eq. (10.29).

3. Derive another version of the FDP, whose filter does not require the steady-state $\mathbf{u_s}$. One alternative is solving instead the time derivative

of Eq. (10.20). Doing so, however, moves the $\mathbf{u_s}$ dependence to the initial condition for the first time derivative of $\mathbf{u}$.

4. Apply the approximate FDP, as well as any other improved version one might derive, to more complex test cases, such as the modified one-dimensional entropy disturbance advection and the three-dimensional flow over a curved surface, known as Görtler problem.

Part IV

References

References

F. Acker, R. B. de R. Borges, and B. Costa. An improved weno-z scheme. *Journal of Computational Physics*, 313:726–753, 2016. (Cited on page 15)

N. A. Adams. Direct numerical simulation of turbulent compression ramp flow. *Theoretical and Computational Fluid Dynamics*, 12(2):109–129, 1998. (Cited on page 71)

E. Åkervik, L. Brandt, D. S. Henningson, J. Hoepffner, O. Marxen, and P. Schlatter. Steady solutions of the Navier-Stokes equations by selective frequency damping. *Physics of Fluids*, 18(6):068102, 2006. (Cited on pages 121, 125, and 127)

M. K. Aktas. *Thermoacoustically Induced and Acoustically Driven Flows and Heat Transfer in Enclosures*. PhD thesis, Drexel University, May 2004. (Cited on page 45)

R. Alexander. The modified newton method in the solution of stiff ordinary differential equations. *SIAM Journal on Numerical Analysis*, 14(6):1006–1021, 1977. (Cited on page 131)

E. L. Allgower and K. Georg. *Introduction to Numerical Continuation Methods*. Number 45 in Classics in Applied Mathematics. SIAM, 2003. (Cited on pages 121 and 124)

L. S. de B. Alves, S. C. Hirata, M. Schuabb, and A. Barletta. Identifying linear absolute instabilities from differential eigenvalue problems using sensitivity analysis. *Journal of Fluid Mechanics*, 870:941–969, 2019. (Cited on pages 143, 182, and 183)

L. S. de B. Alves, R. D. Santos, and C. E. G. Falc ao. Low Mach preconditioned density-based methods with implicit Runge-Kutta schemes in physical-time. *Journal of the Brazilian Society of Mechanical Sciences and Engineering*, 43(341), 2021. (Cited on page 147)

L. S.de B. Alves, R. M. Cotta, and M. D. Mikhailov. Covalidation of hybrid integral transforms and method of lines in nonlinear convection-diffusion with Mathematica. *Journal of the Brazilian Society of Mechanical Sciences - RBCM*, 23(3):303–320, 2001. (Cited on page 43)

G. M. Amdahl. Validity of the single processor approach to achieving large scale computing capabilities. In *AFIPS Conference Proceedings*, volume 30, pages 483–485, 1967. (Cited on page 56)

S. Balay, W. Gropp, L. C. McInnes, and B. F. Smith. Petsc, the portable, extensible toolkit for scientific computation. *Argonne National Laboratory*, 2(17), 1998. (Cited on page 123)

A. Barletta and L. S. de B. Alves. Absolute instability: A toy model and an application to the rayleigh–bénard problem with horizontal flow in porous media. *International Journal of Heat and Mass Transfer*, 104:438–455, 2017. (Cited on pages 141 and 169)

K. Barnstorff. HIFiRE scramjet research flight will advance hypersonic technology, May 2012. URL `https://www.nasa.gov/topics/aeronautics/features/hifire.html`. (Cited on page 161)

H. H. Barros and L S. de B. Alves. Soft wall resistance as a necessary condition to validate numerical simulations in thermoacoustic heat transfer within closed cavities. *International Journal of Thermal Sciences*, 135: 580–588, 2019. (Cited on page 45)

A. Batista and J. J. Kuehl. Local wall temperature effects on the second-mode instability. *Journal of Spacecraft and Rockets*, 57(3):580–595, 2020. (Cited on page 104)

E. R. Benton and G. W. Platzman. A table of solutions of the one-dimensional Burgers equation. *Quarterly of Applied Mathematics*, 30(2): 196–212, 1972. (Cited on page 42)

H. Bippes. Basic experiments on transition in three-dimensional boundary-layers dominated by crossflow instability. *Progress in Aerospace Sciences*, 35:363–412, 1999. (Cited on page 160)

N. P. Bitter and J. E. Shepherd. Stability of highly cooled hypervelocity boundary layers. *Journal of Fluid Mechanics*, 778:586–620, 2015. (Cited on pages 100 and 104)

D. J. Bodony. An analysis of sponge zones for computational fluid mechanics. *Journal of Computational Physics*, 212(2):681–702, 2006. (Cited on pages 169 and 183)

G. Bonfigli and M. Kloker. Secondary instability of crossflow vortices: validation of the stability theory by direct numerical simulation. *Journal of Fluid Mechanics*, 583:229–272, 2007. (Cited on page 161)

R. B. de R. Borges, M. Carmona, B. Costa, and W. S. Don. An improved weighted essentially non-oscillatory scheme for hyperbolic conservation laws. *Journal of Computational Physics*, 227(6):3191–3211, 2008. (Cited on page 15)

J. P. Boris and D. L. Book. Flux-corrected transport. i. SHASTA, a fluid transport algorithm that works. *Journal of Computational Physics*, 11: 38–69, 1973. (Cited on page 15)

G. Brès, J. W. Nichols, S. K. Lele, and F. E. Ham. Towards best practices for jet noise predictions with unstructured large eddy simulations. In *42nd Fluid Dynamics Conference and Exhibit*, 2012-2965, 2012. (Cited on page 19)

L. Brevdo, P. Laure, F. Dias, and T. J. Bridges. Linear pulse structure and signalling in a film flow on an inclined plane. *Journal of Fluid Mechanics*, 396:37–71, 1999. (Cited on page 121)

O. R. Burggraf. Separated laminar boundary layers. Technical Report Advances in Engineering Sciences, Vol. 4, NASA Langley Research Center, 1976. (Cited on page 84)

A. Burtsev, H. R. Quintanilha Jr, V. Theofilis, R. D. Santos, and L. S. de B. Alves. Linear instability mechanisms of supersonic flow past blunt bodies. In *AIAA Scitech Forum*, AIAA 2021-0050, 2021. (Cited on pages 59 and 60)

J. C. Butcher. *Numerical Methods for Ordinary Differential Equations*. John Wiley & Sons, Inc., England, 2008. (Cited on pages 14, 17, 121, and 133)

C. S. Butler and S. J. Laurence. Interaction of second-mode disturbances with an incipiently separated compression-corner flow. *Journal of Fluid Mechanics*, 913:R4, 2021. (Cited on page 102)

D. Canuto and K. Taira. Two-dimensional compressible viscous flow around a circular cylinder. *Journal of Fluid Mechanics*, 785:349–371, 2015. (Cited on page 19)

S. Cao, J. Hao, I. Klioutchnikov, H. Olivier, and C. Y. Wen. Unsteady effects in a hypersonic compression ramp flow with laminar separation. *Journal of Fluid Mechanics*, 912(A3), 2021. (Cited on pages 22 and 90)

J. E. Carter. Numerical solutions of the navier-stokes equations for the supersonic laminar flow over a two-dimensional compression corner. Technical Report 385, NASA Teshnical Report, 1972. (Cited on page 21)

K. W. Cassel, A. I. Ruban, and J. D. A. Walker. An instability in supersonic boundary-layer flow over a compression ramp. *Journal of Fluid Mechanics*, 300:265–285, 1995. (Cited on pages 82, 84, 85, and 86)

A. Cerminara and N. Sandham. Transition mechanisms in cross-flow-dominated hypersonic flows with free-stream acoustic noise. *Journal of Fluid Mechanics*, 896(A21), 2020. (Cited on pages 47 and 51)

N. Cerulus. *Characterisation of the stability of compression corner geometries under supersonic flow conditions*. PhD thesis, University of Liverpool, 2022. (Cited on pages 81, 84, 87, and 88)

S. Chakravarthy and S. Osher. High resolution applications of the Osher upwind scheme for the Euler equations. In *6th Computational Fluid Dynamics Conference Danvers*, 1983. (Cited on page 15)

D. R. Chapman, D. M. Kuehn, and H. K. Larson. Investigation of separated flows in supersonic and subsonic streams with emphasis on the effect of transition. Technical Report 3869, NACA Technical Note, 1957. (Cited on page 20)

D. R. Chapman, D. M. Kuehn, and H. K. Larson. Investigation of separated flows in supersonic and subsonic streams with emphasis on the effect of transition. Technical Report 1356, NACA Technical Report, 1958. (Cited on page 20)

Y. Chauvat, J. M. Moschetta, and J. Gressier. Shock wave numerical structure and the carbuncle phenomenon. *International Journal for Numerical Menthods in Fluids*, 47(8-9):903–909, 2005. (Cited on page 19)

X. Chen, Y. Zhu, and C. Lee. Interactions between second mode and low-frequency waves in a hypersonic boundary layer. *Journal of Fluid Mechanics*, 820:693–735, 2017. (Cited on page 160)

X. Chen, G. L. Huang, and C. B. Lee. Hypersonic boundary layer transition on a concave wall: stationary Görtler vortices. *Journal of Fluid Mechanics*, 865:1–40, 2019. (Cited on page 160)

M. M. Choudhari. Personal communication, 2020. (Cited on page 161)

P. V. Chuvakhov and A. V. Fedorov. Spontaneous radiation of sound by instability of a highly cooled hypersonic boundary layer. *Journal of Fluid Mechanics*, 805:188–206, 2016. (Cited on page 104)

P. V. Chuvakhov, V. Y. Borovoy, I. V. Egorov, V. N. Radchenko, H. Olivier, and A. Roghelia. Effect of small bluntness on formation of Görtler vortices in a supersonic compression corner flow. *Journal of Applied Mechanics and Technical Physics*, 58(6):975–989, 2017. (Cited on pages 21, 77, and 90)

V. Citro, P. Luchini F. Giannetti, and F. Auteri. Efficient stabilization and acceleration of numerical simulation of fluid flows by residual recombination. *Journal of Computational Physics*, 344:234–246, 2017. (Cited on pages 121, 125, 126, and 127)

T. F. Coleman and J. J. Moré. Estimation of sparse jacobian matrices and graph coloring blems. *SIAM Journal on Numerical Analysis*, 20(1):187–209, 1983. (Cited on page 123)

D. A. Cook, J. S. Thome, J. M. Brock, J. W. Nichols, and G. V. Candler. Sensitivity of hypersonic flows to distributed surface roughness using input-output analysis. In *AVIATION Forum*, number 2018-4045 in AIAA, Atlanta, June 2018. (Cited on page 163)

D. A. Cook, J. S. Thome, J. W. Nichols, and G. V. Candler. Receptivity analysis of BOLT to distributed surface roughness using input-output analysis. In *SciTech Forum*, number 2019-0089 in AIAA, Sand Diego, January 2019. (Cited on page 163)

J. F. Coulombel, S. Benzoni-Gavage, and D. Serre. Note on a paper by robinet, gressier, casalis and moschetta. *Journal of Fluid Mechanics*, 469: 401–405, 2002. (Cited on page 19)

G. Cunha, P. Y. Passaggia, and M. Lazareff. Optimization of the selective frequency damping parameters using model reduction. *Physics of Fluids*, 27(094103):1–22, 2015. (Cited on pages 121 and 125)

C. F. Dewey. Near wake of a blunt body at hypersonic speeds. *AIAA Journal*, 3(6):1001–1010, 1965. (Cited on page 18)

D. J. Dinzl and G. V. Candler. Analysis of crossflow instability on HIFiRE-5 using direct numerical simulation. In *53rd AIAA Aerospace Sciences Meeting*, number 2015-0279 in AIAA, pages 1–10, 2015. (Cited on pages 161, 162, and 169)

D. J. Dinzl and G. V. Candler. Direct simulation of hypersonic crossflow instability on an elliptic cone. *AIAA Journal*, 55(6):1769–1782, 2017. (Cited on page 163)

D. Dolling. Fifty years of shock wave / boundary-layer interaction research: what next? *AIAA Journal*, 39(8):1517–1531, 2001. (Cited on pages 20 and 21)

M. Dumbser, J. M. Moschetta, and J. Gressier. A matrix stability analysis of the carbuncle phenomenon. *Journal of Computational Physics*, 197: 647–670, 2004. (Cited on page 19)

A. Dwivedi, G. S. Sidharth, J. W. Nichols, G. V. Candler, and M. R. Jovanović. Reattachment streaks in hypersonic compression ramp flow: an input-output analysis. *Journal of Fluid Mechanics*, 880:113–135, 2019. (Cited on pages 21 and 77)

I. V. Egorov and V. Y. Neiland V. V. Shvedchenko. Three-dimensional flow structures at supersonic flow over the compression ramp. In *49th Aerospace Sciences Meeting*, 2011-730, 2011. (Cited on page 84)

B. Einfeldt. On Godunov-type methods for gas dynamics. *SIAM Journal on Numerical Analysis*, 25(2):294–318, 1988. (Cited on page 16)

V. Elling. The carbuncle phenomenon is incurable. *Acta Mathematica Scientia*, 29(6):1647–1656, 2009. (Cited on page 19)

D. Exposito, S. L. Gai, and A. J. Neely. Wall temperature and bluntness effects on hypersonic laminar separation at a compression corner,. *Journal of Fluid Mechanics*, 922(A1), 2021. (Cited on pages 22 and 77)

A. Fedorov and A. Tumin. High-speed boundary-layer instability: Old terminology and a new framework. *AIAA Journal*, 49(8):1647–1657, 2011. (Cited on page 100)

L. Ferracina and M. N. Spijker. An extension and analysis of the Shu-Osher representation of Runge-Kutta methods. *Mathematical of Computations*, 74(249):201–219, 2004. (Cited on page 18)

L. Ferracina and M. N. Spijker. Computing optimal monotonicity-preserving Runge-Kutta methods. Technical Report MI2005-07, Leiden University, 2005. (Cited on page 18)

L. Ferracina and M. N. Spijker. Strong stability of singly-diagonally-implicit runge-kutta methods. *Applied Numerical Mathematics*, 58:1675–1686, 2008. (Cited on page 18)

T. M. Fischer and U. Dailmann. Primary and secondary stability analysis of a three-dimensional boundary-layer flow. *Physics of Fluids A: Fluid Dynamics*, 3(10):2378–2391, 1991. (Cited on page 161)

J. M. Floryan. On the Görtler instability of boundary-layers. *Progress in Aerospace Sciences*, 28:235–271, 1991. (Cited on page 159)

J. M. Floryan and W. S. Saric. Wavelength selection and growth of Görtler vortices. *AIAA Journal*, 22(11):1529–1538, 1984. (Cited on page 160)

D. V. Gaitonde. Progress in shock wave / boundary-layer interactions. *Progress in Aerospace Sciences*, 72:80–99, 2015. (Cited on pages 20 and 21)

S. K. Godunov. A difference scheme for numerical solution of discontinuous solution of hydrodynamic equations. *Mathematics Sbornik*, 47:271–306, 1959. (Cited on page 15)

G. H. Golub and C. F. Van Loan. *Matrix Computations*. The Johns Hopkins University Press, Baltimore, 3rd edition, 1996. (Cited on page 127)

J. B. Goodman and R. J. LeVeque. On the accuracy of stable schemes for 2d scalar conservation laws. *Mathematics of Computation*, 45(171):15–21, 1985. (Cited on page 15)

S. Gottlieb and C. W. Shu. Total-variation-diminishing Runge-Kutta schemes. *Mathematics of Computations*, 67:73–85, 1998. (Cited on page 17)

S. Gottlieb, D. Ketcheson, and C. W. Shu. High-order strong stability preserving time discretizations. *Journal of Scientific Computing*, 38:251–289, 2009. (Cited on page 17)

J. R. Grisham, B. H. Dennis, and F. K. Lu. Incipient separation in laminar ramp-induced shock-wave/boundary-layer interactions. *AIAA Journal*, 56 (2):524–531, 2018. (Cited on pages 84 and 86)

J. L. Gustafson. Reevaluating Amdahl's law. *Communications of the ACM*, 31(5):532–533, 1988. (Cited on page 56)

P. Hall. The Görtler vortex instability mechanism in three-dimensional boundary layers. *Proceedings of the Royal Society of London. Series A, Mathematical and Physical Sciences*, 399:135–152, 1985. (Cited on page 160)

J. Hao, S. Cao, C. Y. Wen, and H. Olivier. Occurrence of global instability in hypersonic compression corner flow. *Journal of Fluid Mechanics*, 919 (A4), 2021. (Cited on pages 22, 77, 90, and 95)

S. P. Harbison and G. L. Steele Jr. *C - A Reference Manual*. Tartan, INC, 4th edition, 1995. (Cited on page 14)

A. Harten. High resolution schemes for hyperbolic conservation laws. *Journal of Computation Physics*, 49:357–393, 1983. (Cited on pages 14, 15, and 41)

A. Harten, P. D. Lax, and B. van Leer. On upstream differencing and Godunov-type schemes for hyperbolic conservation laws. *SIAM Review*, 25(1):35–61, 1983. (Cited on page 16)

A. Harten, B. Engquist, S. Osher, and S. R. Chakravarthyy. Uniformly high order accurate essentially non-oscillatory schemes, iii. *Journal of Computation Physics*, 131:3–47, 1987. (Cited on page 15)

T. Hendrickson, A. Kartha, and G. V. Candler. An improved ducros sensor for the simulation of compressible flows with shocks. In *Fluid Dynamics Conference*, 2018-3710, 2018. (Cited on page 77)

A. K. Henrick, T. D. Aslam, and J. M. Powers. Mapped weighted essentially non-oscillatory schemes: Achieving optimal order near critical points. *Journal of Computation Physics*, 207:542–567, 2005. (Cited on page 15)

K. Hida. An approximate study on the detached shock wave in front of a circular cylinder and a sphere. *Journal of the Physical Society of Japan*, 8 (6):740–745, 1953. (Cited on page 18)

W. S. Hinman and C. T. Johansen. Interaction theory of hypersonic laminar near-wake flow behind an adiabatic circular cylinder. *Shock Waves*, 26: 717–727, 2016. (Cited on page 19)

W. S. Hinman and C. T. Johansen. Reynolds and Mach number dependence of hypersonic blunt body laminar near wakes. *AIAA Journal*, 55(2):500–508, 2017. (Cited on page 19)

C. Hirsch. *Numerical Computation of Internal and External Flows, Computational Methods for Inviscid and Viscous Flows*. Wiley, 1991. (Cited on page 15)

C. Hirsch. *Numerical Computation of Internal and External Flows*, volume 1: Fundamentals of Computational Fluid Dynamics. Elsevier, United Kingdom, 2007. (Cited on page 14)

M. Högberg and D. Henningson. Secondary instability of cross-flow vortices in Falkner-Skan-Cooke boundary layers. *Journal of Fluid Mechanics*, 368: 339–357, 1998. (Cited on page 161)

M. S. Holden and J. R. Moselle. Theoretical and experimental studies of the shock wave / boundary-layer interaction on compression surfaces in hypersonic flow. Technical Report AF-2410-A-l, CALSPAN Report, 1969. (Cited on page 21)

T. L. Holst. Numerical solution of axisymmetric boattail fields with plume simulators. In *AIAA Conference Paper*, pages 77–224, 1977. (Cited on page 42)

K. Hsu and S. L. Lee. A numerical technique for two-dimensional grid generation with grid control at all of the boundaries. *Journal of Computational Physics*, 96(2):451 – 469, 1991. (Cited on page 17)

P. Huerre and P. A. Monkewitz. Local and global instabilities in spatially developing flows. *Annual Review of Fluid Mechanics*, 22:473–537, 1990. (Cited on pages 159, 165, and 172)

C. Hung and R. MacCormack. Numerical solutions of supersonic and hypersonic laminar compression corner flows. *AIAA Journal*, 14(4):475–481, 1976. (Cited on page 21)

I. Imai. On the flow of a compressible fluid past a circular cylinder. In *Proceedings of the Physico-Mathematical Society of Japan*, volume 20, pages 636–645. The Physical and Mathematical Societies of Japan, 1938. (Cited on page 18)

P. A. Jacobs, R. J. Gollan, A. J. Denman, R. O'Flaherty, D. F. Potter, P. J. Petrie-Reparand, and I. A. Johnston. Eilmer's theory book: Basic model for gas dynamic and thermochemistry. Technical Report 9, University of Queensland, Mechanical Engineering Report, 2010. (Cited on page 19)

E. Janke and P. Balakumar. On the secondary instability of three-dimensional boundary layers. *Theoretical and Computational Fluid Dynamics*, 14:167–194, 2000. (Cited on page 161)

H. Jasak, A. Jemcov, and Z. Tukovic. OpenFOAM: A C++ library for complex physics simulations. In *International workshop on coupled methods in numerical dynamics*, Dubrovnik, Croatia, 2007. (Cited on page 19)

G. S. Jiang and C. W. Shu. Efficient implementation of weighted ENO schemes. *Journal of Computational Physics*, 126:202–228, 1996. (Cited on pages 15, 16, 57, and 183)

B. E. Jordi, C. J. Cotter, and S. J. Sherwin. Encapsulated formulation of the selective frequency damping method. *Physics of Fluids*, 26(034101):1–10, 2014. (Cited on pages 121 and 125)

B. E. Jordi, C. J. Cotter, and S. J. Sherwin. An adaptive selective frequency damping method. *Physics of Fluids*, 27(094104):1–8, 2015. (Cited on pages 121 and 125)

R. D. Joslin and C. L. Streett. The role of stationary cross-flow vortices in boundary-layer transition on swept wings. *Physics of Fluids*, 6(10): 3442–3453, 1994. (Cited on page 161)

M. R. Jovanović. From bypass transition to flow control and data-driven turbulence modeling: An input–output viewpoint. *Annual Review of Fluid Mechanics*, 53:311–345, 2021. (Cited on page 159)

T. J. Juliano and S. P. Schneider. Instability and transition on the HIFiRE-5 in a Mach-6 quiet tunnel. In *40th Fluid Dynamics Conference*, number 2010-5004 in AIAA, 2010. (Cited on page 161)

Y. S. Kachanov and V. Y. Levchenko. The resonant interaction of disturbances at laminar turbulent transition in a boundary layer. *Journal of Fluid Mechanics*, 138:209–247, 1984. (Cited on page 159)

F. Kemm. Heuristical and numerical considerations for the carbuncle phenomenon. *Applied Mathematics and Computation*, 320:596–613, 2018. (Cited on page 19)

D. I. Ketcheson, C. B. Macdonald, and S. Gottlieb. Optimal implicit strong stability preserving Runge-Kutta methods. *Applied Numerical Mathematics*, 59:373–392, 2009. (Cited on page 18)

Y. Khalighi, J. W. Nichols, F. Ham, S. K. Lele, and P. Moin. Unstructured large eddy simulation for prediction of noise issued from turbulent jets in various configurations. In *17th AIAA/CEAS Aeroacoustics Conference*, 2011-2886, 2011. (Cited on page 19)

R. L. Kimmel, D. Adamczak, D. Gaitonde, A. Rougeux, and J. R. Hayes. Hifire-1 boundary layer transition experiment design. In *45th AIAA Aerospace Sciences Meeting and Exhibit*, number 2007-0534 in AIAA, Reno, NV, January 2007. (Cited on page 161)

R. L. Kimmel, D. Adamczak, K. Berger, and M. Choudhari. HIFiRE-5 flight vehicle design. In *40th Fluid Dynamics Conference and Exhibit*, number 2010-4985 in AIAA, pages 1–17, 2010. (Cited on page 161)

C. P. Knisely and X. Zhong. Sound radiation by supersonic unstable modes in hypersonic blunt cone boundary layers. i. linear stability theory. *Physics of Fluids*, 31(024103), 2019a. (Cited on page 104)

C. P. Knisely and X. Zhong. Sound radiation by supersonic unstable modes in hypersonic blunt cone boundary layers. ii. direct numerical simulation. *Physics of Fluids*, 31(024104), 2019b. (Cited on page 104)

D. A. Knoll and D. E. Keyes. Jacobian-free Newton-Krylov method: a survey of approaches and applications. *Journal of Computational Physics*, 193: 357–397, 2004. (Cited on pages 120 and 124)

W. Koch. On the spatio-temporal stability of primary and secondary crossflow vortices in a three-dimensional boundary layer. *Journal of Fluid Mechanics*, 456:85–111, 2002. (Cited on page 161)

W. Koch, F. P. Bertolotti, A. Stolte, and S. Hein. Nonlinear equilibrium solutions in a three-dimensional boundary layer and their secondary instability. *Journal of Fluid Mechanics*, 406:131–174, 2000. (Cited on page 161)

T. S. Kocian, A. J. Moyes, H. L. Reed, S. A. Craig, W. S. Saric, S. P. Schneider, and J. B. Edelman. Hypersonic crossflow instability. *Journal of Spacecraft and Rockets*, 56(2):432–446, 2019. (Cited on page 163)

B. Koren. *Numerical Methods for Advection-Diffusion Problems*, chapter A Robust Upwind Discretization Method for Advection, Diffusion and Source Terms. Centrum voor Wiskunde en Informatica, 1993. (Cited on page 15)

J. J. Kuehl. Thermoacoustic interpretation of second-mode instability. *AIAA Journal*, 56(9):3585–3592, 2018. (Cited on page 104)

M. T. Landahl. Wave breakdown and turbulence. *SIAM Journal of Applied Mathematics*, 28(4):735–756, 1975. (Cited on page 159)

C. B. Laney, editor. *Computational Gas Dynamics*. Cambridge University Press, United Kingdom, 1998. (Cited on page 15)

P. D. Lax and R. D. Richtmyer. Survey of the stability of linear finite difference equations. *Communications on Pure and Applied Mathematics*, IX: 267–293, 1956. (Cited on page 166)

L. Lees. The stability of the laminar boundary layer in a compressible fluid. Technical Report 876, National Advisory Committee for Aeronautics, 1947. (Cited on page 88)

L. Lees and C. C. Lin. Investigation of the stability of the laminar boundary layer in a compressible fluid. Technical Report 1115, National Advisory Committee for Aeronautics, 1946. (Cited on page 88)

J. E. Lewis, T. Kubota, and L. Lees. Experimental investigation of supersonic laminar, two-dimensional boundary-layer separation in a compression corner with and without cooling. *AIAA Journal*, 6(1):7–14, 1968. (Cited on page 21)

I. Leyva. The relentless pursuit of hypersonic flight. *Physics Today*, 70(11): 30–36, 2017. (Cited on page 2)

F. Li, M. Choudhari, C. L. Chang, and J. White. Analysis of instabilities in non-axisymmetric hypersonic boundary layers over cones. In *10th AIAA/ASME Joint Thermophysics and Heat Transfer Conference*, number 2010-4643 in AIAA/ASME, Chicago, July 2010a. (Cited on page 161)

F. Li, M. Choudhari, C. L. Chang, M. Wu, and P. T. Greene. Development and breakdown of Görtler vortices in high speed boundary layers. In *48th AIAA Aerospace Sciences Meeting*, number 2010-0705 in AIAA, 2010b. (Cited on page 160)

F. Li, M. M. Choudhari, and L. Duan. Stationary crossflow breakdown due to mixed mode spectra of secondary instabilities. In *46th AIAA Fluid Dynamics Conference*, 2016-3789, 2016. (Cited on page 161)

V.D. Liseikin. *Grid Generation Methods*. Scientific Computation. Springer Netherlands, 2009. (Cited on page 16)

X. D. Liu, S. Osher, and T. Chan. Weighted essentially non-oscillatory schemes. *Journal of Computational Physics*, 115:200–212, 1994. (Cited on pages 15 and 41)

J. C. Loiseau, M. A. Bucci, S. Cherubini, and J. C. Robinet. *Computational Modelling of Bifurcations and Instabilities in Fluid Dynamics*, volume 50, chapter Time-stepping and Krylov methods for large-scale instability problems. Springer, 2018. (Cited on pages 122 and 126)

H. Lomax, T. H. Pulliam, and D. W. Zingg. *Fudamentals of Computational Fluid Dynamics*. Scientific Computation. Springer & Verlag, Berlin, 2001. (Cited on pages 14 and 121)

L. M. Mack. Boundary layer linear stability theory. Technical report, AGARD–R–709 Special course on stability and transition of laminar flow, 1984. (Cited on page 105)

M. R. Malike, F. LI, M. M. Choudhari, and C. L. Chang. Secondary instability of crossflow vortices and swept-wing boundary-layer transition. *Journal of Fluid Mechanics*, 399:85–115, 1999. (Cited on page 161)

M. P. Martin, S. Xu, and S. M. Xu. Preliminary work on DNS and LES of STBLI. In *33rd AIAA Fluid Dynamics Conference and Exhibit*, 03-3464, 2003. (Cited on pages 71 and 72)

S. N. Martinez and O. R. Tutty. Numerical simulation of Görtler vortices in hypersonic compression ramps. *Computers & Fluids*, 34:225–247, 2005. (Cited on page 160)

D. J. Mavriplis. On convergence acceleration techniques for unstructured meshes. Technical Report 98-44, ICASE Report, 1998. (Cited on pages 121 and 124)

J. F. McCarthy and T. Kubota. A study of wakes behind a circular cylinder at M = 5.7. *AIAA Journal*, 2(4):629–636, 1964. (Cited on page 18)

G. Mengaldo, M. Kravtsova, A. I. Ruban, and S. J. Sherwin. Triple-deck and direct numerical simulation analyses of high-speed subsonic flows past a roughness element. *Journal of Fluid Mechanics*, 774(311–323), 2015. (Cited on pages 84 and 86)

C. L. Merkle and Y. H. Choi. Computation of low-speed flow with heat addition. *AIAA Journal*, 25:831–838, 1987. (Cited on page 44)

J. J. Moré, D. C. Sorensen, K. E. Hillstrom, and B. S. Garbow. *The MINPACK Project, in Sources and Development of Mathematical Software*. Prentice-Hall, 1984. (Cited on page 123)

M. V. Morkovin, R. Reshotko, and T. Herbert. Transition in open flow systems: a reassessment. In *Bulletin of the American Physical Society*, volume 39, pages 1–31, 1994. (Cited on pages 158 and 159)

A. J. Moyes, P. Paredes, T. S. Kocian, and H. L. Reed. Secondary instability analysis of crossflow on a hypersonic yawed straight circular cone. *Journal of Fluid Mechanics*, 812:370–397, 2017. (Cited on page 163)

T. Nagata, A. Noguchi, K. Kusama, T. Nonomura, A. Komuro, A. Ando, and K. Asai. Experimental investigation on compressible flow over a circular cylinder at Reynolds number of between 1000 and 5000. *Journal of Fluid Mechanics*, 893:A13, 2020. (Cited on page 20)

Hypersonic Air Breathing Propulsion Branch at NASA. VULCAN-CFD, November 2009. URL `https://vulcan-cfd.larc.nasa.gov/`. (Cited on page 161)

Langley Research Center at NASA. OVERFLOW CFD code, 2017. URL `https://overflow.larc.nasa.gov/`. (Cited on page 162)

M. S. S. Nunes. Generation of steady-states for stationary and convectively unstable flows using the frequency displacement procedure. Master's thesis, Fluminense Federal University, Niterói, Brazil, 2021. (Cited on pages 17, 47, 48, and 52)

M. Pandolfi and D. D. Ambrosio. Numerical instabilities in upwind methods: analysis and cures for the carbuncle phenomenon. *Journal of Computation Physics*, 166(2):271–301, 2001. (Cited on page 19)

L. Pareschi and G. Russo. Implicit-explicit Runge-Kutta schemes and applications to hyperbolic systems with relaxation. *Journal of Scientific Computing*, 25(1):129–155, 2005. (Cited on page 18)

G. Park, S. L. Gai, and A. J. Neely. Laminar near wake of a circular cylinder at hypersonic speeds. *AIAA Journal*, 48(8):1804–1806, 2010. (Cited on page 20)

G. Park, S. L. Gai, and A. J. Neely. Base flow of circular cylinder at hypersonic speeds. *AIAA Journal*, 54(2):458–468, 2016. (Cited on page 19)

K. M. Peery and S. T. Imlay. Blunt body flow simulations. In *24th AIAA/ASME/SAE/ASEE Joint Propulsion Conference*, 88-2904, Boston, MA, 1988. (Cited on page 18)

I. F. Pinheiro, R. D. Santos L. A. Sphaier, and L. S. de B. Alves. Improving the precision of discrete numerical solutions using the generalized integral transform technique. *Journal of the Brazilian Society of Mechanical Sciences and Engineering*, 42(329), 2020. (Cited on page 43)

T. J. Poinsot and S. K. Lele. Boundary conditions for direct simulations of compressible viscous flows. *Journal of Computational Physics*, 101:104–129, 1992. (Cited on page 44)

K. M. Porter, J. Poggie, and R. L. Kimmel. Laminar and turbulent flow calculations for the HIFiRE-5b flight test. In *47th AIAA Fluid Dynamics Conference*, number 2017-3132 in AIAA, 2017. (Cited on pages 162, 163, and 169)

H. Quintanilha Jr, P. Paredes, A. Hanifi, and V. Theofilis. Transient growth analysis of hypersonic flow over an elliptic cone. *Journal of Fluid Mechanics*, 935(A40), 2022. (Cited on pages 67, 87, 111, and 113)

J. J. Quirk. A contribution to the great Riemann solver debate. *International Journal for Numerical Menthods in Fluids*, 18(6):555–574, 1994. (Cited on page 19)

S. C. Reddy and D. S. Henningson. Energy growth in viscous channel flows. *Journal of Fluid Mechanics*, 252:209–238, 1993. (Cited on page 113)

H. L. Reed, E. Perez, J. Kuehl, T. Kocian, and N. Oliviero. Verification and validation issues in hypersonic stability and transition prediction. *Journal of Spacecraft and Rockets*, 52:29–37, 2015. (Cited on page 163)

D. P. Rizzetta, O. R. Burggraf, and R. Jenson. Triple-deck solutions for viscous supersonic and hypersonic flow past corners. *Journal of Fluid Mechanics*, 89(3):535–552, 1978. (Cited on page 85)

J. C. Robinet, J. Gressier, G. Casalis, and J. M. Moschetta. Shock wave instability and carbuncle phenomenon: Same intrinsic origin? *Journal of Fluid Mechanics*, 417:237–263, 2000. (Cited on page 19)

P. L. Roe. Approximate Reimann solvers, parameter vectors and difference schemes. *Journal of Computational Physics*, 43:357–372, 1981a. (Cited on page 16)

P. L. Roe. *Numerical algorithms for the linear wave equation*. Royal Aircraft Establishment, 1981b. (Cited on page 15)

P. L. Roe. Some contributions to the modelling of discontinuous flows. In B. E. Engquist, S. Osher, and R. C. J. Somerville, editors, *Large-Scale Computations in Fluid Mechanics*, volume 22, pages 163–193. AMS-SIAM, 1985. (Cited on pages 15 and 41)

P. L. Roe and M. J. Baines. Algorithms for advection and shock problems. In *4th Conference on Numerical Methods in Fluid Mechanics*, 1982. (Cited on page 15)

D. H. Rudy, J. L. Thomas, A. Kumar, P. A. Gnoffo, and S. R. Chakravarthy. Computation of laminar hypersonic compression corner flows. *AIAA Journal*, 29(7):1108–1113, 1991. (Cited on page 21)

L. C. Salemi and H. F. Fasel. Synchronization of second-mode instability waves for high-enthalpy hypersonic boundary layers. *Journal of Fluid Mechanics*, 838(R2), 2018. (Cited on page 104)

K. F. S. Santiago and L. S.de B. Alves. Conservative and nondispersive schemes for diffusion terms with strong property variations. *Numerical Heat Transfer, Part B: Fundamentals*, 71(2):133–145, 2017. (Cited on pages 14 and 41)

R. D. Santos. *A study of Runge-Kutta schemes with stronge linear and nonlinear numerical stability*. PhD thesis, Fluminense Federal University, Niterói, Brazil, 2020. (Cited on pages 14, 42, 43, 44, 45, 46, 51, 58, and 87)

R. D. Santos and L. S. de B. Alves. A comparative analysis of explicit, imex and implicit strong stability preserving runge-kutta schemes. *Applied Numerical Mathematics*, 159:204–220, 2021. (Cited on pages 18 and 41)

R. D. Santos, L. S. de B. Alves, N. Cerulus, and V. Theofilis. On two-dimensional steady-states of supersonic flows over compression ramps and their global linear instability. In *AIAA Scitech Forum*, 2019-2321, 2019. (Cited on pages 75, 76, and 79)

W. Saric. Görtler vortices. *Annual Review of Fluid Mechanics*, 26:379–409, 1994. (Cited on page 159)

W. S. Saric, H. L. Reed, and E. B. White. Stability and transition of three-dimensional boundary-layers. *Annual Review of Fluid Dynamics*, 35:413–440, 2003. (Cited on page 160)

P. J. Schmid. Nonmodal stability theory. *Annual Review of Fluid Mechanics*, 39:129–162, 2007. (Cited on page 159)

P. J. Schmid and D. S. Henningson. Optimal energy density growth in Hagen-Poiseuille flow. *Journal of Fluid Mechanics*, 277:197–225, 1994. (Cited on page 113)

P. J. Schmid and D. S. Henningson. *Stability and Transition in Shear-Flows*. Applied Mathematical Sciences. Springer & Verlag, New York, 2001. (Cited on page 111)

B. E. Schmidt and J. E. Shepherd. Oscillations in cylinder wakes at Mach 4. *Journal of Fluid Mechanics*, 785:R3, 2015. (Cited on page 20)

J. Serpieri and M. Kotsonis. Three-dimensional organisation of primary and secondary cross-flow instability. *Journal of Fluid Mechanics*, 799:200–245, 2016. (Cited on page 160)

A. Sescu, R. Alaziz, and M. Afsar. Effect of wall transpiration and heat transfer on görtler vortices in high-speed flows. *AIAA Journal*, 57(3): 1159–1171, 2019. (Cited on page 53)

G. M. Shroff and H. B. Keller. Stabilization of unstable procedures: The recursive projection method. *SIAM Journal of Numerical Analysis*, 30(4): 1099–1120, 1993. (Cited on pages 120 and 126)

C. W. Shu and S. Osher. Efficient implementation of essentially non-oscillatory shock-capturing schemes. *Journal of Computational Physics*, 77:439–471, 1988. (Cited on pages 15, 17, and 183)

C. W. Shu and S. Osher. Efficient implementation of essentially non-oscillatory shock-capturing schemes ii. *Journal of Computational Physics*, 83:32–78, 1989. (Cited on page 15)

G. S. Sidharth, A. Dwivedi G. V. Candler, and J. W. Nichols. Onset of three-dimensionality in supersonic flow over a slender double wedge. *Physical Review Fluids*, 3(093901), 2018. (Cited on pages 21, 77, 90, and 95)

G. A. Sod. A survey of several finite difference methods for systems of nonlinear hyperbolic conservation laws. *Journal of Computational Physics*, 27(1):1–31, 1978. (Cited on page 43)

C. Sparrow. *The Lorenz Equations: Bifurcations, Chaos and Strange Attractors*, volume 41 of *Applied Mathematical Sciences*. Springer-Verlag, New York, 1982. (Cited on page 137)

S. P. Spekreijse. Elliptic grid generation based on laplace equations and algebraic transformations. *Journal of Computational Physics*, 118(1):38 – 61, 1995. (Cited on page 17)

R. J. Spiteri and S. J. Ruuth. A new class of optimal high-order strong-stability- preserving time discretization methods. *SIAM Journal on Numerical Analysis*, 40(2):469–491, 2002. (Cited on page 17)

J. L. Steger and R. L. Sorenson. Automatic mesh-point clustering near a boundary in grid generation with elliptic partial differential equations. *Journal of Computational Physics*, 33(3):405 – 410, 1979. (Cited on page 17)

J. L. Steger and R. F. Warming. Flux vector splitting of the inviscid gas dynamic equations with application to finite-difference methods. *Journal of Computation Physics*, 40:263–293, 1981. (Cited on pages 16 and 41)

K. Stewartson and P. G. Williams. Self-induced separation. *Proceedings of the Royal Society of London. A. Mathematical and Physical Sciences*, 312 (1509):181–206, 1969. (Cited on page 82)

P. K. Subbareddy and G. V. Candler. A fully discrete, kinetic energy consistent finite-volume scheme for compressible flows. *Journal of Computational Physics*, 228:1347–1364, 2009. (Cited on page 161)

P. K. Sweby. High resolution schemes using flux limiters for hyperbolic conservation laws. *SIAM Journal on Numerical Analysis*, 21(5):995–1011, 1984. (Cited on page 15)

P. K. Sweby and M. J. Baines. On convergence of Roe's scheme for the general non-linear scalar wave equation. *Journal of Computational Physics*, 56(1): 135–148, 1984. (Cited on page 15)

K. Tamada and Y. Saito. Note on the flow of a compressible fluid past a circular cylinder. In *Proceedings of the Physico-Mathematical Society of Japan*, volume 20, pages 403–409. The Physical and Mathematical Societies of Japan, 1939. (Cited on page 18)

Tandiono, S. H. Winoto, and D. A. Shah. On the linear and nonlinear development of Görtler vortices. *Physics of Fluids*, 20(094103), 2008. (Cited on page 160)

J. C. Tannehill, D. A. Anderson, and R. H. Pletcher. *Computational Fluid Mechanics and Heat Transfer*. Taylot & Francis, Philadelphia, 1997. (Cited on pages 14 and 16)

R.de S. Teixeira and L. S.de B. Alves. Modeling far field entrainment in compressible flows. *International Journal of Computational Fluid Dynamics*, 26:67–78, 2012. (Cited on pages 121 and 128)

R.de S. Teixeira and L. S.de B. Alves. Minimal gain marching schemes: Searching for unstable steady-states with unsteady solvers. *Theoretical and Computational Fluid Dynamics*, 31(5-6):607–621, 2017. (Cited on pages 122, 129, 131, 136, 140, 166, and 181)

V. Theofilis. Global linear instability. *Annual Review of Fluid Mechanics*, 43:319–352, 2011. (Cited on pages 159 and 165)

V. Theofilis. Global modal and non-modal instability analyses of shock-induced separation bubbles. Technical Report FA9550-17-1-0115, AFOSR, 2020. (Cited on page 71)

V. Theofilis and T. Colonius. An algorithm for the recovery of 2 and 3-d biglobal instabilities of compressible flow over 2-d open cavities. In *33rd Fluid Dynamics Conference and Exhibit*, 2003-4143, 2003. (Cited on page 65)

J. F. Thompson. Elliptic grid generation. *Applied Mathematics and Computation*, 10-11:79 – 105, 1982. (Cited on page 16)

J. F. Thompson, B. K. Soni, and N. P. Weatherill. *Handbook of Grid Generation*. CRC Press, 1998. (Cited on page 17)

E. F. Toro. *Riemann Solvers and Numerical Methods for Fluid Dynamics: A Practical Introduction*. Springer-Verlag, Berlin, Germany, 2009. (Cited on page 16)

G. D. van Albada, B. van Leer, and W. W. Roberts. A comparative study of computational methods in cosmic gas dynamics. *Astronomy and Astrophysics*, 108(1):76–84, 1982. (Cited on page 15)

B. van Leer. Towards the ultimate conservative difference scheme i. the quest of monotonicity. In *Proceedings of the Third International Conference on Numerical Methods in Fluid Mechanics*, volume Fundamental Numerical Techniques of *Lecture Notes in Physics*, pages 163–168, 1973. (Cited on page 15)

B. van Leer. Towards the ultimate conservative difference scheme. ii. monotonicity and conservation combined in a second-order scheme. *Journal of Computation Physics*, 14(4):361–370, 1974. (Cited on page 15)

B. van Leer. Towards the ultimate conservative difference scheme. iv. a new approach to numerical convection. *Journal of Computation Physics*, 23(3): 276–299, 1977. (Cited on page 15)

B. van Leer. Towards the ultimate conservative difference scheme. v. a second-order sequel to Godunov's method. *Journal of Computation Physics*, 32(1):101–136, 1979. (Cited on page 15)

R. T. Veloso, R. D. Santos, and L. S. de B. Alves. Comparative analysis between steady-state generation methods. In *25th International Congress of Mechanical Engineering*, number 2019-1830. ABCM, 2019. (Cited on page 173)

H. K. Versteeg and W. Malalasekera. *An introduction to Computational Fluid Dynamics. The Finite Volume Method*. Prentice Hall, London, 1995. (Cited on page 14)

P. Wassermann and M. Kloker. Mechanisms and passive control of crossflow-vortex-induced transition in a three-dimensional boundary layer. *Journal of Fluid Mechanics*, 456:49–84, 2002. (Cited on page 161)

N. P. Waterson and H. Deconinck. *A Unified Approach to the Design and Applications of Bounded Higher-order Convection Schemes*. Preprint / Von Karman Institute for Fluid Dynamics. VKI, 1995. (Cited on page 15)

P. Woodward and P. Colella. The numerical simulation of two-dimensional fluid flow with strong shocks. *Journal of Computation Physics*, 54:115–173, 1984. (Cited on page 45)

T. A. Zaki and P. A. Durbin. Mode interaction and the bypass route to transition. *Journal of Fluid Mechanics*, 531:85–111, 2005. (Cited on page 159)

S. Zhang, J. Zhu, and C. W. Shu. A brief review on the convergence to steady state solutions of euler equations with high-order WENO schemes. *Advances in Aerodynamics*, 1(16):25, 2019. (Cited on pages 15 and 47)

S. Zhao. *Explicit and Implicit Large Eddy Simulation of Turbulent Combustion with Multi-Scale Forcing*. PhD thesis, Université D'Orléans, 2016. (Cited on page 46)

X. Zhong and X. Wang. Direct numerical simulation on the receptivity, instability, and transition of hypersonic boundary layers. *Annual Review of Fluid Mechanics*, 44(1):527–561, 2012. (Cited on page 158)

J. Zhu and J. Qiu. A new fifth order finite difference WENO scheme for solving hyperbolic conservation laws. *Journal of Computational Physics*, 318:110–121, 2016. (Cited on pages 15 and 47)

J. Zhu and C. W. Shu. Numerical study on the convergence to steady state solutions of a new class of high order WENO schemes. *Journal of Computational Physics*, 349:80–96, 2017. (Cited on pages 15 and 47)

J. Zhu and C. W. Shu. A new type of multi-resolution WENO schemes with increasingly higher order of accuracy. *Journal of Computation Physics*, 375:659–683, 2018. (Cited on pages 15 and 47)

J. Zhu and C. W. Shu. Convergence to steady-state solutions of the new type of high-order multi-resolution WENO schemes: a numerical study. *Communications on Applied Mathematics and Computation*, 2:429–460, 2019. (Cited on pages 15, 47, and 61)